

# Challenges of Li- and Mn-Rich Cathodes Regarding their Scale-Up Process in Li-Ion Batteries

Tanja S. Zünd

Vollständiger Abdruck der von der TUM School of Natural Sciences der Technischen  
Universität München zur Erlangung einer  
Doktorin der Naturwissenschaften (Dr. rer. nat.)  
genehmigten Dissertation.

Vorsitz: Prof. Dr. Marc-Georg Willinger

Prüfer\*innen der Dissertation:

1. Prof. Dr. Hubert A. Gasteiger
2. Prof. Dr.-Ing. Rüdiger Daub

Die Dissertation wurde am 19.06.2023 bei der Technischen Universität München  
eingereicht und durch die TUM School of Natural Science am 07.07.2023  
angenommen.



# Abstract

When reading newspaper articles around the topic of batteries one could get the impression that each week a breakthrough technology arrives on the market that offers high energy and high power batteries based on materials that are naturally abundant and cheap. One of the reasons that extensive research in this area is still needed is the scale-up challenge of such promising technologies. It is a very long way from material research in which a material with a highly interesting energy-storage property is discovered to a large-scale producible battery cell that offers the requested properties for a long lifetime with a minimum of safety concerns under real live conditions.

In this thesis the aim was to show part of this challenges in the framework of a multidisciplinary project for a promising but not yet commercialized cathode active material (CAM). Together with three other Chairs of the Technical University of Munich, the scale-up of the various cell production processes was examined for a high energy and cost-effective lithium- and manganese-rich NCM material (LMR-NCM). The process starts with a design phase where the different perspectives are shown regarding the optimization of an electrode active material on the electrode level vs. the optimization concerning the full-cell performance for given requirements. The next stage of the thesis is focused on two main challenges that appeared during the transfer to the pilot line production, namely the calendaring of the cathode electrode and the formation of the cell. The former required the development of a holistic understanding of the CAM and the electrode pore structure, and the latter was addressed by studying the overall gas evolution with respect to the formation temperature and time. Based on the significant temperature rise that was observed during cycling of the produced multilayer 7 Ah pouch cells, in the second part of the thesis focus is placed on the origin and effect of the cathode active material's inherent voltage hysteresis between the charge and discharge process. The amount of "lost" energy due to the current independent voltage hysteresis was measured time-resolved with the help of *in situ* microcalorimetry. On the material level, different diffraction techniques were used to understand the structural changes that lead to this unusual behaviour.

# Kurzfassung

Liest man Zeitungsartikel zum Thema Batterien, gewinnt man den Eindruck, dass jede Woche eine neue bahnbrechende Technologie auf den Markt kommt, welche hohe Energie und Leistung mit günstigen und reichlich vorhandenen Materialien bietet. Einer der Gründe weshalb in diesem Bereich noch viel geforscht werden muss ist die Herausforderung, diese vielversprechenden Technologien in großem Maßstab umzusetzen. Es ist ein langer Weg von der Materialforschung, bis zu einer im Großmaßstab herstellbaren Batteriezelle, die unter realen Bedingungen ihre Leistung über eine lange Lebensdauer mit einem Minimum an Sicherheitsbedenken erbringt. Ziel dieser Arbeit war es, einen Teil dieser Herausforderungen in einem multidisziplinären Projekt für ein vielversprechendes, aber noch nicht kommerzialisiertes Kathodenaktivmaterial (KAM) aufzuzeigen. Mit drei weiteren Lehrstühlen der Technischen Universität München wird die Hochskalierung der verschiedenen Prozessschritte der Batteriezellproduktion für ein energiereiches und günstiges Li- und Mn-reiches NCM-Material (LMR-NCM) untersucht. Dies beginnt mit einer Designphase, in der die unterschiedlichen Perspektiven hinsichtlich der Optimierung eines Materials auf der Elektrodenoberfläche vs. der Optimierung hinsichtlich der gesamten Zelleistung für gegebene Anforderungen aufgezeigt werden. Die nächste Phase konzentriert sich auf zwei Hauptprobleme, die bei der Überführung in die Pilotproduktion auftraten: das Kalandrieren des Kathodenmaterials und die Formierung der Zelle. Der erste Punkt wird im Hinblick auf ein ganzheitliches Verständnis der Porenstruktur des KAM's und der Elektrode behandelt und der zweite Punkt bezieht sich auf die Gasentwicklung. Auf der Grundlage der während des Betriebs beobachteten Temperaturerhöhung der produzierten 7 Ah-Pouch-Zelle, wird im zweiten Teil der Arbeit der Schwerpunkt auf den Ursprung und die Auswirkungen der Spannungshysterese zwischen dem Lade- und dem Entladevorgang gelegt. Die Verlustenergie aufgrund der stromunabhängigen Überspannung wurde mit *in situ* Mikrokalorimetrie zeitaufgelöst gemessen. Auf der Materialebene wurden verschiedene Beugungstechniken eingesetzt, um die strukturellen Veränderungen zu verstehen, die zu diesem ungewöhnlichen Verhalten führen.

# Contents

<b>1</b>	<b>INTRODUCTION .....</b>	<b>1</b>
<b>2</b>	<b>THEORY .....</b>	<b>7</b>
2.1	THE LITHIUM-ION BATTERY BASIC WORKING PRINCIPLE.....	7
2.2	LIB CATHODE ACTIVE MATERIALS.....	11
2.3	PROSPECTS OF NEXT-GENERATION LI- AND MN-RICH NCMs AS CATHODE ACTIVE MATERIALS.....	14
2.3.1	<i>LMR-NCM Crystal Structure .....</i>	<i>14</i>
2.3.2	<i>The Redox-Processes in LMR-NCMs .....</i>	<i>15</i>
2.3.3	<i>The OCV-Hysteresis of LMR-NCM .....</i>	<i>16</i>
2.3.4	<i>The Gassing behaviour of LMR-NCM .....</i>	<i>18</i>
2.4	LIB ANODE ACTIVE MATERIALS.....	20
2.5	ELECTROLYTES & SEPARATORS FOR LIBS .....	22
2.5.1	<i>LIB Electrolytes.....</i>	<i>22</i>
2.5.2	<i>The Separator .....</i>	<i>23</i>
2.6	LIB CELL FORMATS AND SYSTEMS.....	24
<b>3</b>	<b>SPECIFIC METHODS OF THIS THESIS .....</b>	<b>27</b>
3.1	LIB ENERGY DENSITY CONSIDERATIONS .....	27
3.1.1	<i>Choice of the Development Level for Cell Optimization.....</i>	<i>27</i>
3.1.2	<i>Maximization of the Energy Density at a Given C-rate.....</i>	<i>30</i>
3.1.3	<i>Utilization of the Half-Cell Data in the “Cell Configuration Tool” .....</i>	<i>35</i>
3.2	(LONG-TERM) GASSING MEASUREMENTS .....	37
3.2.1	<i>Temperature/Material Dependence of LMR-NCM Performance and Gassing .....</i>	<i>37</i>
3.2.2	<i>OEMS Measurements of Cell Gassing.....</i>	<i>39</i>
3.2.3	<i>Method to Determine Long-Term Gassing Rates.....</i>	<i>43</i>
<b>4</b>	<b>RESULTS.....</b>	<b>51</b>
4.1	THE CHALLENGE OF UP-SCALING THE PRODUCTION OF LI- AND MN-RICH BASED CELLS.....	52
4.2	PERFORMANCE AND CYCLE LIVE OF MULTILAYER-POUCH CELLS WITH LMR-NCM CATHODES .....	77
4.3	<i>INVESTIGATIONS ON THE ORIGIN OF THE LMR-NCM OCV-HYSTERESIS .....</i>	<i>91</i>
4.4	<i>SOC-DEPENDENT HEAT RELEASE ASSOCIATED WITH THE OCV-HYSTERESIS .....</i>	<i>111</i>
<b>5</b>	<b>CONCLUSIONS AND OUTLOOK.....</b>	<b>129</b>
<b>6</b>	<b>REFERENCES .....</b>	<b>135</b>
<b>7</b>	<b>ACKNOWLEDGEMENTS.....</b>	<b>145</b>

<b>8</b>	<b>SCIENTIFIC CONTRIBUTIONS .....</b>	<b>147</b>
<b>9</b>	<b>CURRICULUM VITAE.....</b>	<b>149</b>

# List of Abbreviations

<b>Abbreviation</b>	<b>Description</b>
AM	active material
BET	Brunauer-Emmett-Teller
BEV	battery electric vehicle
BMS	battery management system
CAM	cathode active material
CB	carbon black
CE	coulombic efficiency
CE	counter electrode
CC	constant current
CCCV	constant current/constant voltage
CV	constant voltage
DEC	diethyl carbonate
DMC	dimethyl carbonate
EC	ethylene carbonate
EE	energy efficiency
EIS	electrochemical impedance spectroscopy
EMC	ethyl methyl carbonate
FCEV	fuel cell electric vehicle
FEC	fluoroethylene carbonate
GWRE	gold wire reference-electrode
HFR	high frequency resistance
ICEV	internal combustion engine vehicle
LAB	lead acid battery
LCO	lithium cobalt oxide ( $\text{LiCoO}_2$ )
LFP	lithium iron phosphate ( $\text{LiFePO}_4$ )
LFR	low frequency resistance
LIB	lithium-ion battery
LMO	lithium metal oxide
LMR-NCM	lithium- and manganese-rich NCM ( $\text{Li}[\text{Li}_x\text{M}_{1-x}]\text{O}_2$ )
LNMO	lithium nickel manganese oxide ( $\text{LiNi}_{0.5}\text{Mn}_{1.5}\text{O}_4$ )
LP57	EC:EMC solvent mixture (3:7 by weight) with 1M $\text{LiPF}_6$

LP57-2	LP57 electrolyte with 2% VC
LTO	lithium titanate ( $\text{Li}_4\text{Ti}_5\text{O}_{12}$ )
MS	mass spectrometer
NCA	lithium nickel cobalt aluminium oxide ( $\text{Li}[\text{Ni}_{1-x-y}\text{Co}_x\text{Al}_y]\text{O}_2$ )
ND	neutron diffraction
NGO	Non-Governmental Organization
NMP	N-methyl-2-pyrrolidone
NMR	nuclear magnetic resonance
NPD	neutron powder diffraction
OCV	open circuit voltage
OEMS	on-line electrochemical mass spectrometry
PE	polyethylene
PP	polypropylene
PVDF	polyvinylidene difluoride
SEI	solid electrolyte interphase
SEM	scanning electron microscopy
SOC	state of charge
SOH	state of health
TM	transition-metal
TR	thermal runaway
VC	vinylene carbonate
WE	working electrode
XPD	x-ray powder diffraction

# 1 Introduction

Ever since Alessandro Volta presented the voltaic pile over 200 years ago, battery technology has been a key factor in the development of many other fields of technology. Today, probably the mostly discussed uses of batteries are for portable electronics, electric mobility, and grid storage. However, the oldest, still widely used rechargeable battery is the lead acid battery (LAB). At rather low costs, it provides high surge currents as a starter battery and serves as motive power battery or as stationary storage battery. LABs covered around 30% of the 2019 battery demand.<sup>1</sup> However, with an energy density of around 30 Wh/kg<sub>cell</sub>, they are far away of the >250 Wh/kg<sub>cell</sub> currently desired for portable electronics or electric vehicles.<sup>2,3</sup> The first commercialization of a Li-ion battery by Sony Corporation used a soft-carbon anode and a lithium-cobalt-oxide (LCO) cathode achieving an energy density of  $\approx 80$  Wh/kg<sub>cell</sub>.<sup>4</sup> In order to reach the energy densities required for their use in electric cars, the host materials of both electrodes have been optimized over the last years: the carbon has been replaced by graphite, optionally with 1-20 wt% of silicon, and for the cathode electrode, Ni-rich layered metal oxides dominate the commercial market. These developments went hand in hand with cell setup improvements, and both were needed to increase the energy density by a factor of three.

Some of the first questions when Li-ion battery research for electric mobility is discussed in public include: Do we need a further improvement of the energy density or what is limiting the use of batteries? Are batteries the solution to change to a fossil fuel free car mobility? To answer these questions, it is necessary to combine different perspectives, but as a first step here a pure energy balance approach is used. The two mainly discussed alternatives for internal combustion engine vehicles (ICEV), namely battery electric vehicles (BEV) and fuel cell electric vehicles (FCEV) are compared. Alternative mobility solutions are only long-term alternatives if their energy is provided from renewable primary energy sources like solar, wind, biomass, geothermal, or hydro energy. Such renewable energy sources are generally affected by their fluctuating availability, but it can be assumed here

that this can be compensated by large energy storage installations (either by stationary batteries, by pumped water storage power plant, by liquid hydrogen storage, etc.). As large-scale battery and fuel cell productions for electric vehicles has evolved very recently, reliable data about long-term production and recycling costs are almost impossible to obtain, and are therefore not considered for this estimation. In the study of Ligen et al.,<sup>5</sup> a comparison of FCEVs and BEVs with ICEVs was made, whereby they assumed the following energy demand: 17 kWh/100 km (BMW i3) with a variance of 15-29 kWh/100 km for BEVs, and 0.9 kg of hydrogen/100 km (Toyota Mirai) with a variance of 0.9-1.2 kg/100 km for FCEVs. Their breakdown energy calculation from grid/pump-to-car shows an efficiency for the transport, storage, and distribution of electricity of for BEVs between 66-78% (the lower number accounts for an intermediate stationary storage), while for the generation of hydrogen for FCEVs and for its transport, storage and distribution an efficiency of 57-60% is given (the lower number is related to 70 MPa compared to 35 MPa H<sub>2</sub> storage). These numbers must further be reduced by the demand for operating the renewable energy source, resulting in efficiencies ( $E_{\text{output}}/ E_{\text{output-operating}}$ ) from 87% for photovoltaics up to 99% for hydro-electric power plants. Finally, by taking the efficiency of the battery engine system (81-87%) and the fuel cell system (45%) in the car into account, an overall energy efficiency from well-to-wheel of 47-67% for BEVs and 22-27% for FCEVs is calculated. These numbers are summarized and compared with ICEVs in Table 1, showing that both of the alternative propulsion technologies are, even when considering an intermediate energy storage, more energy efficient than most combustion engine-powered vehicles that have an overall efficiency of only 14-26%.

**Table 1: Efficiencies of energy transformation from well-to-wheel (as a product of the well-to-grid/pump, the grid/pump-to-car and the car-to-wheel efficiencies) calculated for internal combustion engine vehicles (ICEVs), battery electric vehicles (BEVs), and fuel cell electric vehicles (FCEVs).**

	ICEV	BEV	FCEV
well-to-gid/pump	83-89% <sup>6,7</sup>	87-99 <sup>8</sup>	87-99 <sup>8</sup>
grid/pump-to-car	99% <sup>6</sup>	66-78% <sup>5</sup>	57-60% <sup>5</sup>
Car-to-wheel	17-30% <sup>9-11</sup>	81-87% <sup>7,9</sup>	45% <sup>9</sup>
<b>Well-to-wheel</b>	<b>14-26%</b>	<b>47-67%</b>	<b>22-27%</b>

In Figure 1, a conversion of the grid-to-wheel step by Ligen et al.<sup>5</sup> is provided, including an intermediate storage option (lower efficiency of line 2 in Table 1), in a more representative way with the possible driving range with 100 kWh grid energy.

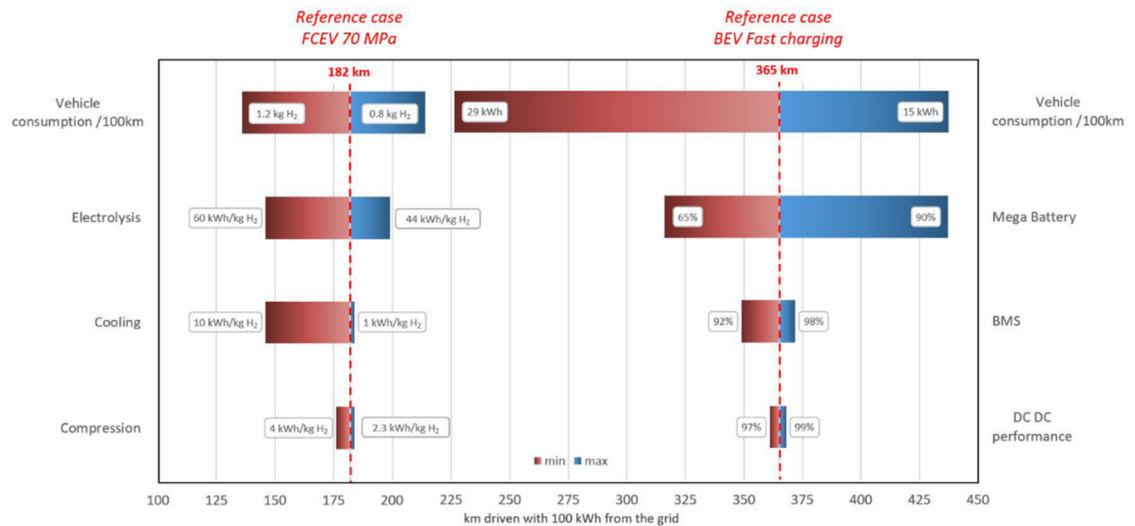


**Figure 1: Comparison of driving ranges of FCEVs (0.8-1.2 kg H<sub>2</sub>/100 km;) and BEVs (15-29 kWh/100 km) with 100 kWh of grid energy, reprinted from “*Mobility from Renewable Electricity: Infrastructure Comparison for Battery and Hydrogen Fuel Cell Vehicle*” by Ligen et al.,<sup>5</sup> licensed under [CC BY 4.0](https://creativecommons.org/licenses/by/4.0/).**

A more recent report published by the NGO “Transport and Environment” includes a similar comparison of grid/pump-to-wheel efficiencies.<sup>12</sup> The authors reported 77 % efficiency for BEVs (compared to 53-68 % by Ligen et al.) and 33 % for FCEV (compared to 26-27% by Ligen et al.). The study assumes a combustion engine efficiency of 30-36% (for petrol/diesel engines), and the author compares these numbers further with the efficiency of eFuels and methane powered engines. The efficiency numbers in this newer study are overall a little higher (due to the more up-to-date efficiency data, but providing fewer included technical details). Consistent is the ratio of efficiency (2.3x higher for BEVs than FCEVs) and the conclusion that the two technologies are currently the most promising alternatives for fossil fuels regarding an efficient energy conversion.

Simply from an energy conversion efficiency perspective, batteries seem to be the first choice. However, hydrogen has similar to fossil fuels ( $\approx 12$  kWh/kg)<sup>13</sup> a very high gravimetric energy density (35 kWh/kg),<sup>14</sup> and the charging speed is around 15 times faster than for BEVs.<sup>5</sup> Based on this, hydrogen fuel cells may be most

suitable for powering high energy demanding vehicles (like busses or trucks), at least until there are engineering solutions like multi-plug charging.

In 2019, Germany needed 725 TWh<sup>15</sup> of energy (sum of all primary energy sources used) for its transport sectors, which divides into 49% for private street transport, 32% for bus and trucks, 14% for flights, and 2% each for water and rail transport (divided by the European average).<sup>16</sup> In the aim of an 80% electrification of the combusting converted energy, it would be necessary to have an additional energy of 100 TWh for cars, respectively 165 TWh for all transport on the street (calculated with averaged values from Table 1). This means in Germany an overall electricity increase of  $\approx 20\text{-}33\%$  (from the 501 TWh used in 2019), which is quite a challenge, especially regarding the fact that a renewable energy increase of 50-80% would be needed, as at the moment around 40%<sup>17</sup> of the used electricity comes from renewable sources. However, if it is considered that an increase in these sources of 65% over the last 10 years has occurred,<sup>18</sup> this seems not impossible.

If the electrical generation challenge is left to engineering and policies, any battery development still must take account of the fact that future batteries allow for mobility which is cost-competitive with combustion engines and that the availability of the required raw materials can be assured in a sustainable manner.

Most of car components have been optimized for more than 100 years, but the battery used in state-of-the-art BEVs is still quite new, and with 40% of the total cost of a BEV, certainly at a point, where any future optimization would have a large impact.<sup>19</sup> If the cost analysis is broken down even further, 60-75% of the battery price arises from its materials prices,<sup>1,20</sup> with the cathode(30-45%)<sup>1,21</sup> being the most cost-intensive one. While other significant cost factors like separators or copper current collectors face mainly mechanical challenges with regards to weight loss and therefore cost, the cathode active materials (CAMs) have to fulfil in addition several electrochemical functions while also their cost must be reduced. The future battery has therefore to increase the energy/cost ratio and simultaneously fulfil the material's availability boundary conditions. The first point can be reached by using materials that are either cheap or have a high energy storage capacity.

A promising, not yet commercialized CAM that offers both characteristics, is a Li- and Mn-rich layered oxide material (LMR-NCM). While the transition metal

composition of state-of-the-art CAMs is approx. 80-85% nickel, 5-10% cobalt, and residual 5-10% aluminium (for NCA) or manganese (for NCM), LMR-NCMs consist of 25-30% Ni, 5-15% Co, and 60-65% Mn. While ongoing research is aimed toward eliminating cobalt,<sup>22,23</sup> its replacement by nickel just delays the discussion about materials availability and cost reduction. In February 2021, the commodity price for Ni (21 USD/kg)<sup>24</sup> was an order of magnitude higher than that of Mn (2 USD/kg)<sup>25</sup> and also the availability differs by order of magnitude.<sup>26,27</sup> From a capacity point of view, LMR-NCM offers a reversible capacity of around 250 mAh/g,<sup>28-30</sup> compared to state-of-the-art Ni-rich materials (i.e., NCAs and NCMs) with capacities limited to 200 mAh/g,<sup>31</sup> which is a remarkable increase.

One of the topics of this thesis is to point out, that such comparisons are too simplistic and that it is necessary to compare a least the full-cell chemistry system rather than only individual material properties. This includes the needed materials balancing and the inactive materials that are required, as well as the inclusion of the actual cell potential when materials are combined and cycled in an application-oriented mode. In the work for this thesis, the question is addressed to what extent cell performance can be predicted by small lab cells, and the full up-scale process is accompanied of LMR-NCM cells from coin half-cells to multilayer, 7 Ah pouch-cells. On the way, mechanical difficulties arising from a semi-automatic production process are discussed. In the end, electrochemical challenges arising from the increased active-to-passive material ratios in the energy density optimized pouch cells are addressed and compared with the initial lab results. The so-called “OCV-hysteresis”, is considered as one of the most challenging characteristics of the LMR-NCM material, and its impact and origin are discussed in more detail in the second part of this work.



## 2 Theory

### 2.1 The Lithium-Ion Battery Basic Working Principle

A lithium-ion battery (LIB) converts reversible electrical energy (from the grid) to chemical energy (in the battery) or vice versa. In Figure 2, a schematic representation of a LIB working principle is shown. More detailed information about the individual components follows in the subsequent sections.

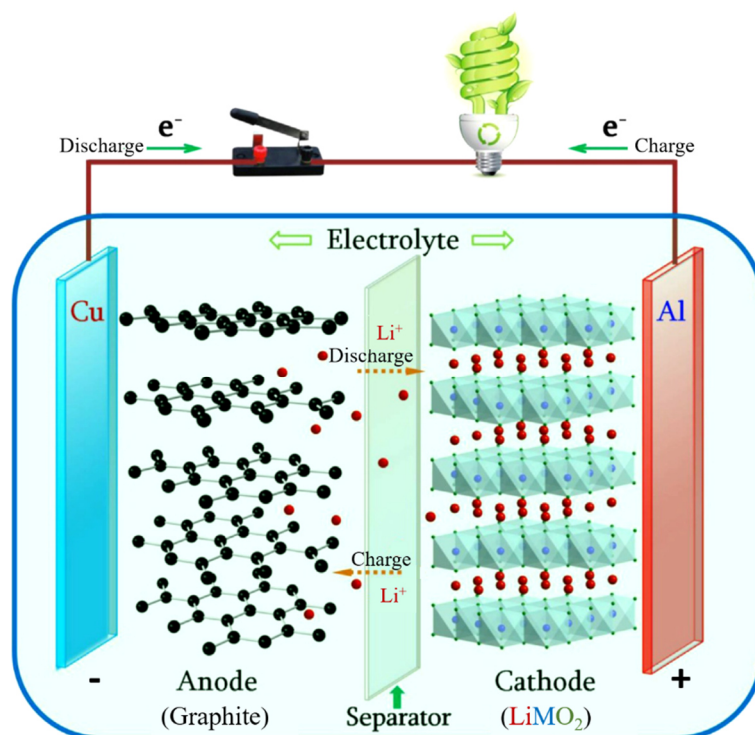
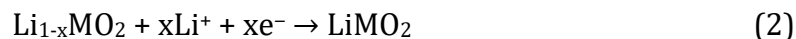


Figure 2: Schematic illustration of the the working principle of lithium-ion batteries, with graphite on the anode side and LMO2 ( $M=Ni_vCo_xMn_yAl_z$ ,  $v+x+y+z=1$ ) on the cathode side, reprinted from "Understanding electrochemical potentials of cathode materials in rechargeable batteries" by Liu et al.,<sup>32</sup> licenced under [CC BY-NC-ND 4.0](https://creativecommons.org/licenses/by-nc-nd/4.0/).

The electrode with the lower lithiation potential (= potential needed to lithiate the active material) is the "negative" electrode. On this electrode, the oxidation reaction occurs in the discharge direction of the battery and the electrode is therefore the anode (by convention, the negative electrode of a LIB is called the anode, independent of the reaction direction). The example in Equation (1) shows the oxidation reaction where the lithiated graphite anode active material is oxidized.

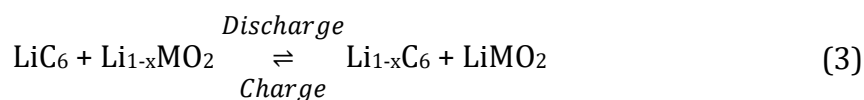


In contrast, the electrode with the higher lithiation potential is the positive electrode, being referred to as the “cathode”. Equation (2) shows the reduction of lithium transition metal oxide, where the transition metal M (or sometimes also oxygen) is reduced.



Both active materials are often mixed with small amounts (0-5 wt%) of conductive agents and binders. The conductive agents serve to electronically connect the active particles better with each other and the current collector (most often the case for the cathode) and/or they open, due to their branched structure, the ionic pathways in the electrolyte phase within the pores of the electrode (applied mostly in anodes). The binder keeps the electrodes flexible and mechanically connects the active material particles with the current collector metal foil. The porous separator electronically isolates the two electrodes while the electrolyte in its pores provides the ion conduction pathway between the electrodes.

The overall reaction of a graphite/lithium transition metal oxide Li-ion battery is shown in Equation (3):



The (dis)charge energy of the battery is defined by the related integral of the cell voltage over the capacity of electron equivalents that can be transferred while (dis)charging. Often this is simplified by the product of the (dis)charge capacity times the average (dis)charge voltage as written in Equation (4). In lithium-ion batteries the so-called “rocking chair” concept describes the back and forward movement of lithium-ions between two electrodes. As each reduced lithium-ion takes up one electron, the capacity of the electrodes can be directly correlated with the amount of lithium that can be reversibly stored within the electrodes. The obtained voltage is the difference between the two electrodes’ lithiation potential minus the overpotential obtained by applying a current.

$$\text{Energy (Wh)} = \text{Capacity(Ah)} \times \phi \text{ Cell Voltage (V)} \quad (4)$$

To compare different active materials, cell setups, or battery systems, the energy is normalized either by weight referred to as gravimetric energy density (Wh/kg), or

by volume, referred to as volumetric energy density (Wh/l). Batteries are further characterized by their electrical power capability which describes the amount of energy that can be released over a given amount of time or, like written in Equation (5), the current that is provided while (dis)charging.

$$\begin{aligned} \text{Power (W)} &= \text{Capacity (Ah)} \times \text{Cell Voltage (V)} / \text{Time (h)} \\ \text{Power (W)} &= \text{Current (A)} \times \text{Cell Voltage (V)} \end{aligned} \quad (5)$$

The unit of the current is generally given in Ampere (A) or Coulomb per second (C/s). For simple comparison of charge discharge capabilities of cells, the applied current is often given with respect to the overall capacity of the battery cell referred to as “C-rate”. The current of the C-rate is defined by X times the cell capacity, where 1/X is the time (in h) during which the capacity of the cell can be fully charged or discharged. Mathematically, this is described by the relation in Equation (6).

$$\text{C - rate (A)} = XC = X(1/h) * \text{Cell Capacity (Ah)} \quad (6)$$

The difference between the charge and discharge process is usually described by efficiencies. The ratio of exchanged charge carriers (capacity) is defined by the round-trip coulombic efficiency (CE) in Equation (7). Values below 100% mean that during the charge of the battery lithium-ions are de-intercalated from the cathode active material without being reversibly intercalated into the anode active material or that additional, non-reversible redox reactions are taking place.

$$\text{Coulombic efficiency CE(\%)} = \frac{\text{Discharge Capacity (Ah)}}{\text{Charge Capacity (Ah)}} \times 100 \quad (7)$$

The round-trip energy efficiency (EE) of a charge/discharge cycle is less than 100% and is a product of the coulombic efficiency and the ratio of the discharge/charge voltages, as given in Equation (8).

$$\begin{aligned} \text{Energy efficiency EE(\%)} &= \frac{\text{Discharge Energy (Wh)}}{\text{Charge Energy (Wh)}} \times 100 \\ &= CE \times \frac{\text{Discharge Voltage (V)}}{\text{Charge Voltage (V)}} \times 100 \end{aligned} \quad (8)$$

The term “overpotential” in general describes the deviation of the measured cell potential from their thermodynamic reversible potential. This can be caused by

several kinetic and transport resistances. The overpotentials lead to a higher charge and a lower discharge potential than the thermodynamically given open circuit voltage (OCV). The non-electrochemically transferred (“loss”) energy that corresponds to the area between the charge/discharge curves is dissipated as heat and corresponds to the colored area in Figure 3. The overall cell resistance consists of ohmic (electrical and bulk material related), activation, and mass transport-related contributions. In Figure 3, the ohmic resistances are separated into the contributions of the electron transport in the current collector system (cc) and the lithium-ion transport through the potential gradient within the electrolyte (ohm, elyte). The mass-transport related overpotential is divided into the individual concentration gradient of lithium-ions due to either solid-state lithium transport within the active materials (conc, an & conc, ca), or due to gradients within the electrolyte phase (conc, elyte). The activation overpotential (act) arises due to the individual charge-transfer resistances at the active material/electrolyte interfaces of anode and cathode.

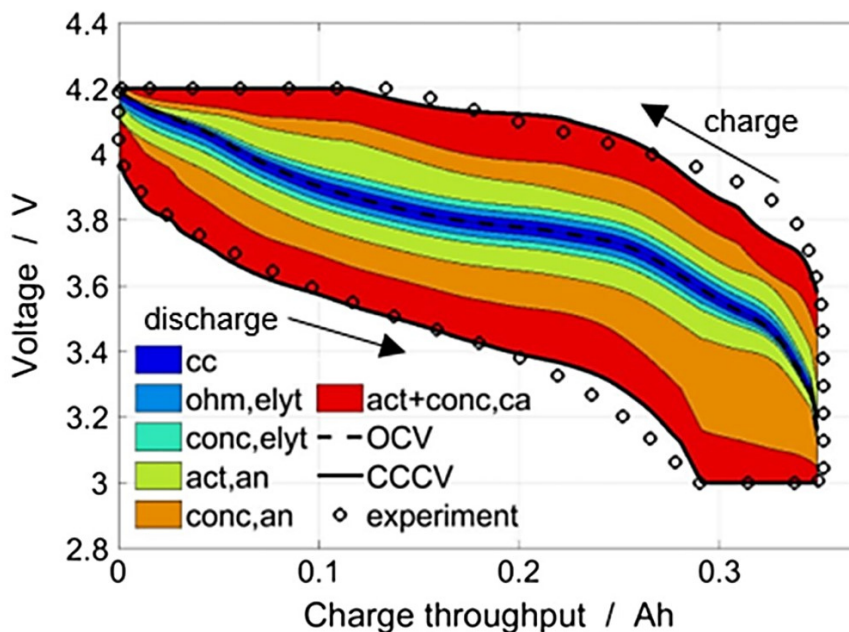


Figure 3: Simulated discharge and charge curves of a NCA-LCO blend/graphite cell at 5C and 20°C with deconvoluted overpotential contributions. Reprinted figure from “Model-Based Overpotential Deconvolution, Partial Impedance Spectroscopy, and Sensitivity Analysis of a Lithium-Ion Cell with Blend Cathode” by Quarti et al.,<sup>33</sup> licensed under [CC BY 4.0](https://creativecommons.org/licenses/by/4.0/).

## 2.2 LIB Cathode Active Materials

Ever since Goodenough and co-workers introduced  $\text{LiCoO}_2$  (LCO)<sup>34</sup> in 1980, which can be paired with a graphite anode, the cathode active material has been the active lithium source and determines the capacity of the full-cell. In terms of the previously used classical LIB described in Section 2.1, it can be seen in Figure 4a) that the gravimetric energy density of the cell is largely governed by the cathode.<sup>35</sup> Furthermore, if the cost of the electrode materials<sup>21</sup> shown in Figure 4b) is included, it is clear that an improvement of the energy/cost term is most effectively reached with the development of the cathode material.

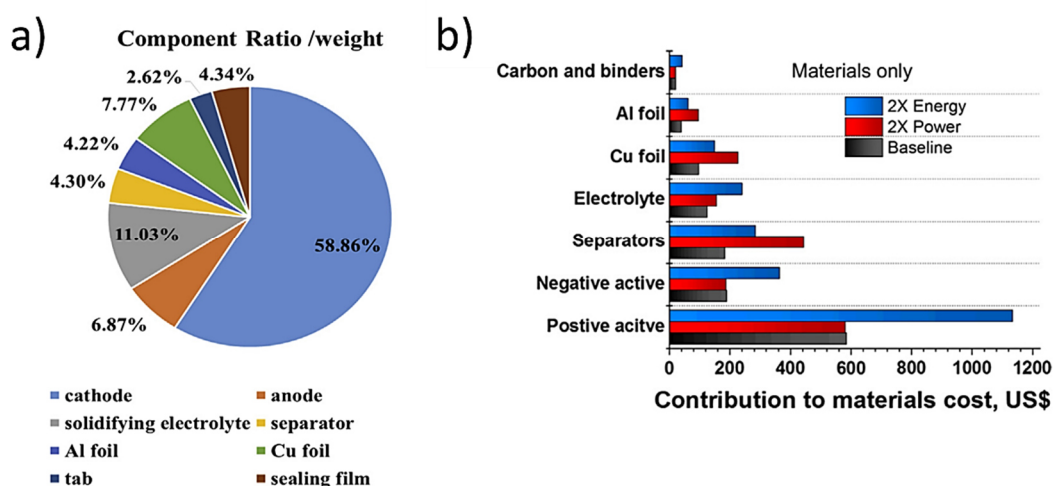


Figure 4: a) The weight ratio of the cell components in a Li/NCA pouch cell, reprinted with permission from “*Practical Evaluation of Li-Ion Batteries*” by Li,<sup>35</sup> copyright 2019 by Elsevier Inc. b) calculated cost breakdown for a baseline 50-kW, 8-kWh PHEV20 based on NCA-Gr. The changes in cost structure from doubling the power or doubling the energy, reprinted with permission from “*Manufacturing Costs of Batteries for Electric Vehicles*” by Gallagher et al.,<sup>21</sup> copyright 2014 by Elsevier B.V.

LCO and generally the  $\text{LMO}_2$  ( $\text{M}=\text{Ni}_v\text{Co}_x\text{Mn}_y\text{Al}_z$ ,  $v+x+y+z=1$ ) materials are cathodes belonging to the so-called layered oxide materials, shown in Figure 5a). The transition metals (M) and the lithium-ions occupy the octahedral sites of alternating layers of a cubic close-packed stacking sequence of the oxide ions.<sup>36</sup> The theoretical capacity for complete lithium extraction in  $\text{LiCoO}_2$  amounts to 274 mAh/g, but the practical capacity is limited to  $\approx 140$  mAh/g, because the structure is unstable at high degrees of delithiation, where poorly reversible phase transitions and/or the irreversible loss of oxygen from the lattice occur.<sup>37</sup>

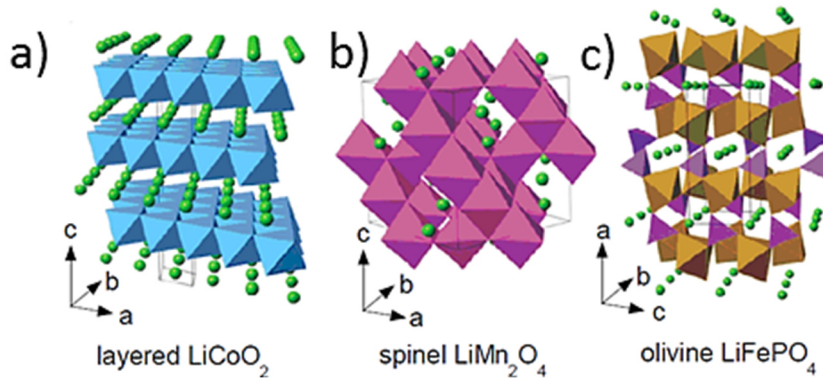


Figure 5: Crystal structure of the three lithium-insertion compounds in which the  $\text{Li}^+$ -ions are mobile through the 2-D (layered), 3-D (spinel), and 1-D (olivine) frameworks. Reprinted from “*Comparative Issues of Cathode Materials for Li-Ion Batteries*” by Julien et al.,<sup>36</sup> licensed under [CC BY 3.0](https://creativecommons.org/licenses/by/3.0/).

In addition to the limited capacity due to structural instabilities of LCO, also the price of cobalt ( $\approx 3$  times higher than for example  $\text{Ni}^{38}$  and  $\approx 26$  times higher than  $\text{Mn}^{25}$ ) as well its availability and the ethical questionable aspects of mining the material<sup>39</sup> has motivated the search for alternatives. Staying with the structure of layered oxides, a widely used approach started to partially substitute the cobalt with nickel and manganese<sup>40</sup> or with nickel and aluminum.<sup>41</sup> The first resulted in the so-called NCM materials which initially were made with a Ni/Co/Mn atomic ratio of 1/1/1 (called NCM-111, with  $\approx 160$  mAh/g), subsequently synthesizing materials with higher Ni content (for example NCM-811, that has a practical capacity of  $\approx 200$  mAh/g). The alternative layered oxide state-of-the-art material is also nickel-rich but instead of manganese a small amount of aluminium is used (called NCA that also delivers  $\approx 200$  mAh/g).<sup>42</sup> For both material classes, the future trend is to reduce the cobalt amount to below 1 % and to further increase the nickel content.<sup>43,44</sup> The use of iron as a redox active metal ( $\approx 500$  times less expensive than cobalt)<sup>38</sup> would be even more cost effective, however, it does not crystallize in the layered oxide structure.<sup>45</sup> Alternatively, iron can be used in a phospho-olivine structure as shown in Figure 5c) as  $\text{LiFePO}_4$  (LFP). Since oxygen is covalently bonded, LFP is structurally very stable and in combination with its relatively low operational voltage window (average discharge voltage of  $\approx 3.3$  V), it provides a long cycle life and fulfils high safety standards.<sup>46</sup> Disadvantages of LFP are its comparatively low specific capacity (165 mAh/g) and, due to the one-dimensional channels for li-ion transport, a slow solid-state lithium diffusion and a low electronic conductivity.<sup>36</sup> The family of spinel type (in Figure 5b) cathode active materials also provides very good structural stability and Materials like  $\text{LiMnO}_4$  or

$\text{LiNi}_{0.5}\text{Mn}_{1.5}\text{O}_4$  (LNMO) are frequently used in applications.  $\text{LMnO}_4$  is mainly added to NCMs due to its thermal stability and high power capability; it is generally used in combination with other cathode active materials because its inherent capacity of  $\approx 110$  mAh/g is not that interesting.<sup>30,47</sup> LNMO provides due to its high voltage plateau at 4.7 V still a high energy density, despite its relatively low capacity of  $\approx 140$  mAh/g. However, most electrolytes are unstable at such high voltages, resulting in electrolyte decomposition and low cycle life.<sup>46,48</sup> An overview over the here discussed cathode active materials and their characteristics is found in Table 2.

**Table 2: Overview of cathode active materials with regards to their reversible specific capacity, average discharge (dis.) potential vs.  $\text{Li}^+/\text{Li}$ , calculated resulting energy densities, and other characteristics.**<sup>30,45,46,49</sup>

Code	Structure	Spec. capacity (mAh/g)	Dis. potential (V vs $\text{Li}^+/\text{Li}$ )	Energy density (Wh/kg)	Characteristics
LCO	layered	150	3.9	585	+ Good cycle life - Expensive
NCM 111	layered	160	3.8	608	+ Increasing energy density with higher Ni content
NCM 622	layered	180	3.7	666	
NCM 811	layered	195	3.7	722	- Decreasing thermal and cycling stability with higher Ni content
NCA	layered	195	3.7	722	+ High energy and power density - Moderate thermal stability
$\text{LMn}_2\text{O}_4$	spinel	110	4.1	451	+ High power and thermal stability - Low cycle stability
LNMO	spinel	140	4.7	658	+ Inexpensive - Electrolyte instabilities
LFP	olivine	165	3.4	561	+ Good thermal and lifetime stability, inexpensive - Limited capacity

Besides the above discussed commercialized cathode active materials, many more candidates have been discussed in the literature as promising next-generation cathode active materials.<sup>50</sup> Many of them belong either to more disordered structural families (rock-salt or polyanionic compounds like  $\text{Li}_{1+x}(\text{FeNb})_{1-x}\text{O}_2$ ,

Li<sub>2</sub>NiO<sub>2</sub>F, or LiMnPO<sub>4</sub>, Li<sub>2</sub>FeSiO<sub>4</sub>) or undergo a classical conversion reaction (e.g. FeF<sub>3</sub>, sulfur,...). However, redox reactions of such compounds are most often accompanied by irreversible side reactions, and are complicated by the presence/formation of electrically non-conducting phases; furthermore, in many cases, the materials do not provide the cyclable lithium by themselves. Advances in related fields like electrolyte stabilities, pre-lithiation of the anodes, or volume-change mitigation strategies could potentially enable the use of some of these materials for future applications.

## 2.3 Prospects of Next-Generation Li- and Mn-Rich NCMs as Cathode Active Materials

With regard to the next-generation cathode active materials, this section focuses on Li- and Mn-rich layered oxides (LMR-NCM), a material that belongs to the layered transition metal oxide family of NCMs but with some structural differences. LMR-NCMs offer attractive performance benefits, but there remain several challenges that currently hamper their use in commercial applications.

### 2.3.1 LMR-NCM Crystal Structure

In terms of its structure, LMR-NCM can be seen as an NCM where a certain amount of transition metals are replaced with lithium, as visualized in Figure 6 by Rozier et al.<sup>51</sup>

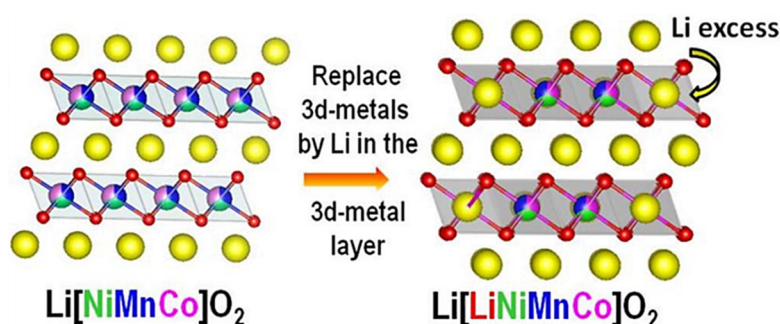


Figure 6: Evolution of the layered oxide chemistry fuelled by cationic substitution within the transition metal layers by partial replacement of Ni/Co/Mn with Li to form Li-rich NMC phases. Reprinted with permission from “Li-Rich Layered Oxide Cathodes for Next-Generation Li-Ion Batteries: Chances and Challenges” by Rozier et al.<sup>51</sup>, copyright 2015 by the Electrochemical Society.

The over-lithiation can be either expressed as  $\text{Li}_{1+x}\text{M}_{1-x}\text{O}_2$  or as  $\text{Li}[\text{Li}_x\text{M}_{1-x}]\text{O}_2$ . The substitution of  $\text{M}^{3+}$  by  $\text{Li}^+$  requires the remaining M elements to have an increasing share of  $\text{M}^{4+}$ , so that the maximum Li content in the transition metal (TM) layer amounts to  $x = 1/3$ .<sup>51</sup>  $\text{Li}[\text{Li}_{1/3}\text{Mn}_{2/3}]\text{O}_2$ , better known as  $\text{Li}_2\text{MnO}_3$ , is one of the well-studied compounds that crystallize in the O3-layered structure.<sup>52-54</sup> In regular (not over-lithiated) NCMs, the transition metals are randomly distributed within the TM metal layer, whereas in  $\text{Li}_2\text{MnO}_3$  one  $\text{LiO}_6$  octahedron is ideally surrounded by six  $\text{MnO}_6$  octahedra in order to form a honeycomb pattern. For the materials discussed within this work, namely with  $x=0.14-0.2 \ll 1/3$ , the in-plane ordering is not as straightforward and in terms of X-ray reflections it is discussed in more detail in Section 4.3. In some of the literature the material is described using a two-phase notation, e.g.,  $y \text{Li}_2\text{MnO}_3 (1-y) \text{LiMO}_2$  ( $y=0.33-0.5$ ), which emphasizes the synthetic background of the material but, as also discussed in Section 4.3, a homogeneous TM distribution with long-range Li ordering appears more reasonable for the material considered in this work.<sup>55</sup>

### 2.3.2 The Redox-Processes in LMR-NCMs

The structural changes due to the over-lithiation lead to interesting follow-up questions. One of them is related to the underlying redox processes. The theoretical capacity of regular NCMs is calculated by assuming each lithium in the Li layer can be de-intercalated as  $\text{Li}^+$  and therefore one of the transition metals must be oxidized to preserve the charge neutrality. For regular NCMs the theoretical capacity (if every TM is oxidized once) is  $\approx 279$  mAh/g. If there is an over-lithiated NCM where some of the TMs are replaced by lithium atoms, they can no longer compensate completely for a full lithium extraction, assuming that the maximum transition metal oxidation state is 4+. Considering the numbers in Table 3 for LMR-NCMs with different degrees of over-lithiation, it can be seen that 1/4 till 1/3 of the capacity cannot be compensated by TM oxidation, implying that it must be compensated by the partial oxidation of the oxygen anions. Charge compensation through oxygen redox has already been discussed in a few instances with regard to regular NCMs,<sup>56</sup> and is the commonly used explanation for the non-TM based charge compensation in over-lithiated NCMs.<sup>57,58</sup>

**Table 3: Theoretical capacities through lithium extraction, TM oxidation, or non-TM based oxidation for NCMs with low (Li/TM=1.14/0.86), mid (Li/TM=1.17/0.83), and high (Li/TM=1.2/0.8) degrees of over-lithiation.**

LMR-NCM material	Low (1.14)	Mid (1.17)	High (1.2)
Theo. capacity through Li extraction	345 mAh/g	361 mAh/g	377 mAh/g
Theo. capacity through TM oxidation	261 mAh/g	256 mAh/g	252 mAh/g
Theo. capacity through non-TM redox	84 mAh/g	105 mAh/g	125 mAh/g

### 2.3.3 The OCV-Hysteresis of LMR-NCM

Even though the OCV-hysteresis is discussed in-depth sections 0 - 4.4, one of its consequences is considered in this section, namely the unique voltage profile of over-lithiated materials. Regarding the voltage profile of LMR-NCMs, three, maybe connected but in appearance different, phenomena are observed and illustrated in Figure 7: a) an activation process during the first charge step, b) discharge voltage fading over cycle life, and c) a current independent voltage hysteresis between the charge and the discharge process (OCV-hysteresis).

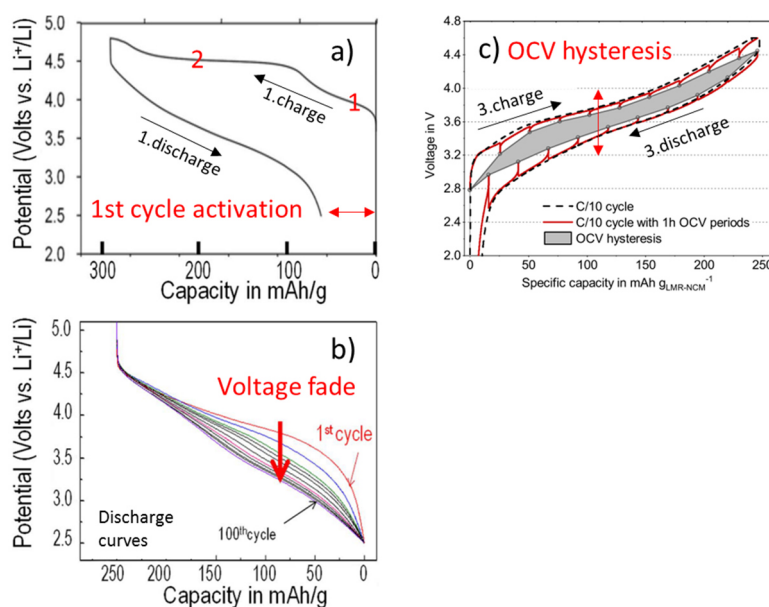


**Figure 7: Illustration of the three voltage profile phenomena discussed in this Section 2.3.3: a) an activation process during the first charge step, b) discharge voltage fading over cycle life, and c) a current independent voltage hysteresis between the charge and the discharge process (OCV-hysteresis). Panel a) and b) are reprinted with permission from “Li-Rich Layered Oxide Cathodes for Next-Generation Li-Ion Batteries: Chances and Challenges” by Rozier et al.,<sup>51</sup> copyright 2015 by the Electrochemical Society, panel c) is reprinted from “Comparative Evaluation of LMR-NCM and NCA Cathode Active Materials in Multilayer Lithium-Ion Pouch Cells: Part II. Rate Capability, Long-Term Stability, and Thermal Behaviour” by Kraft et al.,<sup>59</sup> licensed under [CC BY 4.0](https://creativecommons.org/licenses/by/4.0/).**

One of the drawbacks of LMR-NCMs is often assigned to the poor coulombic efficiency of the first formation cycle.<sup>60-62</sup> However, with the more advanced materials used within this work, very comparable efficiencies were achieved in full-cells within reversible cycling conditions between LMR-NCM (84%) and NCA (85%).<sup>63</sup> The voltage difference between the first and the following charge cycle is still not fully understood. The first-cycle voltage plateau correlates with an initial removal of lithium from the Li layer (indicated with a red 1 in Figure 7a) and secondly a removal of lithium from the TM layer (indicated with a red 2 in Figure 7a)<sup>64,65</sup> accompanied by a switch from cationic to anionic redox activity.<sup>66</sup> Nevertheless, the absolute potential must be dominated by some structural rearrangements to follow afterwards a lower, reversible potential curve. Another drawback of the material is the so-called voltage fading of LMR-NCMs. This “fading” mechanism describes the decrease of lithium site energy and therefore is related to a lowering of the usable energy of the material. The origin of this effect is commonly, assigned to a shift from anionic redox to Mn redox due to a gradual transformation of the layered structure into a spinel-like structure.<sup>67-70</sup> The extent of the voltage fade depends on the transition metal stabilization and with the main material used within this thesis, the decay of the mean discharge voltage is around 0.6 mV/cycle. This is almost three times higher than measured for regular NCMs, but compared to the energy loss between charge and discharge (up to 300 mV/cycle) this seems negligible. The latter phenomena are therefore prioritized in this thesis.

In Section 0, the impact of the OCV-hysteresis on the energy efficiency of the produced battery cells is discussed. With a reduced EE for LMR-NCM cells of 88% compared to the 98% for comparable NCA cells, resulting in a remarkable temperature difference at higher C-rates, this phenomenon particularly relevant for large cells and cell packs, as discussed by Kraft et al.<sup>71</sup> Assuming that the energy inefficiency is due to lost heat, a follow-up question that is important for thermal modelling is, whether the heat release is evenly distributed over the charge and discharge process. These questions in combination with other heat release phenomena within the cell are discussed in Section 4.4.

In a more fundamental approach in Section 4.3, interest has been placed on the question of where does the OCV-hysteresis come from? By the use of *in situ* XRD it was seen that the OCV-hysteresis seems to correlate with a structural hysteresis. With the help of structural refinement of cycled *ex situ* samples, it was further possible to reveal that the structural hysteresis seems to be symmetrical around the TMs (TM-TM distance and TM layer height). All these findings could still be explained by the two most prominent explanations in the literature, namely the TM migration into the Li layer<sup>72</sup> or a hysteresis based on the oxygen redox process.<sup>66</sup> By combining neutron diffraction (ND) that can differentiate better the individual TMs due to their non-weight related scattering factors (in contrast to XRD), there was the hope that one might be able to correlate a possible TM migration with the structural hysteresis. The analysis of the diffraction data itself takes up the major part of the section 4.3, but the discussion of it can also be considered when evaluating other literature in this area. Finally, it can be stated that within the uncertainty of the methods, no correlation could be seen, suggesting that the origin of the OCV-hysteresis is not a simple TM migration mechanism.

#### 2.3.4 The Gassing behaviour of LMR-NCM

Oxygen release is a topic that has to be discussed when talking about a possible commercial application of LMR-NCM. In this thesis, “oxygen release” is often treated in the more general context as gassing. Differentiation is further made between gassing as a challenge with regards to mechanical cell design and cell integrity and gas evolution that can lead to (electro)-chemical follow-up reactions within the cell. The latter phenomena are extensively studied in the literature and the most important reactions for LMR-NCM due to gassing are summarized in Figure 8. Due to either voltage dependent electrolyte decomposition,<sup>73,74</sup> thermally induced FEC decomposition,<sup>75,76</sup> or SOC dependent oxygen release,<sup>77</sup> protons are generated within the cell system. Together with the electrolyte salt, the protons react to HF that further reacts with the cathode surface, forming a resistant LiF layer and dissolving transition metals. Both reactions result in a loss of cyclable lithium, and the TM dissolution further catalyses electrolyte decomposition on the anode side that is accompanied by additional gassing reactions.<sup>78</sup>

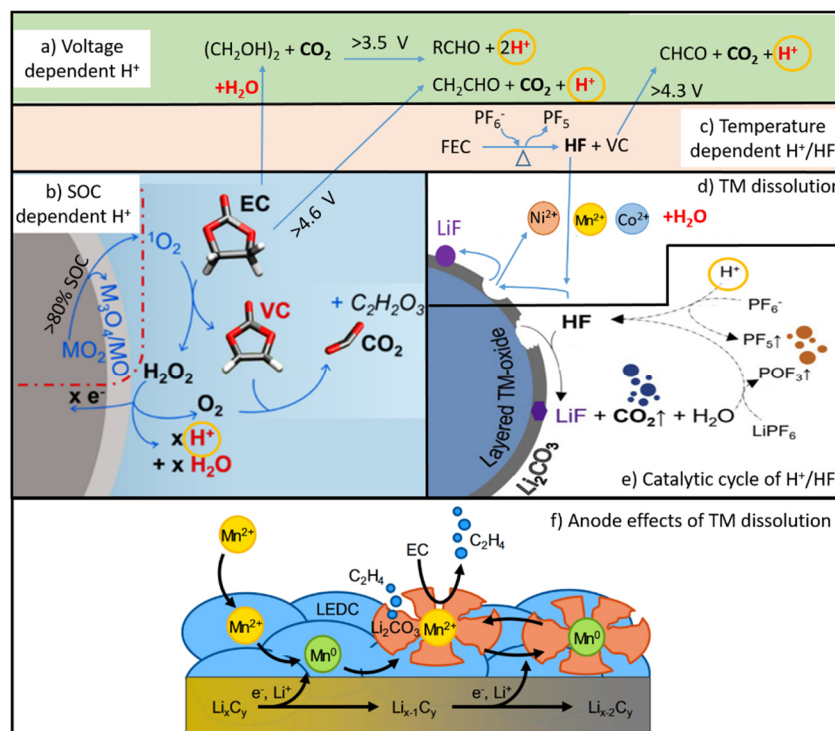


Figure 8: Summary of gassing related reactions in LMR-NCM. Panel a) describes the voltage dependent  $\text{H}^+$  generation described by Metzger et al.<sup>73</sup>, Freiberg et al.<sup>74</sup>, and Pritzl et al.<sup>76</sup> Panel b) describes the SOC dependent  $\text{H}^+$  generation due to singlet oxygen release from the cathode material at high SOC and is reprinted with permission from “*Singlet Oxygen Reactivity with Carbonate Solvents Used for Li-Ion Battery Electrolytes*” by Freiberg et al.,<sup>77</sup> copyright 2015 American Chemical Society. Panel c) describes the thermal FEC decomposition to VC, described by Kim et al.<sup>75</sup> Panel e) describes the catalytic cycle of the generated protons and is reprinted from “*Li<sub>2</sub>CO<sub>3</sub> decomposition in Li-ion batteries induced by the electrochemical oxidation of the electrolyte and of electrolyte*” by Freiberg et al.,<sup>74</sup> licensed under [CC BY-NC-ND 4.0](#). Panel d&f) describe the reactions of the etched-out transition metals and are adapted (separated into panel c & f) from “*Electrolyte and SEI Decomposition Reactions of Transition Metal Ions Investigated by On-Line Electrochemical Mass Spectrometry*” by Solchenbach et al.,<sup>78</sup> licensed under [CC BY 4.0](#).

The mechanical challenges caused by the gas evolving due to any of the undesired reactions shown in Figure 8 are so far almost neglected in the literature. Probably mainly because (mechanical)-gassing studies require realistic ratios of electrode to electrolyte to headspace ratios. This can hardly be achieved in lab-scale cells and therefore multilayer cells are needed, which in turn however, requires cell production equipment. Mechanical challenges due to gassing are related to the pressure build-up inside the battery cell, which may compromise the sealing tightness of the cell, but may also lead to electrical contact problems due to bubbles within the electrode stack that resulting in an inhomogeneous current distribution. A first discussion of these topics is done in Section 3.2 and Section 4.1, but extended studies would certainly help the commercialization of the material.

## 2.4 LIB Anode Active Materials

Even though the cathode is with regards to the energy density and cost reduction the main bottleneck of the current LIB development, it is the anode active material that mainly determines the fast-charging ability of the battery cell and is one of the main reasons for cell aging. The charging rate is limited on the anode side due to the lithium plating process that can occur in parallel to the lithiation of the graphite particles. The higher the charging current, the higher the overpotential (as explained in Section 2.1). If the original reduction potential plus the activation and mass transport overpotential is below the potential for lithium plating (i.e. below 0 V vs. Li<sup>+</sup>/Li), the plating process is favorable.<sup>79</sup> If this plating process arises under non-controlled conditions, it leads to lithium dendrite formation (Li metal branches that grow towards the cathode) which can short-circuit the cell if the electrically insulating separator is penetrated. The same reaction also enhances the so-called solid-electrolyte-interphase (SEI) reaction on the anode side. The SEI is formed by the undesired reduction of electrolyte components on the anode electrode by, parasitic reactions that occur at the interface between the electrolyte and the surface of the anode active material particles. Within this thesis they are sometimes considered because many of these reactions irreversibly consume lithium-ions, which therefore decrease the capacity. Some of the reaction products of the SEI formation lower as well the electrical and the ionic transport through the anode electrode and therefore increase the overpotential of the cell. However, a certain build-up of a surface layer is also necessary to passivate the anode surface and suppress continuous electrolyte reduction reactions.

There are a variety of possible anode materials which have been researched, and Figure 9 summarizes their average discharge potentials and specific capacities given in terms of their theoretical gravimetric (Figure 9a) and volumetric (Figure 9b) capacities.<sup>48</sup> The classical LIB as shown in Figure 2 uses graphite on the anode side. Graphite is an intercalation material and provides a low lithiation potential ( $\approx 0.1$  V vs. Li<sup>+</sup>/Li) and a reversible capacity of around 355 mAh/g. The low potential provides on one hand a high cell potential but on the other hand it is also prone to electrolyte reduction and Li plating.

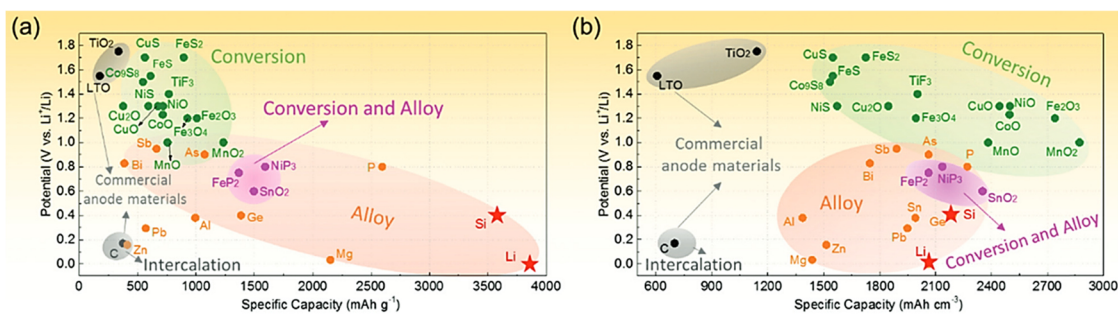


**Figure 9: Approximate range of average discharge potentials versus the specific capacity of the most commonly discussed anode active materials a) gravimetric and b) volumetric capacities. Reprinted with permission from “Guidelines and trends for next-generation rechargeable lithium and lithium-ion batteries” by Wu et al.,<sup>48</sup> copyright 2020 by the Royal Society of Chemistry.**

For applications where cyclability and safety are prioritized over energy density, an alternative commercial material (black in Figure 9) like LTO is used. In energy density optimized cells, state-of-the-art automotive suppliers use small (5-20 wt%) amounts of silicon based compounds within the anode.<sup>80</sup> Silicon itself alloys with lithium and provides a maximum theoretical reversible capacity of 3579 mAh/g forming  $(\text{Li}_{15}\text{Si}_4)$ .<sup>81</sup> However, the full capacity is accompanied by a volume expansion of  $\approx 300\%$ . This expansion leads to a whole cascade of challenges, like continuous growth of the SEI layer and electrical isolation of active material particles within the electrode<sup>82</sup>. To mitigate this problem, the silicon particles are either used as a nano-sized carbon composite,<sup>83</sup> embedded in an amorphous and conductive matrix (as  $\text{SiO}_x$ ,  $x=1-2$ ),<sup>84</sup> or they are only partially lithiated.<sup>85</sup> The addition of the above-mentioned 5-20% of  $\text{SiO}_x$  allows the electrode to be significantly thinner and to increase the charging currents. If higher fractions of small silicon particles are used, surface reactions are also enhanced and too much cyclable lithium is lost. Therefore, various prelithiation<sup>86</sup> methods are currently being researched in order to show which could offer reduced charging times with fully silicon based anodes. The probably most elegant solution would be an anode that would allow homogeneously plate and strip lithium on/from a suitable substrate. So far, the help of high temperature, pressure, special electrolytes, or low cycling rates are still necessary for this solution. These restrictions have to be overcome for a commercially reliable application of this concept.

## 2.5 Electrolytes & Separators for LIBs

### 2.5.1 LIB Electrolytes

The electrolyte system ensures the Li<sup>+</sup>-ion transport between the electrodes. To fulfil this task and to stay inert towards the other cell components, the following requirements have to be fulfilled:

- The lithium salt has to be soluble in a high concentration for good conductivity.
- The Li<sup>+</sup>-ions need to be mobile in an as wide as possible temperature window (e.g., viscosity control over a wide temperature range) for good conductivity.
- The electrolyte must be stable against decomposition within a voltage window of  $\approx 0$  and 4-5 V vs Li<sup>+</sup>/Li.
- The electrolyte must be inert against both electrode materials, the current collector materials as well as the separator within the operated voltage window.
- To increase battery safety, the electrolyte should be non-flammable, with a high boiling point and with a high stability against thermal decomposition.
- To minimize cell weight, the density of the electrolyte should be low.
- The electrolyte should have good wetting properties of the separator and electrodes.

The perfect electrolyte that does not need a trade-off between these points has not been discovered yet, and therefore the right choice depends on the specific application. Standard Li-ion batteries use cyclic ethylene carbonate (EC) in combination with linear carbonates such as dimethyl (DMC), diethyl (DEC), and ethyl methyl carbonate (EMC). EC ensures the dissolution of the salt due to its high dielectric constant, while the linear carbonates decrease the electrolyte viscosity and its freezing point, thus enabling fast Li<sup>+</sup>-ion transport. LiPF<sub>6</sub> is the most used electrolyte salt due to its good solubility and conductivity. This electrolyte system however does have room for improvement regarding electrochemical stability and safety aspects. The carbonates, especially EC are not stable at low potentials; however, by building up an SEI layer on the anode side, this issue can be minimized

but requires further passivating electrolyte properties.<sup>87</sup> The most common SEI-forming additives are vinylene carbonate (VC) and fluoroethylene carbonate (FEC). On the cathode side, the limitation of their stability is at around 4.6 V vs. Li<sup>+</sup>/Li, which further reduces the choice of possible cathode candidates. Various gassing reactions, as described in Figure 8, are the consequences of (electro)-chemical parasitic reactions, and in several studies related to electrolyte additives the goal has been to inhibit these reactions by looking at different additive strategies.<sup>88,89</sup>

A technical solution that once promised to be the brake-through solution for all these problems are solid-state electrolytes. By using a solid, often a glass or a ceramic based ionic conductor, the problem of the thermal stability of classic electrolytes was expected to be solved by ideally also overcoming the electrochemical stability window of liquid electrolytes. In reality, solid electrolytes suffer even more from electrochemical instabilities at their interfaces and still need high cell pressures to overcome contact resistances at the interfaces of the electrolyte and the active materials.<sup>90,91</sup> Although it is indeed the most promising available solution to address the thermal instability of LIBs, and therefore could drastically improve LIB safety, it seems the system itself still needs some more development time to be able to offer this.

### 2.5.2 The Separator

The separator provides electrical separation of the two electrodes while allowing the electrolyte to travel through. The ideal separator should have the following properties:

- Thin and light to keep the cell energy density high.
- Porous in order to allow good Li<sup>+</sup>-ion conductivity between the electrodes.
- Electrochemically inert to avoid reactions within the applied voltage range.
- Mechanically stable to particle penetration (shortcut prevention).
- Thermally stable regarding porosity changes and shrinkage.

Even though thin separators naturally have less mechanical stability towards penetration, the thickness of separators has been substantially decreased over the last decade. Classically a porous layers of 9-25 μm thick polymer films (for example

polypropylene (PP)) have been used for separators. While these materials fulfil the first three points of the list above, the safety aspects seem to be the most critical ones. This used to be addressed with the so-called “shutdown” separators,<sup>92</sup> consisting of 3 layers (PP/polyethylene(PE)/PP) with the middle layer being of a material with lower melting point. In this case, of when the cell temperature gets too high, for example due to overcharge, the middle layer melts and closes the pores and thereby blocks the ionic pathway between anode and cathode. This approach may help successfully against the initial short-circuit, however at a certain temperature (around 160°C) also PP starts to melt and the bigger the cell format, the less time there is available to make the shutdown mechanism work. For better thermal, but also mechanical stability, most of the currently used separators have a thin ceramic coating. The coating makes them very robust against the thermal impact, but is not trivial to apply, as the coating process itself requires the use of binders and solvents. For these coatings, the first three points need to be addressed again and they depend on the chosen cell chemistry. The porosity, which is linearly correlated to the separator performance that is dominated by the tortuosity,<sup>93</sup> is a key parameter to address.

## 2.6 LIB Cell Formats and Systems

In the previous chapters, the individual materials within the cell were discussed. This part addresses the “Cathode-Separator-Electrolyte-Anode” composition in the energy system for possible applications. The final energy system requires a certain power (W) or a combination of voltage (V) and current (A) with in most cases an as high as possible capacity (Ah). The charge averaged discharge cell voltage depends as discussed in Section 2.1 on the current and is for NCM-Graphite based cells normally between 3.5-3.8 V. The capacity of the cell can vary from a few mAh up to 100 Ah and depends on the application as well as the cell format. The latter is related to how separator/anode/separator/cathode layer (upper part in Figure 10) is packed into the cell case. Single layers are used in coin cells (right upper part in Figure 10) but the inherent energy is thus very limited. For applications in most power tools or electric vehicles, one of the three lower shown options in Figure 10 is chosen. All three options have made it into the electric vehicle market and it

would exceed the scope of this work to discuss them in detail, but when choosing a certain cell format, the following points are usually considered:

- Volumetric and gravimetric packing density in a given application.<sup>94</sup>
- Safety, especially propagation and thermal runaway (TR) containment of the cells integrated into an application.
- Fabrication and quality effort/costs.
- Thermal management of the cells in the application.

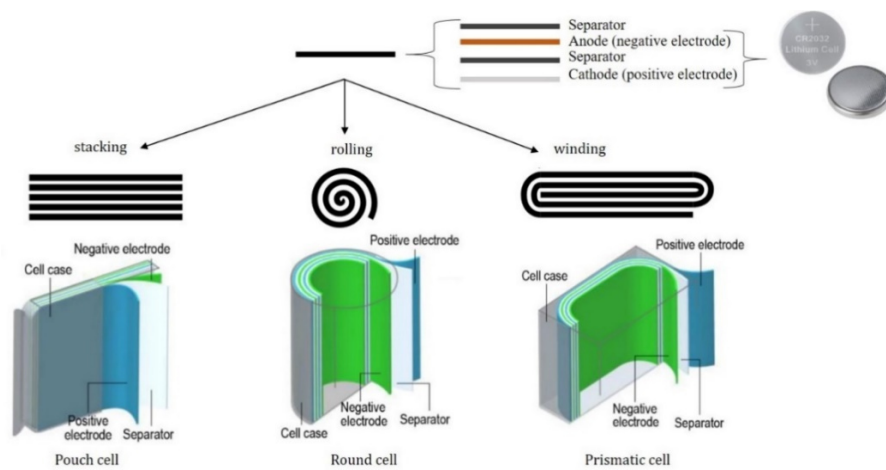


Figure 10: Overview of the most common cell formats (pouch cell, round cell, and prismatic cell) obtained by either stacking, rolling, or winding of the cell material layers. The upper part of the figure is reprinted from “*Implications of the Heat Generation of LMR-NCM on the Thermal Behaviour of Large-Format Lithium-Ion Batteries*” by Kraft et al.,<sup>71</sup> licensed under [CC BY 4.0](https://creativecommons.org/licenses/by/4.0/) and supplemented with the cell stack break down. The lower part of the figure (schematic cell images) is reprinted with permission from “*Making the Case for Electrified Transportation*” by Bilgin,<sup>95</sup> copyright 2015 by IEEE.

Depending on the operating voltage of the energy system, the cells are connected in parallel (left side in Figure 11) and/or in serial (right site in Figure 11). The current and voltage of the connected cells in most applications is controlled by the battery management system (BMS), where additional features like temperature or pressure control are added, and where the status of the battery is monitored. All measurements, diagnostics, and performance data within this work focus on single-cell data and a deeper dive into this topic is not provided.

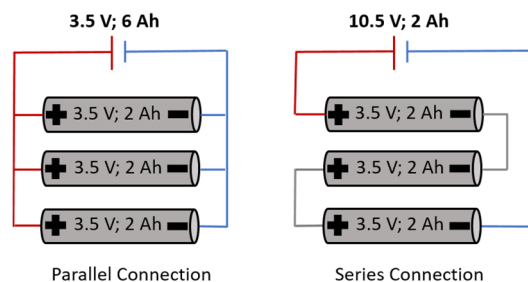


Figure 11: Schematic of a parallel (left side) and a series (right side) circuit with a 2 Ah cells of 3.5 V.



## 3 Specific Methods of this Thesis

### 3.1 LIB Energy Density Considerations

The overall aim of the government-funded project (ExZellTUM II)<sup>96</sup> was to transfer the manganese-rich chemistry from a lab-scale to a semi-automated prototype production line. The first milestone required that the produced cell should have a gravimetric energy density of at least 150 Wh/kg at a 1C discharge rate. The subsequent questions related to these requirements were:

- How can the energy density be maximized at this C-rate?
- On which development level is it necessary to optimize the cell i.e., what can be optimized using coin cells and what requires the final multilayer pouch cells.
- How can the scaling effects be estimated?

The third question was not answered in general within the project, but several areas where scaling effects were observed were highlighted and important scale-up criteria could be isolated. The first two questions were addressed in the design phase of the project for the first time, and are part of the article presented in Section 4.1. The following sections explain the steps that were considered in that article to create the “cell-configuration tool” which is explained in more detail in Section 3.1.3. Some exemplary screening results are presented to explain the development steps of the method, but are for themselves of little value and not in-depth discussed.

#### 3.1.1 Choice of the Development Level for Cell Optimization

Why not use the final multilayer pouch cell format to optimize the cell components? One important aspect is the material requirement and with that, the costs per development cycle. For example, the preparation of electrodes for coin cell testing requires few grams of active materials while several hundred grams are required for multilayer pouch cells. Another issue is also, that often only a limited amount of novel active material are available and that ink making requires much more

material than the actual amount contained in the final cells. Another factor that is significantly reduced by testing on the coin cell level is the manufacturing effort. Typically, one skilled student can produce a coin cell within three days, with around 0.3 hours needed per cell (rough estimated, see Table 4 for details). However, the same outcome took more than two weeks on the pilot line, with two people working at each step on average, resulting in a time requirement of around 4.2 hours cell. The last argument against using the final multilayer pouch cell format for cell optimization is the difficulty to study the effect of a single electrode (working electrode, WE) in multilayer cells, as its performance cannot be easily be decoupled from its counter electrode (CE).

**Table 4: Estimated working hours to build a coin half-cell vs. a multilayer pouch full-cell using the pilot line.**

<b>Step</b>	<b>Lab time /#cells [min/cell]</b>	<b>Lab time /cell [min]</b>	<b>Pilot line time /#cells [min/cell]</b>	<b>Pilot line time /cell [min]</b>
Mixing & coating, WE	120/50	2.4	300/50	6
Mixing & coating, CE			300/50	6
Calendering, WE	30/50	0.6	120/50	2.4
Calendering, CE			120/50	2.4
Cutting to format, WE	2/1	2	120/50	2.4
Cutting to format, CE			120/50	2.4
Separator cutting	2/1	2		
Transfer in & out of glovebox	30/20	1.5		
Cell assembling & filling	5/1	5	60/1	60
Test start & formation	5/1	5	45/1	45
<b>Total</b>		<b>19</b>		<b>127</b>

The last point of the previous paragraph can also be used as a counter argument and leads to the more fundamental question about the scientific advantages and drawbacks of half-cell use during parameter screening. The disadvantages of using half-cells for screening tests must be considered and their impact on the cell performance should be known before using them for full-cell design decisions. The following deviations should be considered:

- The loss of cyclable lithium cannot be considered, as a lithium counter electrode provides an infinite lithium reservoir.
- Long-term cycle life cannot be studied, as lithium dendrite formation would probably be dominant compared to full-cells.
- Another specific issue of half-cells over mid-to long-term cycling is cross talk offsets between the Li-metal anode and the cathode. As, described by Oswald et al,<sup>97</sup> this can lead to much shorter cycle life of half-vs. full-cells.
- The thermal mass of the cell stack in coin cells is negligible compared to the cell housing, so that a coin cell stays at the surrounding temperature, whereas in a scaled-up cell, the possible heating up of the cell during operation must be considered.
- The rate capability of half-cells is often interfering to that of full-cells, due to the high impedance of a lithium metal anode compared to a high-surface area graphite anode. For short-term tests, however, this can be accounted for when using a reference electrode.

Despite of all these shortcomings, it was decided to do the first iteration steps with coin half-cells. The focus in the design phase was clearly on the cathode electrode, as it was based on a new, not yet commercialised LMR-NCM cathode active material. The first milestone of achieving a relatively fast discharge rate (1C) also required a careful optimization of the cathode electrode. For this, different cathode loadings were explored and using half-cell eliminated the need of simultaneously preparing areal capacity-matched graphite anodes. For the design iterations used in this work, a short discharge rate test was chosen (with less than 30 cycles) and the half-cells were slowly charged with a 0.5C rate. With this approach, the impact of cathode porosity could be studied without any artefacts arising from the use of a lithium-metal CE. This approach is a little more challenging for the cathode loading optimization, as the overpotential on the lithium-metal is not negligible, but is tolerable at low charge rates.

Another aspect to consider when using a coin cell format are the CAM/electrolyte and the pore/electrolyte volume ratios. As is seen in Table 5, these ratios vary between the tested cell formats. However, most of the known effects of these ratios (difference in the molar amounts of additives, Li loss due to cross-talk, electrolyte

decomposition and/or consumption) mainly appear as long-term effects and are therefore acceptable for the screening process used in this work.

**Table 5: CAM/electrolyte and pore/electrolyte volume ratios, calculated for the coin and multilayer pouch cell electrodes, as described in Schreiner et al.<sup>63</sup> For the glass fiber (GF) separator, a thickness of 210  $\mu\text{m}$  and a porosity of 90% was assumed. For the PP-based separator, a thickness of 25  $\mu\text{m}$  and 55% porosity was used.**

	<b>Coin half-cell 2 GF-Sep.</b>	<b>Coin full-cell 1 PP-Sep.</b>	<b>Multilayer pouch cell</b>
<b>CAM</b>	21 mg	21 mg	31.900 g
<b>Pore volume</b>	90 $\mu\text{l}$	11 $\mu\text{l}$	21 ml
<b>Electrolyte volume</b>	100 $\mu\text{l}$	30 $\mu\text{l}$	32 ml
<b>CAM/electrolyte ratio</b>	<b>0.21 g/ml</b>	<b>0.7 g/ml</b>	<b>1 g/ml</b>
<b>Electrolyte/pore volume ratio</b>	<b>1.1</b>	<b>2.7</b>	<b>1.5</b>

Other aspects that may have an impact are the compression of the electrodes (in the case of this work, it was attempted to keep it in a similar range of 0.2 MPa) and the electrolyte-to-headspace ratio. The latter point is important when there is interest in the exact electrolyte composition, however it was found to be of minor significance for the initial optimization of the cathode electrode.

### 3.1.2 Maximization of the Energy Density at a Given C-rate

After the best available testing configuration and test sequence was identified, it was necessary to decide what parameter variations were to be screened for. Unlike a full-cell development in industry, the footprint of the cell and the geometric ratios of the electrodes were chosen based on the production site capabilities, and all materials regarding the cell assembly were given. Through the cathode material supplier (BASF, Germany), the active material and a special electrolyte were obtained as well as a proposed electrode composition. For the anode, the active material was acquired from the supplier (SGL Carbon, Germany). Graphite-based anodes are already an industrial standard, so that the optimization focus of this work was on the cathode, and general best practices were used for the anode electrode. By “simply” optimizing the cathode, the following points needed to be decided on:

- Number of cathode layers
- Composition of the cathode
- Loading of the cathode
- Loading ratio between cathode and anode (based on which capacities)
- Porosity of the cathode

The first point was relatively straightforward in view of the aims of the project. As it was desired to maximize the energy density without having to consider cell to cell propagation or cell cooling, it was decided to use the maximum number of layers that fitted into the deep-drawn pocket of the pouch foil. By using this approach, the amount of active material was maximized in the cell relative to the non-active masses of pouch foil and tabs.

For the cathode composition, an already pre-tested recipe was received through the material supplier. To see if this could be further optimized, a higher fraction of CAM (as the proposed one of 92.5% was relatively low) was tested. However, the material is well known to have a low electrical conductivity,<sup>98</sup> which is indicated by the strong dependence of the rate capability on the amount of carbon black (CB) additive to the cathode electrode as shown in Figure 12.

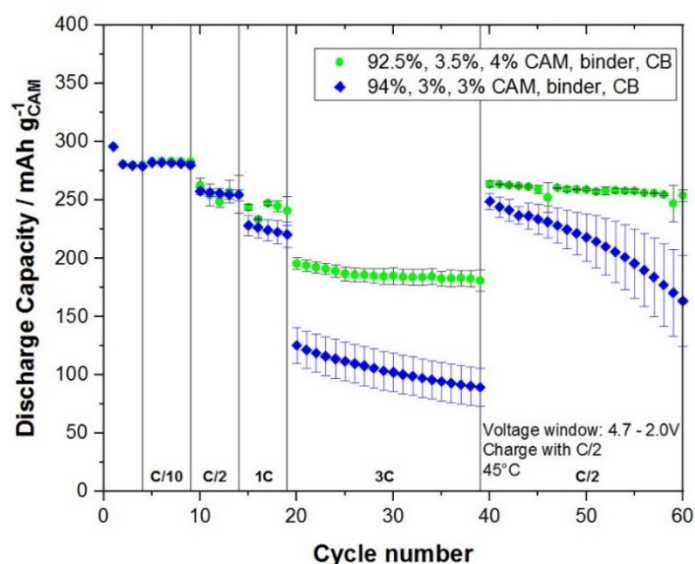


**Figure 12:** Comparison of discharge rate test of cathode electrodes with either 92.5%/3.5%/4% or 94%/3%/3% CAM/binder/carbon black (CB), given in terms of wt%; the CAM loading were  $\approx 7.2 \text{ mg}_{\text{CAM}}/\text{cm}^2$ . The cells were cycled in coin half-cells with glass fiber separators and  $100 \mu\text{l}$  RD2137 (1M  $\text{LiPF}_6$  in 12 vol% FEC, 64 vol% DEC, 24 vol% of a proprietary co-solvent, and 2 wt% of a proprietary stabilizing additive, BASF) electrolyte at  $45^\circ\text{C}$  with a C/2 CCCV charge and the indicated discharge rates. The figure is reprinted with permission from “*Optimization of Li-Rich Layered NMC Cathodes’ Material Composition in regard to the Upscaling Process for Next-Generation Li-Ion Batteries*” by Matthias Lex,<sup>99</sup> a supervised semester thesis at the Technical University of Munich.

The next step was to improve the intrinsic poor electrical conductivity of the material with a better conductive additive than carbon black. For this, two conductive graphites (SFG6L and KS6L both from TIMCAL, Switzerland) as well as carbon nanotubes (the supplier is confidential) were tested, exchanging 2% of the original 4% CB (TIMCAL, Switzerland) with these alternative conductive additives. Figure 13 shows the results of these trials, but no improvements were observed for the tested combinations. On the basis of these results, the proposed recipe of 92.5% AM, 3.5% binder, and 4% CB for the cathode electrode was used for the rest of the project.

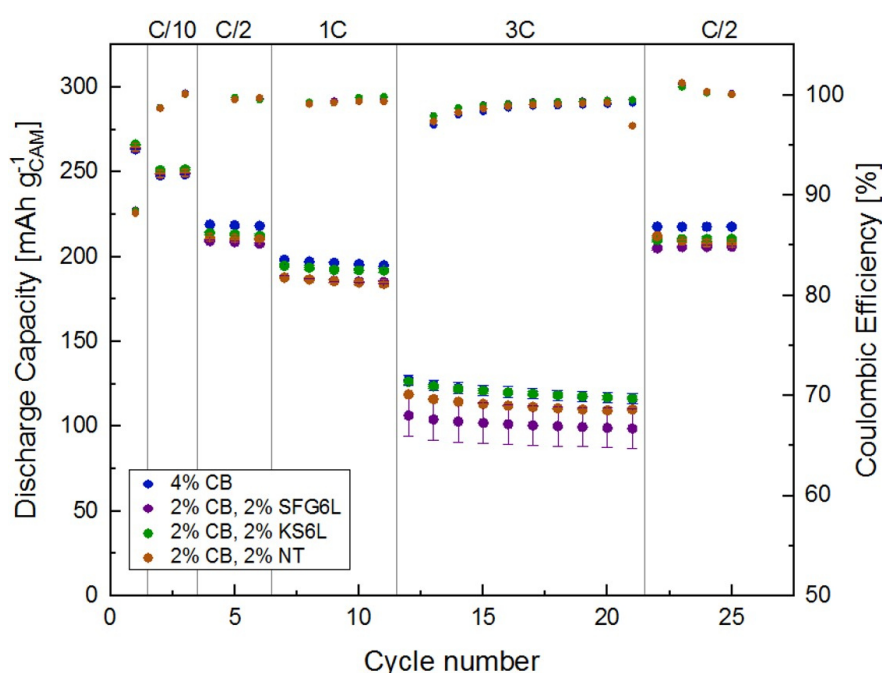


**Figure 13: Comparison of discharge rate tests of cathode electrodes with different conductive carbon compositions.** The electrode were uncompressed (refers to a electrode porosities of 53- 56 vol. %) with a CAM loading of 11-12 mg<sub>CAM</sub>/cm<sup>2</sup>. The cells were cycled in coin half-cells with glass fiber separators and 100  $\mu$ l RD2137 (1M LiPF<sub>6</sub> in 12 vol% FEC, 64 vol% DEC, 24 vol% of a proprietary co-solvent, and 2 wt% of a proprietary stabilizing additive, BASF) electrolyte at 25°C with a C/2 CCCV charge and the indicated discharge rates. The figure is reprinted with permission from of *“Improving the electrical conductivity of HE-NMC in Li-ion batteries by optimized calendaring and conductive carbon composition”* by Rebecca Wilhelm,<sup>100</sup> a supervised bachelor thesis at the Technical University of Munich.

To determine the optimum CAM loading, a rate test in half-cells was performed. With the help of the “cell configuration tool” (explained in more depth in the next section), the sweet spot between a high capacity at (high) C-rates and a high ratio of CAM loading can be found. The former is usually achieved by low CAM loadings due to an improved ionic transport through the electrode, which enables a very homogeneous usage of the active material. However, as seen from a cell weight

optimization perspective, a high AM loading is preferred, as it minimizes the contribution by the inactive masses of the current collectors and the separator.

The “balancing” of cathode and anode areal capacities ( $\text{mAh}/\text{cm}^2$ ) is straightforward with most cathode active materials, but certainly not with LMR-NCM. To avoid lithium plating it is necessary to balance the anode areal capacity to be slightly higher than that of the cathode (usually a balancing factor (BF) between 1.05-1.2 is applied). However, the question is what cathode capacity should be used for this calculation. In industry often the “nominal” or, as specified in the cell configuration tool, the “reversible capacity at C/10” is used. By doing so, any first-cycle inefficiencies are neglected and the assumption is made that the active materials in the anode and the cathode have no or an equal temperature dependency. Another inaccuracy could arise from the different voltage windows in which the half-cells and full-cells are cycled. For example, if a cathode is cycled in a half-cell between 2.0-4.3 V, the same electrode would need to be cycled against a graphite anode between 1.9-4.2 V, considering that the average potential of graphite is at 0.1 V. This aspect is most often considered for the higher voltage limit but rarely for the lower one because for most of the cathode/anode combinations there is not much capacity difference in this region. For an industrial standard electrode, these “half-cell” effects cancel each other almost out. The anode has a first-cycle inefficiency of around 10% and the cathode half-cell shows some inefficiency due to initial over-lithiation and a kinetically very slow re-lithiation at the end of the discharge process. However, for the case of a LMR-NCM, the cathode has a very high and temperature-dependent first-cycle irreversible capacity loss. In Table 6 most of the combinations of the above discussed effects are summarized. In orange, the balancing factor (BF) version most often employed for LIBs is marked using the nominal capacities (1<sup>st</sup> discharge capacities at 25°C) and the loadings were set to the commonly used BF of 1.1. All other, here called effective balancing factors ( $\text{BF}_{\text{eff}}$ ), were calculated with the same loadings as uses for the BF but using the indicated “effective” capacities. In green the ones that would have physical meaning are marked, namely the ratio between all  $\text{Li}^+$ -ions that leave the cathode side and the ones that are used on the anode side (determined by half-cell testing). The resulting BFs are often very close or even below one and anyone working on these should be aware of these numbers when using LMR-NCM electrodes to avoid

lithium plating due to insufficient lithium capability of the anode electrode. For the cell design used in this work, a BF of 1.2 was chosen; regarding the reference capacities to guarantees that also for the green marked  $BF_{eff}$  combination in Table 6, the ratio is above 1.1.

**Table 6: Effective balancing factors ( $BF_{eff}$ ) calculated by using the indicated “effective” capacities with the loadings according to the orange marked balancing factor (BF) that is based on the nominal capacities. In green, the  $BF_{eff}$  with the most physical meaning are marked.**

LMR-NCM Balancing Variations	LMR-NCM [mAh/g]	Graphite 1 <sup>st</sup> DCHA, 355 mAh/g	Graphite 1 <sup>st</sup> CHA 382 mAh/g
25°C, 1 <sup>st</sup> DCHA	261	BF set to 1.1	$BF_{eff} = 1.18$
25°C, 1 <sup>st</sup> CHA	300	$BF_{eff} = 0.96$	$BF_{eff} = 1.03$
45°C, 1 <sup>st</sup> CHA	320	$BF_{eff} = 0.90$	$BF_{eff} = 0.97$
25°C, 1 <sup>st</sup> DCHA (0.1 V corrected)	255	$BF_{eff} = 1.13$	$BF_{eff} = 1.21$

Last but not least, the porosity of the cathode was addressed. Similar to the optimization of the LMR-NCM loading, it was desired to find the sweet spot between energy density and electrode performance. The more the electrode is compressed, the lower the obtained electrode volume and the less electrolyte is needed to fill the pores, thereby reducing electrolyte mass and consequently, increasing the energy density of the cell. Less porosity, however, reduces the ionic conduction through the electrode, furthermore, high compression could lead to CAM particle cracking. Some compression protects the electrode from material loss/damage during manufacturing and can improve the electrical conductivity. In the paper of Section 4.1, the effect of compression was examined with a discharge rate test, and the sweet spot was found by using the “cell configuration tool” (explained in the next section). This study however, showed also one of the limits of the theoretical design prediction, and in the calendaring of the electrode for the multilayer pouch cells quite some challenges were faced when trying to reach the targeted cathode porosity. This is described by Schreiner et al.<sup>63</sup> and is addressed in Section 4.1.

### 3.1.3 Utilization of the Half-Cell Data in the “Cell Configuration Tool”

In the last sections, it was explained in which cases half-cell tests for electrode optimization were found to be useful. As a next step, the Excel-based “cell configuration tool” (available as supporting information from Schreiner et al.<sup>63</sup>) was used to predict the energy density of the final multilayer pouch cells on the basis of half-cell data.

The information that was needed to feed into the “cell configuration tool” are:

- The geometry of all parts in the cell (length, width, height).
- The specification of the cell component raw materials (crystallographic density for electrode materials, material density for all other materials).
- The electrode composition and the desired electrode porosity or density.
- The half-cell cycling information of both electrodes at the formation rate and at any other C-rates of interest.

The half-cell results of the cathode (capacities) were corrected by the anode irreversible loss if the anode irrev. loss > cathode irrev. loss (otherwise no correction is needed because the irreversible loss from the cathode is already accounted for in the half-cell results), and by the voltage window-adapted capacity difference, see Equation (9)&(10):

$$\begin{aligned}
 & \text{Spec. cell capacity (irrev. anode capacity > irrev. cathode capacity)} \\
 & = \text{spec. cathode halfcell capacity} \\
 & \quad - \text{capacity that is lost due to non anode adapted voltage window} \\
 & \quad - (\text{irrev. anode capacity} - \text{irrev. cathode capacity})
 \end{aligned} \tag{9}$$

$$\begin{aligned}
 & \text{Spec. cell capacity (irrev. anode capacity < irrev. cathode capacity)} \\
 & = \text{spec. cathode halfcell capacity} \\
 & \quad - \text{capacity that is lost due to non anode adapted voltage window}
 \end{aligned} \tag{10}$$

Less complicated was the correction as well the average discharge voltage levels from the cathode that were used to obtain the final cell voltage, see Equation (11):

$$\begin{aligned} \emptyset \text{ discharge cell voltage} \\ &= \emptyset \text{ discharge cathode halfcell voltage} \quad (11) \\ &- \emptyset \text{ charge anode halfcell voltage} \end{aligned}$$

With this material information from the half-cell tests, the tool can already be used to calculate the initial cell performance in a surprisingly accurate way as shown for the formation results by Schreiner et al.<sup>63</sup> However, predicting the formation results is probably the easiest case for such tools and many influences for further predictions are not yet considered, like cell aging, cell heating, cell gassing, cell swelling, impedance evolution, etc. Moreover, the tool is simple enough that the taken assumptions can be clearly understood and therefore adaptations and improvements are possible by any user, unlike in more sophisticated tools that can only be used as a black box.

## 3.2 (Long-Term) Gassing Measurements

The general issue of gassing with LMR-NCM materials and the most agreed sources for it are explained in Section 2.3.4. In this section, the options for influencing the cathode gassing and the methods to measure it will be discussed in more detail.

### 3.2.1 Temperature/Material Dependence of LMR-NCM Performance and Gassing

The influence of temperature on cathode gassing has been discussed by Jung et al. for regular NMCs in terms of lattice oxygen release (in the form of O<sub>2</sub>, CO, and CO<sub>2</sub>) and the amount of evolved gas was found to increase by more than two times when the temperature was increased from 25°C to 50°C. Teufl et al.<sup>101</sup> measured a material-dependent gas release for LMR-NCMs. The more the material was over-lithiated, the more gas release was observed by OEMS. The “0.33 Li<sub>2</sub>MnO<sub>3</sub>” based material (which is similar to the one used in this thesis) showed around four times less gassing than the “0.5 Li<sub>2</sub>MnO<sub>3</sub>” based one. The author’s explanation of this observation is that higher the degree of over-lithiation lead to a more extensive lattice oxygen release that in turn is accompanied by follow-up gassing reactions. The authors further correlated an increase of lattice oxygen release with the formation of thicker and more resistive spinel/rock-salt surface layers; thereby, the increased oxygen release adversely affects the full-cell performance during a cycle life test. These findings are consistent with the observation of Erickson et al.,<sup>102</sup> who observed a higher capacity after formation when the formation itself was performed at 0°C or 15°C instead of 30°C or 45°C. In addition, the impedance spectra taken after a low-temperature activation showed a lower overall resistance of the cathode compared to these taken after the high temperature activation. Erickson et al., however, suggested an alternative hypothesis namely that the LMR-NCM bulk structure is better retained due to the softer formation at low temperatures, thereby leading to less TM migration and better enabling lithium re-intercalation. The other possible hypothesis fits more to the idea of Jung et al. and Teufl et al., namely that the “softer” low-temperature formation leads to a lower degree of delithiation, and with it to less oxygen evolution and therefore to a thinner resistive spinel/rock-salt surface layer. Based on the latter hypothesis, the application-oriented follow-up questions are:

- Does a low-temperature formation lead to less gassing in general?
- What influence do these formation conditions have on the long-term gassing behaviour?
- How “robust” are LMR-NCMs that underwent a low-temperature formation towards a subsequent operation at high temperature?
- Are LMR-NCM particles that underwent a low-temperature formation stable or do they simply experience a delayed activation?

To answer the last two questions, we performed a simple cycling test, similar to the one from Erickson et al.,<sup>102</sup> where the 1<sup>st</sup> cycle of the formation was either at 25°C or 45°C and the cycling afterwards either done at 25°C (Figure 14a) or at 45°C (Figure 14b). The cells cycling at 25°C showed a better rate performance, when they had undergone a formation at low temperature but their capacity did not differ significantly at low rates. This trend, however, is reversed when cycling the cell at 45°C (Figure 14b). Moreover, these results partially contradict the one from Erickson where the cells were cycled at 45°C. The one with cold formation suffered more strongly from cycling at elevated temperatures and performed worse in the rate capability test as well as in the capacity retention after 25 cycles.

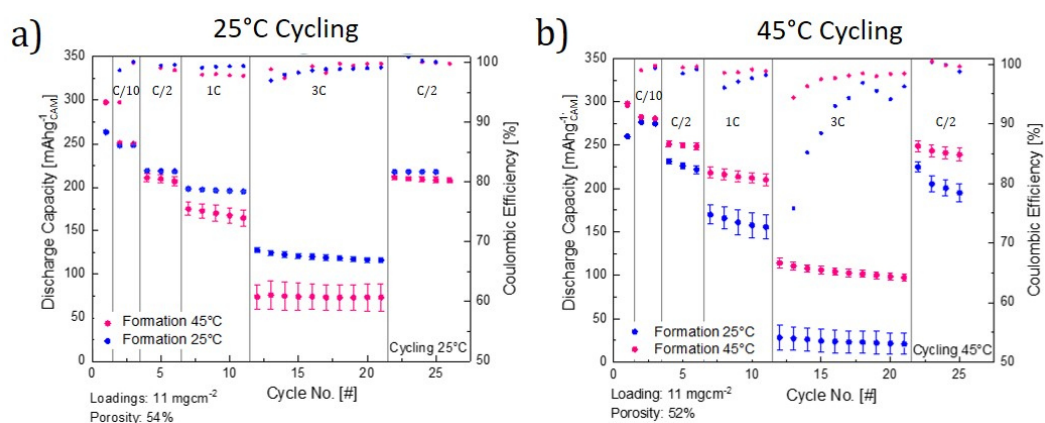


**Figure 14: Discharge rate capability test at 25°C of LMR-NCM/lithium coin half-cells with different 1<sup>st</sup>-cycle activation temperatures at C/15 (CC) between 2.0 V and 4.8 V. The subsequent cycles were conducted between 2.0 V and 4.7 V at different discharge rates (C/2, 1C, 3C, and C/2, all in CC mode) and with a CC charge at C/2 followed by a CV phase until the current decreased to below C/20. The cycling was performed at a) 25°C or b) 45°C. The coin cell setup corresponds to the one used in the article by Schreiner et al.,<sup>63</sup> with the indicated LMR-NCM loadings and the cathode porosities marked in each panel.**

The explanation used to explain these findings follows the idea of Teufl et al.<sup>101</sup> The “soft” formation at 25°C with subsequent cycling at this temperature seems to lead to less cell resistance and therefore fits well with his explanation of a thinner spinel/rock-salt layer. In contrast, the poor performance obtained when the cells

were cycled after the low-temperature formation at 45°C is suspected to be the consequence of an incomplete 1<sup>st</sup>-cycle activation. Therefore, the delithiation and transformation are delayed but not limited anymore to the first cycle. For the case that this assumption is true, an increased gassing effect should also be observed when a change is made from low-temperature activation to high-temperature cycling. This experiment would also be expected to provide the answers for the first two gassing related questions at the beginning of this section. Regarding up-scaling of cells, gassing is never welcome, but during the formation procedure, the evolved gasses can at least be removed at the degassing step (that anyway is needed to remove anode SEI gasses). “Delayed” gassing, occurring after the cell has left the production site is, on the other hand, clearly undesired and should be avoided.

### 3.2.2 OEMS Measurements of Cell Gassing

In the research group of the author of this thesis many special OEMS setups have been developed and studied intensively, which started with the work of Tsiouvaras et al.<sup>103</sup> and Metzger et al.<sup>104</sup> For the approach used in this work, interest was not primarily placed on the mechanistic origin of the gassing but on the overall gas amount. For this, a simplified one-compartment version of the original OEMS cell was used, as shown in Figure 15. Details of the used electrode preparation and electrolyte can be found in the OEMS section in the article by Schreiner et al.<sup>63</sup>



**Figure 15: Adapted OEMS setup of Tsiouvaras et al.<sup>104</sup> that shows the OEMS cell used for measurements done in this thesis. The middle part hosts the cell stack that consists of a conventional anode, the separator, and the cathode. The cathode in this setup is not coated as usual on aluminium foil but on a stainless steel mesh to allow unhindered gas transport from the bottom of the cell to the capillary. More details about the used setup in this thesis can be found in the experimental section in the article by Schreiner et al.<sup>63</sup> The headspace of the cell is around 10 ml. The tubes right and left can be closed by the green valves, which allows the flushing of the cell with either a calibration gas or argon. The capillary is indicated and connects the cell with the mass spectrometer system.**

For the overall gas analysis, the corrected signals of CO<sub>2</sub>, H<sub>2</sub>, CO, and O<sub>2</sub> from the MS were calibrated using a calibration gas. To avoid too much of an under-pressure in the OEMS cell caused by the gas removed through the capillary, the cell was flushed with argon after the first cycle and the subsequent cycles were measured separately. In Figure 16 the different gassing reaction that are attributable to the different gassing mechanism are highlighted, together with the relevant references.

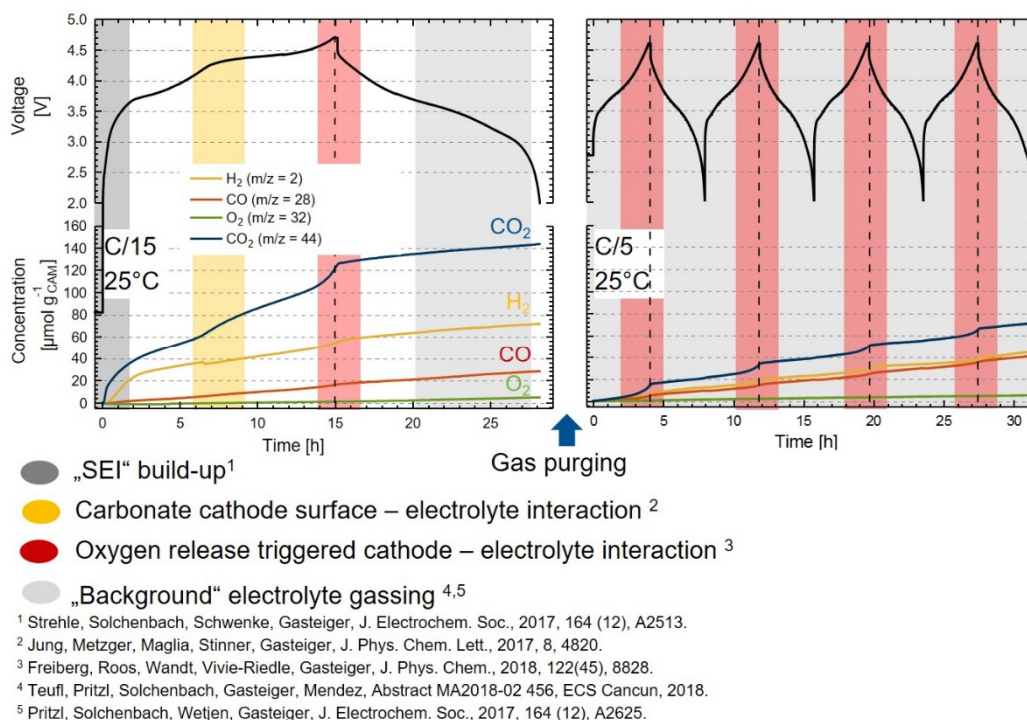


**Figure 16: OEMS measurements with LMR-NCM working electrodes and graphite counter electrodes using an RD2137 (1M LiPF<sub>6</sub> in 12 vol% FEC, 64 vol% DEC, 24 vol% of a proprietary co-solvent, and 2 wt% of a proprietary stabilizing additive, BASF). The upper panels show the voltage profile vs time during a formation cycle (left side) at 25 °C with a C-rate of C/15 and a CV step at 4.7 V till C/30 or max 30 min. The right-hand panel shows the voltage profile of the 4 subsequent cycles at 25 °C with C/5 and a CV step at 4.6 V till C/10 or max. 30 min (note that this was done after flushing the cell with Ar). The lower panels show the amount of released gas (i.e., of CO<sub>2</sub>, CO, H<sub>2</sub>, and O<sub>2</sub> in units of  $\mu\text{mol/g}_{\text{CAM}}$ ) over the first-cycle activation (left side) as well as over cycles 2–5 (right side).**

Next we return to the question whether the formation temperature affects the overall gas amount and what happens after the formation. In Figure 17 the total amounts of evolved gasses are summarized up for four tested temperature combinations of formation (1<sup>st</sup> number of the x-axis label) and cycling (2<sup>nd</sup> number x-axis label).

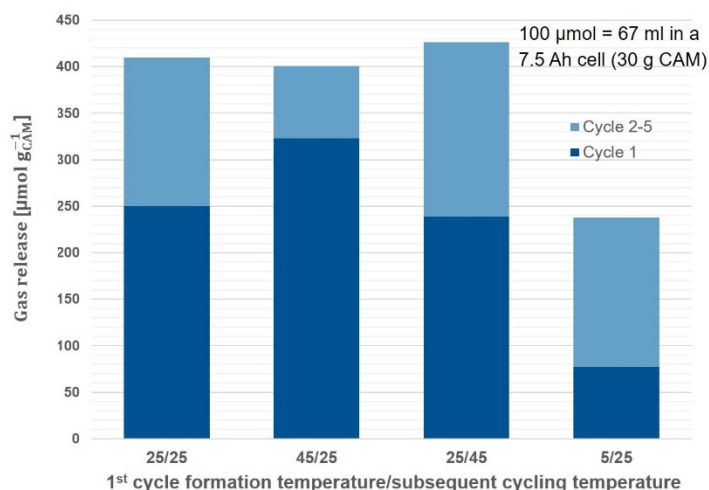


**Figure 17: Summed up total amount of evolved gasses measured for different combination of formation (1<sup>st</sup> cycle) and cycling (cycle 2-5) temperatures (data taken from measurements as shown exemplarily in Figure 16).**

The main observations of Figure 17 are the following:

- The gassing in the first formation cycle increases with increasing formation temperature.
- The formation temperature also influences the extent of gassing in the subsequent cycles, i.e., the higher the formation temperature the lower is the amount of evolved gasses in the subsequent cycles.
- The overall gassing did not change significantly, except for the 5°C formation, the latter measurement is, however, also not completely comparable, as only a partial activation leads to lower capacities in the subsequent 4 cycles.

The results are in agreement with the hypothesis posed at the beginning of this section, i.e., the higher the formation temperature the more the LMR-NCM material is being activated, accompanied by gassing. A delayed activation upon a subsequent temperature increase for the subsequent cycles is as well observed. However, to prove the assumption that this also correlates with the spinel/rock salt layer formation, it is necessary to have additional resistance measurements and/or TEM cross-section images like those provided by Teufl et al.<sup>101</sup> for the LMR-NCMs with different degrees of over-lithiation. For the scale-up project, it was clear from these results that a formation was needed at an elevated temperature in order to minimize gassing after the formation as much as possible.

Despite using the “best” formation conditions, as shown in the paper of Section 0, the tested cells experienced continuous gassing. The cycling had to be stopped after 300 cycles when the first of a series of cells started to burst under the increased internal pressure. In Figure 16 it can be seen that the overall gassing is a combination of the cathode gassing at a high delithiation degree and the “background” gassing that is associated with (thermal) electrolyte instabilities as described by Teufl et al.<sup>105,106</sup> More information on the gassing rate after the 5<sup>th</sup> cycle would allow to give a more accurate projection of the pressure-rise-induced life time restrictions for cells with LMR-NCM cathodes. However, designed for answering specific mechanistic questions, the OEMS method suffers from the following drawbacks when it comes to evaluate the long-term gassing behaviour:

- OEMS measurements are limited to a maximum duration of around 30h (otherwise the decrease of the internal cell pressure influences the gas flow through the capillary into the MS and as the internal pressure is not monitored, the MS signal cannot be anymore converted into a molar concentration).
- For volatile electrolyte component (e.g., DEC), the decrease of the OEMS cell pressure over time leads to an increase of their molar fraction in the headspace. With the rather big headspace of the OEMS cell (10-12 ml), this effect can lead to severe changes of the background signal.
- Only relatively large amounts of electrolyte can be used (~10 fold higher CAM/electrolyte ratio than in a real battery cell), as some excess for flushing and the evaporation due to the headspace and the flow through the capillary has to be considered.
- The measurement effort and costs to determine “only” the gas amounts is very high, as the full OEMS setup including a separate cyler and an OEMS cell is needed.

To overcome these limitations, the development of a pressure sensor-based method was proposed (see next section) in order to quantify long-term gassing rates.

### 3.2.3 Method to Determine Long-Term Gassing Rates

The development of the pressure sensor-based method started with the adaptation of the already described OEMS cell. B. Strehle (a colleague of the research group) had mounted a pressure sensor on the OEMS cell in order to determine the under pressure that evolves during the OEMS measurement and his original setup is shown in Figure 18.

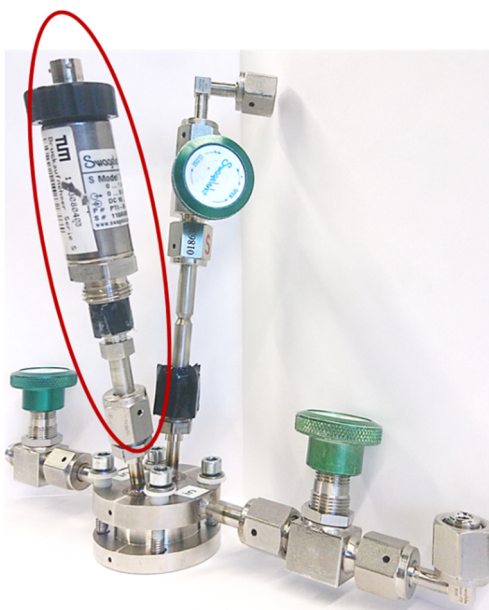


**Figure 18: Adapted OEMS setup from Figure 15 that shows the OEMS cell with the Swagelok pressure sensor (circled in red) mounted on top of the cell casing.**

The used pressure sensor is an original part from Swagelok (PTI-S-AA1.6-21QA-B) that allows an accuracy of 0.5% for the detection of pressure in a range from 0-1.6 bar (i.e., 8 mbar). In order to mount it on the OEMS cell, a tube adapter (from  $\frac{1}{4}$  inch to  $\frac{1}{2}$  inch) was connected to the cell in order to enable the connection to the welded fitting of the welded fitting of the OEMS cell. The first step was to verify that the summed-up amount of evolved gas during an OEMS experiment (calculated from the individual amount of gas constituents recorded by the MS and by using the ideal gas law) is in agreement with the gas amount calculated from the measured gain in pressure (also using the ideal gas law).

The measurements presented in Figure 19 show the gas amount calculated from the pressure sensor signal (blue, tot=240  $\mu\text{mol/g}_{\text{CAM}}$ ) and the OEMS measurement (black, tot=251  $\mu\text{mol/g}_{\text{AM}}$ ) measured over the first formation cycle, as done using the components described before in Figure 15 and Figure 18.

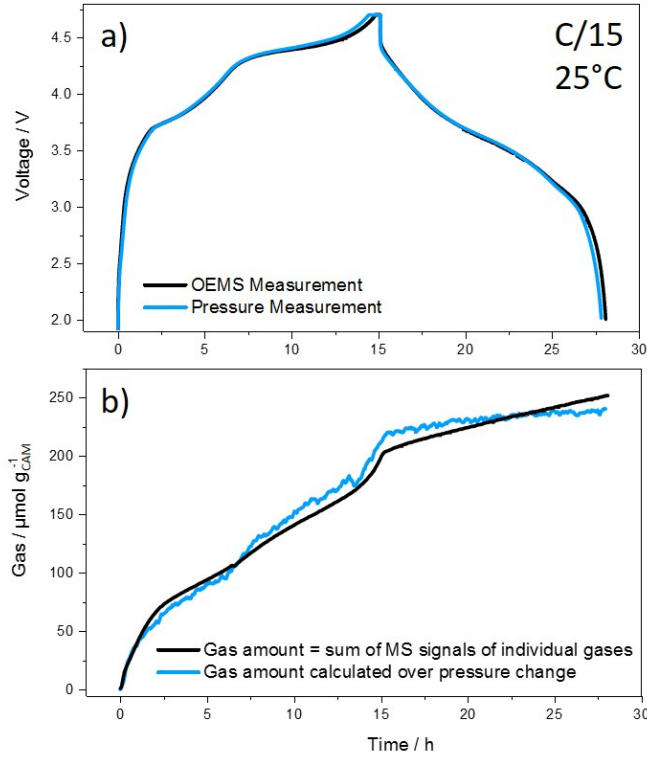


**Figure 19: Comparison of two LMR-NCM/ graphite cell measurements collected in an OEMS-pressure cell as shown in Figure 18, with the inlet explained in Figure 15. a) Voltage curves of the OEMS cells. In black, the curve of the cell connected to the MS is shown and in blue, the cell where the capillary to the MS is closed and the pressure change is recorded. b) Calculated gas amount, either by MS sampling of the gas flow (black) or by measuring the pressure change (blue).**

Even though the absolute values fit quite well (< 5% deviation), the signal of the pressure sensor is rather noisy. An LMR-NCM/graphite OEMS cell (headspace of  $\approx 14$  ml) showed a total gas evaporation of  $\approx 250$   $\mu\text{mol}/g_{\text{CAM}}$  within the first cycle. As it had a cathode loading of  $12$   $\text{mg}_{\text{CAM}}/\text{cm}^2$  and an electrode diameter of  $15$  mm, the expected overall pressure gain would be  $5.6$  mbar according to Equation (12).

$$\Delta p = \frac{\Delta n RT}{V} ;$$

$$\Delta n = \text{cathode loading} \left( \frac{g}{\text{cm}^2} \right) * \text{cathode area}(\text{cm}^2) * \text{gassing} \left( \frac{\text{mol}}{g} \right); \quad (12)$$

$$T = 293 \text{ K}; V = 14 \text{ ml}$$

The accuracy of the pressure transducer of  $0.5\%$  over a pressure range of  $0$ - $1.6$  bar implies an overall accuracy of only  $8$  mbar, which is in the range of the expected pressure change. Therefore, it is not surprising that the calculated amount of evolved gas via the pressure sensor (blue line in Figure 19b) is rather noisy.

As the electrodes used in this work were based on a strongly gassing cathode active material that was already applied at a high loading, a pressure resolution improvement by increasing  $\Delta n$  in Equation (12) is therefore not feasible. However, the overhead volume can be decreased by changing the cell setup. This led to the development of a “T-cell-pressure” setup (shown in Figure 20) which offers the following advantages:

- A subsequent reduced headspace (by a factor of  $\approx 10$  compared to the OEMS cell setup).
- No electrolyte excess is needed and it is therefore closer to application relevant cell setups.
- The smaller dimensions of the cell allows to place more cells in the climate chambers and thus to conduct more experiments in parallel.

In order to minimize the headspace, an inset with a small hole was placed into the connection between the pressure sensor membrane and the cell, so that only a channel with a 1.1 mm diameter is left open as a connection between the cell and the pressure sensor membrane. Furthermore, for the initial measurements, the spring in the T-cell was removed to avoid any fluctuating headspace.

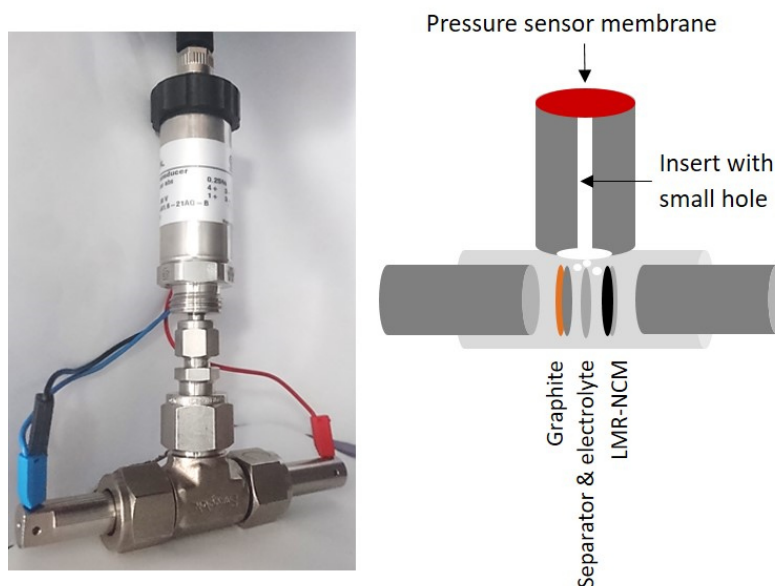


**Figure 20: Image of the “T-cell-pressure” setup which consists of a T-cell setup<sup>107</sup> where the reference electrode part is replaced by the connection to the Swagelok pressure sensor. On the right side, a schematic drawing of the inner part of the “T-cell-pressure” setup is shown.**

In order to quantify the moles of evolved gas, the exact volume of the headspace of the cell must still be determined, which is not trivial. In Table 7, the so-far published setups to measure pressure changes in lab-based cells are summarized. The two systems which offer a promising pressure resolution (e.g., headspace volume to electrode area < 2 ml/cm<sup>2</sup>) are affected by the same challenge of determining the exact headspace volume, and a major part of the related papers are dedicated to describe the method to quantify the headspace and the resulting errors. Therefore, the three methods that have been used are addressed in the following and the non-corrected results based on the presented assumptions are shown.

**Table 7: Summary of pressure measuring setups and their cell headspace to electrode area ratio. Either based on a modified OEMS cell, a T-cell, or a DEMS (differential electrochemical mass spectrometry) cell, each with an attached pressure sensor.**

System	Group/Ref.	Headspace/ electrode area	Head space determination
<b>OEMS cell + P-sensor</b>	Gasteiger see Figure 18	7.9 ml/cm <sup>2</sup>	$\Delta p$ of released vacuumed cell volume into a defined system volume. See Equation (13)
<b>T cell + P-sensor</b>	Gasteiger see Figure 20	1.5 ml/cm <sup>2</sup>	Different methods compared, discussed in the following
<b>DEMS cell + P-sensor</b>	Janek <sup>108</sup>	0.6 ml/cm <sup>2</sup>	$\Delta p$ of different gas flows used to calibrate $\Delta V$
<b>T cell + P-sensor</b>	Garcia-Araez <sup>109</sup>	0.4 ml/cm <sup>2</sup>	$\Delta p$ of released vacuumed cell volume into a defined system volume. See Equation (13)
<b>T cell + P-sensor</b>	Tarascon <sup>110</sup>	7.8 ml/cm <sup>2</sup>	Not given

For the first test, the T-cell with the pressure sensor was simply filled with water and weighed, then the setup was dried and weighed again. From this a volume of 1.45 +/- 0.2 ml was determined, which fits quite well with the 1 - 1.4 ml estimation made by calculating all empty volumes based on the T-cell drawing and adding the volume that connects the cell with the pressure sensor. However, as shown in Figure 21, gassing measurements for an NCA-/graphite system (sample setup as shown in Figure 15, Figure 18, and Figure 20 but with the electrode loading as used by Schreiner et al.<sup>63</sup>) yielded in around 5x less gassing for the T-cell setup compared to two different OEMS setups (one with and one without a pressure sensor).

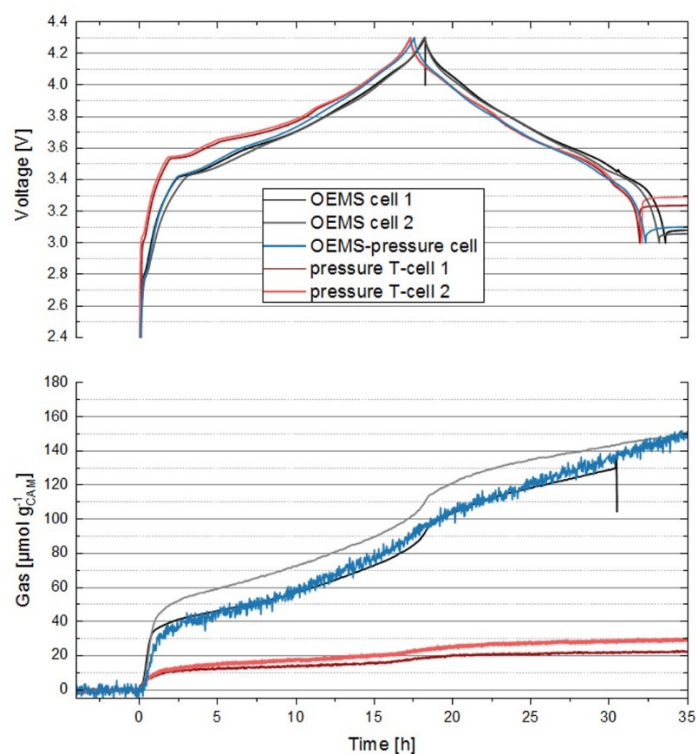


**Figure 21:** Comparison of measured total gassing of two OEMS measurements (black and gray), a pressure measurement in an OEMS cell (blue), and two pressure measurements in a T-cell (light and dark red). All measurements were performed with the NCA-Graphite cell chemistry described by Schreiner et al.,<sup>63</sup> using the cell setups described in Figure 15, Figure 18, and Figure 20.

To exclude any real difference in the gassing behaviour, additional measurements with more and less electrolyte within the same cell setup were made subsequently, but this showed only minor differences for the formation cycle (<20%). The inevitable conclusion was that the headspace volume estimation must be incorrect.

The method used method in the literature but not considered so far is the volume determination by measuring the pressure difference when connecting an evacuated and calibrated volume to the cell that is filled with gas at an ambient pressure. The measuring system is simple but has some experimental difficulties for the here used setup. Figure 22 shows a schematic drawing of the setup to determine the cell volume by the use of Equation (13). The volume of interest, i.e., the internal cell volume ( $V_c$ ), is connected via a valve to the pressure measuring system ( $V_s$ ) that is connected via a second valve to a vacuum pump. By using Equation (13), it is possible to determine  $V_c$  by knowing  $V_s$ . For these measurements the following protocol was used:

1. The system is set under vacuum by having both valves open.
2. The valve next to the vacuum pump is closed and the (low) pressure in the system ( $p_{C+S}^0$ ) is measured.
3. The valve next to the cell is closed and the volume of the system ( $V_S$ ) is set under ambient air by removing the connection to the pump and open the valve next to the pump.
4. The valve next to the pump is closed and the ambient pressure of the system ( $p_S$ ) is measured
5. The valve next to the cell is opened and the pressure change due to the before evacuated cell volume ( $\Delta p_{C+S}$ ) is measured.

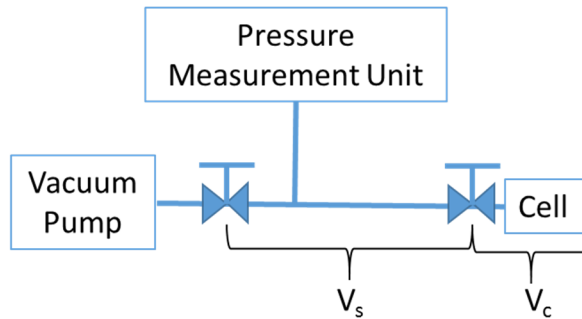


**Figure 22: Schematic drawing of the setup to determine the cell volume ( $V_C$ ) by a known system volume ( $V_S$ ) and a measurable pressure change due to a connection to the previously evacuated cell by a vacuum pump.**

$$(V_S + V_C) * \Delta p_{C+S} = V_C * p_{C+S}^0 + V_S * p_S$$

$$V_C * \Delta p_{C+S} + V_S * \Delta p_{C+S} = V_C * p_{C+S}^0 + V_S * p_S \quad (13)$$

$$V_C = V_S * \frac{p_S - \Delta p_{C+S}}{\Delta p_{C+S} - p_{C+S}^0}$$

By using this method, the volume  $V_C$  indicated in Figure 22 is determined. For this, care needs to be taken because  $V_C$  includes the volume that connects the cell to the system with the valve. For bigger systems (like the OEMS cell), this is a minor contribution because the connection point already contains a valve and therefore only the small connection piece needs to be subtracted (that can be calculated from the Swagelok drawing). For the T-cell, this connection piece needs to include a valve and its volume then needs to be subtracted (between 2-4 ml at least), which is large compared to the assumed volume of the cell (1.45 ml). Therefore, there was an initial hope to find a way to avoid this method, however after looking at the results

in Figure 21, it had to be concluded that a “hidden” volume in the T-cell pressure setup must have been neglected.

Moritz Bock (a Ph.D. student of the research group, who took over the topic) later found this hidden cell volume. He used the pressure method and determined the T-cell-pressure setup volume to be 4.22 ml (which is  $\approx 3$ -fold larger than the original estimate of 1.45 ml). The additional volume is attributed to the headspace behind the “pressure membrane” indicated in Figure 20, this volume is not accessible by liquid water, so that it had not been considered before. The initial measurement does not match yet perfectly with this factor 3 correction, but with the electrolyte difference and other small deviations, the measurement difference to the OEMS cell is in the region of the cell-to-cell variation. Before optimizing this system, it is necessary take into consideration that with the corrected headspace the system has now a headspace to electrode ratio of 4.4 ml/cm<sup>2</sup>. This compromises the initial attempt to improve the measurement accuracy by reducing the cell headspace, and therefore an improved pressure sensor was added (with less inner headspace) for the next generation setup.



## 4 Results

In the following four subsections the published articles of this PhD thesis are presented. Section 4.1 starts with a consideration of the challenges of up-scaling the LMR-NCM material from coin lab cells to multilayer pouch cells made on a pilot-line. The focus is set on processing challenges that are encountered when producing cells with an LMR-NCM based cathode. To clearly distinguish them from other cell materials and setup challenges, all production steps, performance/durability tests and analyses were considered in parallel with analogously produced cells with an NCA based cathode. In the electrode manufacturing process, the calendaring step needed a deeper understanding of the morphological structure of the LMR-NCM material that is characterized by the significant porosity of the secondary particles. Later, with regard to the cell manufacturing section, the formation process was adapted in order to avoid extensive cathode related gassing during the subsequent cycle live tests. Finally, the measured gravimetric energy density of the multilayer pouch cells was compared with the projections made on the basis of coin half-cell.

In Section 0, the electrochemical test results of the multilayer pouch cells designed according to the previous chapter are discussed. One of the main findings of this work is that the reversible OCV-hysteresis between the charge and the discharge of LMR-NCM based cathodes results in an substantial increase of the multilayer pouch cell temperature even at relatively low C-rates due to the current independent additional energy inefficiency caused by the OCV-hysteresis.

The origin of the OCV-hysteresis of LMR-NCMs and the associated heat evaluation during charge and discharge are studied in more detail, in the two following sections. Section 4.3 focuses on investigating the structural origin of the OCV-hysteresis. The OCV-hysteresis within a charge/discharge cycle is correlated to reversible structural changes of the lattice parameters, and the role of transition metal migration is critically discussed and investigated by a combined refinement of XPD and NPD data.

In Section 4.4, the energy inefficiency and the associated heat release of LMR-NCM/graphite cells are quantified. By *in situ* calorimetry it was possible to

determine the SOC resolved heat release of the OCV-hysteresis, which was compared with other energy losses arising from different resistances in the cell.

## 4.1 The Challenge of Up-Scaling the Production of Li- and Mn-rich Based Cells

In this section the article “Comparative Evaluation of LMR-NCM and NCA Cathode Active Materials in Multilayer Lithium-Ion Pouch Cells: Part I. Production, Electrode Characterization, and Formation” is presented. The manuscript was submitted in January 2021 and published in March 2021 as a peer-reviewed publication in the Journal of the Electrochemical Society. It is available as an “open access” article and distributed under the terms of the Creative Commons Attribution 4.0 License ([CC BY](https://creativecommons.org/licenses/by/4.0/)). Tanja Zünd presented some findings of the electrode production part at the Batterieforum in 2019 and 2020 in Berlin. The results of the formation part were shown at the 235<sup>th</sup> Meeting of the Electrochemical Society (2019) in Dallas, USA. The permanent web link to this article can be found under: <https://iopscience.iop.org/article/10.1149/1945-7111/abe50c>.

Lithium- and manganese-rich nickel-cobalt-manganese oxides (LMR-NCMs) offer high reversible specific capacities of up to 280 mAh g<sup>-1</sup>.<sup>51,101,111</sup> So far, most of the promising cell results with LMR-NCMs have been published based on small active area lab cells, characterizing the cathode active material but generally not in a realistic cell environment with respect to cathode loadings, separator, and CAM/electrolyte ratio. The aim of this publication was to evaluate how and to what extend coin half-cell data can be utilized to predict the initial cell energy density of multilayer pouch cells. The approach was accompanied by a investigating the scale-up of the various process steps in manufacturing of multilayer pouch cells in order to validate the simple assumptions used in the cell configuration tool. To highlight the unique challenges associated with LMR-NCM materials and to provide a baseline, all steps were carried out in parallel with a well-established NCA cathode active material. The CAM loading and the density of the cathode electrodes were varied in lab half-cells, using the half-cell data in combination with the cell configuration tool to find the optimum between rate capability and cell -level

energy density. The results show that the LMR-NCM electrode performance depends more strongly on the CAM loading than the NCA electrodes, and for discharge rates up to 1C, an optimum of 11-15 mg/cm<sup>2</sup> was determined for LMR-NCM cells. In contrast, coin half-cell data showed for both cathode active materials that there is no significant capacity decrease for porosities down to 32%, which compared to non-calendered cathodes increases the energy density by up to 18%.

When attempting to produce such low-porosity cathodes on the pilot line calender, the two cathode materials behaved quite differently. While electrode porosities of 32% (2.7 g/cm<sup>3</sup>) could be achieved for NCA electrodes, reflecting the state-of-the-art for cathodes,<sup>112,113</sup> LMR-NCM electrodes were not processable to the same porosity. Scanning electron microscopy (SEM) images of calendered and uncalendered electrode cross-sections of the two materials showed that for the same porosity, NCA electrodes have more space between the secondary agglomerates. This suggested that there must be more porosity within the secondary particle agglomerates of the LMR-NCM material. The so-called “inner particle porosity” of the LMR-NCM material cannot be reduced by calendering without breaking the secondary particles and/or without embossing the current collector foil. By mercury porosimetry it was possible to confirm and quantify the inner porosity of the LMR-NCM secondary agglomerates. They contain around 12% porosity (compared to 4% in the case of the NCA material) at pore diameters (<240 nm) which are mainly attributed to pores within the second agglomerates and only to a small fraction to pores produced by the carbon black additive. The challenges of the extensive gas release during the first cycle of LMR-NCM cathodes have been extensively discussed from a mechanistic point in the literature.<sup>101,106,114,115</sup> In the last section of the article, this gassing issue was considered from an engineering aspect, resulting in an adapted formation protocol to prevent a premature cell opening due to cell gassing. Finally, the predicted energy density of the multilayer pouch cells was compared with those measured after formation, and the deviations were discussed along with further possibilities for improvements.

## Author contributions

The pouch cells were built by the battery production team of D.S., B.S., and F.G while L.K. provided the formation data of the cells. The lab cells were built and measured by R.W. and T.Z. The mercury porosimetry experiments were measured by D.S., M.S. and T.Z. D.S. and M.S. conducted the calendaring experiments. The SEM sample preparation and analysis was done by R.W. and T.Z. with the support of Katia Rodewald. T.Z. conducted the gassing experiments. The up-scaling calculation tool was developed by M.S., D.S., and T.Z. The results of the experiments were analysed and interpreted by D.S. and T.Z. The manuscript was written by D.S. and T.Z. and edited by the co-authors. All authors discussed the data and commented on the results. D.S. and T.Z. contributed equally to this work as co-sharing first authors.



# Comparative Evaluation of LMR-NCM and NCA Cathode Active Materials in Multilayer Lithium-Ion Pouch Cells: Part I. Production, Electrode Characterization, and Formation

David Schreiner,<sup>1,=,z</sup>  Tanja Zünd,<sup>2,=\*</sup>  Florian J. Günter,<sup>1</sup>  Ludwig Kraft,<sup>3,=\*</sup>   
 Benedikt Stumper,<sup>1</sup>  Fabian Linsenmann,<sup>2</sup>  Michael Schübler,<sup>1</sup>  Rebecca Wilhelm,<sup>2,=\*</sup>   
 Andreas Jossen,<sup>3</sup>  Gunther Reinhart,<sup>1</sup> and Hubert A. Gasteiger<sup>2,=\*</sup> 

<sup>1</sup>Institute for Machine Tools and Industrial Management, Technical University of Munich, D-85748 Garching, Germany

<sup>2</sup>Chair of Technical Electrochemistry, Technical University of Munich, D-85748 Garching, Germany

<sup>3</sup>Institute for Electrical Energy Storage Technology, Technical University of Munich, D-80333 Munich, Germany

A lithium- and manganese-rich layered transition metal oxide (LMR-NCM) cathode active material (CAM) is processed on a pilot production line and assembled with graphite anodes to  $\approx 7$  Ah multilayer pouch cells. Each production step is outlined in detail and compared to NCA/graphite reference cells. Using laboratory coin cell data for different CAM loadings and cathode porosities, a simple calculation tool to extrapolate and optimize the energy density of multilayer pouch cells is presented and validated. Scanning electron microscopy and mercury porosimetry measurements of the cathodes elucidate the effect of the CAM morphology on the calendaring process and explain the difficulty of achieving commonly used cathode porosities with LMR-NCM cathodes. Since LMR-NCMs exhibit strong gassing during the first cycles, a modified formation procedure based on on-line electrochemical mass spectroscopy is developed that allows stable cycling of LMR-NCM in multilayer pouch cells. After formation and degassing, LMR-NCM/graphite pouch cells have a 30% higher CAM-specific capacity and a  $\approx 5\%$ – $10\%$  higher cell-level energy density at a rate of C/10 compared to NCA/graphite cells. Rate capability, long-term cycling, and thermal behavior of the pouch cells in comparison with laboratory coin cells are investigated in Part II of this work.

© 2021 The Author(s). Published on behalf of The Electrochemical Society by IOP Publishing Limited. This is an open access article distributed under the terms of the Creative Commons Attribution 4.0 License (CC BY, <http://creativecommons.org/licenses/by/4.0/>), which permits unrestricted reuse of the work in any medium, provided the original work is properly cited. [DOI: 10.1149/1945-7111/abe50c]



Manuscript submitted January 14, 2021; revised manuscript received January 28, 2021. Published March 2, 2021.

Supplementary material for this article is available [online](#)

Since the commercialization of lithium-ion batteries (LIBs), the cathode active material (CAM) capacity has been the limitation for increasing the energy density of LIB cells and battery packs.<sup>1–3</sup> In addition to the performance and safety,<sup>4,5</sup> cathode active materials have a significant impact on the price of LIBs because of the high raw material costs for nickel and cobalt containing CAMs.<sup>6,7</sup> Lithium- and manganese-rich nickel-cobalt-manganese oxides (LMR-NCM) offer high reversible specific capacities up to 280 mAh g<sup>-1</sup><sup>8–10</sup> and show a significant cost advantage over Ni-rich NCMs due to the roughly one order of magnitude lower raw material cost of manganese (2 USD kg<sup>-1</sup>)<sup>11</sup> compared to nickel (21 USD kg<sup>-1</sup>).<sup>11,12</sup> In contrast to these advantages, there are still challenges to overcome for the commercialization of LMR-NCM, such as the observed discharge voltage fading,<sup>10,13–15</sup> the oxygen release in the first few cycles<sup>16</sup> from the near-surface region of the material,<sup>10,17</sup> and a pronounced charge-discharge voltage hysteresis.<sup>1,18</sup>

LMR-NCM cells with high reversible capacities over several hundred cycles have already been demonstrated on a laboratory scale (typically using coin cells) for optimized material compositions, surface coatings, and tailored electrolytes.<sup>9,10,19</sup> Thus, many promising results have been reported for LMR-NCM CAMs at the coin cell level, which, however, are usually based on small CAM loadings (e.g., 3–7 mg<sub>CAM</sub>/cm<sup>2</sup>)<sup>19–22</sup> that are typically assembled with 50–120  $\mu$ l of electrolyte, resulting in a high mass ratio of electrolyte to CAM (e.g.,  $mass_{electrolyte}/mass_{CAM}$  of 13/1 to 48/1).<sup>20,21</sup> Only very few examples can be found in the literature, where full-cell coin cells were assembled with such low amounts of electrolyte that result in  $mass_{electrolyte}/mass_{CAM}$  ratios (e.g.,  $mass_{electrolyte}/mass_{CAM}$  of  $\approx 1.6/1$ )<sup>10,23</sup> that more closely approach those in large-scale cells, viz.,  $mass_{electrolyte}/mass_{CAM} \approx 1/1$ ,<sup>24</sup> also used for the multilayer pouch cells produced in this work (see *Production step 10: electrolyte filling* in the Experimental section). Since

the amount of electrolyte in the cell, often expressed in terms of the  $mass_{electrolyte}/mass_{CAM}$  ratio (sometimes also as  $mass_{electrolyte}/Ah$ )<sup>25,26</sup> is known to critically affect the cycle-life when using active materials with intrinsically low coulombic efficiency (e.g., with silicon based<sup>27,28</sup> or with lithium metal anodes<sup>26</sup>) and/or when using electrolyte additives,<sup>29,30</sup> a rigorous evaluation of new active materials, particularly with regards to cycle-life, can only be obtained by tests with large-scale cells (e.g., with the here used multilayered, large-format pouch cells).

Since the costs for battery cells mainly depend on the costs of the cathode active material<sup>6,7</sup> and the scrap rates within the production,<sup>6,7,31</sup> special attention should be paid to minimize the CAM raw materials costs and to precise process control.<sup>6</sup> Throughout the entire process chain, flaws and uncertainties in the production process are propagated accumulated, which significantly decreases the overall yield.<sup>6</sup> SCHMIDT et al.<sup>32</sup> described and analyzed this propagation of production uncertainties along the process chain and illustrate their influence on the final battery cell.

This paper provides a guideline for each production step of LMR-NCM/graphite cells in comparison to NCA/graphite cells, and also highlights the additional challenges of fabricating LMR-NCM/graphite large-scale multilayer pouch cells compared to small-scale laboratory coin cells. The ability to produce both types of cells, starting from the formulation and mixing of electrode coating slurries all the way to the formation of the finally obtained battery cells using manual methods as well as the pilot scale production line at the Technical University of Munich<sup>33</sup> makes it possible to compare the effects of each production step on the final performance of the cells and to determine the accuracy with which the gravimetric and volumetric energy density of large-scale cells can be projected based on coin cell data. Furthermore, additional ex-situ and operando characterization tools were used to study the influence of the individual process parameters in the various steps to produce laboratory coin cells and multilayer pouch cells, which yielded new insights with regards to the relationship between active material properties, their processability, and the final cell performance.

The here investigated process steps start with the mixing procedure of the individual electrode materials, followed by the coating process. The electrodes are then calendared to the targeted

<sup>=</sup>These authors contributed equally to this work.

\*Electrochemical Society Student Member.

\*\*Electrochemical Society Fellow.

<sup>z</sup>E-mail: david.schreiner@tum.de

thickness to achieve the desired electrode density or porosity, a step that is required to increase the energy density of the final cells as well as to improve the electrical conductivity across the electrode<sup>34</sup> and to minimize the contact resistance between the cathode electrode coating and the current collector.<sup>35</sup> Depending on the desired application and composition of the electrodes, they are generally calendered from an initial porosity of 45%–60% to typically 18%–35%.<sup>1,6,36,37</sup> Depending on the chosen active materials, the lower limit for the electrode porosity can be posed by either limitation in electrode wetting<sup>38</sup> or the onset of mechanical breakage of the active material particles.<sup>39,40</sup> Since the cell performance and rate capability significantly depend on the ionic and electrical conductivity across the electrode thickness,<sup>34</sup> which in turn depend on the extent of electrode compaction and electrode porosity, it is necessary to carefully investigate the calendaring-induced changes of the electrode pore size distribution, which can be done using mercury porosimetry.<sup>41</sup> The achievable compaction of electrodes depends strongly on the morphology of the chosen CAM and can only partially be compensated by using heated calendaring rolls,<sup>42–44</sup> or the close adequate conductive carbon black components.<sup>45</sup>

The other investigated production steps, which differ significantly between preparing large-format cells and laboratory-type coin cells, are the processes of filling the cells with electrolyte and cell formation. A large number of influencing factors in the electrolyte filling process<sup>46</sup> and the relationships between the electrolyte filling process, the wetting of the porous materials in the cell with electrolyte, as well as the cell formation and degassing procedure for a given cell format<sup>47</sup> result in a great variety in the currently used process designs that are described in the literature.<sup>48</sup> Degassing is necessary for large-format cells during their initial formation, since with an increased amount of active material, the gas produced during the first charge increases proportionally with the amount of active material or with the number of electrode layers, while the cell volume stays almost the same in stacked cells that are sealed under vacuum. Therefore, the degassing process is an important part of the large-format cell process chain (in contrast to small-scale cells), and removing the gas produced during or after the first charge and discharge cycle is an industrial standard,<sup>49</sup> even though it is scarcely considered in the literature.

Since studies of small-scale laboratory cells can therefore not fully address all the aspects that need to be considered for the manufacturing of large-format cells, this work examines the production steps of multilayered pouch cells with a target capacity of 5.5 Ah at a discharge rate of 1C (corresponding to  $\approx 6$ –7 Ah at C/10). For this purpose, full-cells with two different cathode active materials are considered, either lithium- and manganese-rich NCM (LMR-NCM) or NCA, highlighting the various challenges in the

large-format cell production process and examining the particular differences between the preparation of small-scale cells and large-format cells. A focus of this paper is the often neglected process step of electrode calendaring in the preparation of small-scale cells, for which the electrodes are frequently only compressed<sup>20,21,50</sup> by applying a constant compression force rather than being calendered or are even non-compacted at all.<sup>14,19,22</sup>

It will be shown that it is not possible to compact LMR-NCM electrodes to commonly used cathode porosities ( $\approx 30$ %–35%) with the same process parameters used for NCA. The differences in pore size distribution and electrode structure for the two CAMs will be examined by mercury porosimetry and scanning electron microscopy (SEM) cross-sectional analysis. Finally, material adapted calendaring parameters are given that allow further processing. Mercury porosimetry is introduced as a method to allow CAM developers to predict the later compaction potential of synthesized CAMs without the possibility of testing it on an industrial calendar. The formation/degassing procedures used for conventional CAMs (e.g., NCM and NCA) cannot be used for LMR-NCM based cells due to the strong first-cycle gassing of this material. Therefore an optimized procedure for the formation and degassing of large-format LMR-NCM/graphite cells is developed using on-line electrochemical mass spectrometry (OEMS) measurements.<sup>51</sup> We also compare the cell performance after the formation of the two cell chemistries on both the material and the cell level, and compare the results with the up-scale prediction based on coin cell pre-experiments. The rate capability, long-term stability, and thermal behavior of the produced large-format multilayer pouch cells are described in Part II of this study.<sup>52</sup>

## Experimental

**Production of multilayer pouch cells.**—The multilayer pouch cells were produced on the pilot scale production line<sup>33</sup> at the Institute for Machine Tools and Industrial Management (*iwb*) of the Technical University of Munich (TUM). The electrode production with the process steps mixing, coating, drying, and calendaring took place in a clean room class 1000/ISO 6. The following process steps of the cell assembly were carried out on a semi-automated assembly line in a dry room with a dew point of  $-40$  °C. To support the discussion of each process step and the corresponding process parameters, Fig. 1 provides an overview of the entire process chain of the multilayer pouch cell production at the *iwb* (processes conducted in the clean are gray colored, those in the dry room are blue colored). Additional cell setup information can be found in the attached Excel-based *cell configuration tool* in the supporting information (available online at [stacks.iop.org/JES/168/030507/mmedia](https://stacks.iop.org/JES/168/030507/mmedia)), where all masses and

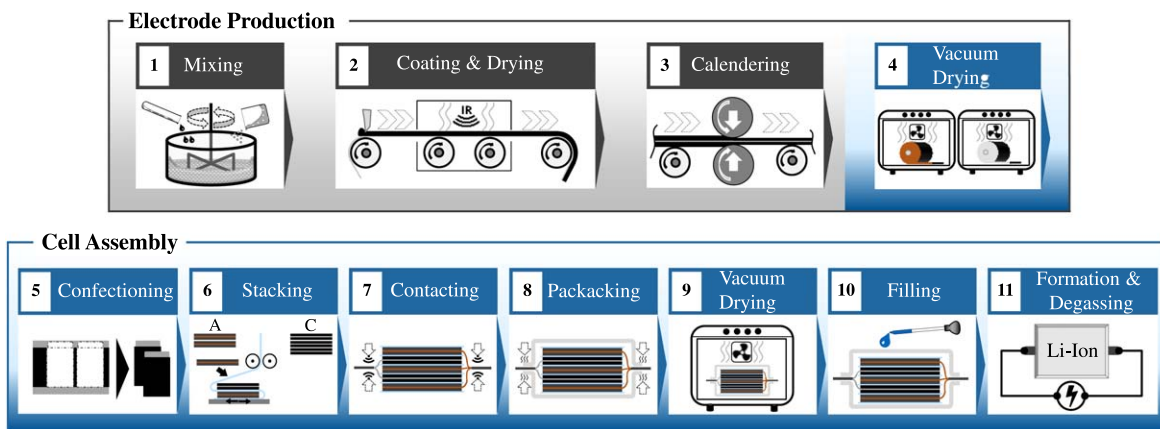


**Figure 1.** Schematic of the battery production process chain of lithium-ion pouch cells at the *iwb*, divided into electrode production (upper row) and cell assembly (lower row). The electrode production consists of the process steps mixing (1), coating and drying (2), calendaring (3) conducted in a clean room (gray colored), as well as vacuum drying of the coils conducted in the dry room with a dew point of  $-40$  °C (blue colored). The cell assembly includes confectioning (5), electrode stacking (6), contacting of the electrode stack (7), packaging (8), vacuum drying of the open pouch cells (9), electrolyte filling (10), as well as the formation and degassing of the cells (11), all of which is conducted in a dry room (blue colored) with a dew point of  $-40$  °C.

of 47% ( $\rho_{\text{coating}} = 2.22 \text{ g cm}^{-3}$ ) to 42% ( $\rho_{\text{coating}} = 2.43 \text{ g cm}^{-3}$ ) at 25 °C. Like the anodes for the LMR-NCM electrodes, the anodes for NCA were also calendered to 30% porosity ( $\rho_{\text{coating}} = 1.55 \text{ g cm}^{-3}$ ).

**Production step 4: vacuum drying (electrode coil).**—The electrode coils were dried in a vacuum oven (TR03 LFC from Waldner Process Systems, Germany) for three alternating drying and vacuum cycles. Each drying cycle was carried out at a drying temperature of 120 °C and begins at ambient pressure in the dry room (dew point –40 °C) and includes the following evacuation cycle:  $p_{\text{evac}1} = 400 \text{ mbar}$ ,  $p_{\text{evac}2} = 200 \text{ mbar}$ ,  $p_{\text{evac}3} = 100 \text{ mbar}$ ,  $p_{\text{evac}4} = 50 \text{ mbar}$ ,  $p_{\text{evac}5} = 30 \text{ mbar}$ ,  $p_{\text{evac}6} = 20 \text{ mbar}$  dwell time ( $t_{\text{evac}1} = 30 \text{ min}$ ,  $t_{\text{evac}2} = \dots = t_{\text{evac}6} = 5 \text{ min}$ ), and venting to ambient pressure level.

**Production step 5: confectioning.**—The separation of anode and cathode was performed by laser cutting with a cutting speed of  $0.3 \text{ m min}^{-1}$  and a laser power of 100 W. The used laser cutting module is a pulsed fiber laser (IGP Photonics, USA) with a wavelength of 1064 nm, a pulse width of 30 ns and a pulse frequency of 500 kHz.<sup>33</sup> The footprint of the anode coating of a thus cut electrode sheet is  $104 \text{ mm} \cdot 76 \text{ mm}$  ( $\equiv 79.04 \text{ cm}^2$  anode coating) with a remaining uncoated current collector foil area of  $67 \text{ mm} \cdot 15 \text{ mm}$  ( $\equiv 10.05 \text{ cm}^2$ ) for current conduction. The footprint of the cathode coating is  $101 \text{ mm} \cdot 73 \text{ mm}$  ( $\equiv 73.73 \text{ cm}^2$  cathode coating), with the same size of uncoated substrate foil ( $\equiv 10.05 \text{ cm}^2$ ) for current conduction.

**Production step 6: stacking.**—Both cell configurations (LMR-NCM/graphite and NCA/graphite) were stacked by z-folding with a configuration of 17 double-sided anode electrodes and 16 double-sided cathode electrodes using a celgard 2500 separator (Celgard LLC, USA) to obtain large-format multilayer pouch cells with an initial capacity at C/10 of 6.9 Ah for LMR-NCM (based on 27.6 g LMR-NCM in the cell and a nominal capacity of  $250 \text{ mAh g}^{-1}$ ) and 6.1 Ah for NCA (based on 30.7 g NCA in the cell and a nominal capacity of  $200 \text{ mAh g}^{-1}$ ). This results in a nominal cell energy of 24 Wh (LMR-NCM) and 23 Wh (NCA) based on averaged discharge voltages of 3.5 V for LMR-NCM cells and 3.7 V, for NCA cells respectively. The z-folding system was developed in cooperation with Manz Automation in a previous research project.<sup>33</sup>

**Production step 7: contacting.**—The substrate foils were initially contacted by ultrasonic welding in two steps with a Branson Ultraweld L20 system. For the LMR-NCM cathodes, the substrate foils were first contacted with an amplitude of  $16 \mu\text{m}$ , welding energy of 180 J, and a clamping force of 124.11 kPa. Subsequently, the conductor tabs were joined to the welded substrate foils with the same parameters. For the NCA cathodes, the substrate foils were initially contacted with an amplitude of  $16 \mu\text{m}$ , welding energy of 200 J, and a clamping force of 124.11 kPa. For contacting the tabs, the welding energy was reduced to 180 J.

For the anodes, both contacting steps were carried out with an amplitude of  $20 \mu\text{m}$ , welding energy of 450 J, and a clamping force of 172.37 kPa.

**Production step 8: packaging.**—The cell stacks were packaged into a flexible pouch bag with a deep-drawn pocket. Three sides of the pouch foil were sealed with a linear sealing module (HH - 4424 003 from Harro Höflinger, Germany) using impulse sealing bars with the following parameters: 3 s sealing time, 3.50 bar sealing pressure, 195 °C sealing temperature, and a residence time of 1 s. One side of the pouch cell was left open for electrolyte filling.

**Production step 9: vacuum drying (cell stack).**—Prior to filling, the cells were dried in the same vacuum oven as in production step 4. The drying process was composed of four cycles with a drying temperature of 60 °C and includes six steps. Each cycle begins at ambient pressure in the dry room (dew point –40 °C) and includes the following evacuation sequence:  $p_{\text{ev-}1} = 400 \text{ mbar}$ ,  $p_{\text{ev-}2} = 200 \text{ mbar}$ ,

$p_{\text{ev-}3} = 100 \text{ mbar}$ ,  $p_{\text{ev-}4} = 50 \text{ mbar}$ ,  $p_{\text{ev-}5} = 30 \text{ mbar}$ , and  $p_{\text{ev-}6} = 20 \text{ mbar}$ ; the dwell time at each pressure setting was 30 min for the first step and 5 min for all subsequent steps, while in between each cycle the cell was vented to ambient pressure.

**Production step 10: electrolyte filling.**—For the LMR-NCM/graphite cells, a 1 M LiPF<sub>6</sub> electrolyte with 12 vol% FEC, 64 vol% DEC, 24 vol% of a proprietary co-solvent, and 2 wt% of a proprietary stabilizing additive was obtained from BASF. The proprietary additive improves full-cell cycle stability and has a similar effect as the one described in Guéguen et al.<sup>54</sup> The total amount of electrolyte added to LMR-NCM/graphite cells ( $V_{\text{electrolyte}}$ ) was set to correspond to 1.5 times the total pore volume of electrodes and separator in the cell ( $V_{\text{pores}}$ ); a value of  $\approx 1.4$ – $1.6$  for this so-called volumetric factor ( $V_{\text{electrolyte}}/V_{\text{pores}}$ ) was found to yield the highest capacity retention for NCM111/graphite multilayer pouch cells.<sup>25</sup> The thus calculated amount of electrolyte was 24.0 ml (or 31.2 g based on its density of  $1.3 \text{ g ml}^{-1}$ ), corresponding to a  $\text{mass}_{\text{electrolyte}}/\text{mass}_{\text{CAM}}$  of 1.1/1. Due to this small amount of electrolyte when compared to the void volume between the flexible pouch foil and the cell stack, a single electrolyte dosing step was selected. Therefore, the filling process was composed of six steps: flushing with inert gas, evacuation, dosing, sealing, venting, and wetting. The process was implemented by an automated filling station from Manz (Germany), whereby the 24.0 ml of electrolyte were dosed in a vacuum chamber at an absolute pressure of 80 mbar. The closing pressure of the sealing bars was set to 3 bar for 3 s, with a sealing temperature of 195 °C. After venting the vacuum chamber, the cells were left to wet for 4 h at 40 °C in a temperature chamber (LabEvent T7210/40/3, Vötsch, Germany) before formation.

For the NCA cells, the same volumetric factor of  $V_{\text{electrolyte}}/V_{\text{pores}} = 1.5$  and the same filling process was used as for the LMR-NCM cells. Here, however, a different electrolyte was used, namely 1 M LiPF<sub>6</sub> in a mixture of ethylene carbonate (EC) and diethyl carbonate (DEC) with a weight ratio of EC:DEC 3:7 plus 2 wt% vinylene carbonate (VC) (LP472,  $1.2 \text{ g ml}^{-1}$ , BASF). Thus, 23.0 ml of electrolyte (or 27.6 g based on its density of  $1.2 \text{ g ml}^{-1}$ ) were added, corresponding to  $\text{mass}_{\text{electrolyte}}/\text{mass}_{\text{CAM}} = 0.9/1$ .

After electrolyte filling and the final sealing of the cells, the mass of added electrolyte was also evaluated by determining the differences between the weight of the sealed cells and that of the cells prior to electrolyte filling. The thus determined electrolyte mass was lower by  $10 \pm 5\%$  for the LMR-NCM/graphite cells and lower by  $11 \pm 1\%$  for the NCA/graphite cells. This electrolyte mass deviation of  $\approx 10\%$  is likely caused by a system specific offset as well as electrolyte evaporation during the electrolyte filling at 80 mbar and the sealing process.

**Production step 11: formation and degassing.**—The formation of the cells was conducted after a 4 h rest period to allow for complete wetting of the electrodes and the separator. Cell cycling was conducted using a BaSyTec CTS system.

The LMR-NCM/graphite cells were initially charged in constant current (CC) mode with C/15 (referenced to a nominal capacity of  $250 \text{ mAh/g}_{\text{CAM}}$ ) to 4.0 V at 40 °C. At 4.0 V, the cells were disconnected and degassed in the electrolyte filling station at 19 °C. For this purpose, the cells were opened by an automated knife (the size of the applied cut was 17 mm by 3 mm). Then the vacuum chamber was flushed with nitrogen and subsequently evacuated to 100 mbar, at which pressure the cells were resealed. After venting the system, the cells were electrically reconnected to the cell test system in the temperature chamber. After this first degassing step, the LMR-NCM/graphite cells were further charged at 40 °C in CC mode with C/15 to 4.7 V (0.1 V higher in this first activation cycle compared to the subsequent charge-discharge cycles, as is required for LMR-NCMs<sup>23,55</sup>) and then discharged in CC mode with C/15 to 4.0 V. At this point, a second degassing step was conducted, following the above given procedure. After this initial formation cycle at 40 °C, the cells were placed in a cell holder

geometrical information for the multilayer pouch cells prepared here are listed.

**Production step 1: mixing.**—The slurry for cathode electrode preparation consists of 92.5 wt% cathode active material, i.e., either LMR-NCM ( $\text{Li}_{1.14}[\text{Ni}_{0.26}\text{Co}_{0.14}\text{Mn}_{0.60}]_{0.86}\text{O}_2$ , which can as well be written as  $0.33 \text{Li}_2\text{MnO}_3 \cdot 0.67 \text{LiNi}_{0.38}\text{Co}_{0.21}\text{Mn}_{0.41}\text{O}_2$  done by Teuff et al.,<sup>10</sup> BASF, Germany) or NCA ( $\text{LiNi}_{0.81}\text{Co}_{0.15}\text{Al}_{0.04}\text{O}_2$ , BASF, Germany) with bulk densities ( $\rho_{\text{CAM}}$ ) of  $4.35 \text{ g cm}^{-3}$  and  $4.65 \text{ g cm}^{-3}$ , respectively, 4 wt% conductive carbon black (Super-C65, Timcal, Switzerland, with a bulk density of  $\rho_{\text{CB}} = 2.0 \text{ g cm}^{-3}$ ), and 3.5 wt% polyvinylidene-fluoride binder (PVdF, Solef 5130, Solvay, Belgium, with a bulk density of  $\rho_{\text{PVdF}} = 1.76 \text{ g cm}^{-3}$ ). In the context of this work, an electrode is defined as the electrode layer composed of active material, binder, and conductive carbon blacks coated onto the current collector foil, i.e., a cathode consists of an aluminum foil, cathode active material, binder, and conductive carbon blacks. The mixing process was carried out with a Speedmixer DAC 3000.1 HP (Hauschild & Co, Germany), whereby the detailed mixing parameters are listed in the Appendix (Fig. A-1). First, the cathode active materials (CAMs) were dry mixed; subsequently, the solids content was reduced sequentially by adding aliquots of anhydrous N-methyl-2-pyrrolidone (NMP) (Sigma-Aldrich, USA). For LMR-NCM based cathodes, the final solids content was set to 58 wt% (Fig. A-1), whereas for NCA a solids content of 70 wt% was used. The lower solids content for LMR-NCM slurries was required due to its a larger Brunauer-Emmet-Teller (BET) specific surface area and its smaller secondary agglomerate diameter determined by laser scattering (BET =  $4.35 \text{ m}^2 \text{ g}^{-1}$ ,  $d_{50} = 10 \pm 1 \mu\text{m}$  diameter) compared to NCA (BET =  $0.26 \text{ m}^2 \text{ g}^{-1}$ ,  $d_{50} = 15 \pm 1 \mu\text{m}$ ). The rheological properties of the slurries were determined with the MCR 302 rheometer (Anton Paar, Austria) using a plate-plate configuration (with a diameter of 25 mm and a gap of  $250 \mu\text{m}$ ) and a test procedure that measured the viscosity vs. the shear rate. At a shear rate of 100 1/s, the viscosity of the LMR-NCM slurry was 3.5 Pa·s and that of the NCA slurry was 10.9 Pa·s. The recommended cathode viscosity in the literature is 5 Pa·s at a shear rate of 100 1/s.<sup>53</sup> Based on our experience, cathode slurries with viscosities between  $\approx 3$ –12 Pa·s at 100 1/s are coatable with the doctor blade.

The slurry for anode preparation (for mixing parameters see Appendix, Fig. A-1) consists of 97 wt% graphite (SGL Carbon SE, Germany, with a bulk density of  $\rho_{\text{G}} = 2.26 \text{ g cm}^{-3}$ ), 1.5 wt% styrene-butadiene rubber (SBR, Zeon Europe GmbH, Japan, with a bulk density of  $\rho_{\text{SBR}} = 1.04 \text{ g cm}^{-3}$ ), and 1.5 wt% carboxymethyl cellulose (CMC Sunrose MAC200, NPI, Japan, with a bulk density of  $\rho_{\text{CMC}} = 1.6 \text{ g cm}^{-3}$ ). Deionized water was premixed with CMC (4.43 wt% solids content), then graphite was added to that solution (to an initial solids content of 75 wt%) and further mixed by sequentially adding deionized water to obtain a final solids content of 57 wt%. Finally, the SBR water mixture (40 wt% solids content) was added and mixed for 5 min at 400 rpm. At a shear rate of 100 1/s, the viscosity of the final anode slurry was  $\approx 6$ –7 Pa·s.

**Production step 2: coating and drying.**—The cathodes were coated onto both sides of the aluminum current collector foil ( $15 \mu\text{m}$ ; type 1050 A from Korff, Switzerland) at a speed of  $1 \text{ m min}^{-1}$ . For the LMR-NCM cathode active material, the average CAM loading per side is  $11.7 \pm 0.2 \text{ mg cm}^{-2}$  (corresponding to  $\approx 2.9 \text{ mAh cm}^{-2}$  based on a nominal specific capacity of  $250 \text{ mAh g}^{-1}$ ), resulting in an uncalendered dry electrode thickness of  $\approx 160 \mu\text{m}$  (this corresponds to the thickness of two cathode coatings and one aluminum current collector); the average weight fraction of the aluminum ( $\text{wt}\%_{\text{alu}}$ ) of the double-sided LMR-NCM electrodes is 13.8%. The constant temperatures for the three dryers were set to 85 °C, 105 °C, and 125 °C. The graphite anodes for the LMR-NCM/graphite cells were coated at a speed of  $0.5 \text{ m min}^{-1}$  onto both sides of a  $11 \mu\text{m}$  thick copper current collector foil (Cu-PHC, hard rolled blank, with

a nominal thickness of  $12 \mu\text{m}$ , Schlenk, Germany). The average anode active material (AAM) loading per side is  $9.5 \pm 0.6 \text{ mg cm}^{-2}$  (corresponding to  $\approx 3.4 \text{ mAh cm}^{-2}$  based on a nominal specific capacity of  $355 \text{ mAh g}^{-1}$ ), resulting in an uncalendered electrode thickness of  $\approx 208 \mu\text{m}$  (corresponding to the thickness of two anode coatings and one copper current collector) after drying (a temperature of 50 °C was set for all three infrared dryers).

The NCA slurry was also coated double-sided at  $1 \text{ m min}^{-1}$  onto the same  $15 \mu\text{m}$  thick aluminum foil. The average CAM loading per side is  $13.0 \pm 0.4 \text{ mg cm}^{-2}$  (corresponding to  $\approx 2.6 \text{ mAh cm}^{-2}$  based on a nominal specific capacity of  $200 \text{ mAh g}^{-1}$ ), resulting in an uncalendered electrode thickness of  $\approx 142 \mu\text{m}$  after drying, whereby the three dryers were set to 55 °C, 70 °C, and 85 °C. The average weight fraction of the aluminum ( $\text{wt}\%_{\text{alu}}$ ) of the double-sided NCA electrodes is 12.6%. The NCA loading was chosen to yield the same cathode areal capacity of  $\approx 2.3 \text{ mAh cm}^{-2}$  at 1C as that which was achieved with the above specified LMR-NCM cathodes. The anodes were also coated double-sided at  $0.5 \text{ m min}^{-1}$  onto the same copper current collector foil. The average loading per side of the anodes used for the NCA/graphite cells is  $10.2 \pm 0.5 \text{ mg cm}^{-2}$  (corresponding to  $\approx 3.6 \text{ mAh cm}^{-2}$ ), resulting in an uncalendered electrode thickness of  $\approx 222 \mu\text{m}$  for the anode electrodes dried as specified above.

**Production step 3: calendaring.**—The calender used for compaction was the EA 102 (Coatema, Germany) with a roll diameter of 400 mm and a maximum line-load of  $1000 \text{ N mm}^{-1}$ , at a constant roller speed of  $0.5 \text{ m min}^{-1}$  in all cases.<sup>41</sup> The thickness of the electrodes before and after calendaring was measured with a tactile dial gauge (40 EWri, Mahr, Germany). The electrode coating porosity ( $\epsilon_{\text{coating}}$ ) is 1 minus the ratio of the bulk volume of the electrode components ( $V_{\text{solid}}$ ) over the volume of the coating ( $V_{\text{coating}}$ ); the latter is determined by summing up the individual bulk volumes of the electrode components based on their bulk material density ( $\rho_i$ ) and their relative weight fraction ( $\text{wt}\%_i$ ) and dividing it by the coating area ( $A_{\text{coating}}$ ) and the measured thickness of the coating ( $d_{\text{coating}} = d_{\text{electrode}} - d_{\text{current-collector}}$ ) and finally multiplying this term by the total mass of the coating on both sides ( $m_{\text{coating}}$ ):

$$\epsilon_{\text{coating}} = 1 - \frac{V_{\text{solid}}}{V_{\text{coating}}} = 1 - \frac{\sum \frac{\text{wt}\%_i}{\rho_i}}{d_{\text{coating}} \times A_{\text{coating}}} \cdot m_{\text{coating}} \quad [1]$$

Since preliminary tests showed that calendaring of the LMR-NCM cathodes turned out to be challenging (discussed in detail later), the influence of the process parameters roll pressure, compaction rate, and temperature of the calendaring rolls were investigated. Based on an initial porosity of 56% ( $\rho_{\text{coating}} = 1.74 \text{ g cm}^{-3}$ ), the roller temperatures of 25 °C, 40 °C, 60 °C, 90 °C, and 120 °C were investigated in a full factorial Design of Experiments (DoE) for the two targeted coating porosity values of 42% ( $\rho_{\text{coating}} = 2.30 \text{ g cm}^{-3}$ ), and 32% ( $\rho_{\text{coating}} = 2.69 \text{ g cm}^{-3}$ ). Based on laboratory coin cell tests and the achievable and processable densities of the electrodes, the final target porosity was set to 42% porosity ( $\rho_{\text{coating}} = 2.30 \text{ g cm}^{-3}$ ), resulting in a compaction rate of  $\approx 22\%$  (from  $167 \mu\text{m}$  to  $131 \mu\text{m}$  thickness of the electrodes including two cathode coatings and one  $15 \mu\text{m}$  aluminum foil). This was achieved by heating the calendaring rolls to 120 °C to compact LMR-NCM electrodes for use in multilayer pouch cells.

The anodes were calendered from a pristine porosity of 55% ( $\rho_{\text{coating}} = 1.00 \text{ g cm}^{-3}$ ) to a porosity of 30% ( $\rho_{\text{coating}} = 1.55 \text{ g cm}^{-3}$ ) at 25 °C. This corresponds to a compaction rate of almost  $\approx 35\%$  (from  $206 \mu\text{m}$  to  $137 \mu\text{m}$  thickness of the electrodes including two anode coatings and one  $11 \mu\text{m}$  copper foil).

Since preliminary tests have shown that calendaring of the NCA electrodes is possible without heating the calendaring rolls, NCA electrode calendaring was performed based on the as-coated porosity

where they are kept under a compression of  $\approx 0.2$  MPa (discussed in more detail in Part II of the paper<sup>22</sup>). Thereafter, the cells were placed in a temperature chamber controlled at 25 °C and discharged in CC mode with C/15 to 2.0 V; this was followed by two stabilization cycles in CC mode at C/10 between 2.0 V and 4.6 V.

The formation and degassing of the NCA/graphite cells was performed at 25 °C. Initially, the cells were charged at C/15 (referenced to a nominal capacity of 200 mAh/g<sub>CAM</sub>) to an upper cut-off voltage of 4.3 V and then discharged to 4.0 V. At this point, the cells were degassed and re-sealed according to the above described procedure. Since there is very little gassing that originates from the NCA CAM compared to the LRM-NCM CAM (further details are provided in the Results and Discussion section), a single degassing step was sufficient for the NCA/graphite cells. Subsequently, the cells were placed in a cell holder where they were kept under a compression of  $\approx 0.2$  MPa and further discharged to 3.0 V at C/15. This was followed by two stabilization cycles at C/10 between 3.0 V and 4.3 V (all at 25 °C).

**Preparation of coin cell based half-cells.—***Electrode preparation.*—The electrodes were produced using the same materials and electrode compositions as for the double-sided coated electrodes for the multilayer pouch cells. The electrode materials were mixed in a planetary mixer (Thinky Corp., USA) using the same sequential dilution procedure as described for the pouch cell electrodes, except that the solids contents of the final slurries were  $\approx 4\%$  lower. The slurries were coated onto the rough side of an aluminum current collector foil (15  $\mu\text{m}$  thick, MTI, USA) with a box-type coating bar (Erichsen, Hemer, Germany), using an automated coater (RK PrintCoat Instruments, United Kingdom). Subsequently, they were dried in a convection oven at 50 °C for 5 h. The electrode coating loadings were varied by the gap size of the coater bar (120–400  $\mu\text{m}$  wet film thickness) to achieve loadings between 6–21 mg<sub>CAM</sub> cm<sup>-2</sup> after the drying step. The electrodes were calendered with a lab calender (Typ GK 300 L, Saueressig, Germany) to 42% or 32% electrode coating porosity.

*Coin cell assembly.*—For the coin cells, cathodes with 14 mm diameter were punched out from the single-side coated electrode sheets. Prior to cell assembly, the cathodes were dried in a glass oven (Büchi, Switzerland) under a dynamic vacuum at 120 °C for 12 h and then transferred into an argon-filled glove box (MBraun, Germany) without exposure to ambient atmosphere. The coin cells were assembled with two glass fiber separators (17 mm diameter, glass microfiber filter 691, VWR, Germany) that were wetted with 100  $\mu\text{l}$  of the same electrolytes as those used for the pouch cells (i.e., the FEC based electrolyte for coin cells with LMR-NCM and the LP472 electrolyte for those with NCA). For all coin cell tests, the counter-electrode was a lithium metal disk (15 mm diameter, 450  $\mu\text{m}$  thick, 99.9%, Rockwood Lithium).

*Coin cell cycling.*—All coin cell tests were performed with a Maccor cycler (series 4000, USA) and with the cells placed in a temperature-controlled chamber at 25 °C.

The lower cut-off potential for the LMR-NCM/lithium half-cells were set to 2.0 V. The upper cut-off potential is set to 4.8 V in the first activation cycle (i.e., 0.1 V higher than in the case of LMR-NCM/graphite cells to obtain the same upper cut-off value for the cathode electrode) that was conducted in CC mode at C/15 (referenced to 250 mAh/g<sub>CAM</sub>); different from the pouch cells, the activation cycle for LMR-NCM/lithium coin cells was conducted at 25 °C (as discussed later, the 40 °C activation was only necessary for pouch cell to address the strong gassing in the activation cycle). The two following stabilization cycles were conducted at C/10 (CC) between 2.0 V and 4.7 V.

The NCA/lithium cells were cycled at 25 °C between 3.0 and 4.4 V. The first formation cycle was performed in CC mode at C/15 (referenced to 200 mAh/g<sub>CAM</sub>). The following two stabilization cycles were carried out at C/10 between the same voltage limits.

After cell formation/stabilization, discharge rate capability tests were conducted. In these tests, the cells were always charged at C/2 followed by a CV (constant voltage) phase until the current decreased to below C/20. The following discharge rates were applied in CC mode: C/2 (3 cycles), 1C (5 cycles), 3C (10 cycles), and finally C/2 again (8 cycles).

**Ex-situ and operando characterization methods.—***Mercury intrusion.*—PoroTec GmbH performed the Mercury porosimetry measurements with the Mercury intrusion porosimeters Pascal 140 and Pascal 440 from ThermoFisher Scientific. The measurements were performed with a penetrometer of 7.4 ml bulb volume and 0.5 ml stem volume. In order to examine a representative sample volume, a sample weight of  $\approx 1$ –1.5 g (=15–25 pieces of  $\approx 2$ –2.5 cm<sup>2</sup> double-side coated electrode pieces) was added to the penetrometer. To obtain statistically significant results, three independent measurements each were taken for the as-coated LMR-NCM (porosity of 56%) and NCA (porosity of 47%) cathodes, as well as for the calendered LMR-NCM and NCA cathodes with porosities of 42% and 32%. By averaging at least three measured values and indicating the standard deviation, it can be ensured that for each porosity level a representative section of the electrode is evaluated by mercury porosimetry. The measured pore diameter ( $D$ ) correlates with the pressure ( $P$ ) required for intrusion of mercury through the Washburn equation (Eq. 2):

$$D = -\frac{4\gamma \cos(\theta)}{P} \quad [2]$$

Data analysis was based on a constant contact angle ( $\theta$ ) of 140° and constant surface tension ( $\gamma$ ) of 0.48 N m<sup>-1</sup> for mercury. The data were measured within a pressure range of 0–400 MPa, corresponding to pores down to a diameter of  $\approx 3$  nm. The measurements were corrected by a blank measurement of the empty penetrometer, and the compressibility of the individual electrode materials was considered negligible.

For the contribution of the conductive carbon black additive, supplementary measurements were performed with the MicroActive AutoPore V 9600, using a contact angle of 140°. To evaluate the carbon black (CB) contribution, CB-only electrodes (66.7/33.3 wt% CB/PVdF and a CB loading of  $\approx 2.5$  mg cm<sup>-2</sup>) and electrodes consisting of NCA without CB (96.5/3.5 wt% NCA/PVdF with an NCA loading of  $\approx 18$  mg cm<sup>-2</sup>) were measured both uncalendered and calendered. A penetrometer with a 5.0 ml bulb and 0.4 ml stem volume was used for these samples. A sample mass of about 0.8 g was used for the NCA coatings without CB to obtain a constant ratio of sample mass to bulb volume of  $\approx 0.2$  g ml<sup>-1</sup>, using  $\approx 25$  pieces of  $\approx 1.0$  cm · 1.5 cm single-side coated electrodes. For the CB-only coating the same number of single-side coated pieces ( $\approx 25$ ) as for the NCA coating without carbon black was used.

*Nitrogen physisorption analysis.*—Surface area and pore volume measurements were performed on a gas sorption analyzer (Autosorb-iQ, Quantachrome, USA) at -196.15 °C using nitrogen as adsorbent. Beforehand, the pristine powders were degassed under vacuum at 120 °C for 12 h. The specific surface area was determined from adsorption isotherms in the relative pressure range of 0.008 <  $p/p_0$  < 0.25 according to the Brunauer-Emmet-Teller (BET) theory. The specific total pore volume of adsorbed nitrogen can be determined at the limiting pressure  $p/p_0 \geq 0.986$  of the adsorption branch and therefore includes pore volumes up to  $\approx 140$  nm. The pore volume ( $V_{pore}$ ) can be calculated with the volume of nitrogen adsorbed ( $V_{ads}$ ) using Eq. 3:

$$V_{pore} = \frac{P^*V_{ads}^*V_m}{RT} \quad [3]$$

where  $P$  is the pressure,  $V_m$  the molar volume of nitrogen at -196.15 °C (i.e., 34.7 cm<sup>3</sup> mol<sup>-1</sup>),  $R$  the universal gas constant, and  $T$  the temperature.

**Particle size determination.**—The size of the secondary agglomerates were determined by dispersing the particles in ethanol and then using laser scattering (LA-950V2, Horiba, Japan); the data were analyzed by means of the Mie scattering theory.

**SEM cross-sectional imaging.**—The electrodes were placed between a z-folded carbon paper (H1410–14, Freudenberg, Germany) that was compressed between two aluminum plates (1.0 cm · 1.0 cm · 0.1 cm). The electrodes were then imbibed by a liquid epoxy resin (EpoThin 2, Buehler, Switzerland); with the resin still liquid, the sample stack was placed into a desiccator, which was then evacuated to ensure complete filling of the pores by the resin. After the resin had hardened, the sample stack was polished with SiC paper (CarbiMet S, P320, Buehler, Switzerland) until the electrode cross-section was fully exposed. Afterward, the electrode was polished using a finer SiC paper (CarbiMetS, P1200, Buehler, Switzerland) and a diamond based polishing suspension (MetaDiSupreme, Polycrystalline Diamond Suspension, 9  $\mu\text{m}$ , Buehler, Switzerland). The final polishing step was performed using a 50 nm  $\text{Al}_2\text{O}_3$  agent (MasterPrep Alumina Suspension, Buehler, Switzerland) on a micro cloth (ChemoMet, Buehler, Switzerland). The scanning electron microscopy (SEM) images were acquired using a Jeol JSM-7500F field emission SEM at 1 kV with an LEI detector and a magnification of 1000.

**OEMS measurements.**—The LMR-NCM slurry to prepare electrodes for on-line electrochemical mass spectrometry (OEMS) was prepared as described above (92.5/4/3.5 wt% CAM/CB/PVdF) and coated with a wet film thickness of 20  $\mu\text{m}$  onto a stainless-steel mesh (SS316, aperture 26  $\mu\text{m}$ , wire diameter 25  $\mu\text{m}$ , The Mesh Company, UK), yielding a LMR-NCM loading of 12–14  $\text{mg cm}^{-2}$  (3–3.5  $\text{mAh cm}^{-2}$  based on 250  $\text{mAh/g}_{\text{CAM}}$ ). In this case, the electrodes for were punched out with a diameter of 15 mm and compressed for 20 s with 2 t to yield a porosity of  $\approx 45\%$ . For the anode side, the same graphite electrode sheet as prepared for the pouch cells was used and punched out with a diameter of 17 mm. The electrodes were dried together with a glass fiber separator of 24 mm diameter in a glass oven (Büchi, Switzerland) under a dynamic vacuum at 120 °C for 12 h and then transferred into an argon-filled glove box without exposure to the atmosphere.

For OEMS measurements, a custom-made cell was used; the specific cell design as well as the OEMS setup were previously published.<sup>50</sup> OEMS cells were assembled with the graphite anode placed onto the bottom part of the OEMS cell, followed by the glass fiber separator soaked with 300  $\mu\text{l}$  of the FEC/DEC based LMR-NCM electrolyte that was used for the coin and multilayer pouch cells. The mesh-supported LMR-NCM cathode was placed on top of the separator and is thus located just below the flow-restricting capillary that leads to the mass spectrometer. The cells were connected to the mass spectrometer, held for 4 h at OCV (open circuit voltage), and were then charged to 4.7 V at a C/12 rate with a final CV phase until a cut-off current of C/24, followed by a discharge to 2.0 V at C/12. After this first activation cycle, the cells were flushed for 2 min with argon to re-pressurize the cell (over the  $\approx 24$  h long activation cycle,  $\approx 1.5$  ml of the 11 ml gas head-space of the OEMS cell are leaked into vacuum through the flow-restricting capillary with a specified leak rate of  $\approx 1 \mu\text{l min}^{-1}$ ). The cell was then stabilized for 4 h at OCV, followed by three cycles at C/4 between 2.0–4.6 V with a CV phase at 4.6 V until a cut-off current of C/8.

To quantify the mass spectrometer signals, a calibration gas containing  $\text{H}_2$ ,  $\text{O}_2$ ,  $\text{CO}_2$ , and CO (each 2000 ppm) in argon (Linde AG, Germany) was used. All mass spectrometer signals were normalized to the signal at a mass-to-charge ratio  $m/z = 36$  (corresponding to the  $^{36}\text{Ar}$  isotope) to correct for minor variations in cell pressure and temperature. Afterward, the signals at  $m/z = 44$  ( $\text{CO}_2$ ),  $m/z = 32$  ( $\text{O}_2$ ),  $m/z = 2$  ( $\text{H}_2$ ), and  $m/z = 28$  (CO) were converted into a gas concentration using the ideal gas law, taking a

gas head-space volume of the OEMS cell of roughly 11 ml into consideration.

**Large-format cell energy density projections from coin cell data.**—The measured half-cell performance in coin cells with the different cathode active materials was utilized to project the performance of large-format multilayer pouch cells with a cell stack configuration of 17/16 double-side coated anode/cathode sheets. The *cell configuration tool* (see Excel file in the supporting information) considers the weight of all inactive cell components (current collector foils and tabs, pouch cell foil), the geometrical overlap of the anodes, the weight of the electrolyte based on the volumetric factor of  $V_{\text{electrolyte}}/V_{\text{pores}}$  (1.5 for the multilayer pouch cells built here), and the separator. The Excel-based tool is designed to project the full-cell multilayer pouch cell energy density based on half-cell coin cell data. For this, the half-cell data are corrected by the 0.1 V lower upper cut-off voltage in CAM/graphite full-cells compared to CAM/lithium half-cells as well as by the smaller capacity of full-cells due to the first-cycle irreversible capacity loss. This loss is either dominated by the SEI loss of the anode or by the cathode first-cycle efficiency (most often the case for NCM based cathodes). The first-cycle efficiency is slightly reduced for the CAM/graphite full-cells compared to CAM/lithium half-cells (by  $\approx 9$   $\text{mAh/g}_{\text{CAM}}$ ), because in this work the lower voltage cut-off in full-cells was chosen to be the same as for half-cells, so that the CAM is slightly less discharged in the full-cells as in the corresponding half-cells.

## Results and Discussion

**LMR-NCM electrode design based on LMR-NCM/Lithium half-cells.**—**Loading dependent discharge rate capability.**—To the best of our knowledge, there is only one study in the literature on the rate capability of LMR-NCM cathodes as a function of loading.<sup>56</sup> Since this relation strongly depends on the individual LMR-NCM material composition and morphology, preliminary investigations were performed with LMR-NCM/lithium half-cells at the coin cell level (Fig. 2). For this purpose, LMR-NCM cathodes with four different loadings were prepared on a laboratory scale, calendered to 42% porosity, and subjected to a rate capability test (see Experimental section).

Already at the two stabilization cycles at C/10 (cycles 2 and 3), the electrodes with the highest LMR-NCM loading of  $\approx 21.1 \text{ mg cm}^{-2}$  ( $\approx 5.3 \text{ mAh cm}^{-2}$  based on a nominal capacity of 250  $\text{mAh/g}_{\text{CAM}}$ ) show a significantly lower specific discharge capacity than the electrodes with the lower LMR-NCM loadings of  $\approx 15.3 \text{ mg cm}^{-2}$  ( $\approx 3.8 \text{ mAh cm}^{-2}$ ), of  $\approx 11.4 \text{ mg cm}^{-2}$  ( $\approx 2.9 \text{ mAh cm}^{-2}$ ), and of  $\approx 6.9 \text{ mg cm}^{-2}$  ( $\approx 1.7 \text{ mAh cm}^{-2}$ ) which all reach about the same specific capacity of  $\approx 250 \text{ mAh/g}_{\text{CAM}}$  (see Fig. 2). This effect is even more apparent at a discharge rate of C/2 (cycles 4–6) and 1C (cycles 7–11), where the three lower loadings still yield essentially identical discharge capacities (e.g.,  $\approx 200 \text{ mAh/g}_{\text{CAM}}$  at 1C), which are much higher than those observed for the LMR-NCM electrodes with the highest loading of  $\approx 21.1 \text{ mg cm}^{-2}$  (e.g., only  $\approx 125 \text{ mAh/g}_{\text{CAM}}$  at 1C). At 3C (cycles 12–21), the specific discharge capacity not only decreases significantly for all LMR-NCM loadings, but now also shows a clear trend of decreasing specific discharge capacity with increasing loading. In the C/2 cycles after the ten cycles at 3C (i.e., cycles 22–29), the specific discharge capacity of all the cells is essentially identical with that recorded in the initial C/2 cycles (cycles 4–6), with  $\approx 225 \text{ mAh/g}_{\text{CAM}}$  for the three lowest loadings and  $\approx 180 \text{ mAh/g}_{\text{CAM}}$  for the highest loading. This retention of the capacity shows that the capacity loss at high C-rates must have been caused mainly by the high concentration overpotentials at high C-rates, which are more pronounced for the high-loaded cathodes, as they are both thicker and are operated at higher geometric current densities (at 3C, e.g., the geometric current densities increase from  $\approx 5.1 \text{ mA cm}^{-2}$  for the  $\approx 6.9 \text{ mg cm}^{-2}$  electrodes with a thickness of  $\approx 33 \mu\text{m}$  to  $\approx 15.9 \text{ mA cm}^{-2}$  for the

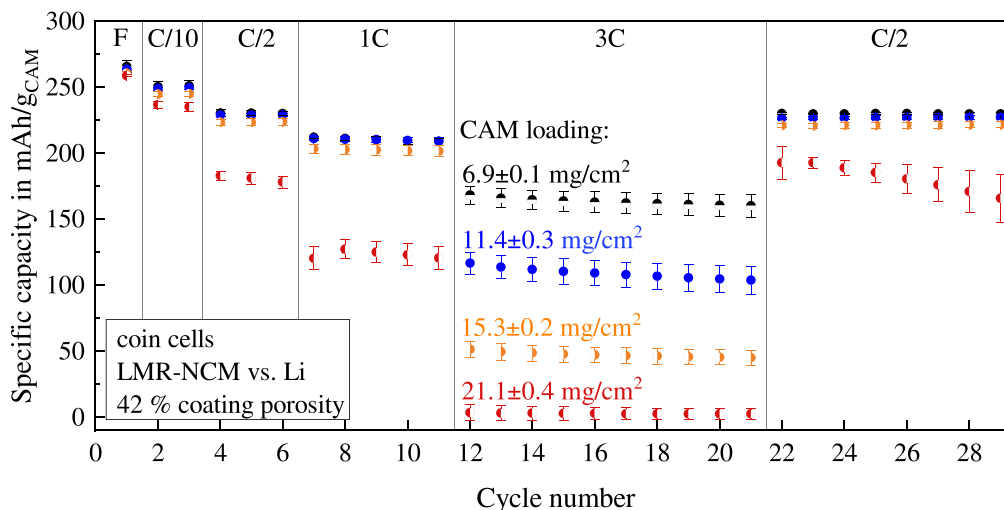


**Figure 2.** Discharge rate capability test at 25 °C of LMR-NCM/lithium coin cells with different LMR-NCM loadings (calendered to a porosity of 42%) after a first-cycle activation at C/15 (CC) between 2.0 V and 4.8 V (referred to as F for formation) and two CC stabilization cycles between 2.0 V and 4.7 V at C/10 (C-rates are referenced to a nominal specific capacity of 250 mAh/g<sub>CAM</sub>). The subsequent cycles are conducted between 2.0 V and 4.7 V at different discharge rates (C/2, 1C, 3C, and C/2, all in CC mode) and with a CC charge at C/2 followed by a CV phase until the current decreased to below C/20. The CAM loadings indicated in the figure represent the average and the standard deviation of three individual cells (except for the  $\approx 15$  mg cm<sup>-2</sup> electrodes, for which only two cells were tested). The capacity data for each CAM loading series were averaged over three independent cells (two in case of the  $\approx 15$  mg cm<sup>-2</sup> electrodes), with the standard deviation as error bars. The FEC/DEC based electrolyte specified in the Experimental section was used.

$\approx 21.1$  mg cm<sup>-2</sup> electrodes with a thickness of  $\approx 107$   $\mu$ m). While for the electrodes with an LRM-NCM loading of  $\approx 21.1$  mg cm<sup>-2</sup> some capacity fading appears to occur toward the end of this rate capability test at C/2 (cycles 22–28), this must not necessarily reflect a degradation of the cathode active material but may be due to a degradation of the metallic lithium anode at the high current densities required for electrodes with such high areal capacities. Thus, meaningful CAM cycle-life tests must be conducted in full-cells rather than half-cells,<sup>57</sup> and LMR-NCM/graphite cycle-life tests with multilayer pouch cells with a nominal areal capacity of  $\approx 2.9$  mAh cm<sup>-2</sup> are presented in Part II of this work.<sup>52</sup>

As discussed in the literature, the energy density of large-format battery cells is primarily a function of the active material loadings and also of the electrode thickness, whereas the rate capability in general decreases for higher active material loadings.<sup>58</sup> Therefore, there is a sweet spot for maximizing the energy density of large-format cells for a given C-rate requirement. For small-scale laboratory cells, energy density is generally not considered and to obtain the best C-rate performance when testing new cathode active materials, rather low CAM loadings are usually used, as is the case for many studies with LMR-NCM cathode active materials.<sup>10,19–22,46</sup> However, as we will demonstrate in the following, small-scale half-cell tests with different CAM loadings can be used to project the performance and energy density of large-format full-cells.

Table I lists the specific discharge (DCH) capacities, the corresponding discharge voltages, and CAM based energy densities obtained from the LMR-NCM/lithium coin cell experiments at C/10, 1C, and 3C for the four different LMR-NCM loadings shown in Fig. 2. These LMR-NCM performance characteristics determined in half-cells were then used to project the performance and energy density of large-format cells with a cell stack configuration of 17/16 double-side coated anode/cathode sheets that were used to construct  $\approx 6.9$  Ah (at C/10) multilayer pouch cells, considering the mass of all inactive components (current collector foils and tabs, pouch cell foil), the electrolyte (for  $V_{\text{electrolyte}}/V_{\text{pores}} = 1.5$ ), and the separator, as specified in the Excel-based calculation tool (see *cell configuration tool* in the supporting information). To project the large-format multilayer pouch cell energy densities, the mean discharge voltages from the half-cell measurements were reduced by 0.1 V, accounting for the higher potential of the graphite anodes used in a full cell setup. Furthermore we reduced the half-cell capacity according to

the first cycle irreversible losses (i.e., by 9 mAh/g<sub>CAM</sub>; see Experimental section).

As can be seen in Table I, the measured specific energy densities on the CAM level (in units of mWh/g<sub>CAM</sub> and referenced to the lithium potential) decrease with increasing LRM-NCM loadings, independent of the applied C-rate. Since the smaller loadings have only a slightly higher discharge capacity and voltage for C/10, the energy density at the cell level rises with increasing LMR-NCM loadings from 168 Wh/kg<sub>cell</sub> (for  $\approx 6.9$  mg cm<sup>-2</sup>) to 222 Wh/kg<sub>cell</sub> (for  $\approx 21.1$  mg cm<sup>-2</sup>). In contrast, the strong decrease in capacity and discharge voltage drop at 3C for high LMR-NCM loadings results in higher energy densities on the cell level for the smaller loadings. For a C-rate of 1C, the highest energy density on the cell level can be found for the intermediate loadings of  $\approx 11.4$  and  $\approx 15.3$  mg cm<sup>-2</sup>, reaching 159–162 Wh/kg<sub>cell</sub>. In Table I, the LMR-NCM loadings that yield the highest cell level energy density at a given C-rate are highlighted (15.3 and 21.1 mg cm<sup>-2</sup> for C/10, 11.4 and 15.3 mg cm<sup>-2</sup> for 1C and 6.9 mg cm<sup>-2</sup> for 3C). As the multilayer pouch cells produced within this work are targeted to operate up to a maximum C-rate of 1C, an LMR-NCM loading of  $\approx 12$  mg cm<sup>-2</sup> was chosen for the multilayer pouch cells.

**Porosity dependent discharge rate capability.**—Based on the above findings, the loading of  $\approx 12$  mg cm<sup>-2</sup> for LMR-NCM/lithium coin cells (corresponding to a nominal areal capacity of  $\approx 3.0$  mAh cm<sup>-2</sup> at 0.1C) was selected to investigate different coating densities in the next step. For comparison, NCA/lithium coin cells with a similar areal capacity of  $\approx 2.7$  mAh cm<sup>-2</sup> ( $\approx 13.5$  mg cm<sup>-2</sup> NCA loading) were examined also. To determine the influence of calendaring on the C-rate performance, the LMR-NCM, as well as the NCA cathodes, were calendered to two porosity levels (42% and 32%) from the as-coated (uncalendar) porosities of 56% and 47%, respectively. The results of the rate capability test conducted in the same way as that described in Fig. 2 is shown in Fig. 3.

The results of the discharge rate capability test with different cathode porosity levels (Fig. 3) show that, except for 3C, the cathode coating porosity within the considered range (i.e., from 56% to 32% for the LMR-NCM cathodes and from 47% to 32% for the NCA cathodes) has a negligible influence on the C-rate performance. Thus, it can be concluded that the cathode porosity does not have a large impact on the achievable capacity until rather high C-rates for

**Table I.** Impact of cathodes with different CAM loadings (calendered to a porosity of 42%) based on the LRM-NCM/lithium coin cell data in Fig. 2 (always using the 2<sup>nd</sup> cycle for each C-rate) on the materials level LMR-NCM performance characteristics and on the projected energy density for multilayer pouch cells with a nominal capacity of  $\approx 6.9$  Ah (at 0.1C). The latter is based on the Excel-based projection tool provided in the supporting information (referred to as cell configuration tool). The given values are averaged over three individual coin cells for each LMR-NCM loading (two in case of the  $15.3$  mg cm<sup>-2</sup> loading).

Coin cell data & energy density	C-rate	CAM loading in mg cm <sup>-2</sup> /areal capacity at 0.1C inmAh cm <sup>-2</sup>			
		6.9 ± 0.1/≈1.7	11.4 ± 0.3/≈2.9	15.3 ± 0.2/≈3.8	21.1 ± 0.4/≈5.3
DCH capacity in mAh/g <sub>CAM</sub>	C/10	251 ± 4	250 ± 1	245 ± 1	238 ± 3
avg. half-cell DCH voltage in V	C/10	3.640 ± 0.004	3.638 ± 0.002	3.633 ± 0.003	3.56 ± 0.01
CAM spec. energy in mWh/g <sub>CAM</sub>	C/10	914 ± 1	908 ± 1	891 ± 1	848 ± 3
cell spec. energy in Wh/kg <sub>cell</sub> <sup>a)</sup>	C/10	168	202	216	<b>222</b>
DCH capacity in mAh/g <sub>CAM</sub>	1C	212 ± 1	211 ± 2	203 ± 3	120 ± 7
avg. half-cell DCH voltage in V	1C	3.50 ± 0.01	3.42 ± 0.04	3.33 ± 0.02	2.83 ± 0.08
CAM spec. energy in mWh/g <sub>CAM</sub>	1C	743 ± 1	723 ± 2	676 ± 3	341 ± 7
cell spec. energy in Wh/kg <sub>cell</sub> <sup>a)</sup>	1C	135	<b>159</b>	<b>162</b>	85
DCH capacity in mAh/g <sub>CAM</sub>	3C	166 ± 7	114 ± 9	50 ± 4	3 ± 5
avg. half-cell DCH voltage in V	3C	3.30 ± 0.03	3.1 ± 0.1	2.93 ± 0.06	2.2 ± 0.1
CAM spec. energy in mWh/g <sub>CAM</sub>	3C	552 ± 7	353 ± 9	145 ± 4	7 ± 5
cell spec. energy in Wh/kg <sub>cell</sub> <sup>a)</sup>	3C	<b>98</b>	75	30	n.a.

a) Calculated with the Excel-based projection tool (see *cell configuration tool* in the supporting information) using the here listed performance characteristics of LMR-NCM/lithium coin cells with different LMR-NCM loadings (using the average loading values). The essential assumptions are: i) 17/16 double-side coated anode/cathode sheets (89.09/83.78 cm<sup>2</sup> for anode/cathode sheet); ii) anode coating porosity of 30%; iii) anode/cathode active areas of 79.04/73.73 cm<sup>2</sup>; with an areal capacity ratio of 1.2/1; iv) Al/Cu current collector thickness of 15/11 μm; v) Celgard 2500 separator (25 μm thick, 55% porosity); vi) electrolyte volume determined by  $V_{electrolyte}/V_{pores} = 1.5$ ; vii) LMR-NCM/graphite full-cell voltages are assumed to be 0.1 V lower than the here listed half-cell voltages and 9 mAh g<sup>-1</sup> lower than the here listed half-cell capacities. All further specifications like current collector tab size/mass, pouch foil mass, etc., are specified in the Excel-based *configuration tool*.

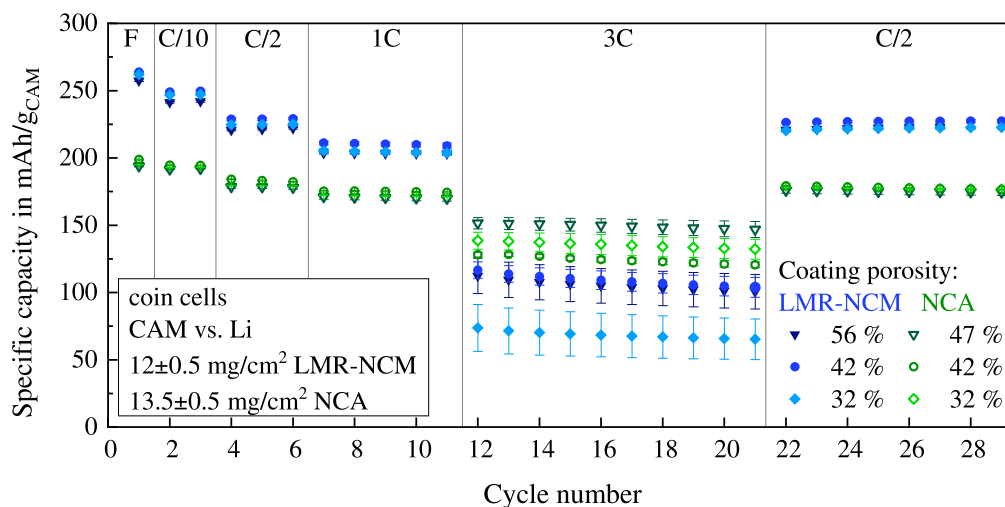


**Figure 3.** Discharge rate capability test at 25 °C of LMR-NCM/lithium and NCA/lithium coin cells with different cathode coating porosities, either as-coated, resulting in 56% and 47% porosity for LMR-NCM and NCA, respectively, or calendered to 42% and 32% (porosities are calculated based on Eq. 1 and are within an accuracy of  $\pm 2$  percentage points). For LMR-NCM/lithium cells, the formation, stabilization, and further cycling were conducted as described in Fig. 2 (C-rates referenced to 250 mAh/g<sub>CAM</sub>); NCA/lithium coin cells were cycled between 3.0 V and 4.4 V (C-rates referenced to 200 mAh/g<sub>CAM</sub>), but otherwise followed the same procedure. The NCA loadings are  $13.5 \pm 0.5$  mg cm<sup>-2</sup> ( $\approx 2.7$  mAh cm<sup>-2</sup> at 0.1C) and the LMR-NCM loadings are  $12 \pm 0.5$  mg cm<sup>-2</sup> ( $\approx 3$  mAh cm<sup>-2</sup> at 0.1C). The shown data points are averaged over three independent cells per porosity (only two for the cells with the 32% porosity LMR-NCM coating), with the standard deviation as error bars.

moderately low porosities of 32%. However, as illustrated in Table II, cathode porosity has a significant impact on the gravimetric and volumetric energy density on a cell level. While the volumetric density change is obvious and follows directly from the decrease of electrode thickness with decreasing cathode porosity, the gravimetric cell energy densities also decrease with decreasing porosity on account of the thus reduced electrolyte volume and mass when maintaining the volumetric factor at  $V_{electrolyte}/V_{pores} = 1.5$ .

The energy densities in Table II show that low LMR-NCM cathode porosities work well on the materials level. The predicted performance at the cell level (done with the *cell configuration tool* in

the supporting information), illustrates the importance of calendering on the cell level specific and volumetric energy density, while having a rather negligible effect on the rate capability up to 1C (see Fig. 3): the cell level specific energy density increases by up to 13%, while the gravimetric energy density increases by up to 18% (actually projected values are given for 0.1C in Table II, but the percentage increase is valid up to 1C).

As will be shown in the next section, calendering of large-scale LMR-NCM cathode coatings to porosities of 32% is not feasible, so that a porosity of 42% was targeted for the final large-scale production of LMR-NCM electrodes and thus for the production

**Table II. Impact of the cathode porosities on the performance of LMR-NCM/lithium coin cells at C/10 (using the 2<sup>nd</sup> C/10 cycle of the discharge rate capability test shown in Fig. 3) on the materials level LMR-NCM performance characteristics and on the predicted energy densities (based on the cell configuration tool given in the supporting information) for a nominal 6.9 Ah pouch cells. Here, the LMR-NCM loadings are  $12 \pm 0.5 \text{ mg cm}^{-2}$  ( $\equiv 3 \text{ mAh cm}^{-2}$  at 0.1C), the given values are averaged over three individual coin cells for each LMR-NCM cathode porosity (only two in case of the 32% porosity), stating the average values and their standard deviations. The values for an NCA cathode calendered to 42% porosity and based on the NCA/lithium coin cell data shown in Fig. 3 are given for comparison (for NCA loadings of  $13.5 \pm 0.5 \text{ mg cm}^{-2}$ , corresponding to  $\equiv 2.7 \text{ mAh cm}^{-2}$  at 0.1C).**

Coin cell data & energy density at C/10	Cathode porosity			
	LMR-NCM 56%	LMR-NCM 42%	LMR-NCM 32%	NCA 42%
DCH capacity in mAh/g <sub>CAM</sub>	242 ± 1	250 ± 1	247 ± 1	197.1 ± 0.5
DCH half-cell voltage in V	3.637 ± 0.001	3.638 ± 0.002	3.636 ± 0.001	3.827 ± 0.001
CAM spec. energy in mWh/g <sub>CAM</sub>	880 ± 1 ( $\equiv 100\%$ )	909 ± 1 ( $\equiv 103\%$ )	898 ± 1 ( $\equiv 102\%$ )	754.3 ± 0.5
cell spec. energy in Wh/kg <sub>cell</sub> <sup>a)</sup>	186 ( $\equiv 100\%$ )	206 (111%)	210 ( $\equiv 113\%$ )	193
cell grav. energy density in Wh/l <sub>cell</sub> <sup>a)</sup>	402 ( $\equiv 100\%$ )	459 ( $\equiv 114\%$ )	475 ( $\equiv 118\%$ )	433

a) Calculated with the Excel-based projection tool (see *cell configuration tool* in the supporting information) using the here listed performance characteristics of LMR-NCM/lithium and NCA/lithium coin cells (using the average loading values). The essential assumptions are: i) 17/16 double-side coated anode/cathode sheets (89.09/83.78 cm<sup>2</sup> for anode/cathode sheet); ii) anode coating porosity of 30%; iii) anode/cathode active areas of 79.04/73.73 cm<sup>2</sup>; with an areal capacity ratio of 1.2/1; iv) Al/Cu current collector thickness of 15/11 μm; v) Celgard C2500 separator (25 μm thick, 55% porosity); vi) electrolyte volume determined by  $V_{\text{electrolyte}}/V_{\text{pores}} = 1.5$ ; vii) LMR-NCM/graphite full-cell voltages are assumed to be 0.1 V lower than the here listed half-cell voltages. All further specifications like current collector tab size/mass, pouch foil mass, etc., are specified in the Excel-based *configuration tool*.

of large-format multilayer LMR-NCM/graphite pouch cells. In order to provide a meaningful comparison between LMR-NCM/graphite and NCA/graphite large-format cells, the NCA cathode coatings were also calendered to a porosity of 42%, even though the large-scale production of NCA cathode coatings with the lower porosity of 32% would be possible without problems.

**Effect of the CAM morphology on the calendering process.—Calendering process.**—The LMR-NCM coating was initially calendered to 42% porosity, a compaction degree that is usually unproblematic for cathode active materials. Figure 4a shows a side view of the calendered electrode (with calendering rolls at 25 °C) coated double-sided with LMR-NCM cathodes before rewinding the electrode to the coil, and Fig. 4b provides a zoomed-in view as well as a representative top view of this electrode. The clearly apparent embossing of the aluminum foil at the coating edge<sup>42</sup> was unexpected for this still rather high porosity of 42% and is not observed for electrodes coated on both sides with NCA cathodes that were also calendered to the same final porosity of 42% with calendering rolls at 25 °C (see Fig. 4c). As will be shown later, this effect is due to the different morphology of the LMR-NCM CAM compared to the NCA CAM. To minimize the embossing of the aluminum foil in the case of the LMR-NCM electrodes, the calendering rolls were heated, which allowed a lowering of the calendering line-load,<sup>41</sup> and thus reduced the extent and number of electrode defects.<sup>42</sup>

Despite calendering to a moderate porosity of 42%, the LMR-NCM electrodes have a pronounced bowl-shape geometry and show strong aluminum foil embossing for the standard calendering procedure (a rolling speed of 0.5 m min<sup>-1</sup>, and calendering rolls at 25 °C, as was used for NCA electrodes), which by GÜNTHER et al.<sup>42</sup> is ascribed to embrittlement for highly compressed cathode materials. Any further processing in the pilot scale production line of electrodes with these severe defects is not possible, because automatic processes for example electrode transport and alignment with vacuum grippers or exact laser cutting require flat and uniform surfaces. A hypothesis to explain this behavior is that the LMR-NCM cathode must have little elastic deformation and is thus also sensitive to current collector foil tears during further processing. The best calendering results for the LMR-NCM electrodes could be achieved with calendering rolls heated to 120 °C (please note that the images shown in Figs. 4a and 4b are for the non-optimized calendering process with calendering rolls at 25 °C).

On the other hand, the NCA electrodes proved to be less sensitive to calendering to 42% porosity and any subsequent processing steps

were unproblematic, so that the standard calendering procedures with calendering rolls at 25 °C could be used.

**Cross-sectional SEM image analysis.**—LMR-NCM (Figs. 5a–5c) and NCA (Figs. 5d–5f) electrodes compacted to the different porosity levels (calculated according to Eq. 1) are shown by cross-sectional SEM images. In addition to the different coating thicknesses from which the porosities were calculated (Eq. 1), these images show the respective agglomerate packing densities and morphologies of the LMR-NCM and NCA electrode coatings.

Comparing the SEM images of the uncalendered LMR-NCM (Fig. 5a) and NCA cathodes (Fig. 5d) cathodes, the packing density of the particles appears comparable, even though the overall cathode porosity of these uncalendered electrodes varies from 47% for the NCA to 56% for the LMR-NCM cathodes. On the other hand, after calendering the LMR-NCM and NCA electrodes to the same overall cathode porosity of either 42% or 32% (calculated according to Eq. 1), the individual LMR-NCM particles appear more densely packed (see Figs. 5b and 5c) compared to the NCA particles (see Figs. 5e and 5f). The porosity values determined by measuring the electrode thickness with a tactile dial gauge agree within 2 percentage points with the porosity determined by measuring the cathode thickness from the SEM images, confirming that the here specified overall porosity values are reliable. Nevertheless, a visual comparison of the cross-sections of the two different cathodes calendered to the same porosity (either 42% or 32%) indicates a larger apparent pore volume in the NCA cathodes compared to the LMR-NCM cathodes. This suggests that there must be an additional internal, optically “hidden” porosity within the here imaged LMR-NCM particles, i.e., within the secondary agglomerates of the LMR-NCM particles.

More detailed SEM images reveal that the large secondary agglomerates are composed of primary particles, as was already shown in the literature for NCA<sup>59,60</sup> and LMR-NCM<sup>20,61</sup> CAMs. For the here used materials, the primary particles of LMR-NCM are much smaller ( $\approx 0.05$ – $0.2 \mu\text{m}$ ) than the primary particles of NCA ( $\approx 0.2$ – $2 \mu\text{m}$ ). Furthermore, laser scattering analysis shows that the secondary agglomerates of the LMR-NCM material have a smaller  $d_{50}$  diameter of  $\approx 10 \mu\text{m}$  compared to  $\approx 15 \mu\text{m}$  sized secondary agglomerates of the NCA material, which is in qualitative agreement with the SEM cross-sections shown in Figs. 5a and 5d. Since the targeted overall porosity for the calendering process based on Eq. 1 does not distinguish between porosity *between* secondary agglomerates and *within* secondary agglomerates, the secondary particles of

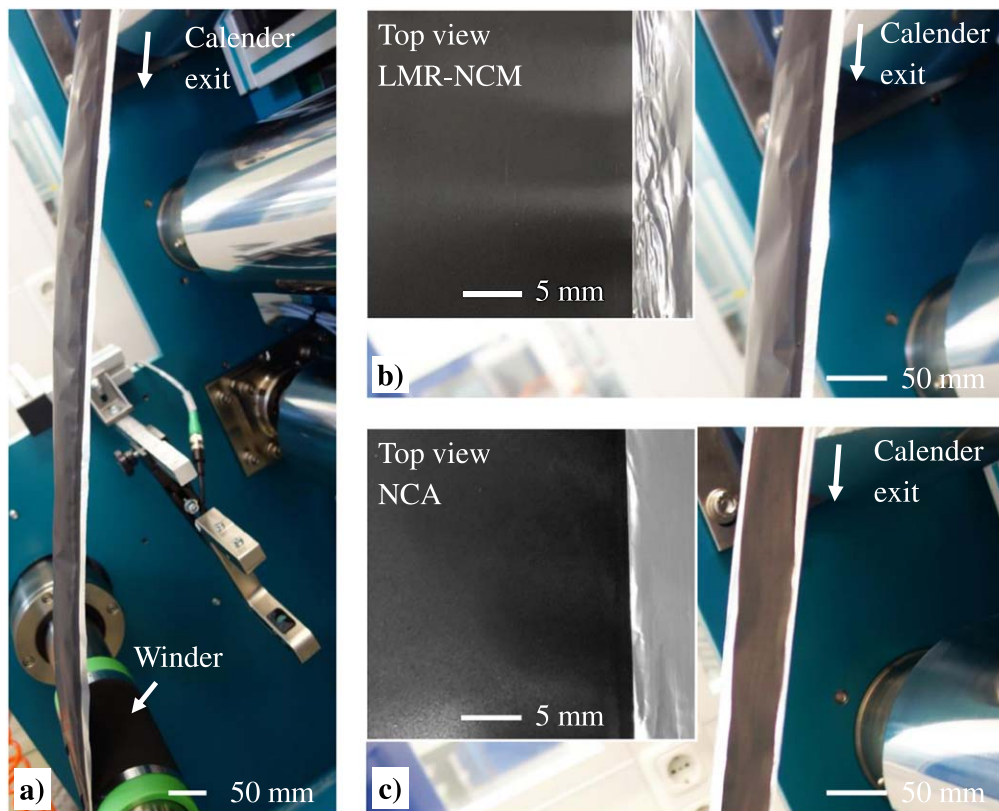


**Figure 4.** (a) Side view of an electrode coated on both sides with LMR-NCM cathodes after calendaring to a porosity of 42% ( $2.32 \text{ g cm}^{-3}$ ); (b) zoomed-in side view as well as top view of an electrode coated on both sides with LMR-NCM cathodes after calendaring to 42% porosity ( $2.45 \text{ g cm}^{-3}$ ). Both electrodes were calendared with the calender EA 102 from Coatema, with a roll diameter of 400 mm and a roller temperature of  $25 \text{ }^\circ\text{C}$ . The depicted side views show the electrodes after the first deflection-roll downstream from the calender gap and in front of the winder.

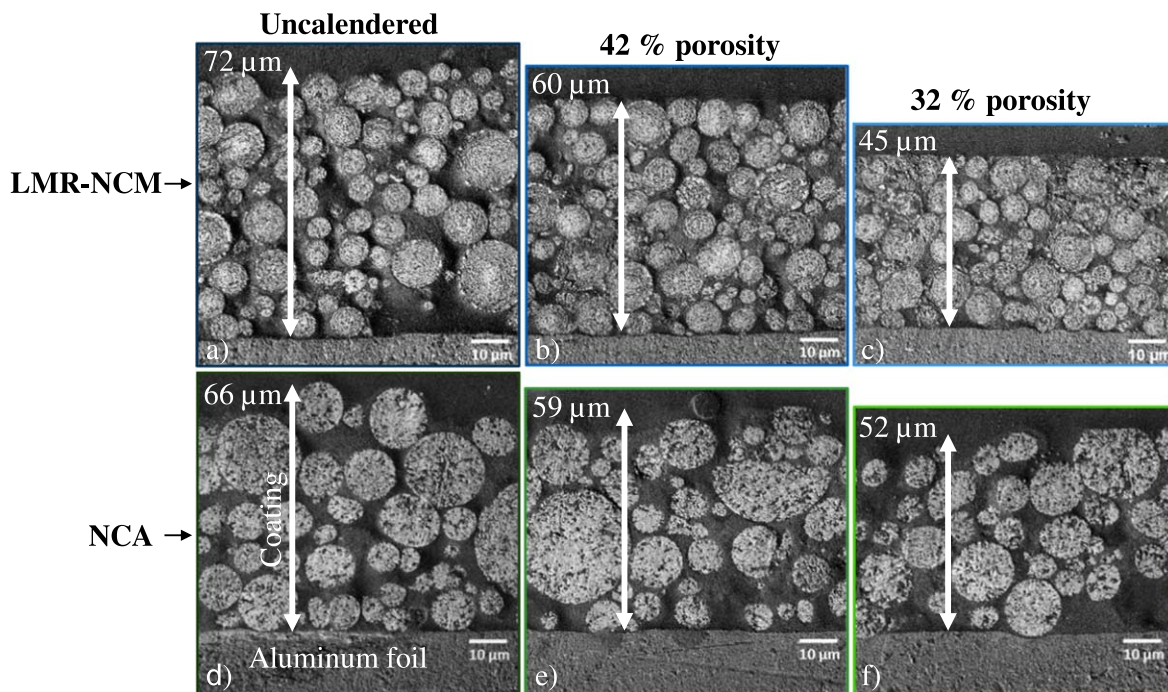


**Figure 5.** SEM cross-sectional images of as-coated and calendared electrodes (for preparation of the cross-sections see SEM cross-sectional imaging in the Experimental section). **First row:** LMR-NCM cathodes (a) uncalendered (with 56% porosity) or calendared to (b) 42% porosity or (c) 32% porosity. **Second row:** NCA cathodes (d) uncalendered (with 47% porosity) or calendared to (e) 42% porosity or (f) 32% porosity. The loading of the LMR-NCM cathodes is  $\approx 12 \pm 1 \text{ mg cm}^{-2}$  and that of the NCA cathodes  $13.5 \pm 0.5 \text{ mg cm}^{-2}$ . The porosities are determined from the electrode thicknesses measured by a tactile dial gauge using Eq. 1.

CAMs without internal porosity (as is usually the case for NCAs<sup>58,59</sup>) would appear less densely packed than the secondary particles of CAMs with significant porosity within the secondary particles, as is hypothesized to be the case for the here examined LMR-NCM material. This argument assumes that there is no significant particle cracking, which indeed has not been observed even when calendering the electrodes to 32% porosity (see Figs. 5c and 5f).

**Mercury porosimetry.**—To quantitatively investigate the qualitatively observed phenomenon of different pore volume fractions in the SEM images (Fig. 5), three mercury intrusion measurements were carried out for the different uncalendered and calendered porosities (Fig. 6) to determine the respective pore size distributions within the cathode coatings. To compare the porosity measured by mercury porosimetry with the overall porosity determined by coating thickness measurements (via Eq. 1), the electrode sample mass normalized pore volume ( $V_{pore}/m_{sample}$ , where  $m_{sample}$  is the mass of the two electrode coatings and the current collector foil) obtained by mercury porosimetry has to be corrected by the mass fraction of the aluminum current collector in the electrode (13.8 wt%<sub>alu</sub> for the LMR-NCM and 12.6 wt%<sub>alu</sub> for the NCA coatings) according to Eq. 4, yielding the pore volume per mass of coating ( $V_{pore}/m_{coating}$ ).

$$\frac{V_{pore}}{m_{coating}} = \frac{V_{pore}}{m_{sample}} * \frac{1}{wt\%_{alu}} \quad [4]$$

Equation 5 can then be used to calculate the cathode porosity, using the average bulk density of the coating ( $V_{coating}/m_{coating}$ ):

$$\epsilon_{coating(Hg)} = \frac{V_{pore}/m_{coating}}{V_{coating}/m_{coating}} = \frac{V_{pore}/m_{coating}}{\frac{1}{\rho_{bulk,sample}} - \frac{wt\%_{alu}}{\rho_{alu}}} \quad [5]$$

where  $\rho_{bulk,sample}$  is the measured mass of the electrode sheet samples in the measurement bulb divided by the sample volume, determined from the bulb volume minus the measured mercury volume at a low pressure of 0.029 MPa (where pores < 50  $\mu\text{m}$  pore diameter are not filled with mercury).

In the literature, the coating porosities deduced from mercury porosimetry data are either calculated via the measured packing density of the coating (Eq. 5), as described by FROBOESE et al.,<sup>62</sup> or by adding the measured pore volumes to the calculated solid volumes using materials bulk densities, as done by SIMON et al.<sup>63</sup> The analysis in this paper is based on Eq. 5, as it has a wider application range (otherwise the exact electrode composition and the precise materials bulk densities must be known). However, the porosities calculated according to SIMON et al.,<sup>63</sup> are within 2 percentage points of the values calculated with Eq. 5. The small variation is a result of the different treatment of Hg-inaccessible pores by the two methods. While this porosity is simply neglected by the method of SIMON et al.,<sup>63</sup> Eq. 5 normalizes the measured porosity by a bulk density where the inaccessible pores are also neglected. For both calculation methods, a uniform mass loading needs to be assumed and therefore accuracy in porosity calculation is expected to be not higher than  $\pm 2$  percentage points anyways (estimated by the variation of porosities calculated by Eq. 1 when measuring the coating thickness with the tactile dial gauge).

Figure 6 shows the logarithmic differential pore volume intrusion ( $dV_{pore}/d\log R$ ) vs the pore diameter that is plotted on a logarithmic scale, so that the areas under the curves in Fig. 6 are proportional to the intruded volume. Based on the analysis outlined below, it is proposed that the pore size distributions in Fig. 6 can be partitioned into three characteristic pore size regions for further evaluation: i) a region with small pores (<240 nm pore diameter), shown by the yellow shaded areas; ii) a region with intermediate pore sizes (light gray areas) with pores between 240 nm up to 8  $\mu\text{m}$  for LMR-NCM coatings and up to 16  $\mu\text{m}$  for NCA coatings; and, iii) a region extending from the intermediate pore size region all the way up to

50  $\mu\text{m}$  (dark gray areas), which includes effects from the coating surface roughness and is thus referred to as “extra porosity” from thereon.

A porous sample composed of (secondary) aggregates of particles frequently shows a pore size distribution with multiple characteristic peaks,<sup>64</sup> whereby such multimodal pore size distributions vary depending on the material.<sup>65</sup> It should be noted that the characteristic pore radius that is obtained by mercury porosimetry represents the opening width distribution of the pores. Therefore, mercury porosimetry always measures the largest entry diameter into a given pore and not the actual pore size.<sup>65</sup> In general, mercury porosimetry can be used to investigate the pore opening width of porous materials between  $\approx 500 \mu\text{m}$  and 3 nm as well as the pore volume distribution.<sup>63</sup>

In the case of the here conducted measurements on electrodes, for which  $\approx 1$ –1.5 g electrode pieces (cut to  $\approx 2$ –2.5 cm<sup>2</sup>) had to be placed into the measurement bulb in order to obtain a sufficient accuracy, there is the additional complication of creating “pore volume” between the various electrode pieces, which needs to be distinguished from the pore volume of the electrode coatings. In a first step to avoid a significant contribution of pore volume arising from filling the gap between the electrode sheets in the measurement bulb, pores above 50  $\mu\text{m}$  will be neglected, as they are in the range of the thickness of the electrode coating and thus cannot represent pores within the electrode coating. To further reduce this upper cut-off diameter is unfortunately not possible, since both of the investigated uncalendered cathodes have a defined pore volume distribution in this area. We believe that these rather large pore sizes are mainly an effect of the surface roughness of the electrodes, as it vanishes for the LMR-NCM coatings calendered to  $\approx 42\%$  and  $\approx 32\%$  as well as for the NCA coatings calendered to  $\approx 32\%$ . It should be noted that these surface roughness effects will also affect the porosities calculated by Eq. 1, where the measured thickness of the coating is used. Unfortunately, there is no common understanding in the literature on how to deal with the challenge of potentially overlapping pore regions. SIMON et al.<sup>62</sup> did not consider pore sizes beyond 10  $\mu\text{m}$  when analyzing their mercury porosimetry data, but also had no defined peaks at larger pore diameters. FROBOESE et al.<sup>61</sup> claim that pore diameters exceeding the  $d_{90}$  diameter ( $d_{90, \text{LMR-NCM}} = 15 \mu\text{m}$ ,  $d_{90, \text{NCA}} = 23 \mu\text{m}$ ) of the electrode materials are associated with the volume between the electrode pieces in the measurement bulb. This would exclude the above described pore volumes between 23–50  $\mu\text{m}$  pores. However, since for practical electrode applications, electrodes are calendered quite strongly, the different data treatment approaches in the large pore size region would not yield very different results, as there is no porosity above 20  $\mu\text{m}$  for strongly calendered electrodes, i.e., for electrodes with substantially lower final porosities compared to their as-coated porosity (in this case, this applies to the LMR-NCM electrodes with  $\approx 42\%$  and  $\approx 32\%$  porosity and to the NCA electrodes with  $\approx 32\%$  porosity).

The remaining contribution of the gap volume between the measured electrode sheets to the electrode coating pore volume below 50  $\mu\text{m}$  is estimated by measuring uncoated aluminum current collector sheets with the same setup (Fig. A-2 in the Appendix). The contribution of the gap between the aluminum sheets that is proportional to the sample mass for a given electrode loading depends on the overall coating properties and contributes  $\approx 2$ –6 percentage points to the overall porosity ( $\approx 6\%$  for calendered samples with the lowest porosities and  $\approx 2\%$  for uncalendered electrodes with high porosity), a value which is subtracted from the pore volume in the pore size range between 8–50  $\mu\text{m}$  (for more details see the explanation for Fig. A-2 in the Appendix). The total pore volumes (porosities) and their fraction for each pore size area (Table III) are corrected by these inter aluminum sheet pore contributions.

Next we will discuss the pore sizes and the pore volumes that we ascribe to the pores between the secondary agglomerates of the cathode active materials in the electrode, marked by the light gray

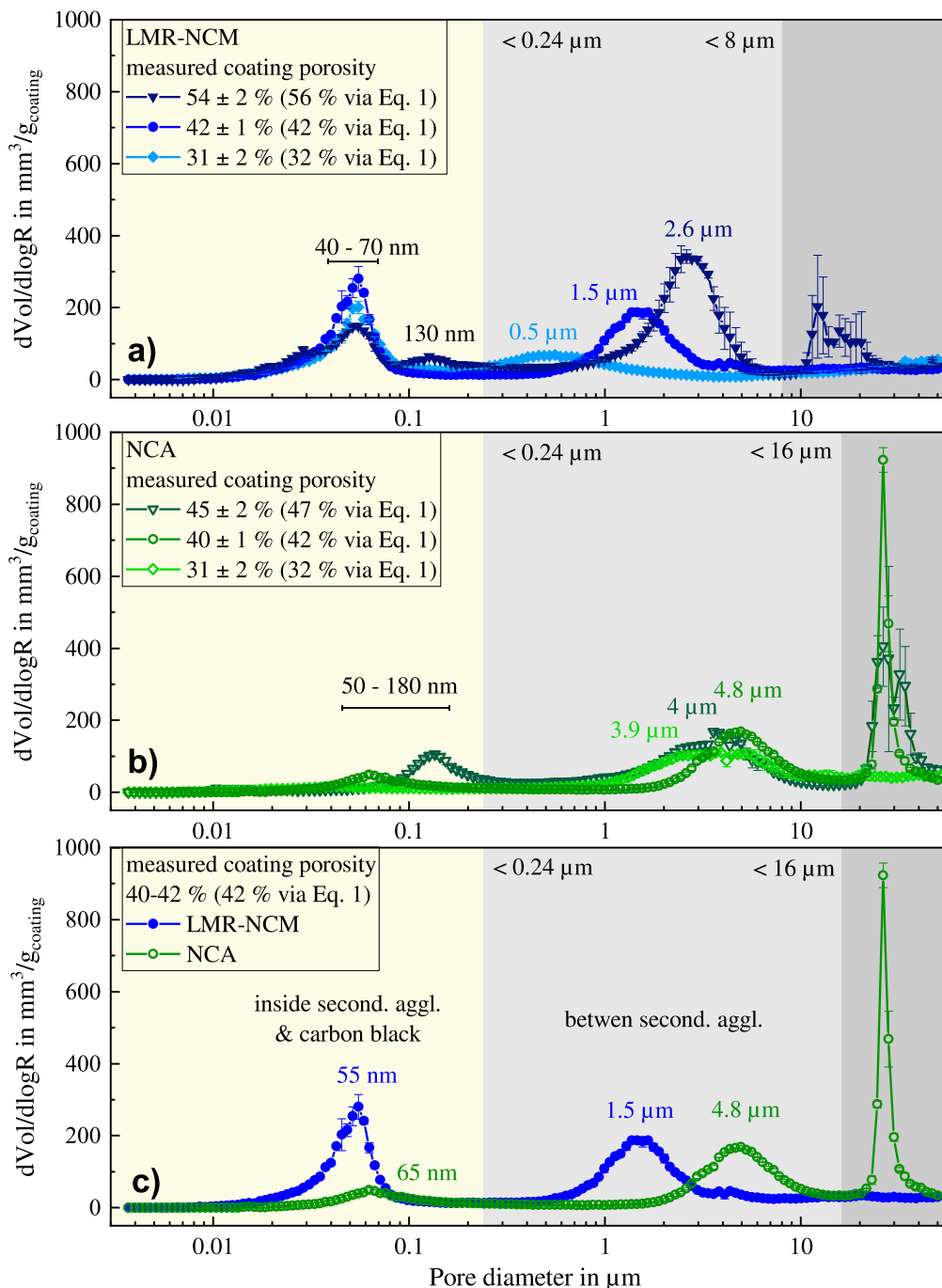


**Figure 6.** Mercury porosimetry based pore size distributions of uncalendered and calendered LMR-NCM and NCA electrode sheets, based on three independent repeat measurements for each electrode type (the standard deviations are marked by error bars): (a) for LMR-NCM coatings; (b) for NCA coatings; (c) comparing the pore size distribution for LMR-NCM and NCA cathodes with an overall porosity of 40%–42%.

areas in Fig. 6. For the LMR-NCM coatings (Fig. 6a), this region ranges between  $\approx 0.24 \mu\text{m}$  and  $8 \mu\text{m}$ , while it extends up to  $\approx 16 \mu\text{m}$  for the NCA coatings (Fig. 6b). The assumption that the pores in the light gray region represent the pore volume between the secondary CAM agglomerates is supported by a simple estimation of the pore diameter of a close packing of spherical particles with tetrahedral voids ( $d_{\text{void}} = 0.255 \cdot d_{\text{particle}}$ ) and octahedral voids ( $d_{\text{void}} = 0.414 \cdot d_{\text{particle}}$ ): this predicts pore diameters of  $\approx 2.5$ – $4 \mu\text{m}$  for the LMR-NCM particles based on their  $d_{50}$  value of  $\approx 10 \mu\text{m}$ , which is in reasonable agreement with the pore size maxima ranging between  $0.5$ – $2.6 \mu\text{m}$  shown in Fig. 6a; furthermore, larger pore diameters of  $\approx 4$ – $6.5 \mu\text{m}$  are predicted for NCA particles based on their  $d_{50}$  value of  $\approx 15 \mu\text{m}$ , which again is in reasonable agreement with the

$3.9$ – $4.8 \mu\text{m}$  pore size maxima shown in Fig. 6b. The pore volume as well as the average pore diameter is shifted to smaller values by compression and hence represents the reduction of the space between the secondary agglomerates.

Last we will consider the volume in pores below  $\approx 240 \text{ nm}$  (yellow region in Fig. 6), which so far were mostly considered as a contribution of the conductive carbon black matrix.<sup>66</sup> To differentiate the pore contributions of the electrode components, an NCA electrode without carbon black and a pure carbon black coating were measured, both uncalendered and calendered (Fig. A-3). Based on these measurements, it can be stated that the small peak at  $\approx 130 \text{ nm}$  of the uncalendered LMR-NCM electrodes (dark blue triangles in Fig. 6a) arises from carbon black contributions. Therefore, the peak

**Table III.** Mercury porosimetry derived pore volumes ( $V_{\text{pore}}$ , in  $\text{mm}^3/\text{g}_{\text{coating}}$ ) and porosities ( $\epsilon_{\text{coating (Hg)}}$  via Eq. 5) of LMR-NCM (abbreviated as LMR) and NCA electrodes divided into three regions, marking: i) the inner porosity of the secondary CAM agglomerates and contributions by the carbon black (yellow area in Fig. 6); ii) the porosity between the secondary CAM agglomerates (light gray area in Fig. 6); and, iii) the ‘extra pores due to surface roughness of the coating (dark gray area in Fig. 6). The summed-up porosities/volumes measured by mercury porosimetry in the last column can be compared with the porosities calculated from thickness measurements via Eq. 1 (1<sup>st</sup> column). The pore volume contribution obtained with uncoated aluminum (see Fig. A-2 in the Appendix) was subtracted.

Overall $\epsilon_{\text{coating}}$ via Eq. 1	Hg $V_{\text{pore}}$ & $\epsilon_{\text{coating (Hg)}}$ via Eq. 5	Pores within second. aggl. & carbon black		Pores between second. aggl.		“Extra” pores between second. aggl.		$V_{\text{pore, overall}}$ & $\epsilon_{\text{coating (Hg)}}$ via Hg porosimetry	
		3–240 nm		0.24–8/16 $\mu\text{m}$		8/16–50 $\mu\text{m}$		3 nm–50 $\mu\text{m}$	
		LMR	NCA	LMR	NCA	LMR	NCA	LMR	NCA
LMR/NCA 56/47%	vol. in $\text{mm}^3/\text{g}_{\text{coating}}$	81	35	156	100	47	62	<b>284 ± 12</b>	<b>198 ± 9</b>
	$\epsilon_{\text{coating (Hg)}}$	16%	8%	30%	23%	8%	14%	<b>54%</b>	<b>45%</b>
42%	vol. in $\text{mm}^3/\text{g}_{\text{coating}}$	82	23	100	86	16	55	<b>199 ± 3</b>	<b>164 ± 3</b>
	$\epsilon_{\text{coating (Hg)}}$	17%	6%	21%	22%	4%	13%	<b>42%</b>	<b>40%</b>
32%	vol. in $\text{mm}^3/\text{g}_{\text{coating}}$	76	15	50	88	18	17	<b>143 ± 7</b>	<b>121 ± 6</b>
	$\epsilon_{\text{coating (Hg)}}$	16%	4%	10%	24%	5%	4%	<b>31%</b>	<b>31%</b>

at  $\approx 55$  nm is considered as porosity within the secondary LMR-NCM agglomerates, consistent with the observation that upon calendaring this peak does not shift to smaller pore diameters and, more importantly, that the pore volume associated with this peak does not change significantly upon calendaring (decreasing only from 81 to 76  $\text{mm}^3/\text{g}_{\text{coating}}$ , as shown later on in Table III). On the other hand, for the NCA electrodes (Fig. 6b) there is no peak in this area that is independent of calendaring. Instead, the uncalendered NCA electrode shows a peak at also  $\approx 130$  nm that upon calendaring shifts towards smaller pore sizes with smaller associated pore volumes (decreasing from 35 to 15  $\text{mm}^3/\text{g}_{\text{coating}}$ , as shown later on in Table III). As this follows the behavior of the pure carbon black coating (see Fig. A-3) and as the NCA coating without carbon black (see Fig. A-3) also shows no defined porosity in this pore size region, the porosity of the carbon black containing NCA electrode in the yellow region of Fig. 6b (i.e. below  $\approx 240$  nm) can clearly and solely be assigned to the contribution from the carbon black.

A direct comparison of LMR-NCM and NCA electrodes calendared to a mercury porosimetry based porosity of 40–42% (Fig. 6c) illustrates the difference in the pore size distribution of the two materials. In the light gray region that marks the pores between the secondary CAM agglomerates, both CAMs appear to have very similar pore volumes (note that the area under the curves in this plot is proportional to the pore volume). On the other hand, in the yellow region that marks the pore volume due to the carbon black contribution for both electrodes in addition to the pore volume within the secondary CAM agglomerates, the pore volume of the LMR-NCM electrode is substantially larger than that of the NCA electrode, which as discussed above is due to its significant porosity within the secondary agglomerates (note that the same mass ratio of carbon black was used in both electrodes).

For a more quantitative comparison of the pore volumes in the different pore size regions of uncalendered and calendared LMR-NCM and NCA electrodes, Table III provides the Mercury porosimetry based pore volume ( $V_{\text{pore}}$ , in  $\text{mm}^3/\text{g}_{\text{coating}}$ ) and porosity ( $\varepsilon_{\text{coating (Hg)}}$ , via Eq. 5) contribution to each pore size region; these are summed up in the last column to the total mercury porosimetry based  $V_{\text{pore}}$  and  $\varepsilon_{\text{coating (Hg)}}$ . The overall coating porosity determined by Eq. 1 ( $\varepsilon_{\text{coating}}$ ) that is given in the first column agrees within 1–2 percentage points with that determined by mercury porosimetry. On average, the porosity determined from mercury porosimetry (last column) is always slightly lower than that determined from tactile gauge measurements and bulk material densities (first column), which may be due to the fact that pores below 3 nm are not accessed in mercury porosimetry measurements and that occluded void volumes in the CAM materials result in a lower bulk material density compared to the crystalline density, which would lead to an overestimate of the porosity when determined by Eq. 1. Despite these minor differences, the overall porosities obtained by these two methods are in quite good quantitative agreement (i.e., within a relative difference of  $< 5\%$ ).

Next we will examine the Mercury porosimetry based pore volumes ( $V_{\text{pore}}$ ) and porosity contributions ( $\varepsilon_{\text{coating (Hg)}}$ ) for uncalendered and calendared electrodes in the lowest pore size region (highlighted in yellow in Fig. 6), which we associate with the volume of the pores inside the secondary agglomerates and/or within the carbon black agglomerates. In case of the NCA electrodes, the relative contribution of  $V_{\text{pore}}$  in this region to the overall pore volume (i.e.,  $V_{\text{pore}}/V_{\text{pore, overall}}$ ) decreases from  $\approx 18\%$  for uncalendered electrodes to  $\approx 14\%$  and  $\approx 12\%$  for electrodes calendared to  $\approx 42\%$  and  $\approx 32\%$  porosity, respectively. As shown by the experiments with NCA electrodes without carbon black and with pure carbon black electrodes (see Fig. A-2 in the Appendix), the pore volume of NCA electrodes in this low pore size region can clearly be attributed to the pore volume contributions by the carbon black additive. Thus, for calendared NCA electrodes, the pore volume in the low pore size region and its contribution to the overall pore volume is rather small (namely  $< 12\%$  with respect to the overall porosity as decreasing electrode porosity above 32% can be

attributed to the CB porosity). On the other hand, for the LMR-NCM electrodes,  $V_{\text{pore}}$  in this region decreases very little upon calendaring (from 81 to 76  $\text{mm}^3/\text{g}_{\text{coating}}$ ), so that  $V_{\text{pore}}/V_{\text{pore, overall}}$  in the low pore size region *increases* from  $\approx 29\%$  for uncalendered electrodes to  $\approx 41\%$  and  $\approx 53\%$  for electrodes calendared to  $\approx 42\%$  and  $\approx 32\%$  porosity, respectively. This large fraction of pores within the secondary LMR-NCM agglomerates explains why the calendaring of LMR-NCM electrodes to  $\approx 32\%$  porosity leads to aluminum foil embossing (see Fig. 4b), as  $\approx 53\%$  of the pore volume at the overall porosity of  $\approx 32\%$  is contained within pores of the secondary LMR-NCM agglomerates that do not break under these calendaring conditions (see Fig. 5c).

The intermediate pore size region ( $\approx 0.24$ – $8/16$   $\mu\text{m}$ , pores between secondary agglomerates in Table III and marked by the light gray area in Fig. 6) is associated with the pores between the secondary CAM agglomerates. For the NCA electrodes,  $V_{\text{pore}}/V_{\text{pore, overall}}$  in this region is  $\approx 51\%$ – $52\%$  for uncalendered ( $\approx 47\%$  porosity) and for lightly calendared electrodes ( $\approx 42\%$  porosity), and then increases to  $\approx 73\%$  upon strong calendaring to  $\approx 32\%$  porosity. This delayed response of  $V_{\text{pore}}/V_{\text{pore, overall}}$  upon calendaring is attributed to the fact that the first calendaring step only reduces the NCA porosity by very little, contrary to the second calendaring step, where the porosity is decreased substantially. On the other hand, for LMR-NCM electrodes,  $V_{\text{pore}}/V_{\text{pore, overall}}$  in the intermediate pore size region decreases from  $\approx 55\%$  for the uncalendered electrodes to  $\approx 50\%$  and  $\approx 35\%$  for the electrodes calendared to  $\approx 42\%$  and  $\approx 32\%$  overall porosity, respectively. This is accompanied by a strong shift of the average pore size from  $\approx 2.6$   $\mu\text{m}$  to  $\approx 0.5$   $\mu\text{m}$  (see Fig. 6a).

Summarizing the above findings for the strongly calendared electrodes ( $\approx 32\%$  porosity), the majority of the pore volume for the NCA electrodes is in the intermediate pore size region ( $\approx 73\%$ ), while it is in the low pore size region for the LMR-NCM electrodes ( $\approx 35\%$ ). At the same time,  $V_{\text{pore}}/V_{\text{pore, overall}}$  in the large size pores (“extra” pores between secondary agglomerates in Table III and dark gray area in Fig. 6) for both LMR-NCM and NCA electrodes calendared to  $\approx 32\%$  porosity has decreased to only  $\approx 13\%$ – $14\%$ .

**Formation and degassing of multilayer pouch cells.**—The challenges of the extensive gas release during the first-cycle activation of LMR-NCM cathodes have already been extensively discussed from a mechanistic point of view in the literature.<sup>10,23,67–69</sup> In this work, we instead address this aspect from an engineering point of view, as the amount of gas released from LMR-NCM cathodes in large-format cells can be quite substantial and can pose a serious problem during their formation. This is perhaps less critical for hardcase cells that undergo formation in an open state (under protective atmosphere) and are only sealed after the complete formation procedure, in addition to having over-pressure safety devices.<sup>70</sup> For pouch cells, however, the formation process is executed in a temporarily sealed state without external pressure on the pouch cell and with a gas pocket provided as space for the gas generated during formation; after formation, the gas generated during formation is eliminated by removing the gas pocket and then tightly re-sealing the pouch cells under vacuum ( $\approx 80$  mbar).<sup>49</sup> As NCM or NCA based cells operate at maximum delithiation degrees of  $< 80\%$ , the cathode active materials show little gassing,<sup>71</sup> so that most of the gas released in the formation cycle is due to SEI formation on the anode.<sup>72</sup> However, LMR-NCM requires a first-cycle activation to 4.7 V and a subsequent upper cut-off voltage of 4.6 V, which particularly in the first cycle leads to oxygen release from the CAM lattice and concomitant electrolyte oxidation that is accompanied by substantial gas evolution.<sup>17,66</sup> This oxygen release was also shown to require EC free electrolytes for cells with LMR-NCM cathodes in order to avoid rapid electrolyte degradation,<sup>23</sup> so that FEC based electrolytes are commonly used, despite the poorer thermal stability of FEC at operating temperatures above 45 °C.<sup>73–75</sup>

To better understand the amount of gas released during the initial cycles of LMR-NCM/graphite cells, OEMS measurements were

conducted to quantify the amount of released gas ( $\text{CO}_2$ ,  $\text{CO}$ ,  $\text{H}_2$ , and  $\text{O}_2$ ) during the first-cycle formation (Fig. 7a) and the following three cycles (Fig. 7b) of LMR-NCM/graphite cells. The amount of released gas (in units of  $\mu\text{mol}/\text{g}_{\text{CAM}}$ ) is given in Fig. 7c for the first activation cycle (left-most bars) conducted either at 25 °C (orange) or 45 °C (red), for the subsequent 3 cycles (cycles 2–4; middle bars) conducted at 25 °C following activation at 25 °C (orange) or 45 °C (red), and summed up for all 4 cycles (right-most bars). The lower dotted area in the left-most bars marks the total gas formation during the very initial charging of the cells to 4 V, which closely represent the gases released by anode SEI formation, as LMR-NCM cathode active materials do not show any gassing below  $\approx 4.2 \text{ V vs Li}^+/\text{Li}$ , i.e., below  $\approx 4.1 \text{ V vs graphite}$ .<sup>10,17</sup> Thus, the gas evolution due to SEI formation is  $\approx 90 \mu\text{mol}/\text{g}_{\text{CAM}}$  at 25 °C and slightly more at 45 °C ( $\approx 105 \mu\text{mol}/\text{g}_{\text{CAM}}$ ); based on this, the expected evolved gas volume (referenced to 25 °C and 1 bar) in our multilayer pouch cells with 27.6 g LMR-NCM would amount to  $\approx 62 \text{ ml}$  and  $\approx 72 \text{ ml}$ , respectively (shown on the right-hand axis of Fig. 7c).

The gas evolved during the first-charge in the segment between 4 V during charge and 4 V during discharge is marked by the striped segments of the left-most bars in Fig. 7c. This is mostly due to gas evolved from the LMR-NCM cathodes (including cross-talk reactions with the anode), as the gas evolution due to anode SEI formation becomes very small once the graphite potential is below  $\approx 0.2 \text{ V Li}^+/\text{Li}$ <sup>76</sup> (as is the case once the cell potential is  $> 4 \text{ V}$  for the LMR-NCM cells). This amounts to  $\approx 110 \mu\text{mol}/\text{g}_{\text{CAM}}$  for the

activation at 25 °C, corresponding to a projected volume of  $\approx 75 \text{ ml}$  for our large-format pouch cells; the former is reasonably close to the  $\approx 150 \mu\text{mol}/\text{g}_{\text{CAM}}$  that TEUFL et al.<sup>10</sup> obtained within the same voltage limits for a similar LMR-NCM material and an FEC/DEC electrolyte without co-solvents and additives. When conducting the activation at 45 °C,  $\approx 150 \mu\text{mol}/\text{g}_{\text{CAM}}$  are evolved (striped segment in the left-most red bar), corresponding to a projected volume of  $\approx 103 \text{ ml}$  for our large-format pouch cells. Finally, in the last segment of the first activation cycle, namely between 4 V and 2 V during discharge, a rather small additional amount of gas is evolved from the LMR-NCM cathodes, as is indicated by the top segment of the left-most bars in Fig. 7c (this is consistent with the study by TEUFL et al.<sup>10</sup>).

Based on this analysis, the larger fraction of the gas evolved during the first-cycle activation of LMR-NCM/graphite cells is caused by the extensive gassing of LMR-NCM cathodes. Furthermore, the major amount of cathode derived gas is formed between 4 V during charge and 4 V during discharge and could be removed with a second degassing step at 4 V during the discharge process. The unmarked area in the formation cycle in Fig. 7c (after 4 V while discharging) is most likely delayed cathode gassing. The cell formation procedure adopted here for large-format LMR-NCM/graphite cells aimed to shift the gassing after the first formation cycle (i.e., from cycles 2–4 in Fig. 7c) into the formation cycle, so that the gas can be vented prior to the final sealing of the cells. This can be accomplished by conducting the first formation cycle at 45 °C rather than at 25 °C, leading to a  $\approx 52\%$  reduction of the gas that is

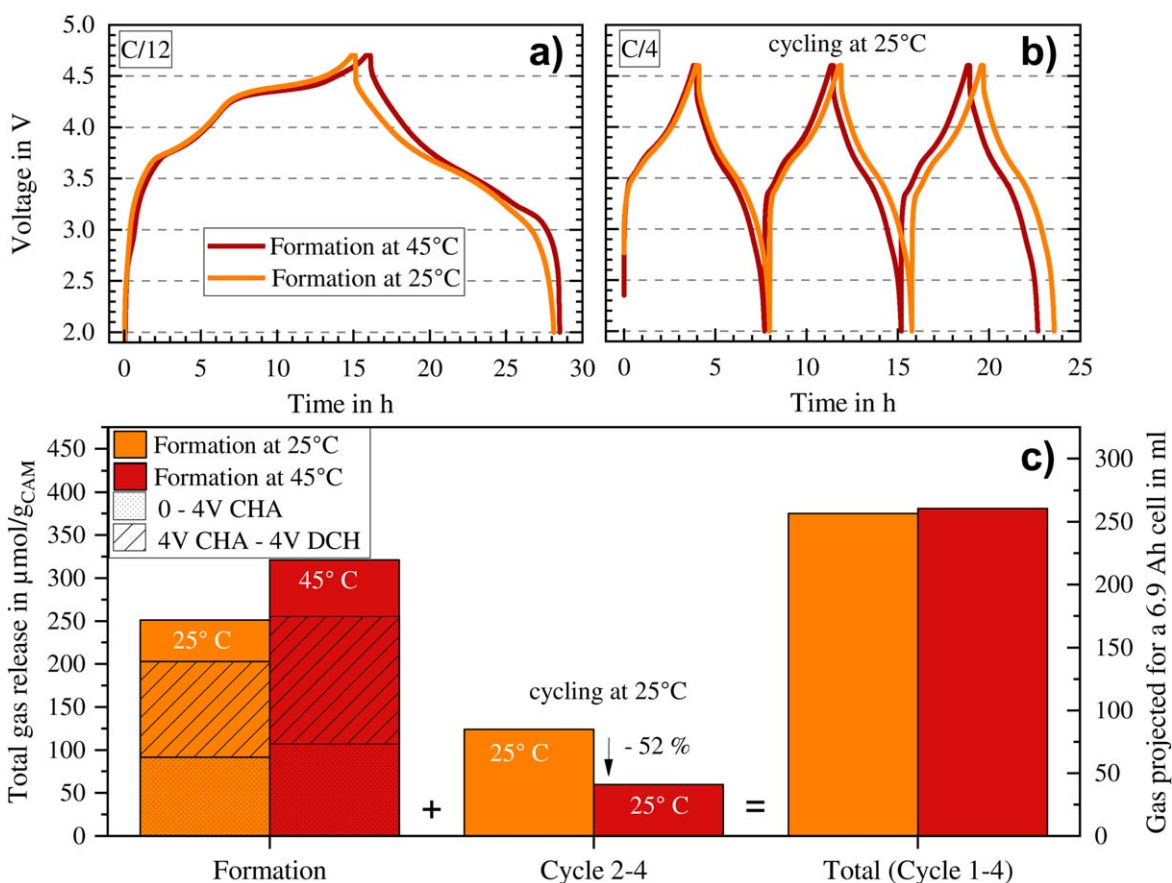


**Figure 7.** OEMS measurements with LMR-NCM working electrodes and graphite counter electrodes using the FEC/DEC based LMR-NCM electrolyte that was used for the coin and multilayer pouch cells. (a) Cell voltage profile vs time during a formation cycle at 25 °C (orange) or 45 °C (red) with a C-rate of C/12 and a CV step at 4.7 V till C/24. (b) Cell voltage profile vs time for three cycles at 25 °C with C/4 and a CV step at 4.6 V till C/8, following the first-cycle activation at 25 °C (orange) or 45 °C (red) (after a 4 h rest period at OCV). (c) Total amount of released gas (i.e., sum of  $\text{CO}_2$ ,  $\text{CO}$ ,  $\text{H}_2$ , and  $\text{O}_2$  in units of  $\mu\text{mol}/\text{g}_{\text{CAM}}$ ) over the first-cycle activation, over cycles 2–4, and summed up for all cycles 1–4. The lower dotted area in the bars for the first-cycle formation shows the gas release up to 4 V during the first charge, the striped areas represent the released gas in the first-cycle between 4 V during charge and 4 V during discharges, while the non-marked upper region of the bars indicates the gas released between 4 V and 2 V during the first-cycle discharge. The right axis corresponds to the gas volume (evaluated at 25 °C and 1 bar) that would be generated in the here produced multilayer pouch cells with 27.6 g LMR-NCM (corresponding to  $\approx 6.9 \text{ Ah}$  at 0.1C).

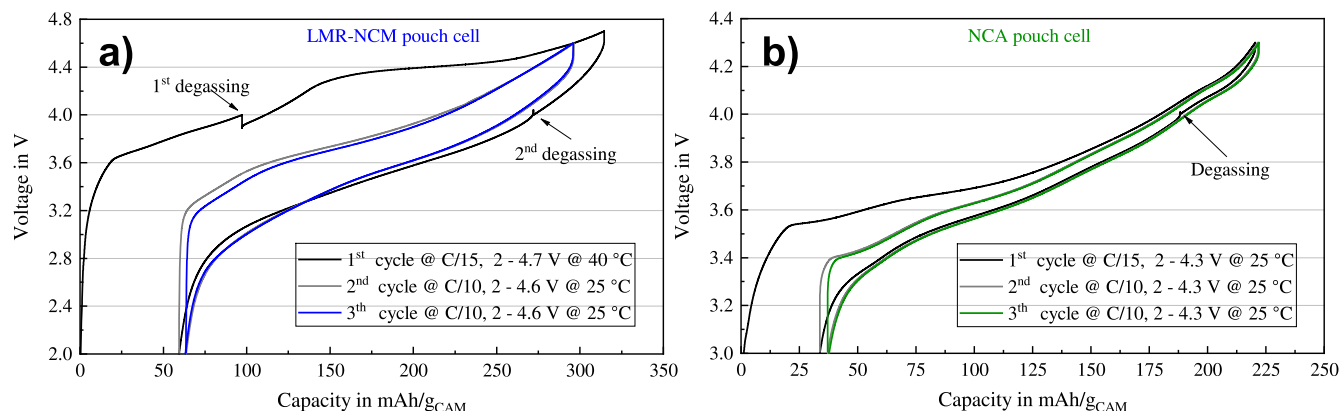


**Figure 8.** Formation cycle followed by two stabilization cycles of LMR-NCM (a) and NCA (b) pouch cells, indicating the degassing steps at 4.0 V in the formation cycle. The cells were cycled without external compression until the last degassing step and afterward compressed in a cell holder with 0.2 MPa.<sup>52</sup>

released in cycles 2–4 (see middle bars in Fig. 7c), namely from  $\approx 85$  ml to  $\approx 41$  ml projected for the here used large-format pouch cells. We found that our large-format LMR-NCM/graphite pouch cells ( $\approx 6.9$  Ah at 0.1C) would burst open after several cycles due to excessive internal gas pressure when activated at 25 °C, while this did not occur until  $\approx 250$  cycles when activated at elevated temperature.

The formation strategy for LMR-NCM/graphite pouch cells developed for this work, therefore, dealt with the additional gassing from the cathode side by conducting a slow formation at 40 °C with two degassing steps, as shown in Fig. 8a. These two steps were incorporated to avoid the accumulation of the anode and the cathode derived gas over the course of the first cycle in order to: i) avoid a further reaction of the evolved gasses with the electrolyte and the electrode interfaces, and ii) to reduce the total amount of gas that might block parts of the anode from contact to the electrolyte, thereby reducing the area of the anode accessible for a homogeneous lithiation. A formation temperature of 40 °C (instead of the 45 °C used for the OEMS study) was selected for the multilayer LMR-NCM pouch cells to assure that, even in the presence of the expected temperature gradients across the thickness of the cell, the temperature would not exceed at any location the critical 45 °C for an FEC based electrolyte. Fig. 8a shows exemplarily the finally chosen formation and stabilization cycles for one of the LMR-NCM multilayer pouch cells. For comparison, the regular formation procedure applied for the NCA pouch cells, with only one degassing step in the first discharge at 4 V, is shown in Fig. 8b.

Particularly in the production of large-format pouch cells, a compromise must be found between a fast removal of the gas and cost-effective processing: since the cells have to be opened and closed for each degassing step, additional degassing steps require more cell packaging material. In each degassing step, the cell is pierced and sealed in the subsequent step, whereby the affected zone moves closer to the cell stack with each repetition. Furthermore, it has to be considered that cell opening and sealing at high SOC poses a significant safety risk, as the energy released in the event of a short circuit scales directly with SOC. Therefore, from a production safety perspective, degassing at low SOCs is desirable to perform the fully automated process, which is of course in contrast to the economic point of view that aims to close the formation process as soon as possible.

**Specifications and initial performance of large-format multilayer pouch cells.**—The LMR-NCM/graphite and the NCA/graphite large-format multilayer pouch cell specifications were determined on the basis of the coin half-cell data at 0.1C (shown in Table II, based on the 3rd cycle in Fig. 3). After formation of the pouch cells, their initial performance at 0.1C (exemplarily shown for one set of cells in Fig. 8) was then compared with the performance characteristics

projected in Table II in combination with the Excel-based *cell configuration tool* given in the supporting information. A summary of the targeted pouch cell specifications and the projected pouch cell performance vs that of the actually produced cells is shown in Table IV.

The actually achieved/measured values for the large-format multilayer pouch cells are based on the mean value of 16 LMR-NCM/graphite pouch cells and of 16 NCA/graphite pouch cells. Generally, the projected values for the LMR-NCM cells were accurate and match very well with the actually measured values. A smaller deviation, however, can be observed for the cell mass that is  $\approx 2.3\%$  lower than targeted, which we believe is due to electrolyte evaporation during filling and during the two degassing steps. For the NCA/graphite pouch cells, the CAM based capacity matches quite well with the projections, but the cell specific capacity shows a discrepancy of 2.7%. This deviation can simply be explained by a loading overbalancing on the anode electrode, whose actual loading was slightly too high ( $10.2 \text{ mg cm}^{-2}$  instead of the desired  $8.8 \text{ mg cm}^{-2}$ ), leading to an areal capacity overbalancing of anode to cathode of 1.4/1 instead of the desired 1.2/1. The unused anode leads to a negligible change in cell performance (max. 1.8% capacity loss due to additional SEI losses), but to a higher than projected cell mass, and thus to a lower than projected cell energy density.

The cell data based on the 3<sup>rd</sup> formation cycle of the LMR-NCM/graphite multilayer pouch cells show promising results, since a higher energy density was achieved with a potentially lower cost CAM (owing to a high manganese content). However, while the specific capacity of the LMR-NCM pouch cells is  $\approx 30\%$  higher in comparison to the NCA pouch cells, the lower mean discharge voltage of the LMR-NCM cells results in only  $\approx 10\%$  higher energy density on the cell level. The first-cycle coulombic efficiency (CE) of the LMR-NCM cells was  $83.9 \pm 1.9\%$ , quite comparable with the CE of the NCA cells of  $84.9 \pm 0.3\%$ . The larger standard deviation of the CE of the LMR-NCM cells can be explained by the fact that the cells experienced a cell temperature change during the first cycle (40 °C until the second degassing step, followed by 25 °C until the end of the first cycle).

In summary, scale-up projections on the basis of coin half-cell data have been shown to predict the initial performance of large-format cells quite accurately. This is of course only valid, as long as aging effects and cell setup dependent temperature effects can be neglected. Further cell characteristics, such as rate capability, long-term cycling, as well as thermal behavior are discussed in Part II of this work.<sup>52</sup>

## Conclusions

To the best of our knowledge, this work examines for the first time the various challenges encountered during the production and formation of large-format multilayer pouch cells with a lithium- and

**Table IV. Targeted specifications and 0.1C performance projections for large-format multilayer LMR-NCM/graphite and NCA/graphite pouch cells, based on the coin half-cell data (given in Table II, based on the 3<sup>rd</sup> cycle in Fig. 3) and the cell configuration tool given in the supporting information. This is compared with the specifications of the actually produced pouch cells calendered to a porosity of  $\approx 42\%$  and their performance characteristics (averaged over 16 LMR-NCM and 16 NCA pouch cells, with the  $\pm$  values marking the standard deviation of the averages).**

Type	CAM mass <sup>a)</sup> in g <sub>CAM</sub>	Cell mass <sup>b)</sup> in g <sub>cell</sub>	CAM spec. DCH capa. <sup>c)</sup> in mAh/g <sub>CAM</sub>	Cell spec. DCH capa. <sup>c)</sup> in Ah	Mean disch. voltage <sup>c)</sup> in V	Cell energy density <sup>c)</sup> in Wh/kg <sub>cell</sub>
LMR-NCM targeted/projected <sup>d)</sup>	28	115	241	6.6	3.54	204
actual LMR-NCM pouch cell data	27.6 $\pm$ 0.5	112 $\pm$ 3	236 $\pm$ 4	6.5 $\pm$ 0.1	3.486 $\pm$ 0.009	202 $\pm$ 4
NCA targeted/projected <sup>d)</sup>	31	113	188	5.8	3.73	190
actual NCA pouch cell data	30.8 $\pm$ 0.8	116 $\pm$ 1	188 $\pm$ 4	5.8 $\pm$ 0.2	3.695 $\pm$ 0.009	185 $\pm$ 6

a) determined by weighing the cathodes before stacking. b) determined by weighing the cells after formation. c) mean discharge value of the 2<sup>nd</sup> cycle at 0.1C after the first formation cycle. d) Calculated with the cell configuration tool in the supporting information, using the cell performance data according to Table II (3<sup>rd</sup> cycle of the cells with  $\approx 42\%$  porosity) and the loading and material specifications according to the pouch cell setup described in the experimental part.

manganese-rich NCM (LMR-NCM) cathode active material (CAM) and graphite anodes, using a pilot scale production line. The performance and energy density of these LMR-NCM/graphite cells with a nominal capacity of  $\approx 6.9$  Ah at 0.1C (based on a nominal specific capacity of  $250 \text{ mAh/g}_{\text{CAM}}$ ) is compared to that of analogously produced large-format NCA/graphite cells with a similar nominal capacity of  $\approx 6.1$  Ah (based on a nominal specific capacity of  $200 \text{ mAh/g}_{\text{CAM}}$ ). The pouch cell specifications were established using an Excel-based cell configuration tool in combination with initial performance data from LMR-NCM/lithium and NCA/lithium coin cells.

Coin half-cell tests investigating the rate capability of LMR-NCM cathodes as a function of CAM loading and degree of calendaring (i.e., of cathode porosity) show, as expected, that the CAM specific performance is best for low loadings in combination with a high porosity. In contrast, with regards to the projected specific energy density for large-format cells (i.e., in  $\text{Wh/kg}_{\text{cell}}$ ), the optimum values for C-rates up to 1C are obtained with LMR-NCM loadings of  $\approx 12 \text{ mg cm}^{-2}$  (corresponding to  $\approx 3.0 \text{ mAh cm}^{-2}$  at 0.1C) and with cathode coating porosities of  $\approx 42\%$ .

Calendering experiments with large-scale electrodes reveal a remarkably different behavior between LMR-NCM and NCA cathode coatings. While the latter can be calendered without difficulties to  $\approx 32\%$  coating porosity (as is the case for NCMs), LMR-NCM coatings cannot be calendered to this porosity without substantial aluminum foil embossing that prevents their use in large-format cells. This phenomenon is examined by a detailed analysis of the structure of the cathode coatings calendered to different porosities by means of SEM cross-sectional analysis and of mercury intrusion porosimetry based pore size distribution measurements. For electrodes calendered to  $\approx 32\%$  coating porosity, the latter reveals that the fractional pore volume contained in pores of less than  $\approx 240 \text{ nm}$  (representative of pores either within the secondary CAM agglomerates or contributed by the carbon black additive) is rather small for NCA coatings ( $\approx 11\%$ ), while it amounts to  $\approx 50\%$  for LMR-NCM coatings due to a large pore volume within the secondary LMR-NCM agglomerates. Therefore, without the undesired breakage of secondary agglomerates, porosities of  $\approx 32\%$  cannot be achieved for LMR-NCM coatings without extensive aluminum foil embossing effects.

Another critical aspect is the different formation requirement for large-format high-capacity pouch cells with NCA (or NCM) vs those with LMR-NCM cathode active materials. This is due to the extensive gassing of LMR-NCMs in the first few cycles, which necessitates a modification of the formation procedure in order to shift most of the CAM related gassing into the first cycle, i.e., before the final sealing of the cells. By means of on-line electrochemical mass spectrometry (OEMS) it was found that a first-cycle formation at elevated temperature is able to shift more than 50% of the CAM related gassing in the three cycles after the formation cycle into the formation cycle. This, combined with two degassing steps in the formation cycle for the LMR-NCM cells (instead of one for NCA) is shown to strongly reduce internal cell pressure build-up after the final sealing of the cells and thus enable long-term cycling stability.

To conclude, 16 LMR-NCM and NCA large-format pouch cells with a measured capacity at C/10 of  $6.5 \pm 0.1$  Ah for LMR-NCM and  $5.8 \pm 0.2$  Ah for NCA were produced at the pilot scale production line at the Technical University of Munich. The average CAM specific capacity at C/10 after formation is  $236 \pm 4 \text{ mAh/g}_{\text{CAM}}$  for the LMR-NCM and  $188 \pm 4 \text{ mAh/g}_{\text{CAM}}$  for the NCA cells, close to their nominal specific capacities of  $250 \text{ mAh/g}_{\text{CAM}}$  and  $200 \text{ mAh/g}_{\text{CAM}}$ , respectively. This results in a  $\approx 30\%$  higher capacity of the LMR-NCM/graphite pouch cells. However, due to their lower average discharge voltage, the cell level energy density of  $203 \pm 4 \text{ Wh/kg}_{\text{cell}}$  for LMR-NCM/graphite large-format cells is only  $\approx 10\%$  larger than that for the NCA/graphite cells ( $185 \pm 6 \text{ Wh/kg}_{\text{cell}}$ ). While this difference is rather small, the lower CAM material costs

for the manganese-rich LMR-NCM compared to nickel-rich NCA is a significant advantage of LMR-NCM based CAMs.

The rate capability, long-term cycling stability, and thermal behavior of the LMR-NCM/graphite and NCA/graphite large-format cells produced here is presented in Part II of this study.<sup>51</sup>

## Acknowledgments

The authors gratefully acknowledge funding from the German Federal Ministry of Education and Research (BMBF) within the projects ExZellTUM II (grant number 03XP0081) and ExZellTUM III (grant number 03XP0255). Thanks also go to Kaleigh Hunt for the optimization of NCA electrodes based on coin cell measurements. Katia Rodewald (WACKER-Chair of Macromolecular Chemistry, TUM) is kindly acknowledged for recording the SEM images. The authors gratefully acknowledge Tobias Teufl and Manuel Mendez from BASF SE for their help and advice on handling the cathode active materials and electrolytes. We also would like to thank Benjamin Strehle for his support and fruitful discussions with regard to the Mercury porosimetry and the OEMS measurements. Anne Berger is acknowledged for her help during the time-consuming mercury porosimetry data analysis. Thanks to Franziska Friedrich for her help in the particle size determination by laser scattering. The authors want to thank the research battery production team of *iwb*, in particular Ajinkya Metkar, Nicolas Billot, Till Günther, Johannes Kriegler, Fabian Konwitschny, Celestine Singer, Hoda Mohseni, Sophie Grabmann, and Joscha Schnell for the manufacturing of the large-format pouch cells.

## Appendix

**Mixing.**—The mixing parameters solid content and mixing speed are plotted in Fig. A-1 vs the mixing time for the three materials used: LMR-NCM, NCA and graphite. One challenge in upscaling, for example, is the heat generated during the mixing process.

For highly viscous media, the heat generated during the mixing process has to be dissipated in order to avoid excessive heating of the slurry. Assuming a constant heat generation per volume, for larger batches the heat transfer via the vessel wall per volume is smaller due to the comparatively smaller surface of the slurry.<sup>77</sup> To avoid a temperature increase of the slurry with larger batch quantities, either the supplied mixing power must be reduced or the relatively smaller surface area must be compensated by a higher cooling rate. The latter approach is limited by the performance of the cooling system, while the first approach requires a reduced mixing intensity, leading to a longer mixing time. Both, elevated temperature and longer mixing times favor the occurrence of slurry gelation. This is particularly critical for nickel-rich cathode materials,<sup>78</sup> as they contain significant amounts of LiOH and  $\text{Li}_2\text{CO}_3$  surface impurities, at part formed in their synthesis<sup>79</sup> and at part from brief exposure to ambient air,<sup>80–82</sup> which promote slurry gelation.<sup>82</sup> As cooling of the here used Speedmixer is not possible during the process, the cooling was carried out externally in a cooled water tank.

**Mercury porosimetry.**—To estimate the error due to the spacing between the electrode sheets that yields an apparent porosity at high pore diameter, the pore size distribution of uncoated aluminum sheets (the same number as that was used in the measurements with actual electrodes) was measured and is scaled in terms of  $\text{mm}^3/\text{g}_{\text{coating}}$  by taking into the weight fraction of aluminum in the electrodes (black dots in Fig. A-2). In comparison with an uncalendered NCA coating (green triangles in Fig. A-2), the pore volume contribution from the aluminum sheets is only significant at high pore diameters, i.e. above  $\approx 10 \mu\text{m}$  (black dots). Although the here used aluminum foil has of course no real porosity, the porosimetry measurements show a porosity of  $28 \pm 1\%$  that corresponds to 9% porosity after adjusting the weight normalization

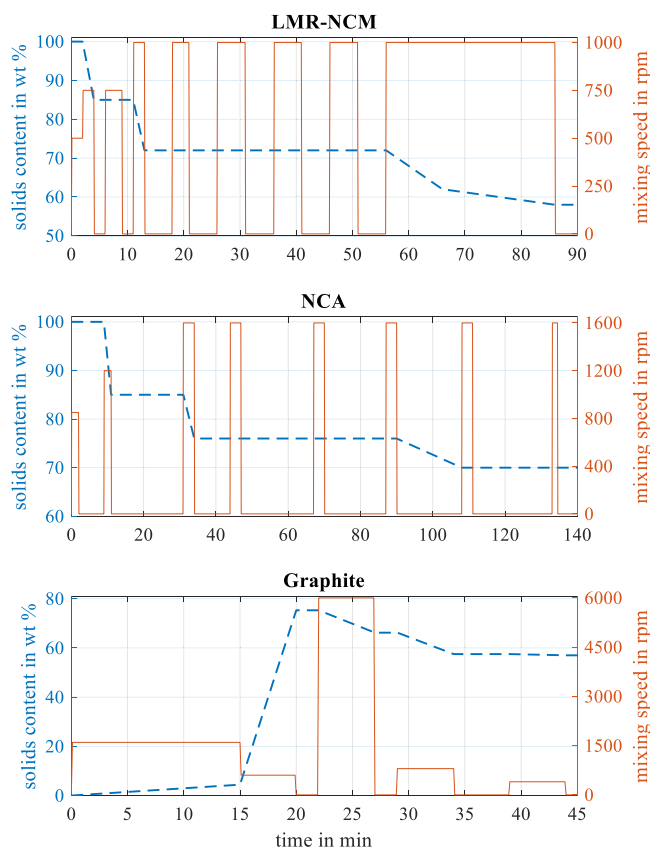


**Figure A-1.** Mixing process sequence for the LMR-NCM, NCA, and graphite slurries. The blue dotted line shows the solids content of the slurry over the mixing time. The orange line shows the mixing speed over the mixing time.

to the NCA coating (because 25 pieces without coating is for a pore range up to  $112 \mu\text{m}$ ). To avoid the significant contribution of the aluminum foil, the data in Fig. 6 are only analyzed up to a pore size of  $50 \mu\text{m}$ , as we cannot see any defined pore areas above and also

pore diameters in the range of the coating thickness are not considered to contribute to the actual porosity of the coating. The remaining contribution of aluminum up to  $50 \mu\text{m}$  to the coating porosity is  $50 \text{ mm}^3/\text{g}_{\text{alu}}$  and contributes  $\approx 2\text{--}6$  percentage points in porosity (6% for samples with low porosities, e.g. the NCA coating at 32% porosity, and 2% for uncalendered electrode coatings with high porosity). This contribution ( $50 \text{ mm}^3/\text{g}_{\text{alu}}$ ) is subtracted from the porosity in the "extra" pores between secondary agglomerates in Table III by multiplying it with the measured sample mass and the weight fraction of aluminum (13.8% in case of LMR-NCM and 12.6% in case of NCA).

To estimate the contribution of carbon black to the overall coating porosity, the pore size distribution of an NCA coating without carbon black and a pure carbon black coating are shown in Fig. A-3 both uncalendered and calendered. The pore size maximum of the non-calendered carbon black coating appears at a pore diameter of  $\approx 180 \text{ nm}$  and shifts to  $\approx 60 \text{ nm}$  and a lower overall pore volume upon calendering. There is no defined peak at  $>10 \mu\text{m}$ , which confirms our previous assumption that in the case of the NCA and LMR-NCM coatings the peak in this region is due to surface roughness of the coating that would be expected to be on the order of the secondary agglomerate size ( $\approx 10\text{--}15 \mu\text{m}$  for the CAMs and on the order of  $0.5\text{--}1 \mu\text{m}$  for the carbon black). On the other hand, an NCA coating without carbon black shows almost no porosity in the yellow area, therefore the porosity in Fig. 6b below  $240 \text{ nm}$  is mainly due to the carbon black in the electrode and not due to pores within the secondary agglomerates of the NCA material. This observation is in good agreement with nitrogen physisorption analysis, where the pores up to  $150 \text{ nm}$  could be quantified: for the pure NCA active material powder, a total pore volume in  $\leq 150 \text{ nm}$  pores of  $1.13 \pm 8 \text{ mm}^3/\text{g}_{\text{CAM}}$  was determined, whereas the same measurement on scratched-off NCA electrode material (scratched off with a scalpel with a regular, i.e. carbon black containing NCA coating) is  $\approx 20$ -fold larger ( $\approx 20\text{--}25 \text{ mm}^3/\text{g}_{\text{coating}}$ ). At the same time, the pore size maxima for the NCA electrode without carbon black (light gray area Fig. A-3) show the same behavior as the regular carbon black containing NCA electrode (see Fig. 6b) and can be attributed to pores in the coating between the secondary agglomerates of the cathode active material. The black arrows indicate the tendency of the pores between the secondary agglomerates to shift to smaller pore diameters and pore volumes

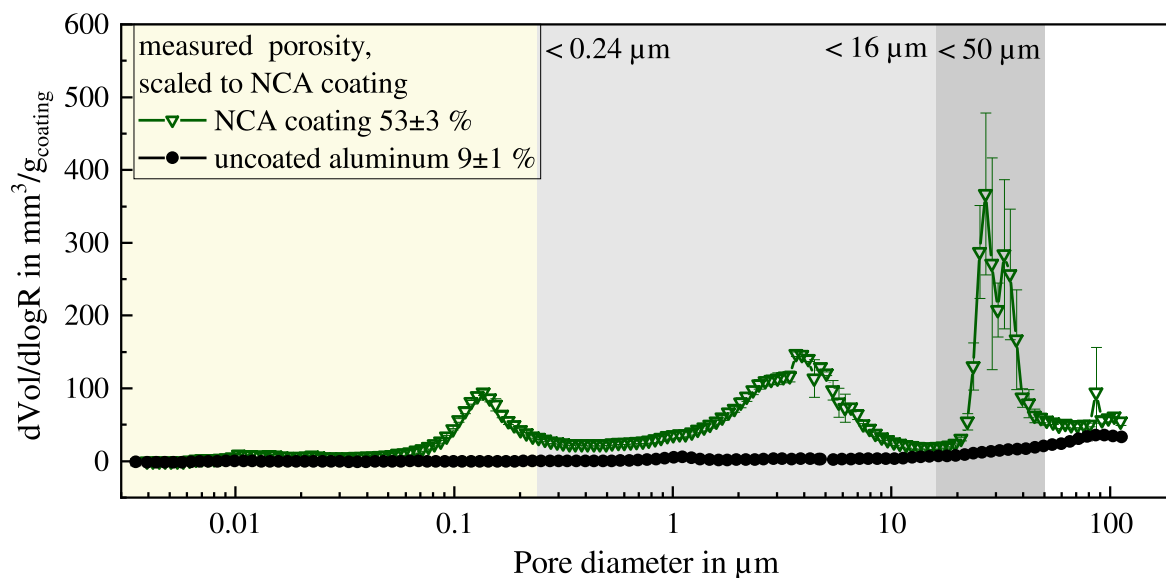


**Figure A-2.** Mercury porosimetry of uncoated aluminum sheets in comparison with the uncalendered NCA electrode sheet that is also shown in Fig. 6b. The deviation of the introduced volume for the indicated pore size is plotted. The uncoated aluminum weight is normalized by the weight fraction of the aluminum sheets (12.6 wt%) in the NCA electrodes. The yellow shaded area marks the porosity within the secondary agglomerates and carbon black pores, the light gray shows the porosity between the secondary NCA agglomerates, and the dark gray area refers to extra pores between the secondary agglomerates.

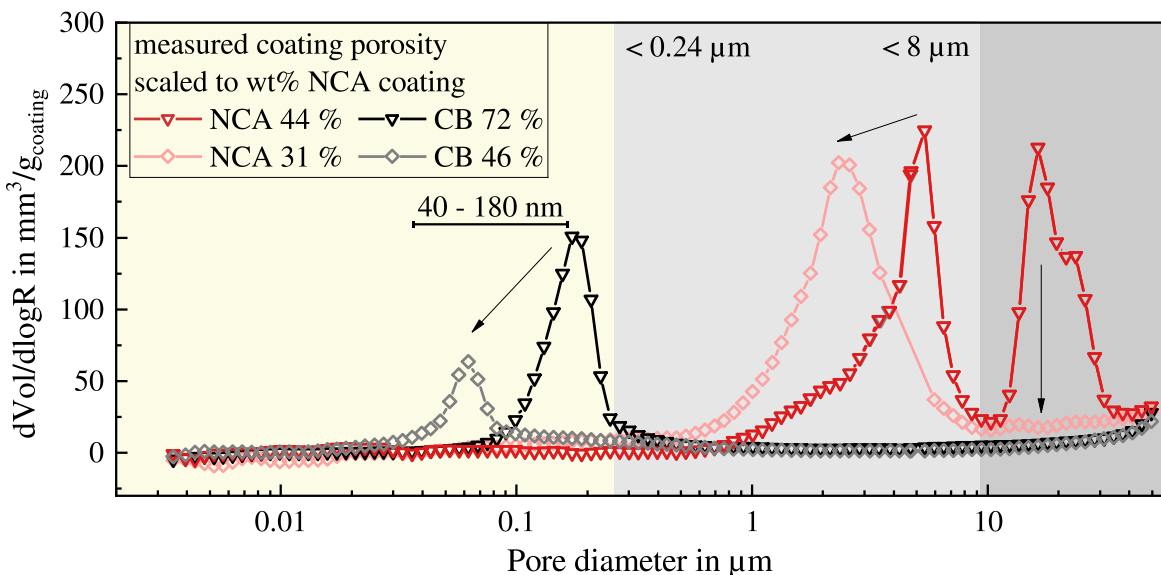


**Figure A-3.** Mercury porosimetry of NCA electrodes without carbon black (NCA/PVdF of 92.5/3.5 wt%) and pure carbon black electrodes (CB/PVdF 66.7/33.2 wt%) both uncalendered and after calendaring. The data were recorded between 3 nm and 100  $\mu\text{m}$  pores, but only porosities up to 50  $\mu\text{m}$  are considered to avoid artifacts of pores between the measured sheets. The yellow shaded area marks the porosity within the secondary agglomerates and carbon black pores, the light gray shows the porosity between the secondary NCA agglomerates, and the dark gray part refers to extra pores between the secondary agglomerates and/or in between the electrode sheet samples. The impact of calendaring for each coating type is marked by the black arrows. The porosity values given in the figure consider a pore diameter range from 3 nm–50  $\mu\text{m}$  and the apparent porosity due to the void space between the electrode sample sheets is corrected for as described in the context of Fig. A-2.

upon calendaring, which is also accompanied by a loss of porosity at  $>10 \mu\text{m}$ .

### ORCID

David Schreiner <https://orcid.org/0000-0001-8035-0438>  
 Tanja Zünd <https://orcid.org/0000-0002-1650-3636>  
 Florian J. Günter <https://orcid.org/0000-0002-5967-6801>  
 Ludwig Kraft <https://orcid.org/0000-0003-4324-426X>  
 Benedikt Stumper <https://orcid.org/0000-0002-4508-6210>  
 Fabian Linsenmann <https://orcid.org/0000-0001-8788-2584>  
 Michael Schüßler <https://orcid.org/0000-0002-4131-7392>  
 Rebecca Wilhelm <https://orcid.org/0000-0002-4161-5197>  
 Andreas Jossen <https://orcid.org/0000-0003-0964-1405>  
 Hubert A. Gasteiger <https://orcid.org/0000-0001-8199-8703>

### References

- D. Andre, S.-J. Kim, P. Lamp, S. F. Lux, F. Maglia, O. Paschos, and B. Stiaszny, *J. Mater. Chem. A*, **3**, 6709 (2015).
- R. Schmich, R. Wagner, G. Hörpel, T. Placke, and M. Winter, *Nat. Energy*, **3**, 267 (2018).
- K. G. Gallagher, S. Goebel, T. Greszler, M. Mathias, W. Oelerich, D. Eroglu, and V. Srinivasan, *Energy Environ. Sci.*, **7**, 1555 (2014).
- S.-T. Myung, F. Maglia, K.-J. Park, C. S. Yoon, P. Lamp, S.-J. Kim, and Y.-K. Sun, *ACS Energy Lett.*, **2**, 196 (2017).
- G.-L. Xu, X. Liu, A. Daali, R. Amine, Z. Chen, and K. Amine, *Adv. Funct. Mater.*, **30**, 2004748 (2020).
- A. Kwade, W. Haselrieder, R. Leithoff, A. Modlinger, F. Dietrich, and K. Droeder, *Nat. Energy*, **3**, 290 (2018).
- J.-H. Schünemann, *Phd. thesis*, Technische Universität Braunschweig (2015).
- P. Rozier and J. M. Tarascon, *J. Electrochem. Soc.*, **162**, A2490 (2015).
- F. Schipper et al., *Inorganics*, **5**, 32 (2017).
- T. Teufl, B. Strehle, P. Müller, H. A. Gasteiger, and M. A. Mendez, *J. Electrochem. Soc.*, **165**, 2718 (2018).
- Manganese price. accessed 02/09/2021 SMM Information & Technology Co, Ltd., <https://price.metal.com/Manganese>.
- Nickel price. accessed 02/09/2021 SMM Information & Technology Co, Ltd., <https://price.metal.com/Nickel>.
- X. Zhang, X. Meng, J. W. Elam, and I. Belharouak, *Solid State Ionics*, **268**, 231 (2014).
- F. Dogan, B. R. Long, J. R. Croy, K. G. Gallagher, H. Iddir, J. T. Russell, M. Balasubramanian, and B. Key, *J. Am. Chem. Soc.*, **137**, 2328 (2015).
- K. Kleiner, B. Strehle, A. R. Baker, S. J. Day, C. C. Tang, I. Buchberger, F.-F. Chesneau, H. A. Gasteiger, and M. Piana, *Chem. Mater.*, **30**, 3656 (2018).
- M. Saubanère, E. McCalla, J.-M. Tarascon, and M.-L. Doublet, *Energy Environ. Sci.*, **9**, 984 (2016).
- B. Strehle, K. Kleiner, R. Jung, F. Chesneau, M. Mendez, H. A. Gasteiger, and M. Piana, *J. Electrochem. Soc.*, **164**, A400 (2017).
- L. Simonin, J.-F. Colin, V. Ranieri, E. Canévet, J.-F. Martin, C. Bourbon, C. Baecht, P. Strobel, L. Daniel, and S. Patoux, *J. Mater. Chem.*, **22**, 11316 (2012).
- P. Oh, S. Myeong, W. Cho, M.-J. Lee, M. Ko, H. Y. Jeong, and J. Cho, *Nano Lett.*, **14**, 5965 (2014).
- D. Becker, M. Börner, A. Friesen, S. Klein, U. Rodehorst, M. Diehl, M. Winter, T. Placke, and R. Schmich, *J. Electrochem. Soc.*, **167**, 60524 (2020).
- J. Helbig, T. Beuse, V. Siozios, T. Placke, M. Winter, and R. Schmich, *J. Electrochem. Soc.*, **167**, 60519 (2020).
- L. Boulet-Roblin, M. E. Kazzi, P. Novák, and C. Villevieille, *J. Electrochem. Soc.*, **162**, A1297 (2015).
- T. Teufl, D. Pritzl, P. Krieg, B. Strehle, M. A. Mendez, and H. A. Gasteiger, *J. Electrochem. Soc.*, **167**, 11 (2020).
- F. T. Wagner, B. Lakshmanan, and M. F. Mathias, *J. Phys. Chem. Lett.*, **1**, 2204 (2010).
- F. J. Günter, C. Burgstaller, F. Konwitschny, and G. Reinhart, *J. Electrochem. Soc.*, **166**, A1709 (2019).
- S. Chen et al., *Joule*, **3**, 1094 (2019).
- R. Petibon, V. L. Chevrier, C. P. Aiken, D. S. Hall, S. R. Hyatt, R. Shunmugasundaram, and J. R. Dahn, *J. Electrochem. Soc.*, **163**, A1146 (2016).
- R. Jung, M. Metzger, D. Haering, S. Solchenbach, C. Marino, N. Tsiouvaras, C. Stinner, and H. A. Gasteiger, *J. Electrochem. Soc.*, **163**, A1705 (2016).
- S. Solchenbach, D. Pritzl, E. J. Y. Kong, J. Landesfeind, and H. A. Gasteiger, *J. Electrochem. Soc.*, **163**, A2265 (2016).
- B. J. Polzin, S. E. Trask, Y. Zhu, M. Bettge, D. P. Abraham, and A. N. Jansen, *Meet. Abstr.*, **MA2014-01**, 213 (2014).
- K.-H. Pettinger, *Handbuch Lithium-Ionen-Batterien*, ed. R. Korthauer (Springer, Berlin) (2013).
- O. Schmidt, M. Thomitzek, F. Röder, S. Thiede, C. Herrmann, and U. Krewer, *J. Electrochem. Soc.*, **167**, 60501 (2020).
- G. Reinhart, T. Zeilinger, J. Kurfer, M. Westermeier, C. Thiemann, M. Glonegger, M. Wunderer, C. Tammer, M. Schweier, and M. Heinz, *Future Trends in Production Engineering*, ed. G. Schuh, R. Neugebauer, and E. Uhlmann (Springer, Berlin) pp. 3 (2013).
- H. Zheng, L. Tan, G. Liu, X. Song, and V. S. Battaglia, *J. Power Sources*, **208**, 52 (2012).
- D. Pritzl, A. E. Bumberger, M. Wetjen, J. Landesfeind, S. Solchenbach, and H. A. Gasteiger, *J. Electrochem. Soc.*, **166**, A582 (2019).
- A. Jossen and W. Weydanz, *Moderne Akkumulatoren richtig einsetzen* (Cuvillier, Göttingen) (2019).
- K. G. Gallagher et al., *J. Electrochem. Soc.*, **163**, A138 (2016).
- Y. Wu, *Lithium-ion Batteries: Fundamentals and Applications* (CRC Press, Boca Raton, Florida) (2015).
- S. Oswald, D. Pritzl, M. Wetjen, and H. A. Gasteiger, *J. Electrochem. Soc.*, **167**, 100511 (2020).

40. H. Bockholt, M. Indrikova, A. Netz, F. Golks, and A. Kwade, *J. Power Sources*, **325**, 140 (2016).
41. C. Meyer, H. Bockholt, W. Haselrieder, and A. Kwade, *J. Mater. Process. Technol.*, **249**, 172 (2017).
42. D. Schreiner, M. Oguntke, T. Günther, and G. Reinhart, *Energy Technol.*, **18**, 1900840 (2019).
43. T. Günther, D. Schreiner, A. Metkar, C. Meyer, A. Kwade, and G. Reinhart, *Energy Technol.*, **5**, 1900026 (2019).
44. C. Meyer, M. Weyhe, W. Haselrieder, and A. Kwade, *Energy Technol.*, **8**, 1900175 (2020).
45. W. Haselrieder, *PhD. thesis*, Technische Universität Braunschweig (2016).
46. T. Knoche and G. Reinhart, *Appl. Mech. Mater.*, **794**, 11 (2015).
47. F. J. Günter, S. Rössler, M. Schulz, W. Braunwarth, R. Gilles, and G. Reinhart, *Energy Technol.*, **8**, 1801108 (2020).
48. T. Knoche, F. Surek, and G. Reinhart, *Procedia CIRP*, **41**, 405 (2016).
49. R. Korthauer, *Lithium-Ion Batteries: Basics and Applications* (Springer, Berlin) (2018).
50. H. Koga, L. Croguennec, M. Ménétrier, P. Manessiez, F. Weill, and C. Delmas, *J. Power Sources*, **236**, 250 (2013).
51. N. Tsiouvaras, S. Meini, I. Buchberger, and H. A. Gasteiger, *J. Electrochem. Soc.*, **160**, A471 (2013).
52. L. Kraft, T. Zünd, D. Schreiner, R. Wilhelm, F. J. Günter, G. Reinhart, H. A. Gasteiger, and A. Jossen, *Comparative Evaluation of LMR-NCM and NCA Cathode Active Materials in Multilayer Lithium-Ion Pouch Cells - Part II: Rate Capability, Long-Term Stability and Thermal Behavior.*, **168**, 020537 (2018).
53. J. Kaiser, V. Wenzel, H. Nirschl, B. Bitsch, N. Willenbacher, M. Baunach, M. Schmitt, S. Jaiser, P. Scharfer, and W. Schabel, *Chem. Ing. Tech.*, **86**, 695 (2014).
54. A. Guéguen, C. Bolli, M. A. Mendez, and E. J. Berg, "Elucidating the Reactivity of Tris(trimethylsilyl)phosphite and Tris(trimethylsilyl)phosphate Additives in Carbonate Electrolytes—A Comparative Online Electrochemical Mass Spectrometry Study." *ACS Applied Energy Materials*, **3**, 290 (2020).
55. D. Ye, G. Zeng, K. Nogita, K. Ozawa, M. Hankel, D. J. Searles, and L. Wang, *Adv. Funct. Mater.*, **25**, 7488 (2015).
56. A. Shah, M. N. Ates, S. Kotz, J. Seo, K. M. Abraham, S. Somu, and A. Busnaina, *J. Electrochem. Soc.*, **161**, A989 (2014).
57. E. Björklund, D. Brandell, M. Hahlin, K. Edström, and R. Younesi, *J. Electrochem. Soc.*, **164**, A3054 (2017).
58. J. B. Quinn, T. Waldmann, K. Richter, M. Kasper, and M. Wohlfahrt-Mehrens, *J. Electrochem. Soc.*, **165**, A3284 (2018).
59. M. M. Besli et al., *J. Mater. Chem. A*, **7**, 12593 (2019).
60. M. M. Besli et al., *Chem. Mater.*, **31**, 491 (2019).
61. J. Nanda, S. K. Martha, and R. Kalyanaraman, *Pramana - J Phys.*, **84**, 1073 (2015).
62. L. Froboese, P. Titscher, B. Westphal, W. Haselrieder, and A. Kwade, *Mater. Charact.*, **133**, 102 (2017).
63. C. Simon, D. Kartouzian, D. Mueller, F. Wilhelm, and H. A. Gasteiger, *J. Electrochem. Soc.*, **164**, F1697 (2017).
64. H. Giesche, *Handbook of Porous Solids*, ed. F. Schüth, S. W. Kenneth, and J. Weitkamp (Wiley, Weinheim) p. 335 (2002).
65. H. Giesche, *Part. Part. Syst. Charact.*, **23**, 9 (2006).
66. H. Bockholt, W. Haselrieder, and A. Kwade, *ECS Trans.*, **50**, 25 (2013).
67. J. Wandt, A. T. S. Freiberg, A. Ogrodnik, and H. A. Gasteiger, *Mater. Today*, **21**, 825 (2018).
68. A. T. S. Freiberg, M. K. Roos, J. Wandt, R. de Vivie-Riedle, and H. A. Gasteiger, *J. Phys. Chem.*, **122**, 8828 (2018).
69. D. Streich, A. Guéguen, M. Mendez, F. Chesneau, P. Novák, and E. J. Berg, *J. Electrochem. Soc.*, **163**, A964 (2016).
70. J. Teufl, D. Pritzl, S. Solchenbach, H. A. Gasteiger, and M. Mendez, *Meet. Abstr.*, **MA2018-02**, 456 (2018).
71. K. Kim, I. Park, S.-Y. Ha, Y. Kim, M.-H. Woo, M.-H. Jeong, W. C. Shin, M. Ue, S. Y. Hong, and N.-S. Choi, *Electrochim. Acta*, **225**, 358 (2017).
72. T. Teufl, D. Pritzl, S. Solchenbach, M. A. Mendez, and H. A. Gasteiger, *Thermal Stability of FEC-Based Electrolytes for High-Voltage Li-Ion Batteries.*, Manuscript in preparation.
73. M. Metzger, B. Strehle, S. Solchenbach, and H. A. Gasteiger, *J. Electrochem. Soc.*, **163**, A798 (2016).
74. R. Poggemann, A. Steiff, and P.-M. Weinspach, *Chem. Ing. Tech.*, **51**, 948 (1979).
75. J. Kim, H. Lee, H. Cha, M. Yoon, M. Park, and J. Cho, *Adv. Energy Mater.*, **8**, 1702028 (2017).
76. H.-J. Noh, S. Youn, C. S. Yoon, and Y.-K. Sun, *J. Power Sources*, **233**, 121 (2013).
77. J. Sicklinger, M. Metzger, H. Beyer, D. Pritzl, and H. A. Gasteiger, *J. Electrochem. Soc.*, **166**, A2322 (2019).
78. R. Jung, R. Morasch, P. Karayaylali, K. Phillips, F. Maglia, C. Stinner, Y. Shao-Horn, and H. A. Gasteiger, *J. Electrochem. Soc.*, **165**, A132 (2018).
79. Y. Chen, S. Song, X. Zhang, and Y. Liu, *J. Electrochem. Soc.*, **1347**, 012012 (2019).



## 4.2 Performance and Cycle Live of Multilayer-Pouch Cells with LMR-NCM Cathodes

This section continues with the presentation of the article “Comparative Evaluation of LMR-NCM and NCA Cathode Active Materials in Multilayer Lithium-Ion Pouch Cells: Part II. Rate Capability, Long-Term Stability, and Thermal Behaviour”. The manuscript was submitted in January 2021 and published in February 2021 as a peer-reviewed publication in the Journal of the Electrochemical Society. It is available as an “open access” article and distributed under the terms of the Creative Commons Attribution 4.0 License ([CC BY](https://creativecommons.org/licenses/by/4.0/)). Ludwig Kraft presented parts of this work at the Batterieforum 2020 in Berlin and Tanja Zünd presented some of the cell lifetime data at the 235<sup>th</sup> Meeting of the Electrochemical Society (2019) in Dallas, USA. The permanent web link to this article can be found under: <https://iopscience.iop.org/article/10.1149/1945-7111/abe5e6>

In this article, the cell performance and cycle life of the multilayer pouch cells built in the first part of this work (Section 4.1) were evaluated. A comparative analysis of LMR-NCM and NCA based multilayer pouch cells was conducted for the different cell tests. At the beginning, the energy efficiency (EE) of the cells at C/10 was determined. While NCA showed an EE of  $\approx 98\%$ , LMR-NCM cells reached only  $\approx 87\%$ . By using intermittent OCV cycling, the energy loss of the LMR-NCM cathodes could be split into an expected overpotential driven, current-dependent part ( $\approx 60\%$ ) and an additional current independent OCV-hysteresis related part ( $\approx 40\%$ ). The OCV-hysteresis phenomenon is an interesting and complex material property, explained in more detail in Section 2.3.3, and studied in Section 4.2 and Section 4.4. The consequences of the low EE were highlighted by comparing the temperature rise during the discharge rate capability test of the two cell types. The lost energy is released as heat and therefore LMR-NCM based cells heated up to  $>50^\circ\text{C}$  at a discharge rate of 3C while NCA cells stayed below  $35^\circ\text{C}$ . The multilayer pouch cell tests at C/2 showed around 30% higher specific capacities for LMR-NCM based cells than for NCA based cells, with both being very comparable to the coin half-cell results. However, because of the lower mean discharge voltage of the LMR-NCM cells, the energy density on the cell level was only  $\approx 11\%$  higher.

In the long-term cycling analysis, LMR-NCM cells faded faster (0.17 mAh/(g cycle) vs. 0.06 mAh/(g cycle)) and their testing had to be stopped after 250 cycles due to gassing issues. Check-up cycles with slow and fast discharge cycles as well as an DCIR pulse allowed a rough aging analysis to be made. The cell resistance increased linearly in both cell types but around 60% faster in the case of the LMR-NCM cells. However, the almost parallel and linear capacity fading of the C/10 and 1C check-up cycles indicates for both cell chemistries an aging mechanism that is dominated by a loss of cyclable lithium rather than by an impedance growth. The NCA cells reached an 80% state of health (SOH) of their initial energy density after 710 cycles, whereas the LMR-NCM crossed this boundary after only 230 cycles. The initial higher energy density of the LMR-NCM cells due to the higher capacity of the LMR-NCM material was reduced to being the same as that of the NCA cells after 200 cycles, mainly due to increased capacity loss in combination with a faster voltage fading of the LMR-NCM cells. In future investigations, attempts will be made to try to find solutions for the challenging electrolyte/cathode interface at high potentials in order to reduce the loss of cyclable lithium.

#### Author contributions

The pouch cells were built by the battery production team of D.S. and F.G. The lab cells were built and measured by R.W. and T.Z. L.K. conducted the pouch cell measurements. The results of the experiments were analysed and interpreted by L.K. and T.Z. The manuscript was written by L.K. and T.Z. and edited by the co-authors. All authors discussed the data and commented on the results. L.K. and T.Z. contributed equally to this work as co-sharing first authors.



# Comparative Evaluation of LMR-NCM and NCA Cathode Active Materials in Multilayer Lithium-Ion Pouch Cells: Part II. Rate Capability, Long-Term Stability, and Thermal Behavior

Ludwig Kraft,<sup>1,\*</sup> Tanja Zünd,<sup>2,\*</sup> David Schreiner,<sup>3</sup> Rebecca Wilhelm,<sup>2,\*</sup> Florian J. Günter,<sup>3</sup> Gunther Reinhart,<sup>3</sup> Hubert A. Gasteiger,<sup>2,\*\*</sup> and Andreas Jossen<sup>1</sup>

<sup>1</sup>Institute for Electrical Energy Storage Technology, Technical University of Munich, D-80333 Munich, Germany

<sup>2</sup>Chair of Technical Electrochemistry, Technical University of Munich, D-85748 Garching, Germany

<sup>3</sup>Institute for Machine Tools and Industrial Management, Technical University of Munich, D-85748 Garching, Germany

A lithium- and manganese-rich layered transition metal oxide-based cathode active material (LMR-NCM) with a reversible capacity of 250 mAh g<sup>-1</sup> vs graphite is compared to an established NCA/graphite combination in multilayer lithium-ion pouch cells with a capacity of 5.5 Ah at a 1C discharge rate. The production of the cells, the electrode characterization as well as the formation is described in Part I of this study. In Part II, the two cell types are evaluated for their rate capability and their long-term stability. The specific capacity of the LMR-NCM pouch cells is ≈30% higher in comparison to the NCA pouch cells. However, due to the lower mean discharge voltage of LMR-NCM, the energy density on the cell level is only 11% higher. At higher discharge currents, a pronounced heat generation of the LMR-NCM pouch cells was observed, which is ascribed to the LMR-NCM voltage hysteresis and is only detectable in large-format cells. The cycling stability of the LMR-NCM cells is somewhat inferior due to their faster capacity and voltage fading, likely also related to electrolyte oxidation. This results in a lower energy density on the cell level after 210 cycles compared to the NCA pouch cells.

© 2021 The Author(s). Published on behalf of The Electrochemical Society by IOP Publishing Limited. This is an open access article distributed under the terms of the Creative Commons Attribution 4.0 License (CC BY, <http://creativecommons.org/licenses/by/4.0/>), which permits unrestricted reuse of the work in any medium, provided the original work is properly cited. [DOI: 10.1149/1945-7111/abe566]



Manuscript submitted January 14, 2021; revised manuscript received February 11, 2021. Published February 23, 2021.

The demand for lithium-ion batteries with a higher capacity and energy density is rising, especially driven by mobile applications like electric vehicles (EVs).<sup>1-4</sup> As a consequence, the specific capacity of the active materials must increase. State-of-the-art cathode active materials (CAMs) are lithium-nickel-cobalt-manganese-oxides (NCMs) or lithium-nickel-cobalt-aluminum-oxides (NCAs). The capacity of NCMs can be increased by a higher Ni content, e.g., from NCM-111 with 150 mAh g<sup>-1</sup> up to 200 mAh g<sup>-1</sup> for NCM-811 for comparable upper cutoff voltages.<sup>1,2,5</sup> The Ni-rich NCA materials exhibit a similar specific capacity of around 200 mAh g<sup>-1</sup>.<sup>6,7</sup> A promising not yet commercialized CAM that offers a higher capacity is Li- and Mn-rich NCM (LMR-NCM) with a reversible capacity of around 250 mAh g<sup>-1</sup>.<sup>8-12</sup>

Material costs account for 45%–75% of the total manufacturing costs on the cell level, and the CAMs have the biggest share of the material costs with 39%–54%.<sup>13-16</sup> This makes Mn-rich materials more cost effective compared to Ni-rich materials. In February 2021, the price of the commodity Ni (21 USD kg<sup>-1</sup>)<sup>17</sup> was an order of magnitude higher than that of Mn (2 USD kg<sup>-1</sup>)<sup>18</sup>. While currently used NCA and NCM CAMs still contain Co, ongoing research aims toward reducing or eliminating Co.<sup>19-21</sup> Similarly, it has also been shown that Co can be eliminated from LMR-NCM CAMs.<sup>22</sup> Based on the stoichiometry of the two CAMs that are investigated in our work, up to 34% can be saved in raw material costs comparing a LMR-NCM (Li<sub>1.14</sub>Ni<sub>0.26</sub>Co<sub>0.14</sub>Mn<sub>0.60</sub>O<sub>2</sub>) to an NCA (LiNi<sub>0.81</sub>Co<sub>0.15</sub>Al<sub>0.04</sub>O<sub>2</sub>) with commodity prices of Co (45 USD kg<sup>-1</sup>)<sup>23</sup>, Li (10 USD kg<sup>-1</sup>)<sup>24</sup>, and Al (2 USD kg<sup>-1</sup>)<sup>25</sup>. Therefore, the high specific capacity combined with the lower material costs render LMR-NCM to a promising CAM for future lithium-ion batteries.<sup>4,11,26,27</sup>

There is a wide variety of lithium-ion cells exhibiting different cell formats, designs, and materials. Reported energy densities of various cells and cell formats range from 83 Wh kg<sup>-1</sup> for high power cells to 267 Wh kg<sup>-1</sup> for high energy cells.<sup>28-31</sup> The energy density on the cell level can be enhanced by thicker and less porous electrodes, by

electrode compositions with a higher active material share, or by the use of active materials with a higher specific capacity, while reducing the share of passive parts like separators, current collectors, tab connectors, or the housing.<sup>1,32</sup> Up-to-date, high energy cells that reach >250 Wh kg<sup>-1</sup> often use a Ni-rich CAM, either NCM-811 or NCA, and a graphite anode that contains a small amount of silicon.<sup>29-31,33</sup> Ding et al.<sup>30</sup> reported energy densities of cylindrical cells used by Tesla in EVs of 236 Wh kg<sup>-1</sup> for an NCA/graphite cell and 260 Wh kg<sup>-1</sup> for an NCA/silicon-graphite cell.

In this work, a LMR-NCM material is evaluated and compared to a commercially available NCA material that serves as a benchmark. Based on our scale-up experiments with laboratory-scale coin cells with LMR-NCM, this CAM was used to design multilayer pouch cells, which were produced on the pilot scale production line at the Technical University of Munich,<sup>34</sup> as described in Part I of this study.<sup>35</sup> To appropriately assess the performance of the LMR-NCM pouch cells, NCA pouch cells with the same electrode and cell configuration were produced on the same line. The cells were standardized by adjusting the loading of the electrode sheets, delivering an areal capacity of 2.3 mAh cm<sup>-2</sup> or a total capacity of 5.5 Ah at a 1C discharge rate. For both cell types, graphite was used as anode material. For simplicity, the LMR-NCM/graphite and NCA/graphite pouch cells will further on be referred to as LMR-NCM and NCA pouch cells, respectively.

The production of the cells, the electrode characterization, as well as their formation is described in Part I of this study.<sup>35</sup> In Part II, the characteristics of both cell types were evaluated by discharge rate capability tests and by an aging study, in which we compare their capacity, mean discharge voltage, and energy density fading, their internal resistance buildup, as well as their self-heating at high discharge rates. While previous publications on LMR-NCM were carried out with small-scale laboratory cells (e.g., coin cells), stating energy densities up to 1000 Wh kg<sup>-1</sup> at the material level,<sup>11,12,26</sup> to the best of our knowledge, there is no published research on large-format LMR-NCM cells that would allow a rigorous assessment of the energy densities achieved on the cell level. Especially the evaluation of self-heating effects at high C-rates and gassing effects during formation and extended aging is only feasible with large-format cells, so that the here presented study with large-format multilayer pouch cells will provide new insights with regards to these aspects.

<sup>\*</sup>These authors contributed equally to this work.

<sup>\*</sup>Electrochemical Society Student Member.

<sup>\*\*</sup>Electrochemical Society Fellow.

<sup>z</sup>E-mail: ludwig.kraft@tum.de

## Experimental

The large-format multilayer pouch cells were produced on the semi-automatic manufacturing pilot line at the Technical University of Munich.<sup>34</sup> To compare the performance of the two CAMs, both pouch cell types were designed to have a similar areal capacity of 2.3 mAh cm<sup>-2</sup> at a 1C discharge, amounting to a total capacity of around 5.5 Ah at 1C. A target capacity of 5.5 Ah at 1C results in an energy of 17.6 Wh for the LMR-NCM and 19.8 Wh for the NCA pouch cells (based on averaged discharge voltages at 1C of 3.2 V for the LMR-NCM and 3.6 V for the NCA cells). The here used multilayer pouch cell design was based on small-scale laboratory coin cell measurements that were conducted in Part I of this study.<sup>35</sup> Details on the electrode production as well as the pouch cell assembly and formation are also provided in Part I of this study.<sup>35</sup>

**Electrode specifications.**—In this study, a LMR-NCM CAM with a stoichiometry of Li<sub>1.14</sub>[Ni<sub>0.26</sub>Co<sub>0.14</sub>Mn<sub>0.60</sub>]<sub>0.86</sub>O<sub>2</sub> (BASF, Germany), which can as well be written as 0.33 Li<sub>2</sub>MnO<sub>3</sub> · 0.67 LiNi<sub>0.38</sub>Co<sub>0.21</sub>Mn<sub>0.41</sub>O<sub>2</sub> and was also investigated by Teuffel et al.,<sup>36</sup> and an NCA with a stoichiometry of LiNi<sub>0.81</sub>Co<sub>0.15</sub>Al<sub>0.04</sub>O<sub>2</sub> (BASF, Germany) were used. The cathodes consisted of 92.5 wt% CAM (LMR-NCM or NCA), 4 wt% conductive carbon (Super-C65, Timcal, Switzerland), 3.5 wt% polyvinylidene-fluoride binder (PVdF, Solef 5130, Solvay, Belgium), and were coated double-sided on a 15 μm aluminum substrate foil (1055 A, Korff, Switzerland). The CAM loading was set to 11.7 mg cm<sup>-2</sup> (≡2.9 mAh cm<sup>-2</sup> at C/10, based on a nominal capacity of 250 mAh g<sup>-1</sup><sub>CAM</sub>) and 13.0 mg cm<sup>-2</sup> (≡2.6 mAh cm<sup>-2</sup> at C/10, based on a nominal capacity of 200 mAh g<sup>-1</sup><sub>CAM</sub>) for the LMR-NCM and NCA electrode sheets, respectively. The nominal capacities of both CAMs relate to LMR-NCM/Li cells in a voltage range of 2.0–4.7 V (250 mAh g<sup>-1</sup><sub>CAM</sub>) and NCA/Li cells in a voltage range of 3.0–4.5 V (200 mAh g<sup>-1</sup><sub>CAM</sub>), and were used for the calculation of the nominal cell capacities as stated in Table I. The cathodes were calendered to an electrode coating porosity of 42%.

The anodes consisted of 97 wt% graphite (SGL Carbon, Germany), 1.5 wt% carboxymethyl cellulose binder (CMC Sunrose MAC200, NPI, Japan), 1.5 wt% styrene-butadiene rubber binder (SBR, Zeon, Japan), and were coated on a 11 μm copper substrate foil (Cu-PHC, hard rolled blank, with a nominal thickness of 12 μm Schlenk, Germany). The graphite electrode loadings were set to 9.5 mg cm<sup>-2</sup> (≡3.4 mAh cm<sup>-2</sup> at C/10, based on a nominal capacity of 355 mAh g<sup>-1</sup><sub>graphite</sub>) for LMR-NCM and 10.2 mg cm<sup>-2</sup> (≡3.6 mAh cm<sup>-2</sup> at C/10, based on a nominal capacity of 355 mAh g<sup>-1</sup><sub>graphite</sub>) for NCA based pouch cells. The anodes were calendered to an electrode coating porosity of 30%. The resulting areal capacity ratios of negative/positive electrode (N/P ratio) were 1.17 for the LMR-NCM and 1.38 for the NCA pouch cells.

**Pouch cell assembly.**—Both cell types contained 16 double-coated cathodes and 17 double-coated anodes. The electrodes were alternately stacked with a z-folded monolayer polypropylene (PP) separator (Celgard 2500, France) with a thickness of 25 μm. An FEC:DEC based electrolyte (1 M LiPF<sub>6</sub> in a 12:64:24 (by volume) mixture of FEC:DEC:co-solvent and 2 wt% of a proprietary additive, BASF, Germany) was used for the LMR-NCM cells, while an

EC:DEC based electrolyte (1 M LiPF<sub>6</sub> in a 3:7 (by weight) mixture of EC:DEC and 2 wt% vinylene carbonate (VC), BASF, Germany) was used for the NCA cells. The proprietary additive improves full-cell cycle stability and has a similar effect as the one described in Ref. 37.

The individual cell specifications are listed in Table I. The CAM mass was determined by weighing the electrode sheets before the assembling process, while the finally determined mass of the cell after the electrolyte filling, the degassing after formation, and the final cell sealing process includes the current collectors, the welded-on tabs, and the pouch foil. For comparison of the cells, the specific capacity used in the later studies was related to the CAM mass. The gravimetric energy density, however, was related to the total pouch cell mass. On account of an error in the production process, the loading of the graphite anodes for the NCA pouch cells was slightly too high, resulting in an N/P ratio of 1.38 instead of the originally intended N/P ratio of 1.2. Assuming a N/P ratio of 1.17 for the NCA pouch cells (as is the case with the LMR-NCM cells), the total cell mass would be reduced by ≈4.4 g (due to a reduced anode loading by 1.6 mg cm<sup>-2</sup> with an active material ratio of 97 wt% and a total anode area of 2687 cm<sup>2</sup>), resulting in 4% higher gravimetric energy density values. Nevertheless, the stated gravimetric energy densities were calculated with the actual cell mass of the NCA pouch cells. For the evaluation of the volumetric energy density, a volume of ≈51.6 cm<sup>3</sup> for the LMR-NCM and ≈49.7 cm<sup>3</sup> for the NCA pouch cells was used (based on the cell thicknesses and the length and width of the deep-drawn pocket of the pouch bag). Unless stated otherwise, the term energy density refers to the gravimetric energy density. Based on a nominal reversible capacity at C/10 of 250 mAh g<sup>-1</sup> for LMR-NCM and 200 mAh g<sup>-1</sup> for NCA, the nominal cell capacity was calculated according to the CAM mass. In all later measurements, the C-rates for the charging and discharging procedures were referred to the nominal cell capacity at C/10 of each cell, as stated in Table I. For a detailed overview of the production and formation process of the LMR-NCM pouch cells, the reader is referred to Part I of this study.<sup>35</sup>

**Coin cell specifications.**—As a reference, experiments with both the LMR-NCM and the NCA cathodes with graphite anodes were also conducted with laboratory 2032-type coin cells. Cathodes with 14 mm diameter and anodes with 15 mm diameter were punched out from a single side coated part of the electrodes used for the pouch cells as described above, i.e., with the same areal capacities as specified above. The electrodes were dried in a glass oven (Büchi, Switzerland) under dynamic vacuum at 120 °C for 12 h. The coin cells were assembled in an argon filled glove box (O<sub>2</sub>, H<sub>2</sub>O < 0.1 ppm, MBraun, Germany) with a separator of 17 mm in diameter and 50 μL of electrolyte. The separator and the electrolyte for the corresponding CAMs were the same for the coin and pouch cells.

**Electrochemical measurements.**—*Cell formation and mounting.*—A formation procedure with a first constant current (CC) C/15 cycle including degassing steps, followed by two CC C/10 cycles was carried out. The LMR-NCM cells were charged to 4.7 V in their first formation cycle to activate the material,<sup>10</sup> in all subsequent cycles, the upper cutoff voltage was set to 4.6 V. A more detailed description of the formation procedure is given in Part I of this study.<sup>35</sup> The LMR-NCM

**Table I. Specifications of the LMR-NCM/graphite and NCA/graphite pouch cells with an identical CAM-based areal capacity of ≈2.3 mAh cm<sup>-2</sup> at 1C. Note that the here used pouch cells represent a subset of the pouch cells presented in Part I of this study.<sup>35</sup>**

Cell type	Number of cells	CAM <sup>a)</sup> mass	Cell mass <sup>b)</sup>	Nominal cell capacity <sup>c)</sup>
LMR-NCM	5	27.64 ± 0.32 g	111.6 ± 1.6 g	6.91 ± 0.08 Ah
NCA	6	31.34 ± 0.41 g	115.8 ± 2.0 g	6.27 ± 0.08 Ah

a) CAM—cathode active material. b) Determined by weighing the cells after formation, degassing, and final sealing of the cells. c) Based on the nominal specific CAM capacity at C/10 (LMR-NCM: 250 mAh g<sup>-1</sup>, NCA: 200 mAh g<sup>-1</sup>).

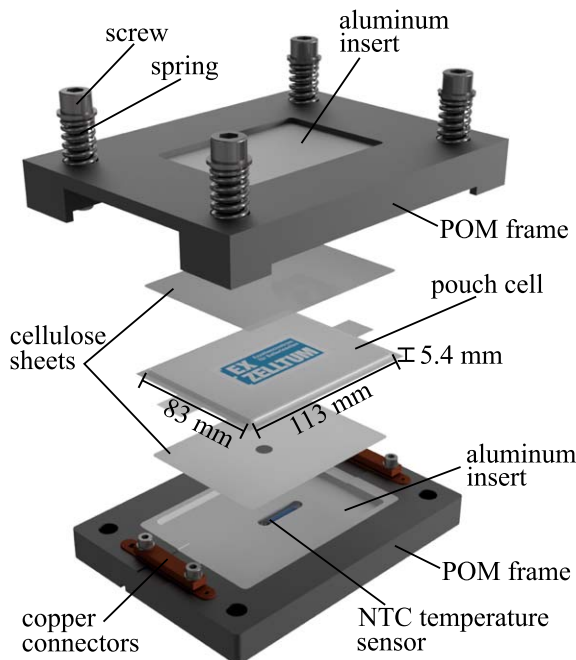


**Figure 1.** Schematic CAD drawing of the cell holder including the pouch cell. The 5.4 mm thickness of the depicted pouch cell represents a mean value of the thicknesses of the LMR-NCM (5.5 mm) and NCA (5.3 mm) cells.

cells were cycled between 2.0 V and 4.6 V and the NCA cells between 3.0 V and 4.3 V. Note that all C-rates are referenced to the nominal specific CAM capacity of  $250 \text{ mAh g}^{-1}$  for LMR-NCM cells and of  $200 \text{ mAh g}^{-1}$  for NCA cells.

The pouch cells were mounted in custom-built cell holders as depicted in Fig. 1. Both the bottom and top part of the cell holder consisted of a thermoplastic polyoxymethylene (POM) frame with an aluminum insert. Via the screw/spring combination a pressure of 0.2 MPa was applied to the pouch cells. Cellulose sheets (Pacopads 5500, Pacothane Technologies, USA) were put between the cell and the aluminum inserts to obtain a homogeneous compressive force across the active area. An integrated negative temperature coefficient (NTC) temperature sensor was attached to measure the temperature on the surface of the pouch cells with a precision of  $\pm 1 \text{ K}$ . All pouch cell measurements were performed with an XCTS battery test system (BaSyTec, Germany) in a controlled climate chamber (WT3-600/40-S, Weiss Umwelttechnik, Germany) at  $25^\circ\text{C}$ . The coin cells were cycled with a Maccor battery tester (series 4000, USA) in a controlled climate chamber (Binder, Germany) at  $25^\circ\text{C}$ . A detailed overview of all measurement procedures is listed in Table II, the tests were consecutively performed in the stated order for each of the cells.

**Initial C/10 cycle and open circuit voltage curve.**—After formation, the cells were charged and discharged with a CC C/10 cycle. In a subsequent CC C/10 cycle, a pause of 1 h was included after each hour, which sums up to ten 1 h pauses during the charge and ten 1 h pauses during the discharge. While pausing, the relaxation of the open circuit voltage (OCV) was measured.

**Discharge rate capability test.**—Next, the discharge rate capability test was carried out with CC discharging with C/10, C/5, and C/2. The preceding charging C-rate was set to the discharging C-rate. The CC charging phase was followed by a constant voltage (CV) phase until a cutoff current of C/20 was reached. For two cells of each cell type, an extended discharge rate capability test was carried out with also 1C, 2C, and 3C discharge rates, whereby the charging current in the CC phase was limited to C/2 (with a CV

phase terminated at C/20) for each discharge rate. The specific capacity was related to the mass of the corresponding CAM, whereas the energy density was related to the total cell mass as stated in Table I. The values for each cycle were averaged over all cells of the corresponding cell type and plotted with the corresponding standard deviation. If the measurement procedure only consisted of two samples, their mean value was plotted with the minimum and maximum value, indicated by the error bars.

**Aging study.**—In the final aging test, the cells were repeatedly cycled with a C/2 CCCV charge (with a cutoff current of C/20) and a C/2 CC discharge. Every 25 cycles, a checkup procedure was carried out. In the checkup procedure, the cells were initially charged with C/10 to a voltage of 3.7 V, which corresponds to a state-of-charge (SOC) of approximately 40% for both cell types, followed by a 1 h resting period at OCV. Then the cell resistance was determined with the direct current internal resistance (DCIR) method by applying a C/2 CC discharge pulse for 10 s and measuring the cell voltage. The resistance is calculated by Ohm's law and the total voltage drop and referenced to the cathode area ( $73.73 \text{ cm}^2$  per layer). After the DCIR test, the cells were first discharged with C/10 to their lower cutoff voltage, and then, the cell capacity was assessed by a full C/10 charge/discharge cycle. Only the four cells (2x LMR-NCM, 2x NCA) that were stressed with the extended rate capability test were additionally discharged with three 1C CC cycles in each checkup.

## Results and Discussion

The comparative evaluation of the performance of the large-format multilayer LMR-NCM and NCA pouch cells is divided into two parts: the rate capability behavior, and the aging behavior of the cells in the long-term cycling study.

**Rate capability behavior.**—The results of the discharge rate capability test, depicting the C-rate dependence of the specific CAM capacity, the charge averaged mean cell discharge voltage, and the gravimetric cell energy density are displayed in Fig. 2; the corresponding values normalized to those at C/10 are stated in Table III.

For low C-rates, i.e., C/10 and C/5, the discharge capacity stayed almost constant for both materials, and the LMR-NCM cells delivered around 30% higher specific capacities. With increasing rates, less capacity can be discharged from the cells, especially for the high C-rates of 2C and 3C. At a 2C discharge, only 88% can be discharged from the LMR-NCM cells and 77% from the NCA cells, when referenced to their capacity at C/10. At a 3C discharge, the LMR-NCM cells delivered 77%, while the NCA cells dropped to 59%. Previous studies with NCA<sup>38,39</sup> and LMR-NCM<sup>10,40,41</sup> showed that the capacity loss at high C-rates is largely due to the poor charge transfer kinetics and/or the slow solid-state diffusion at low SOC. However, it is noteworthy that the capacity loss with increasing C-rate was much more pronounced for LMR-NCM/lithium coin cells that were investigated in Part I of this study<sup>35</sup>: at the same loading ( $\approx 12 \text{ mg cm}^{-2}$ ) and cathode porosity ( $\approx 42\%$ ), the capacity at 3C was only  $\approx 120 \text{ mAh g}_{\text{CAM}}^{-1}$  (see Fig. 2 in Ref. 35), compared to the  $\approx 180 \text{ mAh g}_{\text{CAM}}^{-1}$  obtained here for the LMR-NCM/graphite pouch cells (red symbols in Fig. 2a). As will be shown later, this was most likely linked to the strong cell temperature rise of the LMR-NCM pouch cells at high C-rates.

The mean discharge voltage at C/10 shown in Fig. 2b of the LMR-NCM cells was at 3.5 V, while it was at 3.7 V for the NCA cells. At a 3C rate, the mean discharge voltage of the LMR-NCM cells decreased by  $\approx 660 \text{ mV}$ , which was more than double compared to the  $\approx 310 \text{ mV}$  drop of the NCA cells, revealing the strong rate dependency of the LMR-NCM CAM.

The gravimetric energy density of the pouch cells, displayed in Fig. 2c, is a product of the discharge capacity and the mean discharge voltage, referenced to the total mass of the pouch cells.

**Table II.** Sequence of the measurement procedures applied to the LMR-NCM/graphite and NCA/graphite pouch and coin cells.

Cycling procedure	Cycles	Charge	Stop condition	Discharge	Stop condition	
C/10 cycle	1	CC @ C/10	$U \geq U_{\max}$	CC @ C/10	$U \leq U_{\min}$	
C/10 relax cycle (initial OCV curve)	1	CC @ C/10 Pause	$t \geq 1$ h or $U \geq U_{\max}$ $t \geq 1$ h	CC @ C/10 Pause	$t \geq 1$ h or $U \leq U_{\min}$ $t \geq 1$ h	
Rate capability test	3	CC @ C/10 CV @ $U_{\max}$	$U \geq U_{\max}$ $I \leq C/20$	CC @ C/10	$U \leq U_{\min}$	
	3	CC @ C/5 CV @ $U_{\max}$	$U \geq U_{\max}$ $I \leq C/20$	CC @ C/5	$U \leq U_{\min}$	
	5	CC @ C/2 CV @ $U_{\max}$	$U \geq U_{\max}$ $I \leq C/20$	CC @ C/2	$U \leq U_{\min}$	
	Extended rate capability test <sup>a)</sup>	5	CC @ C/2 CV @ $U_{\max}$	$U \geq U_{\max}$ $I \leq C/20$	CC @ 1C	$U \leq U_{\min}$
		5	CC @ C/2 CV @ $U_{\max}$	$U \geq U_{\max}$ $I \leq C/20$	CC @ 2C	$U \leq U_{\min}$
		5	CC @ C/2 CV @ $U_{\max}$	$U \geq U_{\max}$ $I \leq C/20$	CC @ 3C	$U \leq U_{\min}$
Ageing cycles	25	CC @ C/2 CV @ $U_{\max}$	$U \geq U_{\max}$ $I \leq C/20$	CC @ C/2	$U \leq U_{\min}$	
<b>Checkup procedure</b>	<b>Cycles</b>	<b>Procedure</b>		<b>Stop condition</b>		
Initialization	1	CC charge @ C/10 Pause		$U \geq U_{\text{pulse}}$ $t \geq 1$ h		
Pulse Test	1	CC discharge @ C/2		$t \geq 10$ s		
C/10 cycle	1	CC discharge @ C/10 CC charge @ C/10 CC discharge @ C/10		$U \leq U_{\min}$ $U \geq U_{\max}$ $U \leq U_{\min}$		
1C cycle <sup>a)</sup>	3	CC charge @ C/2 CV charge @ $U_{\max}$ CC discharge @ 1C		$U \geq U_{\max}$ $I \leq C/20$ $U \leq U_{\min}$		

Before the first stated C/10 cycle, the cells underwent a formation procedure consisting of one C/15 and two C/10 cycles. The C-rates refer to the nominal cell capacities listed in Table I. All measurements were performed at an ambient temperature of 25 °C. CC—constant current, CV—constant voltage. LMR-NCM:  $U_{\max} = 4.6$  V,  $U_{\min} = 2.0$  V,  $U_{\text{pulse}} = 3.7$  V. NCA:  $U_{\max} = 4.3$  V,  $U_{\min} = 3.0$  V,  $U_{\text{pulse}} = 3.7$  V. a) Two cells each were discharged with the extended rate capability test and the 1C checkup cycles.

At low discharge rates the energy density was around 200 Wh kg<sup>-1</sup> ( $\approx 433$  Wh l<sup>-1</sup>) for the LMR-NCM and 180 Wh kg<sup>-1</sup> ( $\approx 419$  Wh l<sup>-1</sup>) for the NCA pouch cells. In contrast to the 30% increase in specific capacity, the benefit in gravimetric energy density was only 11%. An adjusted N/P ratio of 1.17 for the NCA pouch cells (rather than the here used N/P ratio of 1.38) would result in 4% higher energy densities, reducing the energy density advantage of the LMR-NCM cells to 7%. One reason for the lower gain in energy density compared to the gain in capacity of the LMR-NCM cells was their lower mean discharge voltage. Nevertheless, in this study, the LMR-NCM pouch cells maintained a higher energy density of  $\approx 11\%$  compared to the NCA pouch cells for C-rates up to 1C; this advantage became even more pronounced at higher rates of 2C (+16%) and 3C (+29%), which, as described later, is related to the substantial LMR-NCM cell temperature rise.

Both pouch cell types described in this work were not designed for a specific application or optimized with regards to their energy density. High energy cells use thinner current collectors and separators as well as lower electrode porosities, which requires less electrolyte.<sup>29,33</sup> All these measures save weight and volume and thereby increase the gravimetric and volumetric energy density on the cell level. Based on the cylindrical cells for EVs reported by Ding et al.<sup>30</sup> with 236 Wh kg<sup>-1</sup> (NCA/graphite) and 260 Wh kg<sup>-1</sup> (NCA/silicon-graphite), by switching the CAM from NCA to LMR-NCM and assuming a gravimetric energy density increase of 7% compared

to the properly balanced NCA/graphite or NCA/silicon-graphite cells, 253 Wh kg<sup>-1</sup> (LMR-NCM/graphite) and 278 Wh kg<sup>-1</sup> (LMR-NCM/silicon-graphite) could be reached.

The performance of the laboratory coin cells served as a comparison for the large-format multilayer pouch cells. As already mentioned above with regards to the discharge rate capability test, the LMR-NCM/graphite coin cells (as well as the LMR-NCM/lithium coin cells measured in Part I<sup>35</sup>) showed a specific capacity that was  $\approx 34\%$  lower than that of the corresponding pouch cells for a 3C discharge (see Fig. 3a). In contrast, the specific capacity of the NCA laboratory coin cells was in good agreement for all C-rates with the NCA pouch cells (see solid gray squares and open gray triangles in Fig. 3a). Just for clarification, for the 2C and 3C discharge in Fig. 3a, the open gray triangles indicating the specific capacity of the NCA coin cells are superposed by the open red triangles for the LMR-NCA coin cells.

While the coin cells can be considered isothermal at an ambient temperature of 25 °C during operation due to their low energy content and high thermal mass, this is not the case for large-format pouch cells. The maximum temperature of the pouch cells was reached at the end of each discharge and is depicted in Fig. 3b. As described in the experimental section, the temperature was measured on the surface of the pouch cells within the cell holder (see Fig. 1). The cell holder, consisting partly of aluminum and the thermoplastic POM, influenced the heat dissipation of the cells. As there were no

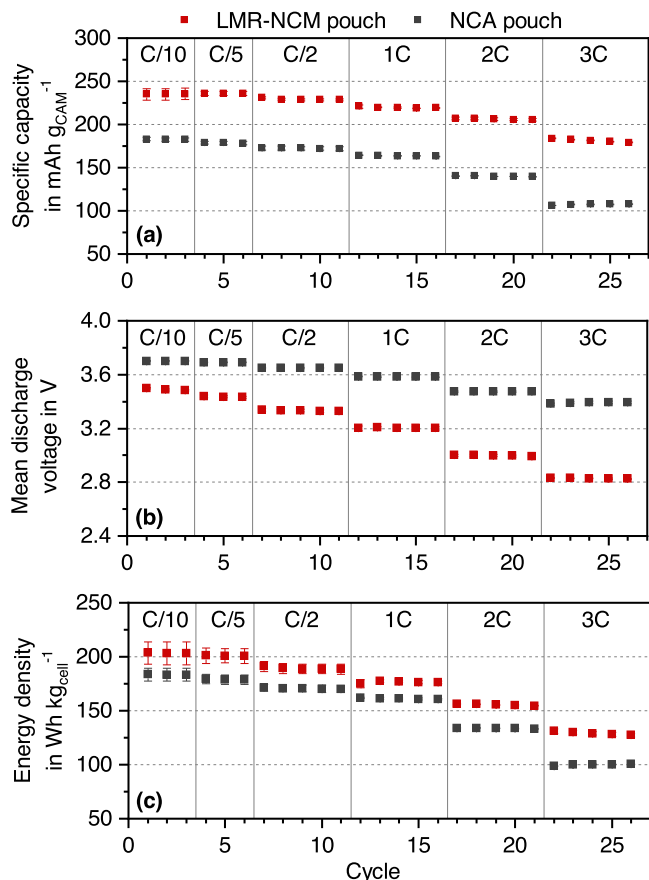


**Figure 2.** Discharge rate capability of the LMR-NCM and NCA pouch cells (as specified in Table I), depicting the C-rate dependence of (a) the specific capacity related to the CAM mass, (b) the mean cell discharge voltage, and (c) the energy density with respect to the total mass of the cell. The cells were discharged with a CC procedure at an ambient temperature of 25 °C in the voltage windows 4.6–2.0 V for LMR-NCM and 4.3–3.0 V for NCA, respectively (see Table II). The error bars for the rates of C/10, C/5, and C/2 represent the standard deviation between 5 LMR-NCM and 6 NCA cells; for the rates of 1C, 2C, and 3C, the error bars mark the minimum/maximum values of 2 cells of each type.

rest periods at the end of discharge during the rate capability test, the cells could not cool down to the 25 °C ambient temperature of the climate chamber and had an initial temperature of around 27.5 °C at the beginning of the rate capability test (see Fig. 3b). The temperature of the LMR-NCM cells strongly increased with increasing C-rates, reaching a temperature of 53 °C for the 3C discharge, while the NCA cells only reached 33 °C.

Figure 3c displays the round-trip energy efficiencies of both the LMR-NCM and NCA pouch and coin cells. The generated heat in a cell can be correlated to the energy that is irreversibly lost between

charge and discharge. After formation, this energy inefficiency is mainly caused by a voltage hysteresis between charge and discharge and therefore pronounced in LMR-NCM cells.<sup>42</sup> During the 3C discharge (following a C/2 CCCV charge, see Table II), the energy loss of the LMR-NCM pouch cells was above 6 Wh (corresponding to an energy efficiency of  $\approx 70\%$ ), while the NCA pouch cells only lost around 2 Wh (corresponding to an energy efficiency of  $\approx 85\%$ ). Table IV lists the mean charge ( $E_{CH}$ ) and discharge ( $E_{DCH}$ ) energies of the LMR-NCM and NCA pouch cells vs discharge rate (DCH C-rate) as well as the resulting round-trip energy efficiencies ( $\eta$ ), defined as

$$\eta = \frac{E_{DCH}}{E_{CH}} \cdot 100\% \quad [1]$$

It also lists the overall dissipated energy per cycle ( $\Delta E_{tot}$ )

$$\Delta E_{tot} = E_{CH} - E_{DCH} \quad [2]$$

Meister et al.<sup>42</sup> classified different anode and cathode materials according to their round-trip energy efficiency for a 1C charge/discharge cycle at an ambient temperature of 20 °C. In their study, graphite had a round-trip energy efficiency of  $\approx 94\%$ , their LMR-NCM (0.5 Li<sub>2</sub>MnO<sub>3</sub> · 0.5 LiNi<sub>0.4</sub>Mn<sub>0.4</sub>Co<sub>0.2</sub>O<sub>2</sub>) had a round-trip energy efficiency of  $\approx 85\%$ , while NCA was not investigated. Their LMR-NCM/graphite combination would result in a round-trip energy efficiency of  $\approx 80\%$ . This round-trip energy efficiency at a 1C rate reflects the results for the LMR-NCM/graphite pouch cells obtained in our study ( $\approx 81\%$  at 1C). Note that these values were measured at an ambient temperature of 20 °C, while our measurements were performed at an ambient temperature of 25 °C.

To further evaluate the difference in round-trip energy efficiency of both cell types, the charge and discharge voltage profiles of each cell type have to be closer examined. The total energy loss related to voltage hysteresis can be split into a resistive part  $\Delta E_R$ , due to cell polarization during operation, and into a current-independent part  $\Delta E_{OCV}$ , originating from the intrinsic active material voltage hysteresis that is particularly pronounced for LMR-NCMs.<sup>26,42</sup>

$$\Delta E_{tot} = \Delta E_R + \Delta E_{OCV} \quad [3]$$

The additional energy that is lost due to parasitic side reactions was neglected in our estimation of the energy losses, as they are minor for the high coulombic efficiencies  $>99.9\%$  for both cell types in our study. The reversible heat (entropy) during a full charge/discharge cycle is considered close to zero (under the assumption that no net entropy can be generated in a reversibly cyclable cell) and therefore insignificant for the total energy loss.

For the evaluation of the energy losses, a C/10 charge/discharge cycle with and without intermittent 1 h OCV rest periods was carried out. The LMR-NCM pouch cells were cycled in a voltage range of 2.0–4.6 V and the NCA pouch cells in a voltage range of 3.0–4.3 V, the results are displayed in Fig. 4. Clearly visible is the pronounced hysteresis of the voltage profile of the LMR-NCM cells. When OCV rest periods are added to the C/10 cycling, represented by the red lines, the purely resistive part is omitted. The cell voltage is allowed

**Table III.** Specific CAM capacity, mean cell discharge voltage, and gravimetric cell-level energy density of the LMR-NCM and NCA pouch cells. The values for the C-rates were referenced to their mean C/10 value and the corresponding standard deviation, based on the data shown in Fig. 2.

	Cell type	C/5	C/2	1C	2C	3C
Specific capacity	LMR-NCM	100.4 ± 2.9 %	97.6 ± 2.8 %	93.5 ± 2.7 %	87.8 ± 2.5 %	77.3 ± 2.2 %
	NCA	97.9 ± 1.1 %	94.4 ± 1.1 %	89.6 ± 1.0 %	76.7 ± 0.9 %	58.8 ± 0.7 %
Mean dis. voltage	LMR-NCM	98.5 ± 0.2 %	95.5 ± 0.2 %	91.8 ± 0.2 %	85.9 ± 0.2 %	81.1 ± 0.2 %
	NCA	99.7 ± 0.1 %	98.6 ± 0.1 %	96.8 ± 0.1 %	93.9 ± 0.1 %	91.6 ± 0.1 %
Energy density	LMR-NCM	99.1 ± 5.1 %	93.3 ± 4.8 %	87.0 ± 4.5 %	76.7 ± 4.0 %	63.7 ± 3.3 %
	NCA	97.7 ± 3.2 %	93.1 ± 3.0 %	88.0 ± 2.8 %	73.0 ± 2.4 %	54.6 ± 1.8 %

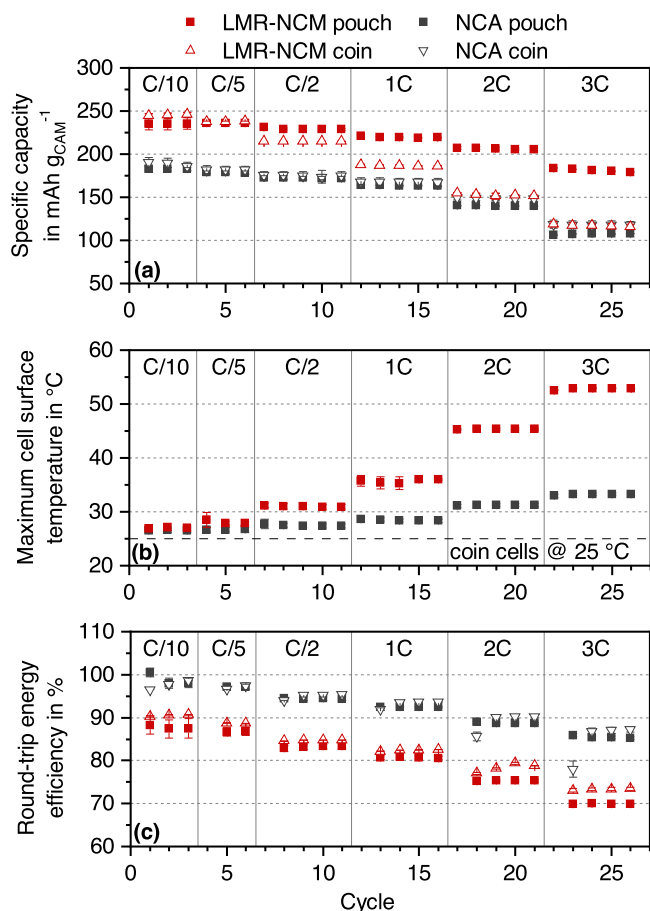


**Figure 3.** (a) Specific capacity related to the CAM mass of the LMR-NCM and NCA pouch cells in comparison to the laboratory coin cell measurements (all with graphite anodes), (b) maximum temperature measured on the surface of the pouch cells within the cell holder, and (c) round-trip energy efficiency calculated from the ratio of charge and discharge energy in a given cycle (note that the first cycle for each new C-rate setting is omitted). The pouch cell data correspond to those depicted in Fig. 2. The error bars for the coin cell measurements (barely visible) represent the standard deviation between 3 individual coin cells of each type.

to relax and the tips of the red curve mark the OCV profile after 1 h rest periods. A connection of these tips leave the gray shaded area that indicates the energy lost due to the LMR-NCM material hysteresis. The voltage profile of the NCA cells showed a minor

hysteresis, which almost vanished completely when OCV rest periods were added to the cycling procedure. For this reason, the gray area in Fig. 4b is quasi not visible and appears as the dotted gray line. Via integration of the C/10 charge/discharge cycle, the energy loss  $\Delta E_{\text{tot}}$  can be derived.<sup>26</sup>

$$\Delta E_{\text{tot}} = \oint I V dt \quad [4]$$

Here,  $I$  and  $V$  refer to the cell current and voltage, respectively. An integration of the gray shaded areas in Fig. 4 yields  $\Delta E_{\text{OCV}}$ .  $\Delta E_{\text{R}}$  is then calculated using Eq. 3 and  $\Delta E_{\text{tot}}$  determined from the black dashed lines in Fig. 4, using Eq. 4. The results are listed in Table V. These energy values, obtained by integration of the voltage curve of a single pouch cell of each type, are in good agreement with the measured C/10 round-trip efficiencies during the rate capability test, as stated in Table IV ( $87.5\% \pm 2.2\%$  for the LMR-NCM and  $98.1\% \pm 1.1\%$  for the NCA pouch cells).

The total energy  $\Delta E_{\text{tot}}$  that was lost over one C/10 charge/discharge cycle was substantially less for the NCA pouch cell, accounting for 2.3% of the charge energy  $E_{\text{CH}}$ . In contrast, the LMR-NCM cell lost 13.5% of the charge energy. More than a third of the total losses in the LMR-NCM cells at C/10 could be attributed to the intrinsic LMR-NCM material OCV hysteresis, whereas the ratio  $\Delta E_{\text{OCV}}/\Delta E_{\text{tot}}$  was only 7% for the NCA cells. The NCA voltage hysteresis was almost only generated by overpotential contributions ( $\Delta E_{\text{R}}$ ).

The energy lost due to the OCV hysteresis of the LMR-NCM pouch cells caused the pronounced temperature rise visible in Fig. 3b. For lower discharge currents, there was enough time to dissipate the excess heat to the cell holders and the ambient air. If the same energy is released in a short time period, it cannot dissipate fast enough, resulting in an increasing cell temperature. The OCV voltage hysteresis of LMR-NCM and the resulting energy inefficiency are major drawbacks for commercialization and are thus in the focus of current research.<sup>26</sup> Regarding the discharge capacities and the round-trip energy efficiencies in the rate capability test, LMR-NCM is rather suited for high energy than high power applications.

**Cycling behavior.**—In the aging study (see Figs. 5 and 6), the large-format LMR-NCM and NCA pouch cells were evaluated with regards to their cycling behavior, using diagnostic checkups every 25 cycles. The dashed lines in Figs. 5a and 5c mark the 80% state-of-health (SOH) thresholds for the specific capacity and energy density, referenced to 80% of the initial capacity and cell energy density during the C/2 discharge in the rate capability test (i.e., 80% of the values in cycle 7 shown in Figs. 2a and 2c). With ongoing cycling, both the LMR-NCM and the NCA cells showed a gradual decline in their specific capacity.

**Table IV.** Mean round-trip energy efficiencies  $\eta$  of the LMR-NCM and NCA pouch cells (data shown in Figs. 2 and 3), listed here for the third cycle of each discharge C-rate. The details of the discharge rate capability test are given in Table II.

Type	DCH C-rate	$E_{\text{CH}}$	$E_{\text{DCH}}$	$\Delta E_{\text{tot}}$	$\eta$
LMR-NCM	C/10	26.6 Wh	23.3 Wh	3.33 Wh	$87.5\% \pm 2.2\%$
	C/5	26.2 Wh	22.7 Wh	3.46 Wh	$86.8\% \pm 1.0\%$
	C/2	25.5 Wh	21.2 Wh	4.31 Wh	$83.1\% \pm 0.6\%$
	1C	24.2 Wh	19.5 Wh	4.64 Wh	$80.8\% \pm 0.5\%$
	2C	22.7 Wh	17.1 Wh	5.62 Wh	$75.3\% \pm 0.3\%$
	3C	20.3 Wh	14.2 Wh	6.10 Wh	$70.0\% \pm 0.1\%$
NCA	C/10	21.9 Wh	21.5 Wh	0.42 Wh	$98.1\% \pm 1.1\%$
	C/5	21.4 Wh	20.8 Wh	0.62 Wh	$97.1\% \pm 0.7\%$
	C/2	20.9 Wh	19.8 Wh	1.17 Wh	$94.4\% \pm 0.4\%$
	1C	20.0 Wh	18.5 Wh	1.51 Wh	$92.4\% \pm 0.2\%$
	2C	17.3 Wh	15.3 Wh	1.94 Wh	$88.7\% \pm 0.3\%$
	3C	13.5 Wh	11.5 Wh	1.96 Wh	$85.4\% \pm 0.3\%$

CH—charge, DCH—discharge, tot—total.

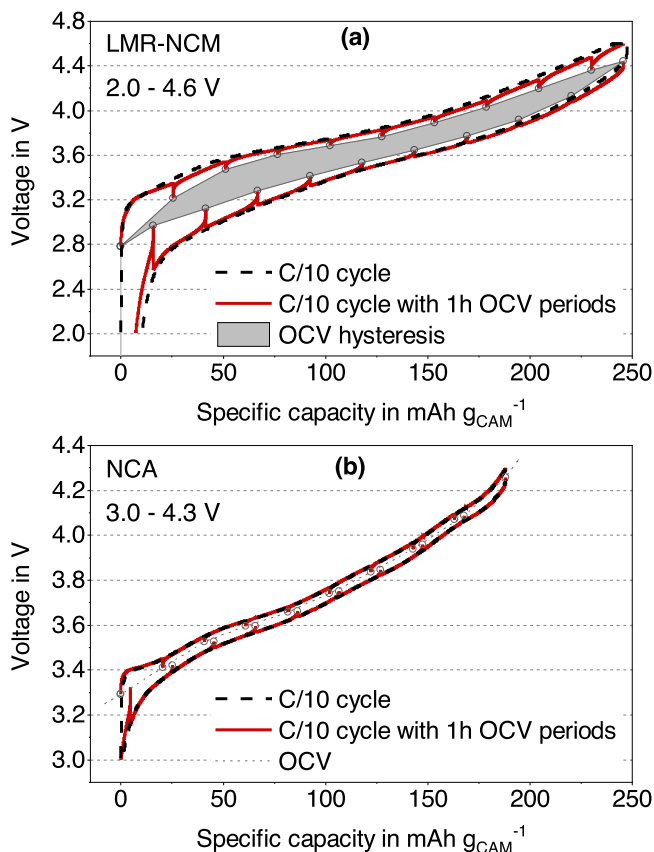


**Figure 4.** C/10 cycle procedures with and without 1 h OCV rest periods (see Table II) of an (a) LMR-NCM (2.0–4.6 V) and a (b) NCA (3.0–4.3 V) pouch cell at an ambient temperature of 25 °C.

After approximately 250 cycles, too much gas was generated in the LMR-NCM pouch cells, which caused a rupture of the pouch foil. The strong gassing of the LMR-NCM cells likely derives from two effects: i) the oxidative decomposition of the electrolyte due to its reaction with released lattice oxygen at the very high degrees of delithiation of the LMR-NCM at 100% SOC<sup>43</sup>; ii) the gradual thermal decomposition of FEC,<sup>44</sup> which is particularly problematic for electrolytes with high FEC content. While we did not determine the gas composition, the literature suggests the evolution of mostly CO<sub>2</sub> at room temperature and over a few cycles with FEC based electrolytes,<sup>36,45</sup> whereas at elevated temperatures and over extended cycling in FEC/DEC (2:8 by volume) electrolyte also substantial amounts of H<sub>2</sub> were observed.<sup>46</sup> Even though the electrochemical behavior of the cells was still stable, the tests were stopped for safety reasons.

The NCA cells showed a more stable cycling behavior. For a better comparison of the two active materials, the NCA cell data are only plotted up to 300 cycles in Fig. 5; an overview of all the data up to 1600 cycles for the NCA pouch cells and up to 1000 cycles for the NCA coin cells is given in the Appendix in Fig. A-2, indicating the state-of-the-art performance of the large-format multilayer pouch cells. While the upscaling from coin to pouch cells for a state-of-the-art reference material is adequate, effects related to temperature and

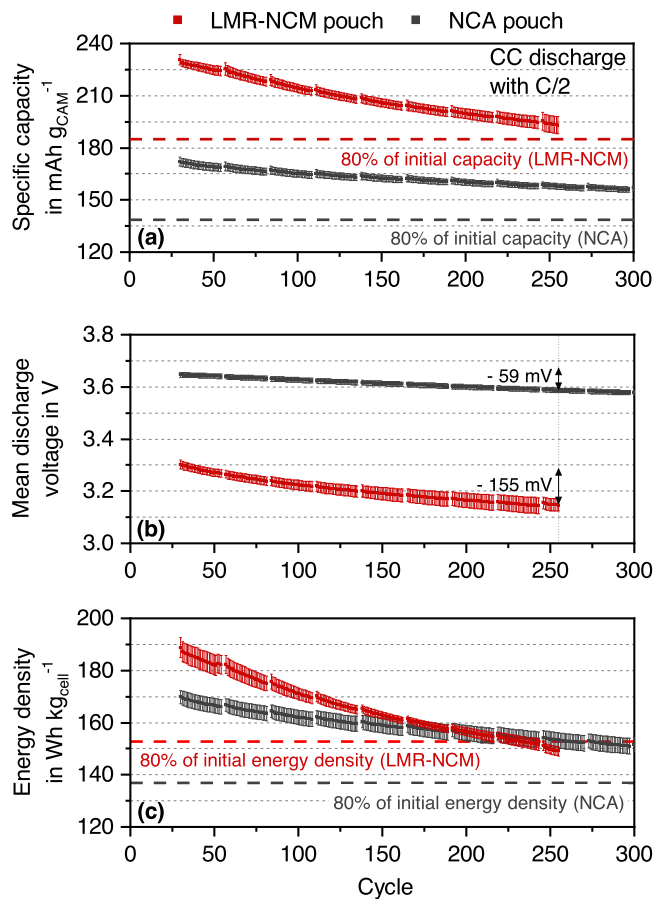


**Figure 5.** Cycle stability of the LMR-NCM and NCA pouch cells with regards to their (a) specific capacity related to the CAM mass, (b) mean cell discharge voltage, and (c) energy density related to the total mass of the cell. The cells were charged and discharged with a C/2 CC procedure including a CV phase at the end of charge at an ambient temperature of 25 °C in the voltage windows 2.0–4.6 V for LMR-NCM and 3.0–4.3 V for NCA, respectively (see Table II). Shown are the average values from 6 LMR-NCM and 5 NCA pouch cells, with error bars representing the standard deviation. The 80% initial capacity and energy density values marked by the dashed horizontal lines are referenced to the respective values in cycle 7 shown in Figs. 2a and 2c.

gas evolution that occur in LMR-NCM cells can clearly not be appropriately predicted from coin cell data, as they are operated isothermally and do not capture cell rupture effects from extensive gassing. Furthermore, small-scale laboratory cells generally have a higher electrolyte to active material ratio<sup>35</sup> that affects the aging behavior, which likely explains the slightly better capacity retention of the NCA coin vs NCA pouch cells (see Fig. A-2).

The specific capacity of the LMR-NCM pouch cells decreased faster, but remained higher than for the NCA pouch cells as shown in Fig. 5a. An extrapolation of the specific capacity of the LMR-NCM cells projects a crossover with the 80% threshold at approximately 350 cycles, as seen in Fig. A-1 in the Appendix. The NCA cells reached this point after 980 cycles (see Fig. A-2), as is also listed in Table VI. The aging behavior of both cell types is in good agreement

**Table V.** Energy losses derived from integrating the C/10 cycling curves. The total energy loss is divided into the hysteresis ( $\Delta E_{OCV}$ ) and the overpotential ( $\Delta E_R$ ) driven part.

Cell type	$\Delta E_{tot}$	$\Delta E_{OCV}$	$\Delta E_R$	$\Delta E_{OCV} : \Delta E_R$	$\eta$	$\Delta E_{tot}/E_{CH}$
LMR-NCM	3.54 Wh	1.31 Wh	2.23 Wh	37 : 63	86.5%	13.5%
NCA	0.50 Wh	0.04 Wh	0.46 Wh	7 : 93	97.7%	2.3%

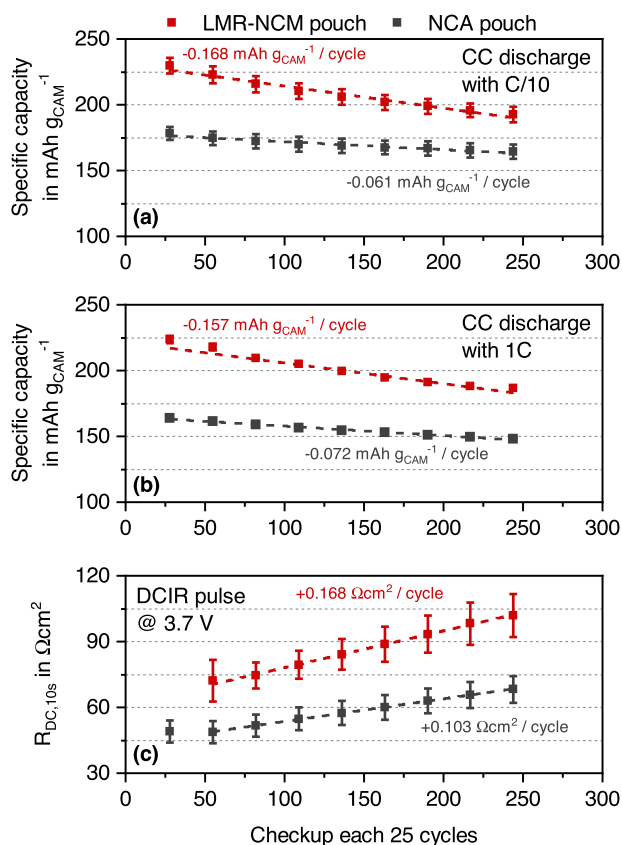


**Figure 6.** Checkup cycles (see Table II) of the LMR-NCM and NCA pouch cell tests shown in Fig. 5 with regards to their (a) specific C/10 discharge capacity related to the CAM mass, (b) specific 1C discharge capacity related to the CAM mass, and (c) DCIR for a 10 s C/2 discharge after charging the cells to a voltage of 3.7 V. The dashed lines indicate a linear regression of the mean values of the data points. In (a) and (c), average values from 6 LMR-NCM and 5 NCA pouch cells are shown, and the error bars represent the standard deviation. In (b), only average values of 2 cells of each type are shown, with the error bars representing their minimum/maximum values.

with published data on core-shell or surface-coated LMR-NCM in LMR-NCM/graphite cells<sup>11,12</sup> and of NCA in NCA/graphite cells.<sup>6,47–49</sup>

In Fig. 5b, the mean discharge voltage of the NCA cells showed a decrease of 59 mV after 255 cycles, which was less pronounced than the loss of 155 mV of the LMR-NCM cells. Voltage fading during prolonged cycling is a known issue of LMR-NCM and is caused by structural reordering from a layered to a spinel-like structure.<sup>11,12,27,50–53</sup> This has an additional, negative impact on the energy density decay displayed in Fig. 5c. In the beginning of the cycle-life test, the LMR-NCM cells offered a 11% higher cell energy density, but due to their faster degradation, their cell energy density became the same as that of the NCA cells at cycle 210. After 230 cycles, the LMR-NCM cells reached their 80% SOH criterion (red dashed line in Fig. 5c), whereas the NCA cells could be cycled 710 times until they reached 80% SOH (gray dashed line in Fig. 5c). The number of cycles up to 80% SOH with regards to their specific capacity and energy density for the two cell types are summarized in Table VI. Note that the LMR-NCM cells were charged to 4.6 V while the NCA cells were only charged to 4.3 V. At such high voltages, the electrolyte stability plays an important role and determines the aging behavior of these cells. Electrolyte oxidation at the cathode was probably one cause for an accelerated aging.<sup>36,43,45</sup> While higher temperatures also lead to an accelerated aging of lithium-ion cells,<sup>47,54–57</sup> this would not explain the comparatively faster degradation of the LMR-NCM cells since their average surface temperature during this aging test at C/2 of 29 °C (max. 31 °C) was similar to the 27 °C of that of the NCA cells (max. 28 °C).

**Table VI.** C/2 cycling stability defined by the 80% SOH criterion of the LMR-NCM and NCA pouch cells based on the data shown in Fig. 5.

80% SOH	LMR-NCM	NCA
Specific capacity	350 cycles <sup>a)</sup>	980 cycles
Energy density	230 cycles	710 cycles

a) extrapolation, see Fig. A-1 in the Appendix.

During the checkup cycles, the remaining capacity was assessed by a C/10 cycle, displayed in Fig. 6a. By applying a lower current, the cell polarization due to internal resistances, e.g., caused by growing passive layers or contact losses, is less. The influence of the internal resistance buildup on the capacity was evaluated with an additional 1C discharge, as seen in Fig. 6b. As described in the experimental section, only two pouch cells of each type were stressed with the 1C cycling procedure and therefore smaller error bars appear in Fig. 6b. By comparing the capacity of the C/10 with the 1C discharge, the capacity fading of the LMR-NCM cells is essentially independent of the C-rate, which suggests that the main degradation mechanism is the loss of cyclable lithium (e.g., via electrolyte oxidation) rather than an impedance buildup, at least for discharge C-rates up to 1C. For the NCA cells, the capacity fading at 1C is only ≈20% faster than at C/10, again suggesting that this decrease is not dominated by an impedance buildup.

The DCIR method was used to determine the internal cell resistance, employing a discharge pulse after a relaxation time of 1 h at 3.7 V (see Table II), which corresponded to a SOC of about 40% for both cell types. The first checkup of the LMR-NCM cells before the aging study was measured at a different voltage and was therefore left out. Here it should be noted, however, that the cell resistance is a strong function of SOC and thus cell voltage for both LMR-NCM<sup>10</sup> and for NCA<sup>6</sup> with a minimum resistance at mid-range SOCs. Based on the cathode-resolved impedance of NCM-811,<sup>58</sup> this resistance versus SOC behavior reflects that of the CAM. Moreover, because of the strong voltage hysteresis for LMR-NCM, the resistance also depends on whether the cell was charged or discharged before applying a DCIR pulse.<sup>10</sup> While the LMR-NCM cells exhibited ≈2-fold higher resistances, the resistances of both cell types rose equally by ≈40% between the 50th and the 250th cycle.

Therefore, the faster capacity and cell energy density degradation of the LMR-NCM cells compared to the NCA cells is unlikely due to polarization effects. Instead, based on the similar capacity fading rates of C/10 and 1C for both cell types (Figs. 6a and 6b), the performance degradation seems to be due to a loss of cyclable lithium. That the latter would be more pronounced at the higher cathode potentials of the LMR-NCM cells is not surprising, enhanced by the reaction of the electrolyte with lattice oxygen at the high degrees of delithiation at 100% SOC for this material.<sup>43</sup> Therefore, a more stable electrolyte system is still required for LMR-NCM CAMs, particularly for elevated temperatures due to the thermal instabilities of FEC in combination with LiPF<sub>6</sub>.<sup>44,46</sup> Moreover, surface modifications of LMR-NCM materials could also reduce detrimental side reactions and improve the overall cycling stability.<sup>11,12</sup>

## Conclusions

In this study, the LMR-NCM cathode active material, offering a high reversible capacity of 250 mAh g<sup>-1</sup>, was employed with graphite anodes in large-format multilayer pouch cells, which were produced on a pilot scale production line. Comparable NCA/graphite pouch cells were produced and served as a reference for an evaluation of the performance of the LMR-NCM cells. The two pouch cell types were standardized to deliver an areal capacity of 2.3 mAh cm<sup>-2</sup> or a total capacity of 5.5 Ah at a 1C discharge rate.

The characteristics of both cell types were compared against each other in a discharge rate capability test and an aging test.

Distinct differences between the two cell types were the wider voltage window of the LMR-NCM cells with a lower cutoff voltage of 2.0 V and an upper cutoff voltage of 4.6 V as well as the hysteresis of the voltage profile between charge and discharge even at C/10, while the NCA cells were cycled between 3.0–4.3 V and showed almost no voltage hysteresis. The LMR-NCM cells exhibited a specific capacity of  $235 \text{ mAh g}^{-1}$  for low discharge currents  $\leq C/5$ , which amounted to a 30% increase compared to the  $180 \text{ mAh g}^{-1}$  of the NCA cells. However, because of the voltage hysteresis and the lower mean discharge voltage, the energy density of the LMR-NCM pouch cells was only  $\approx 11\%$  higher in comparison to the NCA cells.

The aging behavior was evaluated with a C/2 cycling test and initially showed a better performance of the LMR-NCM cells. However, both the specific capacity and the energy density showed a faster degradation, so that the LMR-NCM pouch cells were projected to reach their 80% SOH criterion with respect to the specific capacity after approximately 350 cycles, whereas the 80% of the initial energy density was reached after already 230 cycles, due to a faster voltage fading. On the other hand, these 80% SOH criteria were reached after 980 cycles and 710 cycles, respectively for the NCA cells. Checkup cycles including the measured cell resistances showed that the increasing cell resistance was not dominating the overall capacity decay, and that instead the performance degradation of both the LMR-NCM and the NCA cells is rather due to a loss of cyclable lithium. The overall cycle life of the LMR-NCM pouch cells was limited to  $\approx 250$  cycles due to cell rupture caused by the strong gassing of the LMR-NCM cells.

In conclusion, LMR-NCM proved to be a high capacitive CAM, which is comparatively cheap because of its high manganese share compared to cobalt and nickel. Long-term stability issues still have to be addressed, e.g., a surface treatment of LMR-NCM could bring improvements on the material level, and should be examined in combination with an adequate electrolyte system. Because of the heat accumulation for discharge rates above C/2, an application of LMR-NCM in large-format cells should be critically assessed together with the accompanying cooling system. This issue will be addressed in our future research. Generally, the material is more suited for high energy than high power applications.

### Acknowledgments

This work was financially supported by the German Federal Ministry of Education and Research (BMBF) under grant number 03XP0081 (ExZellTUM II) and 03XP0255 (ExZellTUM III). For the production of the large-format pouch cells, special thanks go to the battery production research team of iwB, in particular to Benedikt Stumper, Ajinkya Metkar, Nicolas Billot, Till Günther, Johannes Kriegler, Fabian Konwitschny, Celestine Singer, Hoda Mohseni, Sophie Grabmann, and Joscha Schnell. The authors gratefully acknowledge Tobias Teufl and Manuel Mendez from BASF SE for the helpful scientific discussions, Robin Schregle for his contribution to the CAD drawing of the cell holder, and Fabian Linsenmann for his critical feedback.

### Appendix

The measured cycling data of the LMR-NCM pouch cells was limited to approximately 250 cycles due to gassing induced rupture of the cells. To have an assessment of the 80% SOH criterion regarding the specific capacity of the cells, an extrapolation was carried out, yielding a projected crossover after approximately 350 cycles (see Fig. A-1). The following fitting function ( $R^2 = 0.9986$ ) was used for this extrapolation (see black line in Fig. A-1), with  $x$  representing the cycle number and  $y$  the specific capacity in  $\text{mAh g}_{\text{CAM}}^{-1}$ :

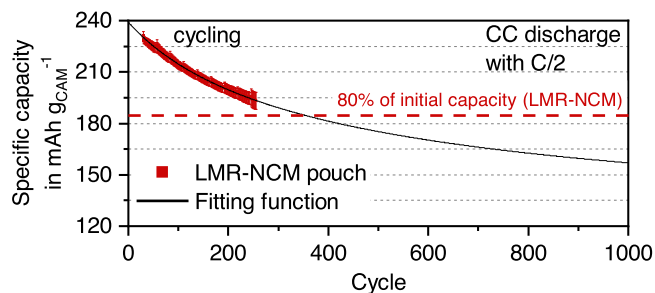


**Figure A-1.** Extrapolation of the specific capacity related to the mass of the active material during C/2 cycling of the LMR-NCM pouch cells.

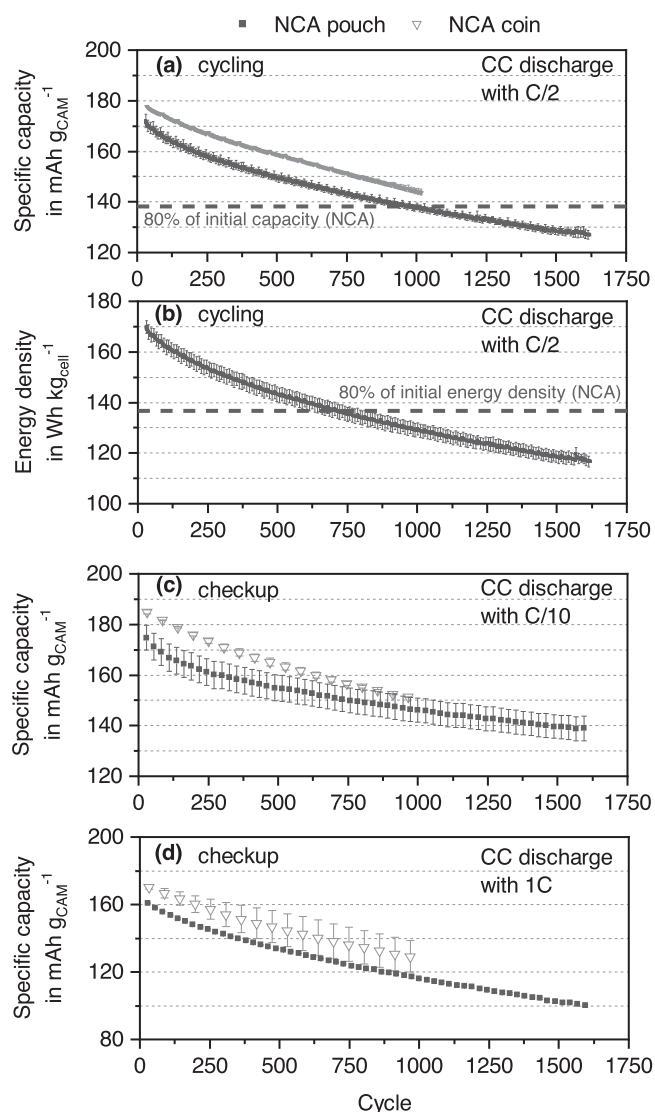


**Figure A-2.** Cycle stability including all cycles and checkups of the NCA pouch and coin cells. (a) Specific capacity related to the mass of the active material and (b) energy density related to the total mass of the cell during C/2 cycling (only displayed for the NCA pouch cells). (c) Specific C/10 discharge capacity and (d) specific 1C discharge capacity related to the mass of the active material during the checkups every 25 C/2 cycles. The cells were charged with a C/2 CC procedure including a CV phase at the end of charge at an ambient temperature of  $25^\circ\text{C}$  in the voltage window 3.0–4.3 V (see Table II).

$$y = \frac{2107}{\sqrt{218.8 + x}} + 96.61 \quad [\text{A-1}]$$

To allow for a more clear comparison between the LMR-NCM and the NCA cells, Fig. 5 only shows the initial 300 cycles for the NCA cells. The total cycling stability of the NCA pouch cells including the laboratory NCA coin cells is displayed in Fig. A-2. The coin cells were cycled up to 1000 cycles while the pouch cell aging test was carried out for over 1600 cycles. The energy density in Fig. A-2b is only displayed for the pouch cells, because this value is related to the total cell mass, which is not representative for coin cells.

## ORCID

Ludwig Kraft  <https://orcid.org/0000-0003-4324-426X>  
 Tanja Zünd  <https://orcid.org/0000-0002-1650-3636>  
 David Schreiner  <https://orcid.org/0000-0001-8035-0438>  
 Rebecca Wilhelm  <https://orcid.org/0000-0002-4161-5197>  
 Florian J. Günter  <https://orcid.org/0000-0002-5967-6801>  
 Hubert A. Gasteiger  <https://orcid.org/0000-0001-8199-8703>  
 Andreas Jossen  <https://orcid.org/0000-0003-0964-1405>

## References

- D. Andre, S.-J. Kim, P. Lamp, S. F. Lux, F. Maglia, O. Paschos, and B. Staszny, "Future generations of cathode materials: an automotive industry perspective." *Journal of Materials Chemistry A*, **3**, 6709 (2015).
- S.-T. Myung, F. Maglia, K.-J. Park, C. S. Yoon, P. Lamp, S.-J. Kim, and Y.-K. Sun, "Nickel-rich layered cathode materials for automotive lithium-ion batteries: achievements and perspectives." *ACS Energy Lett.*, **2**, 196 (2017).
- M. A. Hannan, M. M. Hoque, A. Mohamed, and A. Ayob, "Review of energy storage systems for electric vehicle applications: issues and challenges." *Renew. Sustain. Energy Rev.*, **69**, 771 (2017).
- R. Schmich, R. Wagner, G. Höppl, T. Placke, and M. Winter, "Performance and cost of materials for lithium-based rechargeable automotive batteries." *Nat. Energy*, **3**, 267 (2018).
- C. S. Yoon, K.-J. Park, U.-H. Kim, K. H. Kang, H.-H. Ryu, and Y.-K. Sun, "High-energy Ni-rich Li[Ni<sub>x</sub>Co<sub>1-x-y</sub>Mn<sub>1-x-y</sub>]O<sub>2</sub> cathodes via compositional partitioning for next-generation electric vehicles." *Chemistry of Materials*, **29**, 10436 (2017).
- R. Weber, A. J. Louli, K. P. Plucknett, and J. R. Dahn, "Resistance growth in lithium-ion pouch cells with LiNi<sub>0.80</sub>Co<sub>0.15</sub>Al<sub>0.05</sub>O<sub>2</sub> positive electrodes and proposed mechanism for voltage dependent charge-transfer resistance." *J. Electrochem. Soc.*, **166**, A1779 (2019).
- S. Hwang and E. A. Stach, "Using in situ and operando methods to characterize phase changes in charged lithium nickel cobalt aluminum oxide cathode materials." *J. Phys. D*, **53**, 113002 (2020).
- J. R. Croy, M. Balasubramanian, K. G. Gallagher, and A. K. Burrell, "Review of the U.S. department of energy's deep effort to understand voltage fade in Li- and Mn-rich cathodes." *Acc. Chem. Res.*, **48**, 2813 (2015).
- G. E. Blomgren, "The development and future of lithium ion batteries." *J. Electrochem. Soc.*, **164**, A5019 (2016).
- T. Teufl, D. Pritzl, S. Solchenbach, H. A. Gasteiger, and M. A. Mendez, "State of charge dependent resistance build-up in Li- and Mn-rich layered oxides during lithium extraction and insertion." *J. Electrochem. Soc.*, **166**, A1275 (2019).
- D. Becker, M. Börner, A. Friesen, S. Klein, U. Rodehorst, M. Diehl, M. Winter, T. Placke, and R. Schmich, "Towards high-performance Li-rich NCM—graphite cells by germanium-polymer coating of the positive electrode material." *J. Electrochem. Soc.*, **167**, 060524 (2020).
- J. Helbig, T. Beuse, V. Sizios, T. Placke, M. Winter, and R. Schmich, "Li—Mn-rich cathode materials with low-cobalt content and core-shell particle design for high-energy lithium ion batteries." *J. Electrochem. Soc.*, **167**, 060519 (2020).
- K. G. Gallagher and P. A. Nelson, "Manufacturing costs of batteries for electric vehicles." *Lithium-Ion Batteries: Advances and Applications*, ed. G. Pistoia (Elsevier, Amsterdam) p. 97 (2014).
- O. Gröger, H. A. Gasteiger, and J.-P. Suchsland, "Review—electromobility: batteries or fuel cells?" *J. Electrochem. Soc.*, **162**, A2605 (2015).
- A. Kwade, W. Haselrieder, R. Leithoff, A. Modlinger, F. Dietrich, and K. Droeder, "Current status and challenges for automotive battery production technologies." *Nat. Energy*, **3**, 290 (2018).
- UK Electric Vehicle and Battery Production Potential to 2040. March 2020. <https://faraday.ac.uk/publications/ev-economics-study/>.
- SMM Information & Technology Co, Ltd., Nickel price. Accessed 2/9/2021 <https://price.metal.com/Nickel>.
- SMM Information & Technology Co, Ltd., Manganese price. Accessed 2/9/2021 <https://price.metal.com/Manganese>.
- Y.-K. Sun, D.-J. Lee, Y. J. Lee, Z. Chen, and S.-T. Myung, "Cobalt-free nickel rich layered oxide cathodes for lithium-ion batteries." *ACS Applied Materials & Interfaces*, **5**, 11434 (2013).
- N. Zhang, N. Zaker, H. Li, A. Liu, J. Inglis, L. Jing, J. Li, Y. Li, G. A. Botton, and J. R. Dahn, "Cobalt-free nickel-rich positive electrode materials with a core-shell structure." *Chemistry of Materials*, **31**, 10150 (2019).
- H. Li, M. Cormier, N. Zhang, J. Inglis, J. Li, and J. R. Dahn, "Is cobalt needed in ni-rich positive electrode materials for lithium ion batteries?" *J. Electrochem. Soc.*, **166**, A429 (2019).
- W.-C. Chen, Y.-F. Song, C.-C. Wang, Y. Liu, D. T. Morris, P. A. Pianetta, J. C. Andrews, H.-C. Wu, and N.-L. Wu, "Study on the synthesis-microstructure-performance relationship of layered Li-excess nickel-manganese oxide as a Li-ion battery cathode prepared by high-temperature calcination." *Journal of Materials Chemistry A*, **1**, 10847 (2013).
- Trading Economics, Cobalt price. Accessed 2/9/2021 <https://tradingeconomics.com/commodity/cobalt>.
- Trading Economics, Lithium price. Accessed 2/9/2021 <https://tradingeconomics.com/commodity/lithium>.
- Trading Economics, Aluminum price. Accessed 2/9/2021 <https://tradingeconomics.com/commodity/aluminum>.
- G. Assat, S. L. Glazier, C. Delacourt, and J.-M. Tarascon, "Probing the thermal effects of voltage hysteresis in anionic redox-based lithium-rich cathodes using isothermal calorimetry." *Nat. Energy*, **4**, 647 (2019).
- N. Leifer, T. Penki, R. Nanda, J. Grinblat, S. Luski, D. Aurbach, and G. Goobes, "Linking structure to performance of Li<sub>1.2</sub>Mn<sub>0.54</sub>Ni<sub>0.13</sub>Co<sub>0.13</sub>O<sub>2</sub> (Li and Mn rich NMC) cathode materials synthesized by different methods." *Physical Chemistry Chemical Physics: PCCP*, **22**, 9098 (2020).
- J. B. Quinn, T. Waldmann, K. Richter, M. Kasper, and M. Wohlfahrt-Mehrens, "Energy density of cylindrical li-ion cells: a comparison of commercial 18650 to the 21700 cells." *J. Electrochem. Soc.*, **165**, A3284 (2018).
- M. J. Lain, J. Brandon, and E. Kendrick, "Design strategies for high power vs high energy lithium ion cells." *Batteries*, **5**, 64 (2019).
- Y. Ding, Z. P. Cano, A. Yu, J. Lu, and Z. Chen, "Automotive li-ion batteries: current status and future perspectives." *Electrochemical Energy Reviews*, **2**, 1 (2019).
- H. Popp, N. Zhang, M. Jahn, M. Arrinda, S. Ritz, M. Faber, D. U. Sauer, P. Azais, and I. Cendoya, "Ante-mortem analysis, electrical, thermal, and ageing testing of state-of-the-art cylindrical lithium-ion cells." *E & I Elektrotechnik und Informationstechnik*, **8**, 104 (2020).
- M. Singh, J. Kaiser, and H. Hahn, "Thick electrodes for high energy lithium ion batteries." *J. Electrochem. Soc.*, **162**, A1196 (2015).
- J. Sturm, A. Rheinfield, I. Zilberman, F. B. Spingler, S. Kosch, F. Frie, and A. Jossen, "Modeling and simulation of inhomogeneities in a 18650 nickel-rich, silicon-graphite lithium-ion cell during fast charging." *Journal of Power Sources*, **412**, 204 (2019).
- G. Reinhart, T. Zeilinger, J. Kurfer, M. Westermeier, C. Thiemann, M. Glonegger, M. Wunderer, C. Tammer, M. Schweier, and M. Heinz, "Research and demonstration center for the production of large-area lithium-ion cells." *Future Trends in Production Engineering*, ed. G. Schuh, R. Neugebauer, and E. Uhlmann (Springer, Berlin, Heidelberg) Vol. 12, p. 3 (2013).
- D. Schreiner et al., "Comparative evaluation of lmr-ncm and nca cathode active materials in multilayer lithium-ion pouch cells—part I: production, electrode characterization, and formation." *J. Electrochem. Soc.*, **168**, 030507 (2021).
- T. Teufl, B. Strehle, P. Müller, H. A. Gasteiger, and M. A. Mendez, "Oxygen release and surface degradation of Li- and Mn-rich layered oxides in variation of the Li<sub>2</sub>MnO<sub>3</sub> content." *J. Electrochem. Soc.*, **165**, A2718 (2018).
- A. Guéguen, C. Bolli, M. A. Mendez, and E. J. Berg, "Elucidating the reactivity of tris(trimethylsilyl)phosphite and tris(trimethylsilyl)phosphate additives in carbonate electrolytes—a comparative online electrochemical mass spectrometry study." *ACS Appl. Energy Mater.*, **3**, 290 (2020).
- S.-H. Kang, W.-S. Yoon, K.-W. Nam, X.-Q. Yang, and D. P. Abraham, "Investigating the first-cycle irreversibility of lithium metal oxide cathodes for Li batteries." *J. Mater. Sci.*, **43**, 4701 (2008).
- S. S. Zhang, "Identifying rate limitation and a guide to design of fast-charging Li-ion battery." *InfoMat*, **2**, 942 (2020).
- J. Zheng, W. Shi, M. Gu, J. Xiao, P. Zuo, C. Wang, and J.-G. Zhang, "Electrochemical kinetics and performance of layered composite cathode material Li[Li<sub>0.2</sub>Ni<sub>0.2</sub>Mn<sub>0.6</sub>]O<sub>2</sub>." *J. Electrochem. Soc.*, **160**, A2212 (2013).
- W. Mao, G. Ai, Y. Dai, Y. Fu, X. Song, H. Lopez, and V. Battaglia, "Nature of the impedance at low states of charge for high-capacity, lithium and manganese-rich cathode materials." *J. Electrochem. Soc.*, **163**, A3091 (2016).
- P. Meister, H. Jia, J. Li, R. Kloepsch, M. Winter, and T. Placke, "Best practice: performance and cost evaluation of lithium ion battery active materials with special emphasis on energy efficiency." *Chemistry of Materials*, **28**, 7203 (2016).
- J. Wandt, A. T. Freiberg, A. Ogdronik, and H. A. Gasteiger, "Singlet oxygen evolution from layered transition metal oxide cathode materials and its implications for lithium-ion batteries." *Mater. Today*, **21**, 825 (2018).
- K. Kim, I. Park, S.-Y. Ha, Y. Kim, M.-H. Woo, M.-H. Jeong, W. C. Shin, M. Ue, S. Y. Hong, and N.-S. Choi, "Understanding the thermal instability of fluoroethylene carbonate in LiPF<sub>6</sub>-based electrolytes for lithium ion batteries." *Electrochimica Acta*, **225**, 358 (2017).
- T. Teufl, D. Pritzl, P. Krieg, B. Strehle, M. A. Mendez, and H. A. Gasteiger, "Operating EC-based electrolytes with Li- and Mn-rich NCMs: the role of O<sub>2</sub>-release on the choice of the cyclic carbonate." *J. Electrochem. Soc.*, **167**, 110505 (2020).
- T. Teufl, D. Pritzl, S. Solchenbach, M. A. Mendez, and H. A. Gasteiger, (2021), Thermal stability of FEC-based electrolytes for high-voltage Li-ion batteries, Manuscript in preparation.
- M. Uitz, M. Stenad, S. Breuer, C. Täubert, T. Traußnig, V. Hennige, I. Hanzu, and M. Wilkening, "Aging of Tesla's 18650 lithium-ion cells: correlating solid-electrolyte-interphase evolution with fading in capacity and power." *J. Electrochem. Soc.*, **164**, A3503 (2017).
- S. Hildebrand, C. Vollmer, M. Winter, and F. M. Schappacher, "Al<sub>2</sub>O<sub>3</sub>, SiO<sub>2</sub> and TiO<sub>2</sub> as coatings for Safer LiNi<sub>0.8</sub>Co<sub>0.15</sub>Al<sub>0.05</sub>O<sub>2</sub> cathodes: electrochemical

- performance and thermal analysis by accelerating rate calorimetry." *J. Electrochem. Soc.*, **164**, A2190 (2017).
49. J. Li, J. Harlow, N. Stakheiko, N. Zhang, J. Paulsen, and J. Dahn, "Dependence of cell failure on cut-off voltage ranges and observation of kinetic hindrance in  $\text{LiNi}_{0.8}\text{Co}_{0.15}\text{Al}_{0.05}\text{O}_2$ ." *J. Electrochem. Soc.*, **165**, A2682 (2018).
50. D. Mohanty, A. S. Sefat, J. Li, R. A. Meisner, A. J. Rondinone, E. A. Payzant, D. P. Abraham, D. L. Wood, and C. Daniel, "Correlating cation ordering and voltage fade in a lithium-manganese-rich lithium-ion battery cathode oxide: a joint magnetic susceptibility and TEM study." *Physical Chemistry Chemical Physics: PCCP*, **15**, 19496 (2013).
51. D. Mohanty, J. Li, D. P. Abraham, A. Huq, E. A. Payzant, D. L. Wood, and C. Daniel, "Unraveling the voltage-fade mechanism in high-energy-density lithium-ion batteries: origin of the tetrahedral cations for spinel conversion." *Chemistry of Materials*, **26**, 6272 (2014).
52. M. Sathya et al., "Origin of voltage decay in high-capacity layered oxide electrodes." *Nat. Mater.*, **14**, 230 (2015).
53. K. Kleiner, B. Strehle, A. R. Baker, S. J. Day, C. C. Tang, I. Buchberger, F.-F. Chesneau, H. A. Gasteiger, and M. Piana, "Origin of high capacity and poor cycling stability of Li-rich layered oxides: a long-duration in situ synchrotron powder diffraction study." *Chemistry of Materials*, **30**, 3656 (2018).
54. M. Wohlfahrt-Mehrens, C. Vogler, and J. Garche, "Aging mechanisms of lithium cathode materials." *Journal of Power Sources*, **127**, 58 (2004).
55. J. Vetter, P. Novák, M. R. Wagner, C. Veit, K.-C. Möller, J. O. Besenhard, M. Winter, M. Wohlfahrt-Mehrens, C. Vogler, and A. Hammouche, "Ageing mechanisms in lithium-ion batteries." *Journal of Power Sources*, **147**, 269 (2005).
56. Y. Wu, P. Keil, S. F. Schuster, and A. Jossen, "Impact of temperature and discharge rate on the aging of a  $\text{LiCoO}_2/\text{LiNi}_{0.8}\text{Co}_{0.15}\text{Al}_{0.05}\text{O}_2$  lithium-ion pouch cell." *J. Electrochem. Soc.*, **164**, A1438 (2017).
57. P. Keil and A. Jossen, "Impact of dynamic driving loads and regenerative braking on the aging of lithium-ion batteries in electric vehicles." *J. Electrochem. Soc.*, **164**, A3081 (2017).
58. F. Friedrich, B. Strehle, A. T. S. Freiberg, K. Kleiner, S. J. Day, C. Erk, M. Piana, and H. A. Gasteiger, "Choice-capacity fading mechanisms of NCM-811 cathodes in lithium-ion batteries studied by X-ray diffraction and other diagnostics." *J. Electrochem. Soc.*, **166**, A3760 (2019).



### 4.3 Investigations on the Origin of the LMR-NCM OCV-Hysteresis

The paper with the title “Correlating the Voltage Hysteresis in Li- and Mn-Rich Layered Oxides to Reversible Structural Changes by Using X-Ray and Neutron Powder Diffraction” is presented in this section. The manuscript was submitted in October 2021 and published in February 2022 as a peer-reviewed publication in the Journal of the Electrochemical Society. It is available as an “open access” article and distributed under the terms of the Creative Commons Attribution 4.0 License (CC BY). The main findings of this study were presented by Benjamin Strehle at the 236<sup>th</sup> Meeting of the Electrochemical Society (2019) in Atlanta, USA and by Tanja Zünd at the Battery Gordon Research Conference (2020) in Ventura, USA. The permanent web link to this article can be found under: <https://iopscience.iop.org/article/10.1149/1945-7111/ac4540/meta>

In Section 0, the pronounced voltage hysteresis was addressed between the charge and discharge reaction. The state of charge (SOC) was found to differ by up to one third of the overall capacity at the same measured voltage and has to be considered when addressing the energy efficiency and the thermal management of LMR-NCM cells. This voltage hysteresis is largely independent of the applied current and is maintained under open circuit voltage (OCV) conditions and is therefore also called OCV-hysteresis.<sup>116</sup> In the literature, the origin of this hysteresis phenomenon is mainly ascribed to (i) the reversible migration of transition metals between the TM- and the Li layer,<sup>72</sup> (ii) the oxygen redox,<sup>117</sup> or (iii) the combination of both processes.<sup>62,118</sup>

*In situ* laboratory X-ray powder diffraction (L-XPD) was applied to monitor the lattice parameter evolution within the initial three charge/discharge cycles. It was found, that the unit cell volume vs. SOC showed an analogous hysteresis behaviour between the charge and discharge direction as the OCV. Furthermore, by dividing the unit cell volume into the lattice parameter *a* (along the layer) and *c* (across the layers) it was found that they follow the expected dependence of the cationic and anionic redox processes, as known from stoichiometric NCMs.<sup>119,121</sup> By varying the degree of over-lithiation of LMR-NCMs and by performing window-opening experiments, it was found that the extent of OCV-and the hysteresis of the lattice

parameters increases with the passed-through SOC window. By correlating the lattice parameters to their corresponding OCV instead of the SOC, the hysteresis was found to vanish and a linear volume to OCV relationship of  $-2 \text{ \AA}^3/\text{V}$  uniquely describes the three LMR-NCM materials that only differ in their degree of over-lithiation. By Rietveld refinements of *ex situ* LMR-NCM samples of electrodes cycled to different SOC, it was hoped to be able to explain the above described hysteresis phenomena, by finding a correlation of the lattice parameter hysteresis with TM migration. In a first step, the lattice parameter  $c$  was divided into its TM environment  $h_{\text{TM}}$  and its Li environment  $h_{\text{Li}}$ . While  $h_{\text{TM}}$  followed the behaviour of  $a$ ,  $h_{\text{Li}}$  dominated the  $c$  lattice parameter and showed an almost inverse behaviour. The observation confirmed that the lattice hysteresis evolves uniformly around the TM layer. However, the quantification of all TMs (i.e., Ni, Co, and Mn) and Li on two layers with just one dataset is not recommended, as the sum of all scattering factors is used and therefore the analysis would suffer from many inter-dependencies. By allowing just one TM and Li to migrate at the same time, the data from both, X-ray and neutron powder diffraction (NPD) were fitted simultaneously. The Rietveld refinements revealed several pitfalls, for example that the overall scattering intensity of the TM layer in comparison to the Li and O layers was quite low in NPD as the stoichiometric summation of the negative and positive scattering lengths of the TMs resulted in a near-zero value. Moreover, the XPD is biased by the choice of the atomic form factors, which would require knowing the exact oxidation states of the elements that are not known when considering the possibility of anionic redox. In the article, this and several other challenges were critically discussed, and different structural models and refinement strategies were compared. By ultimately refining the Ni amount on the Li layer at four different SOC within the second cycle, a maximum of 2.4% Ni migration was found that however, did not correlate with the unit cell volume or voltage hysteresis. At the same time, the uncertainty of the evaluated structural parameters was rather high. Therefore, it had to be concluded that there is either no correlation between the Ni migration and the voltage hysteresis or that the Ni migration needed to explain the hysteresis would be  $< 2.5\%$ ; in the latter case a more precise quantification of the SOC-dependent Ni migration would be required.

Author contributions

B.S. and T.Z. conducted all the diffraction experiments and analysed the data. S.S. was in charge of the DFT simulations. A.K. and T.Z. developed the multilayer pouch cell setup. V.B. supported the NPD experiments as a beamline scientist of the SPODI instrument. The manuscript was written by B.S. and T.Z. and further revised by the co-authors. B.S. and T.Z. contributed equally to this work as co-sharing first authors.





# Correlating the Voltage Hysteresis in Li- and Mn-Rich Layered Oxides to Reversible Structural Changes by Using X-ray and Neutron Powder Diffraction

Benjamin Strehle,<sup>1,\*</sup> Tanja Zünd,<sup>1,\*</sup> Sabrina Siculo,<sup>2</sup> Aleksandr Kiessling,<sup>1</sup> Volodymyr Baran,<sup>3</sup> and Hubert A. Gasteiger<sup>1,\*\*</sup>

<sup>1</sup>Chair of Technical Electrochemistry, Department of Chemistry and Catalysis Research Center, Technical University of Munich, D-85748 Garching, Germany

<sup>2</sup>BASF SE, Quantum Chemistry for Solid State Group, D-67056 Ludwigshafen, Germany

<sup>3</sup>Heinz Maier-Leibnitz Zentrum, Technical University of Munich, D-85748 Garching, Germany

Li- and Mn-rich layered oxides (LMR-NCMs) are promising cathode active materials (CAMs) in future lithium-ion batteries (LIBs) due to their high energy density. However, the material undergoes a unique open circuit voltage (OCV) hysteresis between charge and discharge after activation, which compromises its roundtrip energy efficiency and affects the thermal management requirements for a LIB system. The hysteresis is believed to be caused by transition metal (TM) migration and/or by oxygen redox activities. Using in-situ X-ray powder diffraction (XPD), we monitor the lattice parameters of over-lithiated NCMs during the initial cycles and show that also the lattice parameters feature a distinct path dependence. When correlated to the OCV instead of the state of charge (SOC), this hysteresis vanishes for the unit cell volume and gives a linear correlation that is identical for different degrees of over-lithiation. We further aimed at elucidating the role of TM migration on the hysteresis phenomena by applying joint Rietveld refinements to a series of ex-situ XPD and neutron powder diffraction (NPD) samples. We critically discuss the limitations of this approach and compare the results with DFT simulations, showing that the quantification of TM migration in LMR-NCMs by diffraction is not as straightforward as often believed.

© 2022 The Author(s). Published on behalf of The Electrochemical Society by IOP Publishing Limited. This is an open access article distributed under the terms of the Creative Commons Attribution 4.0 License (CC BY, <http://creativecommons.org/licenses/by/4.0/>), which permits unrestricted reuse of the work in any medium, provided the original work is properly cited. [DOI: 10.1149/1945-7111/ac4540]



Manuscript submitted October 2, 2021; revised manuscript received November 23, 2021. Published February 22, 2022. This was paper 346 presented at the Dallas, Texas, Meeting of the Society, May 26–May 30, 2019.

Supplementary material for this article is available [online](#)

Driven by mobile applications like electric vehicles (EVs),<sup>1–3</sup> the demand for affordable lithium-ion batteries with a higher energy density is rising. Targets of 100 \$/kWh are necessary to achieve comparable vehicle costs at acceptable driving ranges.<sup>4,5</sup> The only way to reach these ambitious goals is an increase of battery energy density by increasing the specific capacity of the active materials and by using abundant and inexpensive materials. On the cathode side, lithium- and manganese-rich layered oxides, often abbreviated as LMR-NCMs, provide high specific capacities of up to 250 mAh g<sup>-1</sup> at low material costs that are achieved by replacing a major part of the conventionally used nickel with inexpensive manganese.<sup>6,7</sup> The specific capacity increase of the so-called “over-lithiated” NCMs compared to conventional NCMs originates from a slight rearrangement of the layered structure, Li[Li<sub>δ</sub>TM<sub>1-δ</sub>]O<sub>2</sub> (with TM = Mn, Ni, and Co), in the pristine cathode active materials (CAMs). Stoichiometric NCMs with  $\delta$  being close to 0 offer a theoretical specific capacity of around 277 mAh g<sup>-1</sup>, but due to their structural instabilities at lithium contents of  $x_{Li} < 0.2$  that are caused by the release of lattice oxygen and due to their first cycle efficiency of maximum 90%, their practically usable specific capacity remains limited to approximately 200 mAh g<sup>-1</sup>.<sup>8,9</sup> On the other hand, in LMR-NCMs, a part of the transition metals (TMs) in the TM layer is replaced by lithium,<sup>10–12</sup> leading to an over-lithiated structure with theoretical specific capacities of 346–377 mAh g<sup>-1</sup> for  $\delta = 0.14–0.20$ .<sup>13</sup> In contrast to stoichiometric NCMs, the over-lithiated structure can be reversibly cycled beyond the onset of oxygen release down to  $x_{Li} \approx 0.1$  and delivers first charge capacities of  $\approx 320–340$  mAh g<sup>-1</sup>.<sup>13</sup> Even though not all of the removed lithium from the first activation charge can be re-intercalated, the material delivers a reversible specific capacity of around 250 mAh g<sup>-1</sup>, 25% more than stoichiometric NCMs can reach under practical cycling

conditions. Despite their high specific capacity and low material costs, issues such as oxygen evolution and the associated stability problems,<sup>13–15</sup> the low electrode densities of the first generation of LMR-NCMs,<sup>16</sup> the comparably high impedances,<sup>17</sup> and the well-known voltage fading phenomenon<sup>18</sup> still hamper the commercialization of LMR-NCMs. Amongst these issues, voltage fading over cycle-life is often discussed as one of the most detrimental challenges, but Kraft et al. have shown that the voltage fading over 250 cycles in large-format LMR-NCM/graphite full-cells is in the range of  $\approx 155$  mV (compared to  $\approx 60$  mV for NCA/graphite cells), and therefore reduces the energy density by less than 5%.<sup>19</sup> With regards to actual applications, they further show that the well-known open circuit voltage (OCV) hysteresis LMR-NCMs does lead to lower energy efficiencies compared to stoichiometric NCAs even at low C-rates (e.g., 88% for LMR-NCM/graphite vs 98% NCA/graphite at C/10), resulting in a more pronounced temperature increase when operating large-format cells at high C-rates. One last point to consider with LMR-NCM based cells is that current battery management systems would have to be adapted, as they typically determine the state of charge (SOC) from the measured cell voltage.<sup>20,21</sup> For materials with a significant voltage hysteresis like LMR-NCMs and silicon, however, the SOC at a given cell voltage can differ substantially depending on the cycling history of the cell.

The voltage hysteresis of over-lithiated NCMs is well-known since their early days after invention.<sup>22</sup> The fact that the charge and discharge curves after activation remain separated by up to several hundreds of mV, even under OCV conditions of a few hours, shows that the voltage hysteresis is an intrinsic bulk property of LMR-NCMs.<sup>23</sup> It is thus not surprising that over time a variety of other properties of LMR-NCMs were also found to be path-dependent, such as its resistance (determined by the direct current internal resistance (DCIR) method)<sup>17</sup> and, more explicitly, the charge-transfer resistance (from EIS measurements) and the lithium diffusion coefficient (from GITT experiments).<sup>24</sup> On the atomic level, there are several publications about the charge/discharge hysteresis of the oxidation states, both for the transition metals<sup>24,25</sup>

<sup>\*</sup>These authors contributed equally to this work.

<sup>\*</sup>Electrochemical Society Student Member.

<sup>\*\*</sup>Electrochemical Society Fellow.

<sup>z</sup>E-mail: [tanja.zuend@tum.de](mailto:tanja.zuend@tum.de)

and oxygen<sup>24</sup> as well as of the TM-O bond distances (from EXAFS analysis).<sup>26</sup> Even though X-ray powder diffraction (XPD) is frequently applied to analyze the structural changes of CAMs during lithiation/delithiation, Konishi et al. were the only ones who reported on the lattice parameter hysteresis (in the rhombohedral representation) of LMR-NCMs, but without diving deeply into possible reasons for their observations.<sup>25</sup> However, the evolution of the lattice parameters upon lithiation/delithiation, especially when measured under in-situ or operando conditions in a battery cell, can be a powerful tool to gain an understanding about the underlying mechanism(s) of the observed hysteresis phenomena. There is a lively discussion in the literature, which assigns the hysteresis in LMR-NCMs either to a path dependence of the transition metal (TM) migration,<sup>23,27–29</sup> the anionic redox,<sup>24</sup> or a combination of both.<sup>30</sup> TM migration typically means that transitions metals, which originally reside in the TM layer (TM<sub>TM</sub>), move upon cycling (ir) reversibly into the lithium layer (TM<sub>Li</sub>), whereas anionic redox refers to the O<sup>2-</sup>/O<sup>n-</sup> couple (n < 2), which occurs independently or in conjunction with the cationic redox in over-lithiated CAMs. Alternatively, a recently published study considers the anionic redox as the reversible formation of molecular O<sub>2</sub> trapped in voids within the particles, which is induced by the in-plane TM<sub>TM</sub> disordering after the removal of Li<sub>TM</sub> during the activation charge.<sup>31</sup>

As known from the intensively studied stoichiometric NCMs,<sup>32–35</sup> both the redox processes and the TM distribution are important descriptors of the lattice dimensions, because they affect the attractive and repulsive interactions of the two metal layers inside the oxide lattice. This renders diffraction methods to be very promising for elucidating the origin of the voltage hysteresis in LMR-NCMs. Beyond that, Rietveld refinements of high-quality (ex-situ) diffraction data enable the quantification of migrated TMs upon cycling.<sup>29,30,36</sup> Since the literature considers the distribution of typically Li, Ni, and Mn in LMR-NCMs on either octahedral and/or tetrahedral sites, it is not possible to perform the refinement solely based on XPD data, as this would result in severe correlations between all of the refined parameters. Therefore, it is beneficial to rely for such complex systems on complementary diffraction datasets, e.g., XPD and neutron powder diffraction (NPD), and to perform joint Rietveld refinements.<sup>37–39</sup>

In the present study, we applied in-situ XPD on our laboratory diffractometer to monitor the lattice parameter evolution of an over-lithiated CAM over the course of the initial charge/discharge cycles. The in-situ approach makes it possible to correlate the lattice dimensions to the SOC, which is equivalent to the overall lithium content in the material, but also to the OCV at which the diffractograms were recorded during intermittent rest phases. Further in-situ experiments were conducted to shed light on the lattice parameter dependence on the degree of over-lithiation and on the cycling conditions, varying the effective SOC window. Subsequently, ex-situ diffraction data were collected again on the laboratory diffractometer (L-XPD) as well as at a synchrotron (S-XPD) and a neutron source (NPD), which were analyzed by Rietveld refinements. Here, we are especially interested into the quantification of migrating TMs by applying a joint refinement approach. By evaluating different structural models and looking at several influencing factors during the refinement, we critically discuss the meaningfulness of the refinement results, and, in combination with DFT simulations, the role of TM migration on the hysteresis in Li- and Mn-rich layered oxides.

## Experimental

**Materials and electrode preparation.**—As in our previous gassing study,<sup>13</sup> we used three different Li- and Mn-rich layered oxides with varying degrees of over-lithiation. Following the Li[Li<sub>δ</sub>TM<sub>1-δ</sub>]O<sub>2</sub> notation for the pristine CAMs, BASF SE (Germany) provided a low- ( $\delta = 0.14$ ), mid- ( $\delta = 0.17$ ), and high-lithium material ( $\delta = 0.20$ ), which in an alternative notation correspond to the compositions 0.33 Li<sub>2</sub>MnO<sub>3</sub> · 0.67 LiTMO<sub>2</sub>, 0.42 Li<sub>2</sub>MnO<sub>3</sub> · 0.58 LiTMO<sub>2</sub>, and 0.50

Li<sub>2</sub>MnO<sub>3</sub> · 0.50 LiTMO<sub>2</sub> that were examined by Teuffl et al.<sup>13</sup> The high-lithium material is the same as in our previous work, whereas the other two CAMs are follow-up batches with similar composition and properties. Since the main work in the present study was done with the mid-lithium material, its precise composition was determined at the Mikroanalytisches Labor Pascher (Remagen, Germany). After dissolving the CAM by pressurized acid digestion in aqua regia, the (metal) composition was determined as Li[Li<sub>0.17</sub>Ni<sub>0.19</sub>Co<sub>0.10</sub>Mn<sub>0.54</sub>]O<sub>2</sub> by means of inductively coupled plasma atomic emission spectroscopy (ICP-AES). Here, we included surface impurities into the calculation, from which a total of  $\approx 1$  wt% could be identified mainly as carbonates. In order to assign the residual mass stoichiometrically to lattice oxygen (assuming no oxygen vacancies in the pristine material, as confirmed by Csernica et al.<sup>40</sup>), there has to be another total amount of  $\approx 2$  wt% of impurities. This corresponds to a theoretical specific capacity of 350 mAh g<sup>-1</sup><sub>CAM</sub> for complete lithium extraction (compared to 361 mAh g<sup>-1</sup><sub>NCM</sub> for the pure LMR-NCM in the absence of the  $\approx 3$  wt% of impurities). Please note that capacity values are normalized to the mass of the as-received CAM powder (i.e., 350 mAh g<sup>-1</sup><sub>CAM</sub>) and that we used the Li[Li<sub>δ</sub>TM<sub>1-δ</sub>]O<sub>2</sub> notation throughout our work.

LMR-NCM cathode coatings were prepared by mixing 94 wt% of CAM powder, 3 wt% of Super C65 conductive carbon (Timcal, Switzerland), and 3 wt% of polyvinylidene fluoride binder (PVDF, either Kynar HSV 900, Arkema, France or Solef 5130, Solvay, Belgium) with *N*-methyl-2-pyrrolidone (NMP, anhydrous, 99.5%, Sigma-Aldrich, Germany) at a solids content of 62 wt% in a planetary orbital mixer (Thinky, USA) in several steps. The final slurry was cast onto an aluminum foil (thickness 15  $\mu$ m, MTL, USA) using a 200  $\mu$ m four-edge blade. The coated foil was dried overnight in a convection oven at 50 °C. This procedure results in relatively high loadings of  $\approx 14$ –20 mg<sub>CAM</sub> cm<sup>-2</sup>, which improves the signal-to-background ratio for the in-situ L-XPD experiments. In order to obtain enough cycled CAM powder for the ex-situ NPD measurements, we also prepared double-sided cathode sheets by coating the backside of the Al foil after the first drying step. The cathode sheets were calendered (GK 300-L, Saueressig, Germany) to a porosity of around 45%. For coin cells, disk-shaped electrodes with a diameter of 14 mm were punched out from the single-sided sheets and then dried overnight in a vacuum oven (Büchi, Switzerland) at 120 °C, before transferring them inertly into an argon-filled glove box (<1 ppm O<sub>2</sub> and H<sub>2</sub>O, MBraun, Germany). For single- and multi-layer pouch cells, quadratic-shaped electrodes with a coated area of 9 cm<sup>2</sup> were cut out and then dried overnight in the oven chamber of the glove box at 90 °C under dynamic vacuum.

**X-ray powder diffraction.**—X-ray powder diffraction (XPD) experiments were mainly conducted at our in-house STOE STADI P diffractometer (STOE, Germany) in Debye–Scherrer geometry, using Mo-K<sub>α1</sub> radiation (0.7093 Å), a Ge(111) monochromator, and a Mythen 1 K detector, and taking one data point every 0.015°/2 $\theta$ . These will further on be referred to as “L-XPD” measurements, which were used (i) to monitor the evolution of lattice parameters during the first cycles from in-situ single-layer pouch cell data and (ii) to obtain structural information from ex-situ capillary data.

The in-situ L-XPD data were recorded in a similar fashion as in our previous publication.<sup>41</sup> The 9 cm<sup>2</sup> single-sided cathode was assembled with an over-sized lithium counter-electrode (10.9 cm<sup>2</sup>, thickness 450  $\mu$ m, Albemarle, USA), a glass-fiber separator (14.4 cm<sup>2</sup>, glass microfiber filter 691, VWR, Germany), and 400  $\mu$ l of LP57 electrolyte (1 M LIPF<sub>6</sub> in EC:EMC = 3:7 by weight, BASF SE) in a relatively thin pouch foil (12  $\mu$ m-thick Al layer, Gruber-Folien, Germany). The pouch cell was fixed without external compression between two metal plates (with a 15 mm hole in the center of the battery stack) and then connected to the diffractometer as well as a potentiostat (SP200, Biologic, France), as shown in Fig. S1 (available online in the Supporting Information at [stacks.iop.org/JES/169/020554/mmedia](https://stacks.iop.org/JES/169/020554/mmedia)). The cell was aligned in the direction of the X-ray beam on the basis of the most intense (003) reflection of the pristine CAM. Electrochemical cycling was done at a C-rate of

C/10 (based on a nominal specific capacity of 300 mAh g<sup>-1</sup> used throughout this study) in the cell voltage window between 2.0 and 4.8 V. The room temperature remained within 24 ± 2 °C. Diffractograms were recorded every 25 mAh g<sup>-1</sup> (15 mAh g<sup>-1</sup> when studying smaller voltage windows) during intermittent OCV periods of 50 min in the 2θ range of 6°–48° (*Q* range 0.9–7.2 Å<sup>-1</sup>, acquisition time ≈40 min, start after the first ≈5 min of the OCV break). The XPD patterns were collected at fixed SOC of 0, 25, 50 mAh g<sup>-1</sup>, etc. for all succeeding cycles (plus additional diffractograms after running into the cut-off voltages).

Ex-situ L-XPD measurements of cycled cathode electrodes were conducted in 0.3 mm Lindemann glass or borosilicate glass capillaries (both from Hilgenberg, Germany) in the 2θ range of 3°–60° (*Q* range 0.5–8.9 Å<sup>-1</sup>, acquisition time ≈14 h). For this, 2325-type coin cells with a cathode electrode (14 mm diameter), a lithium metal anode (15 mm diameter), two glass-fiber separators (16 mm diameter), and 80 μl of LP57 electrolyte were cycled at C/10 and 25 °C in the cell voltage window of 2.0–4.8 V to the desired SOC either during charge or discharge of the second cycle (Series 4000 battery cyler, Maccor, USA). The coin cells were opened in the glove box to harvest the cathode electrodes, and the scratched-off cathode electrode material, without any prior washing, was loaded and airtightly sealed into the capillaries.

Some additional capillaries were sent to the Material Science beamline MS-X04SA of the Swiss Light Source (Paul Scherrer Institute, Villigen, Switzerland), where they were stored for ≈5 months prior to the measurements.<sup>42</sup> X-ray diffractograms were measured at ambient temperature in Debye–Scherrer geometry using synchrotron radiation at 22 keV (0.5646 Å; equipped with a Si(111) double-crystal monochromator and Mythen II microstrip detector) in the 2θ range of 1°–90° (*Q* range 0.2–15.7 Å<sup>-1</sup>, exposure time 4 min sample, one data point every 0.0036°/2θ), which will further on be abbreviated as ex-situ “S-XPD” measurements.

**Neutron powder diffraction.**—Since the ex-situ NPD measurements require (cycled) CAM in the gram scale, we assembled hand-made multi-layer pouch cells in our laboratory, which consisted of two single-sided and two double-sided cathode sheets (i.e., in total six cathode layers at 9 cm<sup>2</sup> each). Their loading deviation was set to be less than 0.5 mg<sub>CAM</sub> cm<sup>-2</sup> per layer and the absolute capacity of the pouch cells amounted to ≈260 ± 50 mAh (based on a nominal specific capacity of 300 mAh g<sup>-1</sup>). Three over-sized lithium metal anodes (10.9 cm<sup>2</sup>) were placed between the cathode sheets, alternating within total six glass-fiber separators (14.4 cm<sup>2</sup>) and packed in a battery pouch foil (40 μm-thick Al layer, DNP, Japan) with 2.4 ml of LP57 electrolyte. As done above for the coin cells, the pouch cells were cycled at C/10 and 25 °C in the voltage window of 2.0–4.8 V (and fixed in a cell holder with a homogeneous compression of ≈2 bar). After reaching the desired SOC in either charge or discharge direction within the first two cycles, the cells were opened in the glove box to harvest the cathode electrodes. For this, the cathode electrodes were scratched off the Al foil with a scalpel, hand-mixed in a mortar using the material from three nominally identical cells, and dried overnight in a vacuum oven at room temperature. The samples were loaded in thin-walled 6 mm vanadium cans (thickness 0.15 mm), which were metal-sealed using an indium wire (loading ≈1.7 ± 0.1 g<sub>CAM</sub>; for the pristine CAM powder, a 10 mm vanadium can was used). A tiny fraction of the cathode electrode material was filled in X-ray capillaries for ex-situ L-XPD measurements.

The samples were prepared within two weeks prior to the high-resolution neutron powder diffraction (NPD) measurements at the SPODI beamline of the research reactor FRM II (Garching, Germany), which operates in Debye–Scherrer geometry with thermal neutrons at a constant wavelength of 1.5481 Å by using a Ge(551) monochromator and a <sup>3</sup>He multidetector system.<sup>43</sup> The NPD patterns were collected at ambient temperature for constantly rotating samples in the 2θ range of 1°–152° (*Q* range 0.1–7.9 Å<sup>-1</sup>, acquisition time ≈5 h sample, one data point every 0.05°/2θ) and

afterwards corrected for geometrical aberrations and detector non-linearities, as described by Hoelzel et al.<sup>43</sup> To perform a joint refinement of L-XPD and NPD data, X-ray diffractograms of the same samples were recorded in parallel at our in-house instrument.

**Analysis of diffraction data.**—The structural complexity of Li- and Mn-rich layered oxides first raises the question about the proper structural model if it comes to the analysis of diffraction data.<sup>10,12</sup> The incorporation of additional lithium in the TM layer causes an in-plane Li/TM ordering of the pristine LMR-NCM materials, which becomes visible as small, typically very broad superstructure peaks in the powder diffraction patterns.<sup>10,44</sup> In the literature, the authors choose most commonly between three different models: (i) the rhombohedral model (*R*–3*m*) known from conventional layered oxides, which neglects the in-plane ordering and distributes all ions randomly in the TM layer;<sup>22,36,40</sup> (ii) the monoclinic model (*C2/m*), which takes the ordering into account by dividing each layer into two crystallographic sites at a ratio of 1/2;<sup>30,44</sup> and, (iii) a composite model comprising a rhombohedral and monoclinic phase, which are typically assigned to the LiTMO<sub>2</sub> and Li<sub>2</sub>MnO<sub>3</sub> composition, respectively.<sup>25,44</sup> As none of our diffractograms show a clear splitting of the main reflections (e.g., of the (003) peak, as was observed by Konishi et al.<sup>25</sup>), not even a shoulder, which would justify the application of the composite model, we do not use it in this work. Furthermore, it is well-known that the superstructure peaks gradually vanish within the first battery cycle(s),<sup>45,46</sup> which puts the monoclinic model in question. The monoclinic model also has more than double the amount of refinement parameters than the rhombohedral model, which involves the danger of severe correlations between interdependent (structural) parameters. All these considerations make the rhombohedral model the main approach to analyze diffraction data in the course of this work, as was done previously by Kleiner et al.<sup>36</sup>

Standard reference materials (i.e., silicon and at the synchrotron also NAC (Na<sub>2</sub>Ca<sub>3</sub>Al<sub>2</sub>F<sub>14</sub>)) were measured before each set of samples. Silicon was used to perform an angle correction of the L-XPD raw data with the WinXPOW software<sup>47</sup> and to determine the accurate wavelength of the X-ray and neutron beamline. In addition, silicon and NAC were used to determine the instrumental peak broadening with the Thompson-Cox-Hastings pseudo-Voigt function, whose parameters were fixed during the subsequent refinement of the samples. The diffraction data were all refined with the software package TOPAS.<sup>48</sup>

The in-situ L-XPD data are used to monitor the lattice parameters during the initial cycles. Here, the rhombohedral model is the common approach in the literature.<sup>23,49,50</sup> To extract the lattice parameters *a* and *c* as well as the unit cell volume *V*, the LMR-NCM phase was refined with a structure-independent Pawley fit. The multi-pattern datasets were analyzed by means of sequential refinements, which also include the Al reflections in the diffractograms. The error of the extracted lattice parameters is on the order of ≈0.01%–0.05% (based on their estimated standard deviations relative to the refined values), which is deemed to be sufficiently precise, as the lattice parameters change by a few percent during a charge/discharge cycle. For the mid-lithium material (*δ* = 0.17), the state of charge of each diffraction pattern was converted into the overall lithium content, *x*<sub>Li</sub>, by considering its theoretical specific capacity (350 mAh g<sup>-1</sup>, using the above described results from elemental analysis) and its total lithium content (i.e., 1 + *δ* = 1.17 based on the Li[Li<sub>δ</sub>TM<sub>1-δ</sub>]O<sub>2</sub> notation):

$$x_{\text{Li}} = \frac{350 \text{ mAh g}^{-1} - \text{SOC} [\text{mAh g}^{-1}]}{350 \text{ mAh g}^{-1}} \cdot 1.17 \quad [1]$$

Here, it is assumed that the electrochemically measured capacity solely originates from lithium insertion/extraction into the LMR-NCM material and that the extent of parasitic reactions is negligible. The OCV value of each diffractogram was averaged from the last minute of the 50 min OCV step used for data collection, where the

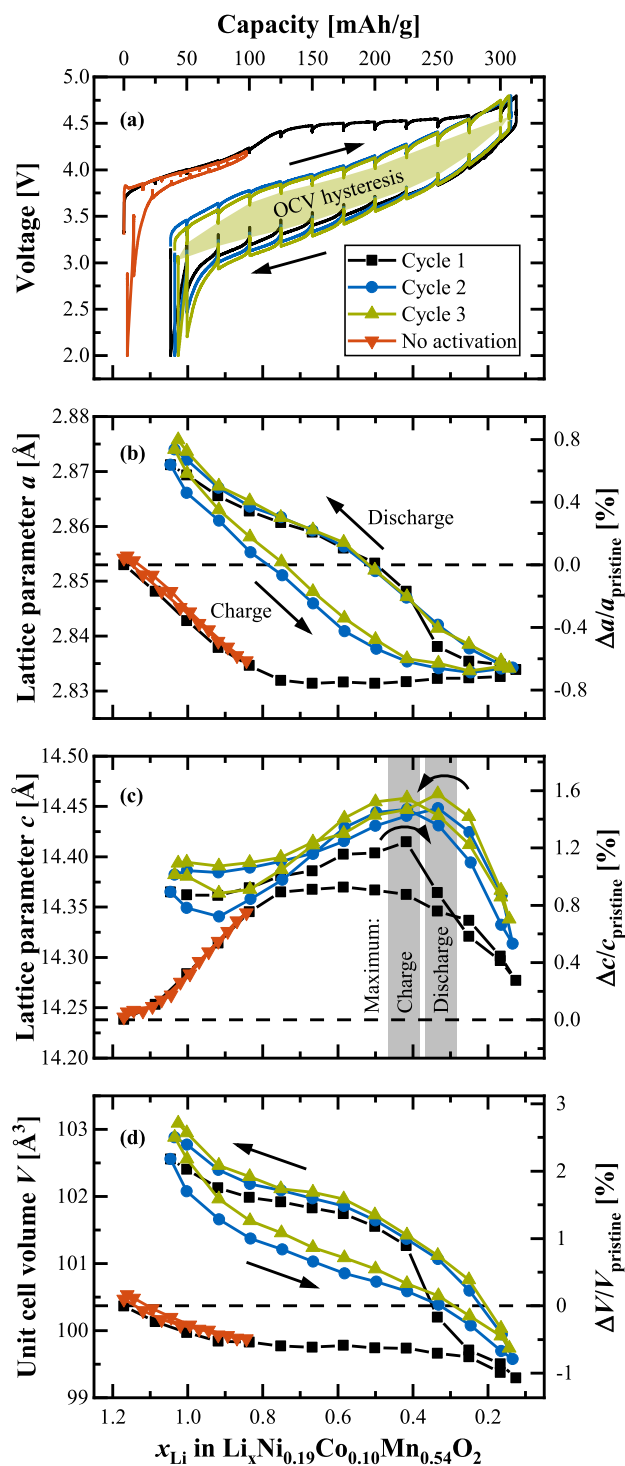


**Figure 1.** Lattice parameter evolution of the mid-lithium LMR-NCM ( $\delta = 0.17$ ) during the initial cycles, as obtained from two independent in-situ L-XPd experiments in a half-cell configuration (i.e., with a lithium metal anode). “Cycle 1–3” were measured at C/10 in the full voltage window of 2.0–4.8 V, whereas the curve labeled “no activation” shows the first cycle in the smaller window of 2.0–4.2 V. The diffractograms were collected during OCV breaks every 25 and 15 mAh g<sup>-1</sup>, respectively. The panels show from top to bottom (a) the voltage curves, (b) the lattice parameter a, (c) the lattice parameter c, and (d) the unit cell volume V as a function of the overall lithium content,  $x_{\text{Li}}$  (lower x-axis), which was calculated according to the respective SOC (upper x-axis, see Eq. 1). In panel (a), the OCV share of the total voltage hysteresis is shown for cycle 3 by the green shaded area. The right y-axes illustrate the lattice parameter changes in percentage terms relative to the pristine state.

remaining voltage relaxation,  $dV/dt$ , was in the range of  $\approx 5\text{--}25$  mV h<sup>-1</sup> (depending on SOC and charge/discharge; for OCV holds of 10 h, it was  $<1$  mV h<sup>-1</sup>). According to Croy et al., this approach closely represents the OCV function of the CAM at the time scales of interest.<sup>23</sup>

All ex-situ data of the mid-lithium material were processed by Rietveld refinements. Here, the site occupancy factors are of particular interest, since they might provide insights into the lithium de-/intercalation mechanism and the migration of transition metals into the lithium layer. Important refinement details are given in paragraph S3 of the Supporting Information. Regarding the joint refinement of L-XPd and NPD data, some parameters (viz., background, zero shift, absorption, peak broadening, and scale factor) were refined on a local level independent for each dataset, whereas the lattice parameters and structural parameters (viz., fractional coordinates, atomic displacement parameters, and site occupancy factors) were optimized on a global level together for both datasets. We used three different structural models, which will be introduced as the extended rhombohedral *model 1*, the simplified rhombohedral *model 2*, and the monoclinic *model 3* in the Results and Discussion section (together with the corresponding refinement results).

Beyond the Supporting Information, we also attached the diffraction raw data of the ex-situ L-XPd and NPD samples (.xy and .xyc file types) as well as the input files for the TOPAS refinement program (.inp file type) as supplementary data to this work (see attached .zip folder which comprises all above files). With the *LMR-NCM\_Pawley\_Refinement.inp* input file, the lattice parameters and the sample broadening can be optimized in a first step by means of an independent Pawley fit for each dataset, while *LMR-NCM\_Rhombohedral\_Refinement.inp* and *LMR-NCM\_Monoclinic\_Refinement.inp* allow for testing the (joint) Rietveld refinement of the here presented structural models (and beyond).

**DFT simulation.**—Spin-polarized calculations in the framework of DFT have been performed using the Vienna Ab-initio Simulation Package (VASP)<sup>51–54</sup> with projector augmented wave pseudopotentials.<sup>55,56</sup> The exchange-correlation functional of choice is the strongly constrained and appropriately normed (SCAN) meta-generalized gradient approximation supplemented with the long-range van der Waals interaction from rVV10, the revised Vydrov-Van Voorhis nonlocal correlation functional, which performs very well on layered compounds.<sup>57</sup> Within a  $4 \times 5 \times 1$  supercell of the conventional rhombohedral cell, all structures have been fully relaxed until the forces were lower than  $10^{-2}$  eV·Å<sup>-1</sup> with a cut-off energy of 600 eV at the  $\Gamma$ -point only, which is justified by the large dimensions of the supercell. In selected cases, a pre-relaxation by means of short molecular dynamics at 300 K helped to find a better local minimum. Because VASP cannot handle partial occupancies, structures with integer occupancies compatible with the experimental site occupancy factors have been generated with the combinatorial approach implemented in the supercell software.<sup>58</sup>

The material with the mid-lithium composition, Li[Li<sub>0.17</sub>Ni<sub>0.19</sub>Co<sub>0.10</sub>Mn<sub>0.54</sub>]O<sub>2</sub>, has been simulated with a  $4 \times 5 \times 1$  supercell of the conventional rhombohedral cell and thus contains 60 formula units. The supercell contains 72 Li (60 in the Li layer and 12 in the TM layer), 12 Ni, 6 Co, 30 Mn and 120 O that corresponds to the formula unit (f.u.) Li<sub>1.2</sub>Ni<sub>0.2</sub>Co<sub>0.1</sub>Mn<sub>0.5</sub>O<sub>2</sub> of the model composition (which represents the over-lithiation degree of the high-lithium material, since simulating the precise lithium content of the mid-lithium material would have required an excessively large supercell). With a supercell of this size, the sheer number of possible ways to distribute the cations into the Li and TM sub-lattices is astronomical. A good structural candidate has been determined by letting the combinatorial calculator supercell find the cation distribution with the lowest electrostatic energy within a point-charge approximation based on given oxidation states (viz., Li<sup>+</sup>, Ni<sup>2+</sup>, Co<sup>3+</sup>, Mn<sup>4+</sup>, and O<sup>2-</sup>). The key features associated with the progressive delithiation of the material are analyzed by investigating structural models at different Li contents and comparing their

thermodynamic stability at each composition. Already at this point, it is important to reiterate that the extremely large configurational space renders it virtually impossible to determine with certainty the true ground state for a given composition (bar the construction of an exhaustive compositional phase diagram, which falls beyond the scope of this work). Calculation of the voltage profile also requires the knowledge of the compositional convex hull. Therefore, we will not report on voltages but rather compare the total energies of structures with the same composition.

## Results and Discussion

**SOC dependence of lattice parameters.**—Most of our previous work on Li- and Mn-rich layered oxides, including studies about their gassing behavior,<sup>59</sup> resistance build-up,<sup>17</sup> and the irreversible TM migration during long-term cycling,<sup>36</sup> used exclusively materials with a medium degree of over-lithiation ( $\delta = 0.17$ ). Here, the work of Teuff et al. revealed a path-dependent resistance hysteresis of this particular LMR-NCM within a charge/discharge cycle.<sup>17</sup> It is thus reasonable to focus first on a very similar CAM to monitor its lattice parameters during the first battery cycles and to look for any structural hysteresis behavior. Figure 1 shows the results from two in-situ L-XPD measurements of the mid-lithium material, whose pristine composition was determined to be  $\text{Li}[\text{Li}_{0.17}\text{Ni}_{0.19}\text{Co}_{0.10}\text{Mn}_{0.54}]\text{O}_2$  by elemental analysis. The voltage curves obtained in a half-cell (i.e., with a lithium metal anode) and the lattice parameters (i.e.,  $a$ ,  $c$ , and the unit cell volume  $V$ ; as based on the rhombohedral model) are plotted vs the exchanged capacity (upper x-axis) and the lithium content,  $x_{\text{Li}}$  (lower x-axis), of the CAM, which are equivalent measures of the state of charge (see Eq. 1). Three consecutive cycles (the first cycle in black and the 2nd and 3rd cycle in blue and green, respectively) of one cell operated at C/10 in the full voltage window of 2.0–4.8 V are compared to the first cycle (in red) of another cell, that was reversed at 4.2 V, just before reaching the activation plateau. The electrochemistry matches our previous work and is not affected by the simplified pouch cell setup or X-radiation, with the expected capacities of  $\approx 313 \text{ mAh g}^{-1}$  for the first activation charge and  $\approx 276\text{--}264 \text{ mAh g}^{-1}$  for the following discharge cycles. The vertical spikes in the voltage curves indicate the intermittent OCV periods used for XPD data collection. Connecting the final OCV values at each SOC, as exemplarily done for cycle 3 in Fig. 1a, makes it obvious that the main part of the voltage hysteresis, especially in the mid-SOC regime, is maintained during OCV and reaches almost up to  $\approx 400 \text{ mV}$ .

Let us now turn towards the lattice parameters. We directly discuss the refinement results, because the raw data do not contribute any additional information. For the sake of completeness, paragraph S1 of the Supporting Information (SI) shows a contour plot of the in-situ L-XPD patterns of “Cycle 1–3” and two Pawley fits in the discharged and charged state, respectively (see Figs. S2 and S3). At a first glance, the lattice parameters  $a$  and  $c$  in Fig. 1 seem to resemble the voltage characteristics: the first-cycle charge curve that differs from the subsequent charge curves (Fig. 1a) is reflected in the behavior of  $a$  (Fig. 1b) and  $c$  (Fig. 1c) that also show different functionalities in the first compared to the subsequent cycles. The first-cycle activation charge (upper black line in Fig. 1a) can be divided into a sloping region until  $\approx 4.4 \text{ V}$  (corresponding to  $1.17 > x_{\text{Li}} > 0.76$ ) and an extended voltage plateau at  $\approx 4.5 \text{ V}$  ( $0.76 > x_{\text{Li}} > 0.23$ ). In a similar manner, the lattice parameters change monotonically in the sloping region (lower black lines in Figs. 1b and 1c), then remain approximately constant during the voltage plateau, and move (slightly) back at the end of the first charge. Following the activation, there is a drastic change of the lattice parameters, which also feature a pronounced hysteretic behavior during charge and discharge. Former in-situ XPD studies have seen similar lattice parameter trends within the initial cycles, e.g., for  $\text{Li}[\text{Li}_{0.20}\text{Ni}_{0.15}\text{Co}_{0.10}\text{Mn}_{0.55}]\text{O}_2$  by Mohanty et al.<sup>50</sup> and for  $\text{Li}[\text{Li}_{0.20}\text{Ni}_{0.20}\text{Mn}_{0.60}]\text{O}_2$  by Croy et al.,<sup>23</sup> but the hysteresis in the evolution of the lattice parameters over a charge/discharge cycle was not so obvious there, as in the former study the

lattice parameters were only plotted vs time while in the latter study there were too few data points over a charge/discharge cycle. To the best of our knowledge, only Konishi et al. reported a clear lattice parameter hysteresis for  $\text{Li}[\text{Li}_{0.20}\text{Ni}_{0.13}\text{Co}_{0.13}\text{Mn}_{0.54}]\text{O}_2$ , whereby the hysteresis was assigned to the  $\text{LiTMO}_2$ -like phase in their 2-phase refinement with a composite model comprising a rhombohedral ( $\text{LiTMO}_2$ -like) and monoclinic ( $\text{Li}_2\text{MnO}_3$ -like) phase.<sup>25</sup>

Since Li- and Mn-rich layered oxides are closely related to conventional NCM materials, most authors apply the same structural and electronic considerations to explain the change of the lattice parameters. The lattice parameter  $a$  reflects the intra-layer nearest-neighbor distances, which are all the same for Li-Li in the Li layer, TM-TM in the TM layer, and O-O in the O layer, respectively. As the transition metals decrease their ionic radii upon oxidation, the contraction of the lattice parameter  $a$  during charging is however dominated by the TM-TM distance.<sup>32,60</sup> As shown in Fig. 1b (lower black line), the lattice parameter  $a$  decreases by  $\approx 0.8\%$  from  $\approx 2.854$  to  $\approx 2.831 \text{ \AA}$  during the sloping region of the first charge and remains almost constant afterwards. This result fits to several spectroscopic studies,<sup>24,30,61</sup> which have shown that the TM oxidation only occurs during the first part of the activation. Assuming that all TMs get oxidized to their 4+ state, starting from  $\text{Ni}^{2+}$ ,  $\text{Co}^{3+}$ , and  $\text{Mn}^{4+}$  in the pristine material, the TM redox can theoretically compensate for  $144 \text{ mAh g}^{-1}$  ( $\Delta x_{\text{Li}} = 0.48$ ), what is reasonably close the exchanged capacity of  $\approx 123 \text{ mAh g}^{-1}$  ( $\Delta x_{\text{Li}} \approx 0.41$ ) until the end of the sloping voltage region at 4.4 V. If the cycling is restricted to this region, i.e., if the charge is stopped prior to reaching the subsequent voltage plateau at  $\approx 4.5 \text{ V}$ , the lattice parameters move reversibly back (see red lines labeled “no activation” in Fig. 1). Such a “non-activated” LMR-NCM shows no voltage fade over extended cycling and thus may be considered as a conventional layered oxide.<sup>17</sup> On the other hand, after a full activation charge to 4.8 V, the lattice parameter  $a$  changes afterwards between  $\approx 2.874$  and  $\approx 2.834 \text{ \AA}$  ( $\Delta a/a_{\text{pristine}} \approx 1.4\%$ ) in a hysteresis loop (see upper black as well as green and blue lines in Fig. 1b). It thus exceeds its value in the pristine material by  $\approx 0.02 \text{ \AA}$  ( $\approx 0.7\%$ ) at the end of discharge. This could be explained by the additional activation of the  $\text{Mn}^{3+}/\text{Mn}^{4+}$  redox couple, as was evidenced through HAXPES measurements by Assat et al. ( $\approx 10\% \text{ Mn}^{3+}$  in the discharged state).<sup>24,62</sup>

The lattice parameter  $c$  is a measure of the inter-layer distances. Due to the alternating stacking of O-Li-O and O-TM-O layers,  $c$  can be separated into a lithium,  $h_{\text{Li}}$ , and TM layer height,  $h_{\text{TM}}$ , respectively.<sup>33</sup> De Biasi et al. have investigated many regular NCM materials, ranging from NCM-111 to NCM-851005, by operando XPD.<sup>32</sup> In their study, the lattice parameter  $c$  increases by  $\approx 1.5\%$  until the delithiation reaches  $x_{\text{Li}}$  values of  $\approx 0.4\text{--}0.5$ , what is explained by the increasing Coulomb repulsion of  $\text{O}^{2-}$  anions facing each other in the depleting Li layers (and thus referring to the  $h_{\text{Li}}$  component). Upon further delithiation,  $c$  falls back and even below the value in the discharged (lithiated) state, reaching up to minus 4.7% for NCM-851005 (at  $x_{\text{Li}} \approx 0.1$ ). The repulsive interactions get diminished through an increasing covalent bond character between the transition metals (especially Ni) and oxygen, which in turn reduces the effective negative charge of the O atoms.<sup>32,34,63</sup> Thus, oxygen is involved into the charge compensation of regular layered oxides, but its participation is confined to the standard TM-O hybridization model. This model is not sufficient for Li- and Mn-rich layered oxides, which experience a TM-independent anionic redox during cycling (typically expressed as  $\text{O}^{2-}/\text{O}^{n-}$  redox,  $n < 2$ ).<sup>24,30,61</sup> According to these spectroscopic studies, the anionic redox gets activated during the voltage plateau at  $\approx 4.5 \text{ V}$  in the first charge and stays present in the following cycles. In general, the lattice parameter  $c$  of the mid-lithium LMR-NCM resembles the trends known from regular NCMs, with  $c$  increasing until a delithiation level of  $x_{\text{Li}} \approx 0.4$  and then decreasing again (see Fig. 1c). The magnitude of this change in  $c$  is however significantly smaller. The maximum difference  $\Delta c/c_{\text{pristine}}$  amounts to less than 1% within one cycle. This damping effect could be rationalized by the  $\text{O}^{2-}/\text{O}^{n-}$  redox, which distributes over the entire SOC range

after activation.<sup>24,62</sup> Assuming that the anionic redox scales approximately linearly with the extent of delithiation, it reduces the Coulomb repulsion at high  $x_{\text{Li}}$  values (i.e., low SOCs), what in turn diminishes the  $c$  increase at  $x_{\text{Li}} > 0.4$ . For  $x_{\text{Li}} < 0.4$  (i.e., high SOCs), the anionic redox might compete with the TM–O hybridization,<sup>64</sup> thus damping the subsequent decrease of  $c$ . Please note that the Ni–O bonding (important for Ni-rich stoichiometric oxides) tends towards stronger covalency than the Mn–O bonding (important for Mn-rich over-lithiated oxides), which has a more ionic nature.<sup>65</sup> Assat et al. report that the  $\text{O}^{2-}/\text{O}^{\text{n-}}$  redox is not evenly distributed during charge and discharge.<sup>24</sup> This could explain the hysteretic behavior of  $c$ , which does not manifest as a simple hysteresis loop. In contrast to the lattice parameter  $a$ , the charge and discharge curves of  $c$  intersect at  $\approx 0.67$  and  $\approx 0.40$ . Furthermore, their maxima are shifted on the  $x_{\text{Li}}$  axis (viz., at  $\approx 0.42$  during charge and at  $\approx 0.33$  during discharge; as highlighted by the grey bars in Fig. 1c). At this point, we have to call to mind that the lattice parameter  $c$  consists of two individual layer heights,  $h_{\text{Li}}$  and  $h_{\text{TM}}$ , which might evolve quite differently compared to their summed-up value of  $c$ . Their calculation however requires the  $z$ -coordinate of oxygen from Rietveld refinements, what will be done later.

Let us examine once again the first activation charge. As discussed above, the Li- and Mn-rich layered oxide can be regarded as a regular NCM material in the sloping region, i.e.,  $c$  decreases due to TM oxidation and  $c$  increases due to Coulomb repulsion of the  $\text{O}^{2-}$  anions. During the voltage plateau, where the lattice parameters remain almost constant, the anionic redox comes into play. Another not yet considered aspect is the lithium extraction, which includes both the lithium ions from the Li layer ( $\text{Li}_{\text{Li}}$ ) and from the TM layer ( $\text{Li}_{\text{TM}}$ ). Liu et al. investigated the delithiation process of  $\text{Li}[\text{Li}_{0.20}\text{Ni}_{0.15}\text{Co}_{0.10}\text{Mn}_{0.55}]\text{O}_2$  by operando NPD.<sup>66</sup> They determined the  $\text{Li}_{\text{Li}}/\text{Li}_{\text{TM}}$  extraction ratio to be  $\approx 24/1$  in the sloping region and  $\approx 2.6/1$  in the plateau region at  $\approx 4.5$  V, and also found out that  $\text{Li}_{\text{TM}}$  cannot be re-intercalated during the subsequent discharge. Hence, the lithium ions in the TM layer get predominantly and permanently removed in the voltage plateau region during the first charge. It is however difficult to estimate the consequences for the lattice parameters, because the  $\text{Li}_{\text{TM}}$  removal goes along with the depopulation of  $\text{Li}_{\text{Li}}\text{-O-Li}_{\text{TM}}$  configurations<sup>64</sup> and the loss of in-plane ordering in the TM layer.<sup>31,46</sup> Both processes connect the  $\text{Li}_{\text{TM}}$  removal to the anionic redox, as they make it energetically favorable. Even though most lithium ions in the TM layer are extracted during the activation charge, NMR measurements by Jiang et al. have shown that their complete removal might require up to  $\approx 10$  cycles.<sup>46</sup> This possibly explains why the lattice parameters increase irreversibly from cycle to cycle in Fig. 1 (e.g., when comparing the discharge curves of the lattice parameters). Here, the difference of the discharge curves between cycle 2 and 3 is smaller than between cycle 1 and 2. We also want to mention that the first three lattice parameter values of the first discharge ( $0.33 < x_{\text{Li}} < 0.17$ ) are shifted towards lower values compared to the preceding charge,

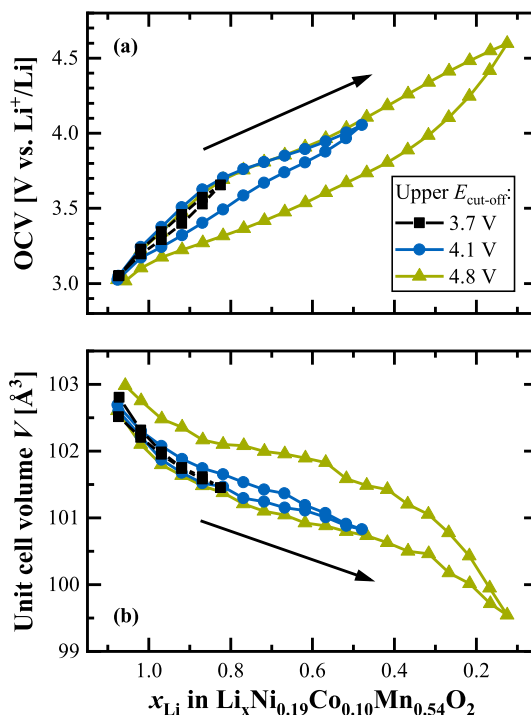


**Figure 2.** Charge window opening experiment at C/10 with the fully activated mid-lithium LMR-NCM (after 2 activation cycles between 2.0–4.8 V), where the upper cut-off voltage is stepwise increased from 3.7 to 4.1 to 4.8 V (lower cut-off voltage fixed to 2.0 V, what is also the starting point). As a function of the lithium content, panel (a) shows the open circuit voltage, at which the diffractograms were measured every  $15 \text{ mAh g}^{-1}$ , and panel (b) depicts the unit cell volume from the corresponding Pawley fits.

probably due to a temporary misalignment of the pouch cell resulting from CAM gassing at the end of the activation charge (which also continues during OCV).<sup>59</sup> The comparison with a second in-situ L-XPD measurement (cell #2 in Fig. S4 of the SI) however shows that this artefact does not affect the progression of the lattice parameters.

The unit cell volume  $V$  (see Fig. 1d) represents the net response of the crystal lattice upon lithium insertion/extraction. Its behavior is similar to that of the lattice parameter  $a$ , also showing a hysteresis loop after the first activation cycle. This resemblance is reasonable because  $a$  affects the unit cell volume to the second power (according to  $V = \sqrt{3/2} \cdot a^2 \cdot c$ ) and the relative changes of  $a$  are larger than for  $c$ . The unit cell volume is an important measure for the tendency of a CAM particle to crack during cycling. The larger the volume change, the larger the mechanical stress of the particles due to (i) the anisotropic change of the lattice parameters  $a$  and  $c$  and (ii) the different orientation of the primary particles inside the

**Table I.** Comparison of lattice parameter changes in regular NCMs and in the mid-lithium LMR-NCM. The NCM data were taken from the operando XPD study of de Biasi et al. and present the therein investigated NCM materials with the lowest (NCM-111, 33% Ni on TM basis) and highest Ni content (NCM-851005, 85% Ni), respectively.<sup>32</sup> As in our work, the CAMs were cycled in half-cells at C/10, but in the voltage window of 3.0–4.6 V. The lattice parameter changes are given as the difference between the completely discharged (lithiated,  $x_{\text{Li,dis}}$ ) and charged (delithiated,  $x_{\text{Li,cha}}$ ) state of the respective charge cycle and are normalized to the starting value (in a given particular cycle). For the unit cell volume  $V$ , this procedure always yields the maximum difference within a cycle, whereas  $a$  and  $c$  might run through minima and maxima, respectively. The  $\Delta x_{\text{Li}}$  range is calculated according to  $\Delta x_{\text{Li}} = x_{\text{Li,dis}} - x_{\text{Li,cha}}$ .

Material	Cycle	$x_{\text{Li,dis}}$ [–]	$x_{\text{Li,cha}}$ [–]	$\Delta x_{\text{Li}}$ [–]	$\Delta a/a_0$ [%]	$\Delta c/c_0$ [%]	$\Delta V/V_0$ [%]
<b>Regular NCMs</b> <sup>32</sup>							
NCM-111	4 (reversible)	0.94	0.21	0.73	–1.2	$\pm 0.0$	–2.3
NCM-851005	4 (reversible)	0.89	0.09	0.80	–1.7	–4.7	–8.0
<b>Over-lithiated NCMs</b>							
Mid-lithium LMR-NCM	1 (activation)	1.17	0.13	1.04	–0.7	+0.3	–1.1
Mid-lithium LMR-NCM	2 + 3 (reversible)	1.04	0.13	0.91	–1.3	–0.3	–3.0

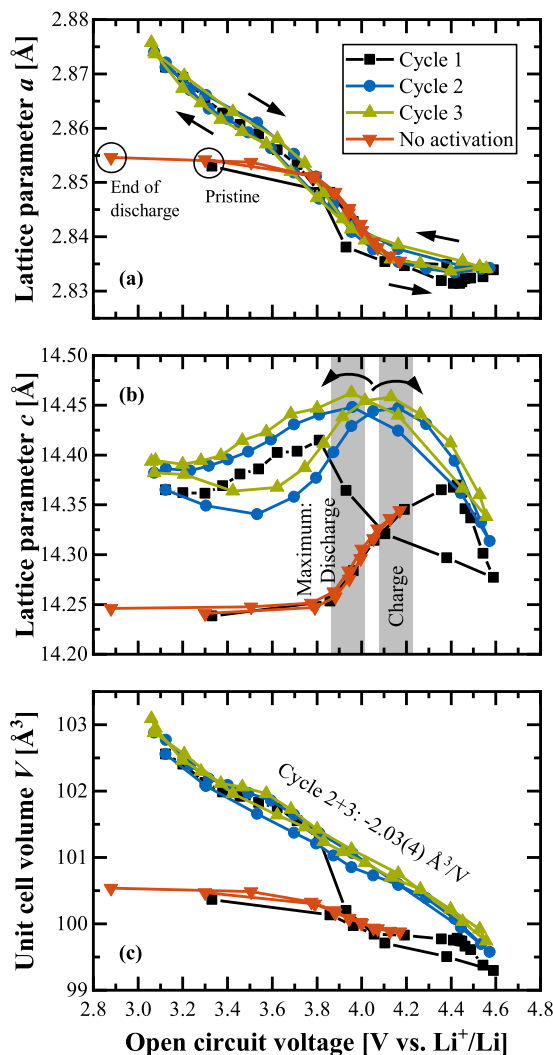


**Figure 3.** Lattice parameter data (taken from Fig. 1) for the mid-lithium LMR-NCM shown as a function of OCV at which the diffractograms were collected during the in-situ L-XPd experiments. (a), (b) Evolution of the lattice parameters *a* and *b* during the first three cycles at C/10. (c) Evolution of the corresponding unit cell volume, whereby the linear regression of the “cycle 2+3” data results in  $V = 109.0(1) \text{ \AA}^3 - 2.03(4) \text{ \AA}^3/\text{V} \cdot \text{OCV}$ , with  $R^2 = 0.985$ .

secondary agglomerates of a typical polycrystalline CAM.<sup>63,67</sup> In Table I, we compare the relative lattice parameter changes of the over-lithiated NCM in Fig. 1 with two regular NCMs from the study of de Biasi et al.<sup>32</sup> In their work, NCM-111 and NCM-851005 are the end members with respect to the range of Ni content (33%<sub>Ni</sub> vs 85%<sub>Ni</sub> on TM basis). It is well-known in the literature that the degree of cracking increases with the Ni content<sup>63,67</sup> and with the upper cut-off potential.<sup>68,69</sup> Since increasing both parameters yields higher delithiation levels (i.e., lower  $x_{\text{Li,cha}}$  values), this trend can be explained in good approximation by the steep volume contraction at  $x_{\text{Li}}$  values smaller than  $\approx 0.3$ .<sup>32,70</sup> The overall volume contraction of the mid-lithium LMR-NCM (amounting to  $-1.1\%$  during activation and  $-3.0\%$  reversibly in the following cycles) is much closer to NCM-111 ( $-2.3\%$ ) than to NCM-851005 ( $-8.0\%$ ), even though its delithiation level ( $x_{\text{Li,cha}} = 0.13$ ) resembles the latter one (0.09). This discrepancy is largely driven by the smaller change of the lattice parameter *c*, whereas the reversible change of *a* is rather similar among the different CAMs. Despite the broader SOC range of Li- and Mn-rich layered oxides, we thus hypothesize that they are less prone to particle cracking and its detrimental consequences (such as

CAM loss, TM dissolution, and surface reconstruction) than their Ni-rich (polycrystalline) competitors.

The “no activation” dataset in Fig. 1 revealed that the structural hysteresis observed in cycle 2 and onwards is directly connected to the activation plateau at  $\approx 4.5$  V. This raises the question if there is any chance to re-establish the pre-activated state without hysteresis even after passing this plateau. Therefore, we performed a charge window opening experiment.<sup>24,25</sup> After two cycles in the full voltage window of 2.0–4.8 V to activate the mid-lithium LMR-NCM material, Fig. 2 shows three consecutive cycles, where the upper cut-off voltage during charge was stepwise increased from 3.7 to 4.1 to 4.8 V, while always going back to 2.0 V during discharge. The extent of OCV hysteresis (see Fig. 2a) and lattice parameter hysteresis (exemplary shown for the unit cell volume in Fig. 2b) depends on the SOC range (equivalent to  $\Delta x_{\text{Li}}$ ) that the CAM has passed through in every single cycle. Konishi et al. made the same observation for the OCV as well as the lattice parameters *a* and *c* of the LiTMO<sub>2</sub>-like phase in their 2-phase refinement.<sup>25</sup> For the smallest SOC window of  $\approx 74 \text{ mAh g}^{-1}$  ( $\Delta x_{\text{Li}} \approx 0.25$ ) measured until 3.7 V (black lines in Fig. 2), the charge/discharge values of the unit cell volume agree within the error of measurement, while the OCV differs by a maximum of  $\approx 60$  mV (at  $x_{\text{Li}} \approx 0.92$ ). Since the voltage relaxation is not completed after 50 min resting ( $dV/dt \approx 5 \text{ mV h}^{-1}$ ), this difference would get even smaller during a prolonged OCV step. Hence, the fully activated LMR-NCM exhibits almost no path dependence when cycled under this condition, but the hysteresis grows strongly when charged further (blue and green lines). As already described for the voltage by Assat et al.,<sup>24</sup> the in-situ L-XPd data also show on a structural level that the hysteresis raises mainly at the end of charge and stays open until the end of the discharge. Furthermore, the voltage and lattice parameter hysteresis must have the same driving force. In Fig. S5 in paragraph S2 of the SI, this measurement is contrasted with a discharge window opening experiment.

**OCV dependence of lattice parameters.**—Since the diffractograms were measured under open circuit voltage conditions, the lattice parameters of the mid-lithium material in Fig. 1 are re-plotted in Fig. 3 vs the OCV value averaged over the last minute of the 50 min rest phase. Here, we directly see a completely different dependency than when plotted vs the state of charge as was done in Fig. 1: When plotted vs OCV, the lattice parameter *a* exhibits almost no hysteresis between charge and discharge after the first activation charge (see Fig. 3a). Only upon closer inspection, it can be noticed that the *a* values during charge are slightly higher than during discharge (directions during charge and discharge marked by arrows) for OCVs smaller than  $\approx 4.0$  V, where both curves intersect (this subtle difference was not be resolved in the study by Konishi et al.<sup>25</sup>). Interestingly, the “no activation” data (red lines) coincide perfectly with the charge curve. In the previous paragraph, we assigned any changes of *a* as to mainly originating from TM redox activities, which are initially restricted to the potential range of  $\approx 3.6$ – $4.2$  V, but expand to lower potentials after activation (probably due to  $\text{Mn}^{3+}/\text{Mn}^{4+}$  redox). As the hysteresis of *a* when plotted vs OCV is negligibly small (Fig. 3a) compared to when it is plotted vs SOC (Fig. 1b), the TM redox seems to be uniquely associated with the thermodynamic state of the CAM that is marked by the OCV, whereas there seems to be no causal relationship to the lithium content. In contrast, the lattice parameter *c* still shows a hysteretic behavior even when plotted vs OCV (as shown in Fig. 3b). Due to the large voltage drop after current reversal at the upper cut-off, the maximum of the charge curve, that was at a lower SOC than during discharge (see Fig. 1c), is now at a higher OCV than the discharge curve (viz., at  $\approx 4.15 \text{ V}_{\text{charge}}$  vs  $\approx 3.95 \text{ V}_{\text{discharge}}$ , as highlighted by the grey bars).

The most interesting observation is the behavior of the unit cell volume *V* (see Fig. 3c) which, within the accuracy of the in-situ L-XPd measurements, exhibits no hysteresis after the first activation charge, with *V* changing linearly with OCV by about  $-2 \text{ \AA}^3 \text{ V}^{-1}$ . As

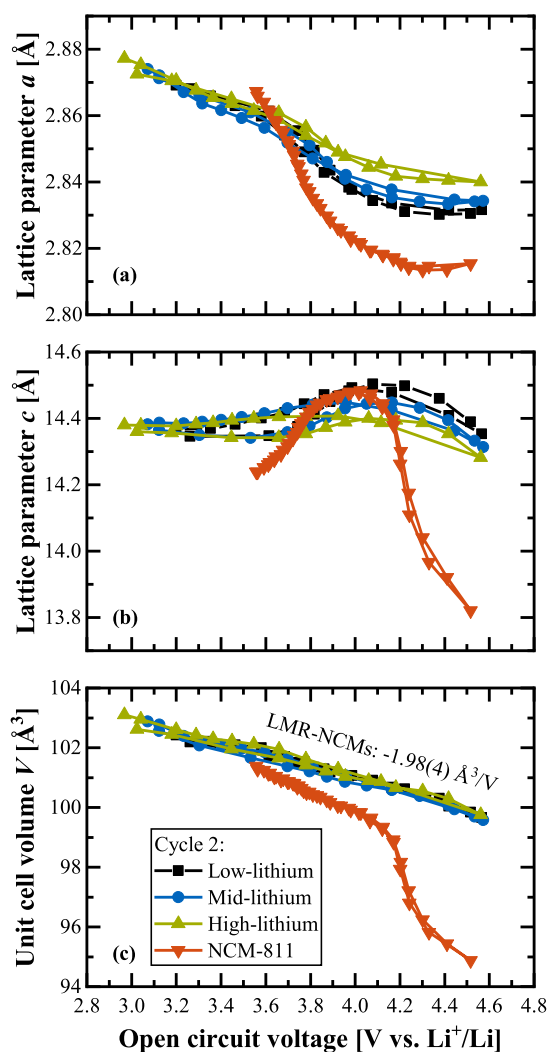


**Figure 4.** Evolution of the lattice parameters of three different LMR-NCMs during the second cycle (i.e., after activation) vs OCV, as determined from in-situ L-XPD experiments at C/10 in the voltage window of 2.0–4.8 V. The CAMs differ with respect to the degree of over-lithiation, ranging from a low-lithium ( $\delta = 0.14$ ) over a mid-lithium ( $\delta = 0.17$ , same data as in Fig. 3) to a high-lithium material ( $\delta = 0.20$ ). They are additionally contrasted with stoichiometric NCM-811 ( $\delta = 0.01$ ), which was investigated at C/7.5 between 3.0–4.6 V (data taken from Fig. S6 in the SI of Friedrich et al.,<sup>41</sup> published by ECS, licensed as CC BY 4.0). In panel (c), the linear regression of all three LMR-NCMs results in  $V = 108.9(1) \text{ \AA}^3 - 1.98(4) \text{ \AA}^3/V \cdot \text{OCV}$ , with  $R^2 = 0.977$ .

for any given OCV, the lithium content ( $x_{\text{Li}}$ ) is different between the charge and the discharge reaction by up to  $\Delta x_{\text{Li}} \approx 0.33$  (see blue/green lines in Fig. 1a). The linear and direction-independent relationship between  $V$  and OCV in turn means that very different lithium contents can yield the same unit cell volume: for example,  $[\text{Li}_{0.75}\text{TM}_{0.83}\text{O}_2]_{\text{charge}}$  and  $[\text{Li}_{0.42}\text{TM}_{0.83}\text{O}_2]_{\text{discharge}}$  both have an OCV of  $\approx 3.80$  V and a unit cell volume of  $\approx 101.3 \text{ \AA}^3$  within the second cycle. Such a behavior is quite remarkable and completely unknown for regular NCMs that exhibit no charge/discharge hysteresis and for which the lattice parameters uniquely scale both with the SOC and OCV.<sup>41</sup> The red lines in Figs. 1 and 3 show that the same is true for LMR-NCMs if they are not cycled into their activation plateau (labeled as “no activation”), contrary to the irreversible changes induced by cycling into the activation plateau.

So far, we only discussed the mid-lithium material, but it is also interesting to examine the lattice parameter changes for different degrees of over-lithiation. Figure 4 compares their OCV dependence

during the second cycle for the already introduced mid-lithium material ( $\delta = 0.17$  in  $\text{Li}[\text{Li}_\delta\text{TM}_{1-\delta}]\text{O}_2$ , same data as in Fig. 3) as well as for a low- ( $\delta = 0.14$ ) and high-lithium material ( $\delta = 0.20$ ). Beyond that, the Mn-rich over-lithiated CAMs are contrasted with the Ni-rich stoichiometric NCM-811. A zoomed-in view of the data for only the LMR-NCMs is given in Fig. S6 in paragraph S2 of the SI.

Starting again with the lattice parameter  $a$ , Fig. 4a shows that  $a$  decreases as the OCV increases from  $\approx 3.6$  to 4.2 V (i.e., in the region that is ascribed to the  $\text{Ni}^{2+}/\text{Ni}^{3+}/\text{Ni}^{4+}$  and  $\text{Co}^{3+}/\text{Co}^{4+}$  redox). The decrease is the higher the lower the degree of over-lithiation, with  $a$  decreasing to only  $\approx 2.840 \text{ \AA}$  for the high-lithium material while decreasing to  $\approx 2.833$  and  $\approx 2.830 \text{ \AA}$  for the mid- and low-lithium material, respectively. The lower the degree of over-lithiation, the more transition metals are present in the transition metal layer and the lower is their average oxidation state (i.e., 3.33+, 3.41+, and 3.50+ in the pristine LMR-NCMs with low-, mid-, and high-lithium content, respectively; according to  $(3-\delta)/(1-\delta)$ ). Consequently, for lower over-lithiation, more charge can be compensated by the classical TM redox until their formal 4+ state, apparently resulting in the observed larger  $a$  parameter changes. The lattice parameter  $a$  of NCM-811 varies exactly in the same voltage window, but its change is  $\approx 2$ –3 times stronger (note that the average TM oxidation state is 3+ in pristine stoichiometric NCMs, because  $\delta$  is essentially 0). The rise of  $a$  at potentials below  $\approx 3.6$  V (better visible in Fig. S6), which only occurs after activation and is not present in NCM-811, increases with increasing over-lithiation. It is reaching both lower OCV values (viz., from  $\approx 3.20 \text{ V}_{\text{low}}$  to  $\approx 2.97 \text{ V}_{\text{high}}$  at the end of the second discharge) and higher  $a$  values (viz., from  $\approx 2.869 \text{ \AA}_{\text{low}}$  to  $\approx 2.877 \text{ \AA}_{\text{high}}$ ; same data points). This trend could be explained by an increasing  $\text{Mn}^{3+}/\text{Mn}^{4+}$  redox fraction,<sup>24,62</sup> which is a concomitant feature of the anionic redox. To the best of our knowledge, there is no spectroscopic comparison of several Li- and Mn-rich layered oxides in one single publication, but the strong increase of irreversible  $\text{O}_2$  loss (at the end of the activation charge; as was studied by Teufl et al.<sup>13</sup>) suggests that its reversible  $\text{O}^{2-}/\text{O}^{\text{n-}}$  redox counterpart also grows with increasing over-lithiation. This argument is in line with the increasing damping effect of the lattice parameter  $c$  (as shown in Fig. 4b). Both the initial rise (due to Coulomb repulsion) and the following drop (due to TM-O hybridization) get reduced with increasing over-lithiation and are much smaller compared to NCM-811, because the anionic redox most likely competes with the afore-mentioned electrostatic effects.

Despite the shifting ratio of cationic and anionic redox, which becomes visible in the individual lattice parameters  $a$  and  $c$ , the unit cell volume  $V$  vs OCV is essentially identical among the investigated LMR-NCMs, with a uniform slope of about  $-2 \text{ \AA}^3 \text{ V}^{-1}$  (see Fig. 4). This indicates that the  $V = f(\text{OCV})$  representation is some kind of universal curve, as it uniquely describes all three LMR-NCMs independent of their degree of over-lithiation. There is obviously a close relationship between the crystal lattice dimensions and the open circuit voltage, but we do not yet know which structural and/or electronic parameter(s) command them.

As already noted above, the overall relative volume change of  $\Delta V/V_0 \approx 2.5\%$ – $3.0\%$  in the second cycle over an SOC range of  $\Delta \text{SOC} \approx 240$ – $270 \text{ mAh g}^{-1}_{\text{CAM}}$  for all of the here examined LMR-NCMs, almost independent of their degree of over-lithiation ( $\delta = 0.14$ – $0.20$ ), is much smaller than that of NCM-811 that exhibits  $\Delta V/V_0 \approx 6.3\%$  for  $\Delta \text{SOC} \approx 220 \text{ mAh g}^{-1}_{\text{CAM}}$ . Based on this, one would expect that the tendency for CAM particle cracking should be reduced for LMR-NCMs compared to Ni-rich NCMs.

**Determination of the lithium and transition metal layer heights.**—Before discussing possible reasons of the observed hysteresis phenomena, let us first deconvolute the lattice parameter  $c$ . This requires a determination of the  $z$ -coordinate of oxygen,  $z_{\text{O},\text{O}}$ , in order to calculate the lithium,  $h_{\text{Li}}$ , and TM layer heights,  $h_{\text{TM}}$ , according to<sup>60</sup>

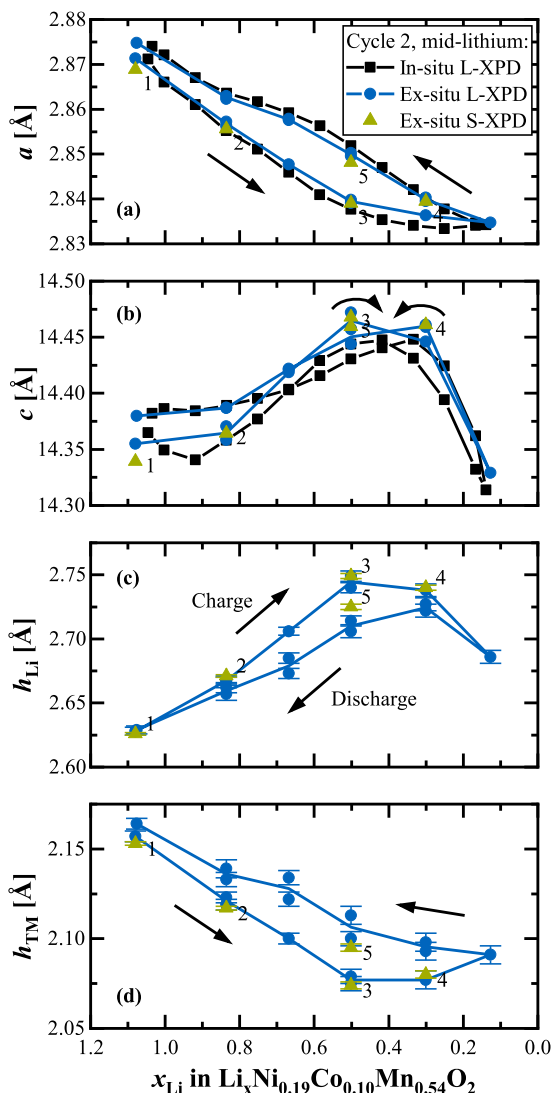


**Figure 5.** Determination of structural parameters over the course of the second charge/discharge cycle of the mid-lithium LMR-NCM material based on ex-situ XPD data from harvested electrodes, either acquired at the laboratory diffractometer (L-XPD; blue circles, with blue lines connecting their average values) or at the synchrotron (S-XPD; green triangles, labeled with numbers: 1/2/3 on the charge branch and 4/5 on the discharge branch). (a), (b) Lattice parameters  $a$  and  $c$  derived from ex-situ L-XPD and S-XPD data, including a comparison with the in-situ L-XPD derived data shown in Fig. 1. (c), (d) Determination of the lithium layer height,  $h_{\text{Li}}$ , and of the transition metal layer height,  $h_{\text{TM}}$ , via Rietveld refinements using the following rhombohedral model:  $[\text{Li}_{x-u}\text{Ni}_v]_{3a}[\text{Li}_u\text{TM}_{0.83-v}]_{3b}[\text{O}_w]_{6c}$  with  $u_{\text{Li}} = 0$  (except for the completely discharged samples with  $x_{\text{Li}} > 1$ , so that the occupation of the Li layer would be mistakenly greater than 1) and  $w_{\text{O}} = 1$ . The error bars correspond to the estimated standard deviation (e.s.d.) of each sample, as given out by the refinement program. Please note that some points of the ex-situ L-XPD dataset were measured twice with two independent samples.

$$3a \text{ site: } h_{\text{Li}} = 2 \cdot (1/3 - z_{6c,\text{O}}) \cdot c \quad [2]$$

$$3b \text{ site: } h_{\text{TM}} = 2 \cdot (z_{6c,\text{O}} - 1/6) \cdot c = 1/3 \cdot c - h_{\text{Li}} \quad [3]$$

Please note that the definition of the 3a/3b sites as Li/TM layers might also be opposite to that which is used in some instances in the literature.

The layer heights are a good starting point for Rietveld refinements. Liu et al. have shown in a detailed study about the sensitivity of the analysis of diffraction data (with stoichiometric NCA as a test case) that  $z_{6c,\text{O}}$  is barely correlated to any other structural parameter.<sup>39</sup> It is thus the structural parameter that can be determined most accurately from X-ray powder diffraction data. Since in-situ data are usually biased due to overlapping reflections from other cell components (e.g., Al)<sup>41</sup> and have low counting statistics (in particular at laboratory diffractometers), which makes the detailed evaluation of structural parameters (other than lattice parameters) really challenging, we decided to rely just on ex-situ data for Rietveld refinements. Here, the cathode was cycled to the desired SOC, then the CAM powder was scratched off and air-tightly sealed in capillaries (see Experimental section for more details). Focusing on the quasi-reversible hysteresis after activation, Fig. 5 shows the Rietveld refinement results of the mid-lithium material within the second cycle, where ex-situ L-XPD measurements were conducted every  $\approx 50 \text{ mAh g}^{-1}$  during charge/discharge (blue circles/lines). Additionally, we sent some samples to the Swiss Light Source to obtain high-quality ex-situ S-XPD data (green triangles). The two upper panels of Fig. 5 compare the lattice parameters to the in-situ L-XPD data from V 1 (black squares/lines), while the layer heights,  $h_{\text{Li}}$  and  $h_{\text{TM}}$ , derived from the ex-situ XPD data are depicted in the two lower panels.

The lattice parameters  $a$  and  $c$  derived from ex-situ L-XPD data are in good agreement with those derived from in-situ L-XPD data and show the same characteristic hysteresis features. For the lattice parameter  $a$  in Fig. 5a, the ex-situ determined hysteresis loop (blue circles/line) is however slightly smaller, as the data points lie consistently in between the in-situ determined values (black squares/line). This might be due to a continued relaxation of the material within the first hours and days after transitioning into the OCV condition. In contrast, the lattice parameter  $c$  (see Fig. 5b) is shifted upwards for most of the ex-situ derived data, especially at  $x_{\text{Li}}$  values smaller than  $\approx 0.8$ . Even though the shifts of  $a$  and  $c$  are not all in the same direction, the observed differences could be at least partially explained by a small misalignment of the in-situ pouch cell (see also Fig. S4 of the SI). Whatever the reason for these relatively small differences might be, a comparison of the ex-situ L-XPD derived lattice parameters that were measured within a few days after cell disassembly (blue circles) and those obtained by ex-situ S-XPD that were measured only after  $\approx 5$  months (green triangles) are in excellent agreement. This proves that the extended storage in the glass capillaries does not affect the harvested electrode samples (in call cases, the samples were sealed into the glass capillaries immediately after harvesting the electrodes), which is an important prerequisite for the much more time-consuming NPD experiments presented later. Furthermore, we can conclude here that the ex-situ approach is suitable for the quantification of detailed structural parameters under defined state of charge conditions.

The individual components  $h_{\text{Li}}$  and  $h_{\text{TM}}$  of the lattice parameter  $c$  are derived from ex-situ XPD data and presented in Figs. 5c and 5d, respectively. Surprisingly, their hysteresis behavior is much simpler than that of  $c$  (see Fig. 5b), because the charge branch is permanently higher than the discharge branch for  $h_{\text{Li}}$  or vice versa for  $h_{\text{TM}}$ . The general evolution of  $c$  over the charge/discharge cycle is dominated by the  $h_{\text{Li}}$  component (since its changes are typically higher than the changes of  $h_{\text{TM}}$ ),<sup>33,63</sup> which is why any changes of  $c$  are typically explained with respect to this component (as we also did in the previous paragraphs). On the other hand, the evolution of the  $h_{\text{TM}}$  component resembles that of the lattice parameter  $a$  (see Fig. 5a). This means that the contraction/expansion of the  $\text{TM-O}_6$  octahedra in the TM layer is fairly isotropic, as they respond uniformly in the  $ab$  plane (seen in  $a$ ) and along the  $c$  direction (seen in  $h_{\text{TM}}$ ) to the actual oxidation state (and ionic radius) of the TMs.<sup>63</sup>

Let us shortly comment on the accuracy of the quantification of the layer heights. Their relative error of 0.10%–0.25% (based on the estimated standard deviation given by the refinement program and

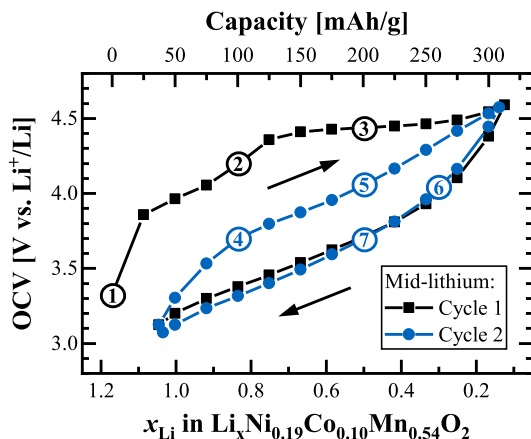


**Figure 6.** Selection of data points for the joint Rietveld refinement of ex-situ L-XPD and NPD data from the mid-lithium LMR-NCM, illustrated via the OCV vs SOC curves for the first (in black) and second charge/discharge cycle (in blue). The curves were extracted from the data shown in Fig. 1, which were recorded at C/10 with intermittent OCV periods. Using a nomenclature that specifies the cycle number (#), whether it is a charge or discharge step (CHA or DIS), and the measured SOC (in mAh g<sup>-1</sup>), the points marked in the figure, given in chronological order, correspond to: ① pristine, ② #1-CHA-100, ③ #1-CHA-200, ④ #2-CHA-100, ⑤ #2-CHA-200, ⑥ #2-DIS-260, and ⑦ #2-DIS-200.

marked by the error bars in Figs. 5c, 5d) is roughly one order of magnitude higher than that of the lattice parameter  $c$ . The reproducibility among two nominally identical data points is fairly good, even though some other structural parameters might differ strongly (especially  $v_{\text{Ni}}/\text{Ni}_{\text{Li}}$  and  $b_{3a,\text{Li}}$ ). This underlines the weak interdependence of  $z_{6c,\text{O}}$  with other structural parameters.<sup>39</sup> Comparing the L-XPD to the S-XPD data, they coincide nicely on the charge branch (S-XPD data points 1, 2 and 3), but there are deviations on the discharge branch (points 4 and 5; note that the high-SOC point 4 appears to be on the charge branch). Taking all this into consideration, we believe that the ex-situ XPD data correctly describe the separation of the charge/discharge curves, but that the actual values of the layer heights and thus the extent of hysteresis have some uncertainty.

**Origin of the reversible structural changes.**—In the literature, hysteresis phenomena in Li- and Mn-rich layered oxides are usually ascribed to a path dependence of TM migration,<sup>28,29,36,71</sup> which was first proposed by the Argonne National Laboratory.<sup>18,23,27</sup> This migration process might involve both Ni and/or Mn moving from their native spot in the TM layer into tetrahedral and/or octahedral sites in the Li layer. As long as this process is reversible, it is believed that it causes the voltage hysteresis during charge/discharge cycling, whereas the irreversible capture of TMs in the Li layer would lead to voltage fade during long-term cycling. Assat et al. reported instead that the anionic redox is the real cause for hysteresis phenomena and that any structural rearrangements are just a consequence of that.<sup>24</sup> On the other hand, Gent et al. proposed a coupled  $\{\text{O}^{2-} + \text{TM}\} \rightarrow \{\text{O}^- + \text{TM}_{\text{mig}}\} + e^-$  process, where  $\text{TM}_{\text{mig}}$  indicates a migrated TM into the Li layer, thus combining both afore-mentioned theories.<sup>30</sup> House et al. showed a link between the superstructure ordering and the anionic redox. Both in alkali-rich  $\text{Na}_x[\text{Li}_\delta\text{Mn}_{1-\delta}]\text{O}_2$  compounds<sup>72</sup> and in  $\text{Li}_{1.20}\text{Ni}_{0.13}\text{Co}_{0.13}\text{Mn}_{0.54}\text{O}_2$ ,<sup>31</sup> they showed that molecular  $\text{O}_2$  is reversibly formed and trapped in the bulk, which would connect the voltage hysteresis to the in-plane TM migration in the TM layer (after  $\text{Li}_{\text{TM}}$  removal).<sup>72</sup> Recently, Csernica et al. proposed an oxygen vacancy model, where the oxygen deficiency penetrates into the bulk of the material by a diffusion process, while maintaining the native layered phase.<sup>40</sup> An oxygen vacancy leads to an undercoordinated transition metal, which promotes its migration into the Li layer. Csernica’s model

provides an atomistic link between cation disordering and oxygen release, both of which occur progressively upon cycling and could thus explain together the voltage fade.<sup>40</sup>

Assat et al. and Gent et al. are one of the few publications who quantified the extent of anionic redox and/or TM migration within one cycle and visualized their path dependence as a function of SOC (as we have done for the lattice dimensions in Figs. 1 and 5). Their results are however not identical. Assat et al. have shown by HAXPES measurements for  $\text{Li}_{1.20}\text{Ni}_{0.13}\text{Co}_{0.13}\text{Mn}_{0.54}\text{O}_2$  within the first two cycles that the fraction of oxidized lattice oxygen, %  $\text{O}^{n-}$ , is consistently higher during charge than during discharge (see Fig. 2 in their paper).<sup>24</sup> In contrast, Gent et al. reported for  $\text{Li}_{1.17}\text{Ni}_{0.21}\text{Co}_{0.08}\text{Mn}_{0.54}\text{O}_2$  within the first activation cycle that %  $\text{O}^{n-}$  (measured by STXM-XAS) and %  $\text{TM}_{\text{Li}}$  (measured by S-XPD) are smaller during charge than during discharge (see Fig. 6 in their paper).<sup>30</sup> Even though Assat et al. mention that their result conflicts with the hysteresis loop of the Ni oxidation state (which shows the same trend, but should be opposite for charge balancing), there is obviously not a general consensus yet in the literature—at least when attempting to quantify these sensitive parameters which are apparently difficult to determine.

The structural parameters determined in the present study might help to qualitatively track the path dependence during charge/discharge. Assuming a significant fraction of %  $\text{O}^{n-}$  and/or %  $\text{TM}_{\text{Li}}$ , the O-O repulsion in the Li layer gets reduced compared to 0%  $\text{O}^{n-}$  and/or  $\text{TM}_{\text{Li}}$ , what leads to smaller  $h_{\text{Li}}$  values. On the other hand, the TM-O attraction in the TM layer might get reduced as well, what in turn increases  $a$  and  $h_{\text{TM}}$ . According to the observed trends in Fig. 5 ( $h_{\text{Li}}$ : charge > discharge;  $a$  and  $h_{\text{TM}}$ : charge < discharge), these considerations support the findings by Gent et al.<sup>30</sup> In a simplified picture, the anionic redox and/or TM migration mainly occur at high SOC during charge, but revert at low SOC during discharge, i.e., the hysteresis is maximized in the mid-SOC regime (what is actually true for the OCV and lattice dimensions; see Figs. 1 and 5). It is however not really clear where the (energetic) penalty for such a huge delay comes from Refs. 23, 27, 73. An alternative explanation for the analogous hysteresis of  $a$  and  $h_{\text{TM}}$  is the path dependence of the cationic redox, which is spectroscopically easier to access than the anionic redox and which basically follows the OCV hysteresis.<sup>24,25</sup> The large number of (potentially) hysteretic parameters, including the open circuit voltage, lattice parameters, TM migration, cationic and anionic redox, raises the fundamental question about their “true” causal chain, which is lively discussed in the literature. Since there are so many different perspectives at the moment, it is difficult, if not impossible, to unequivocally assign the lattice parameter hysteresis to one particular parameter.

To break complexity down, we want to focus on TM migration in the following. The distribution of transition metals in Li- and Mn-rich layered oxides is usually investigated by (i) diffraction, using either XPD<sup>30,45,74–76</sup> or NPD data,<sup>29,44</sup> and (ii) a combination of microscopy techniques such as HAADF-STEM, EELS, and electron diffraction.<sup>77–79</sup> While microscopy is a local probe, which often resolves changes of the TM arrangement close to the particle surface, diffraction is a bulk method, which allows quantifying the TM distribution by the use of proper structural models to obtain average information for the entire CAM particle. There are single examples of other techniques such as X-ray diffraction spectroscopy (XDS),<sup>71,80</sup> atomic resolution STEM-EDS mapping,<sup>81</sup> and <sup>6</sup>Li MAS NMR spectroscopy,<sup>28</sup> but they are not used on a routine basis. Despite being the main technique, diffraction is full of pitfalls, especially due to the possible correlation of interdependent (structural) parameters, which hampers their precise quantification.<sup>39</sup> This problem can be minimized by the joint Rietveld refinement of complementary diffraction datasets, typically XPD and NPD,<sup>82–84</sup> but there are also a few examples in the battery field about the additional use of resonant X-ray diffraction (at energies close to the K edge of the transition metals).<sup>37,38,85</sup> As the scattering power of the elements varies among these different datasets, the joint

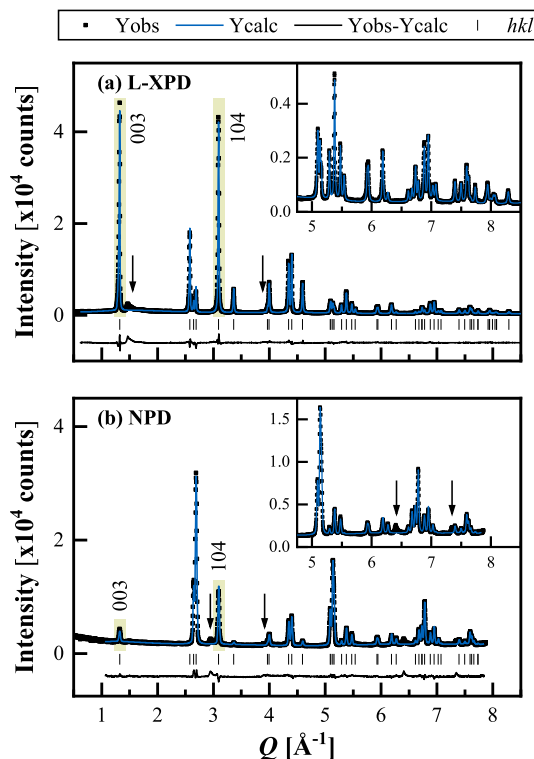


**Figure 7.** Joint Rietveld refinement of the pristine mid-lithium LMR-NCM powder, using (a) the L-XPD and (b) the NPD dataset with the rhombohedral model 2 (described later in detail). The observed (black points), calculated (blue lines), and difference diffraction profiles (black lines) are shown together with the position of the Bragg peaks (black ticks) as a function of  $Q$  (in order to compensate for different wavelengths;  $Q = 4\pi/\lambda \cdot \sin \theta = 2\pi/d$ ). The insets show a magnification of the high- $Q$  range. The arrows indicate superstructure peaks due to in-plane ordering in the TM layer, which are not described by the rhombohedral model. The green highlighted regions mark the (003) and (104) reflections.

**Table II.** Fractional contribution of the scattering power from each crystallographic site relative to the total scattering power of the compound at  $2\theta = 0$ ,  $f_i^*$ , as described by Yin et al.<sup>89</sup> The calculation is done for the ideal composition of the pristine mid-lithium LMR-NCM,  $[\text{Li}]_{3a}[\text{Li}_{0.17}\text{Ni}_{0.19}\text{Co}_{0.10}\text{Mn}_{0.54}]_{3b}[\text{O}]_{6c}$ , using X-ray form factors of neutral atoms ( $f_{\text{Li}} = 3$ ,  $f_{\text{Ni}} = 28$ ,  $f_{\text{Co}} = 27$ ,  $f_{\text{Mn}} = 25$ , and  $f_{\text{O}} = 8$ ; all in number of electrons) and neutron scattering lengths as implemented in Topas ( $f_{\text{Li}} = -1.9$ ,  $f_{\text{Ni}} = 10.3$ ,  $f_{\text{Co}} = 2.49$ ,  $f_{\text{Mn}} = -3.73$ ,  $f_{\text{O}} = 5.803$ ; all in fm).<sup>48</sup>

Crystallographic site		Fractional scattering power	
		XPD	NPD
3a (Li layer)	$f_{3a,\text{Li}}^*$	0.073	0.139
3b (TM layer)	$f_{3b,\text{TM}}^*$	0.537	0.010
6c (O layer)	$f_{6c,\text{O}}^*$	0.390	0.851

refinement approach allows refining more elements on a single crystallographic site than only one dataset could do. This is in particular advantageous for Li- and Mn-rich layered oxides, because (i) Li can be extracted from two layers ( $\text{Li}_{\text{Li}}$  vs  $\text{Li}_{\text{TM}}$ ), and (ii) both Ni and Mn are considered to migrate into the Li layer ( $\text{Ni}_{\text{Li}}$  vs  $\text{Mn}_{\text{Li}}$ ). In contrast to XPD, where the X-ray atomic form factor scales with the number of electrons in the atom, NPD is sensitive to light elements (such as Li and O) and to elements with similar atomic numbers (such as Ni and Mn), as the neutron scattering length varies irregularly with atomic number and isotope.<sup>39</sup>

Figure 6 shows the OCV curve of the mid-lithium LMR-NCM plotted vs the lithium content for the first and second cycle, marking the selected samples of harvested cathodes for the combined refinement of ex-situ L-XPD and NPD data. Here, NPD needs CAM powder in the gram scale, which was prepared in multi-layer pouch cells (see Experimental section for more details). Apart from the pristine LMR-NCM (sample ①), we chose two samples from the first charge (②+③), two from the second charge (④+⑤), and two from the second discharge (⑥+⑦). During the first activation charge (in black), sample ② is at the end of the sloping region, whereas ③ resides in the middle of the voltage plateau. Their comparison might allow discerning the lithium extraction mechanism ( $\text{Li}_{\text{Li}}$  vs  $\text{Li}_{\text{TM}}$ ). For the quasi-reversible hysteresis of the second cycle (in blue), we selected charge/discharge samples with either the same SOC or lithium content (i.e., ⑤↔⑦ in Fig. 6) or with the same OCV (and thus the same unit cell volume, i.e., ④↔⑦ and ⑥↔③), analogous to what was done by Mohanty et al.<sup>29</sup> Even though the number of data points is too little to resolve any hypothetical hysteresis loop of TM migration, their comparison might help to answer the question whether the amount of migrated TMs is similar at a given SOC or at a given OCV and hence whether there is any correlation to the lattice dimensions.

**L-XPD and NPD diffractograms.**—Before moving on to the Rietveld refinement results, it is worth to have a look on the diffractograms. Figure 7 shows the L-XPD and NPD diffractograms of the pristine mid-lithium LMR-NCM, which was measured as pure powder. We used a rhombohedral model for the combined refinement, as will be discussed later in detail. Both datasets cover a similar  $Q$  range and have comparable intensities, thus contributing equally to the refinement.

The in-plane Li/TM ordering in the TM layer is typically discussed on the basis of the small superstructure reflections following the intense (003) peak in the L-XPD pattern (at  $\approx 1.4\text{--}2.0 \text{ \AA}^{-1}$ , marked by the left arrow in Fig. 7a). Interestingly, there are several peaks at  $\approx 2.9$ ,<sup>44,86</sup>  $\approx 3.9$ ,<sup>86</sup> and  $\approx 7.3 \text{ \AA}^{-1}$  in the NPD pattern (as highlighted by the arrows in Fig. 7b), which are also not included in the rhombohedral model. They are only described by the monoclinic model and are thus another indicator for Li/TM ordering (see monoclinic refinement in Fig. S7 in paragraph S3 of the SI). As the ordering is not perfect, both in  $c$  direction (due to the presence of stacking faults) and in the  $ab$  plane (due to the off-stoichiometric Li/TM ratio), the superstructure peaks are quite broad and have a low intensity.<sup>82,86,87</sup> The peak at  $\approx 3.9 \text{ \AA}^{-1}$  in the NPD profile also appears in the L-XPD pattern (better visible on a logarithmic intensity scale).

To qualitatively estimate the cation mixing in pristine layered oxides, it is common to compute the integrated intensity ratio of the (003) and (104) reflections from XPD data (higher ratios point towards less migrated TMs).<sup>60,88</sup> While these two reflections are the most intense peaks in the L-XPD pattern, they are relatively weak in the NPD pattern (see yellow highlighted regions in Fig. 7). This discrepancy raises the question about the sensitivity of the NPD dataset with regard to the quantification of TM migration. Here, it is useful to apply the “diffraction parameter space” concept introduced by Yin et al.<sup>89</sup> which allows calculating the zero-angle scattering power,  $f_i^*$ , of each crystallographic site  $i$  according to

$$f_i^* = \frac{m_i \cdot \left| \sum_{\text{all atoms } j \text{ on site } i} c_j \cdot f_j \right|}{\sum_{\text{all sites } i} m_i \cdot \left| \sum_{\text{all atoms } j \text{ on site } i} c_j \cdot f_j \right|} \quad [4]$$

where  $m_i$  is the multiplicity,  $c_j$  the fractional occupancy, and  $f_j$  the scattering power of each atom  $j$  residing at the site  $i$ . This term is normalized by the sum over all sites. Consequently,  $f_i^*$  is the fractional contribution of the scattering power from each crystallographic site  $i$  relative to the total scattering power of the compound at  $2\theta = 0$ , with  $\sum_{\text{all sites } i} f_i^* = 1$ . As described in more detail

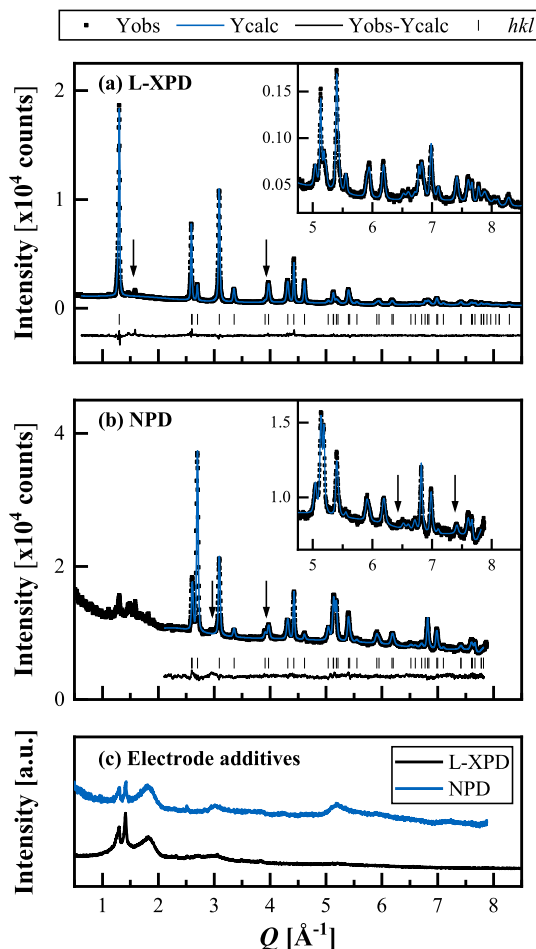


**Figure 8.** Joint Rietveld refinement of the harvested electrode sample #2-CHA-200 (specified in Fig. 6), using (a) the L-XPD and (b) the NPD dataset with the rhombohedral *model 2*. As for all harvested electrode samples (Ⓜ–Ⓢ), the minimum  $Q$  value for fitting the NPD pattern,  $Q_{\min}^{\text{NPD}}$ , was set to  $2.1 \text{ \AA}^{-1}$ . The arrows indicate the expected positions of the superstructure peaks. Panel (c) shows the diffraction patterns of a 1/1 g/g mixture of conductive carbon (Super C65) and PVDF binder (Solef 5130) on an arbitrary intensity scale.

in the original publication by Yin et al.,<sup>89</sup> this concept is based on the simplified scenario for the hypothetical  $F_{000}$  reflection, where the phase factor  $\omega_i$  of the site  $i$  is 1, and therefore the net scattering power of the  $m$  atoms comprising on this site is equal to  $m$  times the scattering power of a single one of these atoms. The individual scattering power of each atom,  $f_j$ , either corresponds to the X-ray atomic form factor or the neutron coherent scattering length.

In the rhombohedral model, there are three octahedral sites: 3a (Li layer), 3b (TM layer), and 6c (O layer). Table II summarizes their fractional scattering power,  $f_i^*$ , for the “ideal” pristine mid-lithium LMR-NCM (without any cation mixing) in both datasets. In the XPD pattern, the TM layer has the strongest scattering power amounting to  $\approx 54\%$  due to the high number of electrons, whereas the O and Li layer amount to  $\approx 39\%$  and  $\approx 7\%$ , respectively. Thus, all sites have a measurable contribution to the diffractogram. This is in stark contrast with the NPD pattern, which is dominated by the O layer with a share of  $\approx 85\%$ , whereas the TM layer contributes only with  $\approx 1\%$  to the total scattering power. The unfavorable combination of Ni (medium abundance and high positive scattering length, see caption of Table II) and Mn (high abundance and negative scattering length, see caption of Table II) effectively cancels out the scattering power of this site. The domination of the O layer is not altered by lithium extraction (in cycled samples) or by the incorporation of occupancy defects such as TM migration (e.g.,

$\text{Ni}_{\text{Li}}$  and  $\text{Mn}_{\text{Li}}$ ) and oxygen vacancies (considering that the expected extent of these defects is less than 10%). We conclude that the sensitivity of the recorded NPD patterns for the quantification of site occupancy factors in this particular compound is not as high as typically believed in the literature.

Figure 8 illustrates the diffractograms of the cycled sample #2-CHA-200 (see also Fig. 6). All harvested electrode samples have in common that the NPD background is substantially increased compared to the pristine LMR-NCM powder (compare Figs. 8b with 7b), probably due to the presence of hydrogen in the PVDF binder and electrolyte residuals (hydrogen has a large incoherent neutron scattering cross-section).<sup>29,90</sup> Furthermore, there are several foreign reflections in the  $Q$  range of  $1\text{--}2 \text{ \AA}^{-1}$ . According to the simple mixture of conductive carbon and PVDF binder (at a mass ratio of 1/1) in Fig. 8c, these reflections could be mainly assigned to the two electrode additives. As hydrogen and carbon are relatively strong neutron scatterers, the electrode additives are much more visible in the NPD profile than in the L-XPD pattern. Consequently, the weak (003) reflection in the NPD pattern had to be omitted from the joint refinement of harvested electrode samples ( $Q_{\min}^{\text{NPD}} = 2.1 \text{ \AA}^{-1}$  for the samples Ⓜ–Ⓢ in Fig. 6). On the other hand, the superstructure peaks (expected positions indicated by the arrows in Fig. 8) are either superimposed by stronger reflections of the LMR-NCM phase and the electrode additives or they are difficult to distinguish from the background. This applies to all other harvested electrode samples as well, which is why we decided to additionally exclude the first superstructure region in the L-XPD pattern from any monoclinic refinement ( $1.4 < Q_{\text{excluded}}^{\text{L-XPD}} < 2.3 \text{ \AA}^{-1}$ ), because the electrode additives’ peaks might falsify the refinement results. For the sake of comparability and due to their poor description without any extra broadening, these peaks were also excluded from the monoclinic refinement of the pristine LMR-NCM powder sample.

**Results of the joint Rietveld refinement.**—In the literature, there are numerous structural models used for the Rietveld refinement of diffraction data from Li- and Mn-rich layered oxides, which reach from rhombohedral to monoclinic all the way to composite models with increasing complexity. In Table SV in paragraph S4 of the SI, we tried to give an overview of structural models by comparing 15 publications from different research groups (i.e., with respect to the investigated CAM, the type of diffraction data, and the number of refined structural parameters). Here, we made the following observations: (i) In some publications, it is not clear how all of the structural parameters are actually treated during the refinement (especially atomic displacement parameters, ADPs). This makes it difficult for the reader to evaluate the quality of the applied model. (ii) Even for the same base model, the amount of refined (or constrained) structural parameters might differ significantly (especially site occupancy factors, SOFs). A high number of refined parameters potentially causes severe correlations and thus restricts their validity. (iii) Finally, the application of composite models is in our opinion mostly not well justified on the basis of the raw data, e.g., by the occurrence of peak splitting. It is further not always clear how the overall composition is maintained when the phase fractions are freely refined (without adapting, e.g., the TM distribution among the two phases).

Since the literature reports are largely different, we want to start the joint Rietveld refinement with a simple rhombohedral model for the X-ray and neutron diffraction data of the mid-lithium LMR-NCM material (with the sample specifications given in Fig. 6). This model referred to as *model 1* looks as follows in the crystallographic notation:  $[\text{Li}_{x-u}\text{Ni}_v]_{3a}[\text{Li}_u\text{TM}_{0.83-v}]_{3b}[\text{O}_w]_{6c}$  (corresponding to  $\text{Li}_{x-u}\text{Ni}_v[\text{Li}_u\text{TM}_{0.83-v}]\text{O}_{2w}$  in the formula unit notation). Here, the three most common fractional occupancies are freely refined: (i) the Li distribution in the Li/TM layers, which finds expression in the parameter  $u_{\text{Li}}$  (equivalent to  $\text{Li}_{\text{TM}}$ ), (ii) the migrated Ni into the Li layer ( $v_{\text{Ni}}$ , equivalent to  $\text{Ni}_{\text{Li}}$ ), and (iii) the oxygen vacancies ( $w_{\text{O}}$ , equivalent to O). The overall lithium content,  $x_{\text{Li}}$ , is determined by the SOC of the cycled samples according to Eq. 1. Since the 3a/

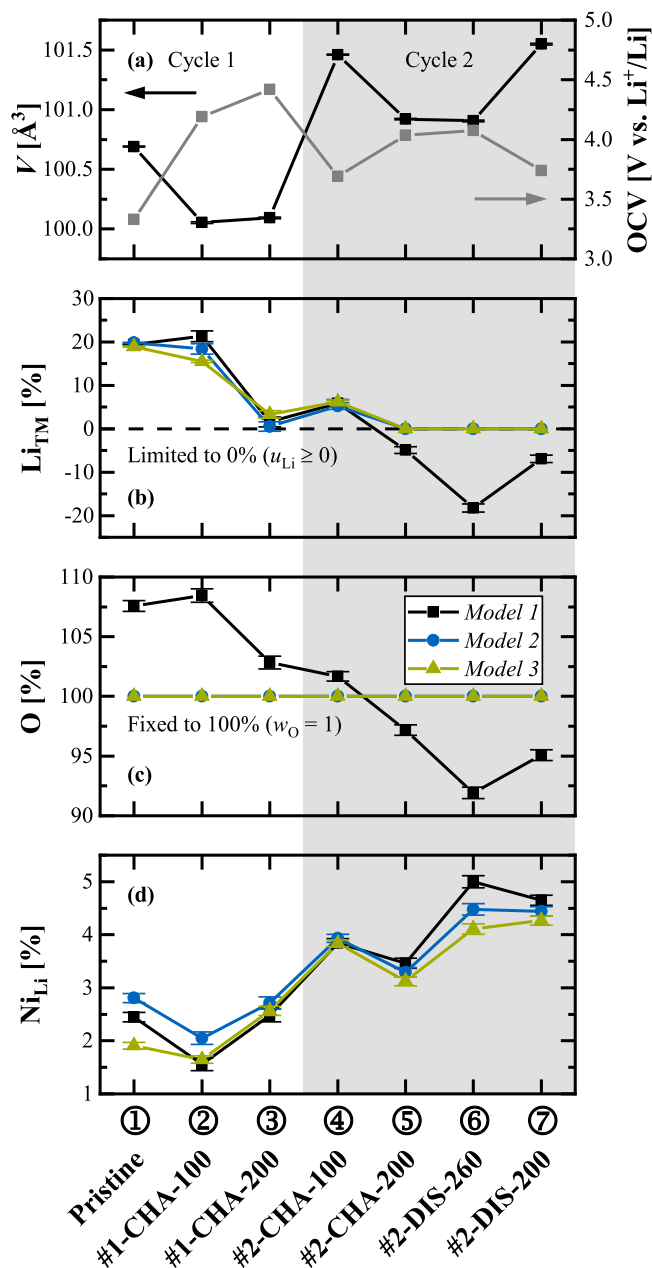


**Figure 9.** Summary of the combined L-XPD and NPD Rietveld refinement for the seven mid-level LMR-NCM samples described in Fig. 6. (a) Refined unit cell volume (in the rhombohedral representation; left y-axis) and open circuit voltage after 2 h (right y-axis). The following panels show the refined (or fixed) amount of (b) lithium in the TM layer ( $\text{Li}_{\text{TM}} = u_{\text{Li}} \cdot 100\%$ ), (c) oxygen in the O layer ( $\text{O} = w_{\text{O}} \cdot 100\%$ ), and (d) nickel in the Li layer ( $\text{Ni}_{\text{Li}} = v_{\text{Ni}} \cdot 100\%$ ) according to three different structural models: (i) the extended rhombohedral *model 1* with  $[\text{Li}_{x-u}\text{Ni}_v\text{Li}_{3a}[\text{Li}_u\text{TM}_{0.83-v}]_{3b}\text{O}_{w/6c}]$ , (ii) the simplified rhombohedral *model 2* ( $u_{\text{Li}} \geq 0$ ,  $w_{\text{O}} = 1$ ), and (iii) its monoclinic counterpart, *model 3*, which also accounts for the in-plane Li/TM ordering in the TM layer. The overall lithium content,  $x_{\text{Li}}$ , is determined by the state of charge (see Eq. 1). For further refinement results see Tables SII-SIV in paragraph S3 of the SI. The gray highlighted area marks the refinement results for the electrode samples harvested in the second cycle.

3b metal sites are fully occupied in the pristine state,  $u_{\text{Li}}$  and  $v_{\text{Ni}}$  are constrained with respect to each other ( $u_{\text{Li}} = 0.17 + v_{\text{Ni}}$  at  $x_{\text{Li}} = 1.17$ ). This reduces the number of freely refined site occupancy factors (SOFs) to two. The calculated values of  $\text{Li}_{\text{TM}}$ ,  $\text{Ni}_{\text{Li}}$ , and  $\text{O}$ , which represent the afore-mentioned SOFs in percentage terms, are summarized in Fig. 9 for all seven samples (together with their unit cell volume and OCV).

Starting with  $\text{Li}_{\text{TM}}$  (see black data points for *model 1* in Fig. 9b), the lithium occupation in the transition metal layer stays at its pristine value of  $\approx 20\%$  until the end of the sloping region (sample ②), but drops to  $\approx 2\%$  in the middle of the first charge plateau (③) and reaches even negative values in the second cycle (⑤–⑦), which are physically meaningless, but mathematically possible in the least squares refinement (without applying any constraints with respect to the SOFs). This result is qualitatively in line with the operando NPD study of Liu et al.,<sup>66</sup> who reported that the delithiation mechanism operates solely through the extraction of lithium from the lithium layer ( $\text{Li}_{\text{Li}}$ ) in the sloping region, but involves the extraction of lithium from the transition metal layer ( $\text{Li}_{\text{TM}}$ ) during the activation plateau, whereby the latter cannot be re-intercalated within the first discharge (constant level of  $\approx 6\%$ – $7\%$  in their study). We observe  $\approx 6\%$   $\text{Li}_{\text{TM}}$  for sample ④ at the beginning of the second charge (#2-CHA-100). Since the SOC provides a lower limit of the actual lithium content due to the possibility of parasitic reactions at high voltages,<sup>39,84</sup>  $x_{\text{Li}}$  is definitely greater than 1 in the discharged state ( $x_{\text{Li}} \approx 1.05$  at the end of the first discharge, see lower x-axis in Fig. 6), what in turn imposes the partial occupation of  $\text{Li}_{\text{TM}}$  after activation.

Approaching the delithiation process by DFT simulation of the model material,  $\text{Li}_{60}[\text{Li}_{12}\text{Ni}_{12}\text{Co}_6\text{Mn}_{30}]\text{O}_{120}$ , Table SVI in paragraph S5 of the SI shows that the potential energy surface for these systems exhibits a multitude of nearly degenerate local minima for each delithiation step. We start the analysis considering the removal of 13 Li ( $x_{\text{Li}} = 0.98$ ). Among the calculated structures, it is energetically more favorable to remove Li from the Li layer only, leaving the 12 Li in the TM layer intact. The layered structure is retained; of the 47 Li in the Li layer, only one in the central layer seems to have changed its coordination to tetrahedral. Further delithiation of in total 42 Li ( $x_{\text{Li}} = 0.50$ ) brings us experimentally to the middle of the voltage plateau in the first charge. By DFT, we found that the most stable structure was achieved by removing all Li from the TM layer, while maintaining the layered structure. An alternative model where 6 Li still reside in the TM layer has been found to be 18 meV/atom higher in energy. To sum up, the DFT results qualitatively agree with the experimental data of the first activation charge. Hence, we are confident that the CAM activation follows the energetically favorable delithiation pathway.

The oxygen content of *model 1* in Fig. 9c changes from almost +10% to  $-10\%$  upon progressive cycling. Former gassing studies of the mid-lithium material suggest the oxygen release to be on the order of  $\approx 3\%$  within the first two cycles, originating from the near-surface region of the primary particles.<sup>13,59</sup> Despite the presence of intragranular nanopores in pristine CAMs and further intragranular cracking upon cycling, which inject oxygen vacancies also into the bulk lattice,<sup>68,91,92</sup> the refined level seems to be unlikely. Recently, Csernica et al. estimated the oxygen release, including bulk oxygen vacancies, for a similar LMR-NCM material ( $\delta = 0.18$ ) on the basis of XAS data.<sup>40</sup> They reported  $\approx 3.3\%$  lost oxygen after the first cycle, which is consistent with the gassing studies.<sup>13,59</sup> After 500 cycles, the oxygen release amounted to  $\approx 6.5\%$  and is thus far below the here refined changes of almost 20% within the first two cycles. This variation also exceeds the maximum of  $\approx 10\%$  of reversibly trapped lattice oxygen in the form of molecular  $\text{O}_2$ , as was reported by House et al.<sup>31</sup> Beyond that, O values greater than 100% are again physically meaningless and the parameter  $w_{\text{O}}$  is strongly correlated to the NPD scale factor ( $\approx 70\%$ – $80\%$ ), which can be explained by the overwhelming scattering power from the O layer in the NPD pattern (see Table II). This makes the neutron data insensitive to the oxygen occupancy, as was also observed by Csernica et al.<sup>40</sup> In view of these findings, it seems to be reasonable to neglect oxygen vacancies from refinements of LMR-NCM samples within the initial cycles.

The refined amount of Ni migrated into the lithium layer,  $\text{Ni}_{\text{Li}}$ , lies in the range of  $\approx 1.6\%$  to  $\approx 5.0\%$  for all of the examined samples (see Fig. 9d). Gent et al. determined comparable  $\text{TM}_{\text{Li}}$  values from  $\approx 2.6\%$  in their pristine LMR-NCM until  $\approx 7.5\%$  at the end of the

first charge. Please note that their reported %  $\text{TM}_{\text{Li}}$  values are divided by the total TM stoichiometry, %  $\text{TM}_{\text{Li}}$  (as used by Gent et al.) =  $\text{TM}_{\text{Li}}$  (as used in this work)/(1- $\delta$ ) with  $\delta = 0.17$ .<sup>30</sup> Since NPD could help to differentiate the migrating TM species due to the sign of their neutron scattering length (Ni and Co positive, Mn negative), we also tried joint Rietveld fits with  $\text{Mn}_{\text{Li}}$  instead of  $\text{Ni}_{\text{Li}}$ . However, the refinements gave unreliable  $\text{Li}_{\text{TM}}$  values of up to  $\approx 40\%$  for the cycled samples. As Li and Mn have both negative neutron scattering lengths, they are highly correlated ( $\approx 80\%$ ) and it is thus not viable to refine their distribution in the metal layers simultaneously (analogous to the difficulty to differentiate the transition metals from XPD data). Refining simultaneously Li, Ni, and Mn would lead to a 100% correlation among the three parameters. In this context, we should recall that diffraction probes the scattering power of crystallographic sites, but not of their individual constituents. This restricts the number of simultaneously refined SOFs on a single site to the available number of complementary diffraction datasets. The combination of L-XPD and NPD, as used in this work, enables a maximum of two SOFs on the same site(s). If the scattering power of two elements is however unfavorably close in one of the datasets (e.g., Li and Mn in NPD, Ni and Mn in regular XPD), their simultaneous refinement might lead to severe correlations and hence to erroneous results.

Since *model 1* led, in part, to physically meaningless results, we explored another rhombohedral model, referred to as *model 2*, in which the lower limit for  $\text{Li}_{\text{TM}}$  is set to 0% ( $u_{\text{Li}} \geq 0$ ) and which assumes that there are no oxygen vacancies ( $w_{\text{O}} = 1$ ; see blue data points in Fig. 9). These constraints change the refined  $\text{Ni}_{\text{Li}}$  values by a maximum of 0.5% (absolute) for the samples ② and ③ compared to *model 1*, which is mainly driven by excluding oxygen vacancies ( $v_{\text{Ni}}$  and  $w_{\text{O}}$  are inversely proportional). In a former publication, we also refined the migrated Ni amount into the tetrahedral sites of the Li layer,  $\text{Ni}_{\text{Li}}^{\text{tet}}$ , for the completely charged state (at 4.6 V).<sup>36</sup> Including  $\text{Ni}_{\text{Li}}^{\text{tet}}$  to the mid/high-SOC samples ⑥ and ⑦ however leads to small values of  $\approx 1\%$ , in contrast to a constantly high level of  $\approx 8\%$ – $9\%$  over 100 cycles in the previous study (since  $\text{Ni}_{\text{Li}}^{\text{tet}}$  resides on a 6c site, its amount is calculated according to  $\text{Ni}_{\text{Li}}^{\text{tet}} = 2 \cdot \text{SOF}(6c) \cdot 100\%$  to enable direct comparability with the 3a/3b metal sites). We therefore did not include tetrahedral sites in any of the refinements. Replacing  $\text{Ni}_{\text{Li}}$  again by  $\text{Mn}_{\text{Li}}$ , while constraining  $\text{Li}_{\text{TM}}$  to remain constant, shows the same trend for the migrating TM.  $\text{Mn}_{\text{Li}}$  ( $\approx 2.1\%$ – $6.0\%$ ) is up to  $\approx 0.6\%$  higher than  $\text{Ni}_{\text{Li}}$  ( $\approx 2.0\%$ – $4.5\%$ ); only for sample ⑥  $\text{Mn}_{\text{Li}}$  is higher by  $\approx 1.5\%$  (see full comparison in Fig. S8 of the SI). Even though it is difficult to identify the migrating TM species by this comparison,  $\text{Ni}_{\text{Li}}$  is the preferred choice for the further analysis, because Ni can be simultaneously refined with Li, but Mn cannot.

Lastly, we also tested a monoclinic model, referred to as *model 3* (see green data points in Fig. 9), where the superstructure region in the L-XPD pattern was excluded from the refinement ( $1.4 < Q_{\text{excluded}}^{\text{L-XPD}} < 2.3 \text{ \AA}^{-1}$ , as discussed in the context of Fig. 8). This approach does not only consider the inter-layer Li/TM arrangement, but it also accounts for their in-plane ordering by dividing each layer into two crystallographic sites (Li layer: 2c/4h, TM layer: 2b/4g, O layer: 4i/8j). Due to the different multiplicities, special care must be taken to maintain the overall stoichiometry. The monoclinic *model 3* has the following crystallographic notation:  $[\text{Li}_{x-u}\text{Ni}_v]_{2c,4h}[\text{Li}_{3u}\text{Ni}_m\text{Mn}_p]_{2b}[\text{Ni}_{0.285-u/2-3v/2}\text{Co}_{0.15}\text{Mn}_{0.81-p/2}]_{4g}[\text{O}_w]_{4i,8j}$ , which translates into the formula unit  $\text{Li}_{x-u}\text{Ni}_v[(\text{Li}_u\text{Ni}_{0/3}\text{Mn}_p/3)^{2b}(\text{Ni}_{0.19-u/3-v}\text{Co}_{0.10}\text{Mn}_{0.54-p/3})^{4g}]\text{O}_{2w}$ . Since the in-plane Li/TM ordering matters mainly for the TM layer, the Li and O layer were not split into two parts (i.e., the distribution in these layers is homogenous). Beyond the known parameters  $u_{\text{Li}}$ ,  $v_{\text{Ni}}$  and  $w_{\text{O}}$  from the rhombohedral models,  $o_{\text{Ni}}$  and  $p_{\text{Mn}}$  describe the distribution of Ni and Mn in the TM layer, respectively. Please note that  $\text{Li}_{\text{TM}}$  was only put on the 2b site, as it is also the case in the archetypal  $\text{Li}_2\text{MnO}_3$  (=  $\text{Li}[(\text{Li}_{1/3})^{2b}(\text{Mn}_{2/3})^{4g}]\text{O}_2$ ).<sup>93</sup> Limiting  $\text{Li}_{\text{TM}}$  again to greater or equal than 0% ( $u_{\text{Li}} \geq 0$ ) and also neglecting oxygen vacancies ( $w_{\text{O}} = 1$ ), there is a maximum amount of four refined SOFs (viz.,  $u_{\text{Li}}$ ,  $v_{\text{Ni}}$ ,

$o_{\text{Ni}}$ , and  $p_{\text{Mn}}$ ). This number reduces to three for most of the cycled samples due to constraints ( $3u_{\text{Li}} + o_{\text{Ni}} + p_{\text{Mn}} \leq 1$  at the 2b site for the samples ② and ④,  $u_{\text{Li}} \geq 0$  for ③–⑦) and further to two for the pristine sample ① due to full occupation ( $u_{\text{Li}} = 0.17 + v_{\text{Ni}}$  and  $p_{\text{Mn}} = 0.49 - 3v_{\text{Ni}} - o_{\text{Ni}}$ ). The results are pretty close to the rhombohedral counterpart, *model 2*.  $\text{Li}_{\text{TM}}$  agrees within  $\pm 3\%$  and  $\text{Ni}_{\text{Li}}$  differs at the maximum by  $\approx 0.4\%$  (for the samples ② and ③) and  $\approx 0.9\%$  (for the pristine sample ①). Furthermore,  $o_{\text{Ni}}$  and  $p_{\text{Mn}}$  confirm the expected TM distribution in the TM layer (see Table SIV in the SI). Due to the similar ionic radii of  $\text{Li}^+$  and  $\text{Ni}^{2+}$ , Ni resides mainly on the 2b site (2b/4g ratio  $\approx 2/1$  in the f.u. notation),<sup>44</sup> but Mn accumulates on the 4g site (2b/4g ratio not greater than  $\approx 1/3$ ).

**Comparison of the migrated  $\text{Ni}_{\text{Li}}$  amount.**—Overall, the refined amount of Ni migrated into the Li layer follows the same trends among the three tested structural models (see Fig. 9d). The quality factors of the Rietveld fit (viz.,  $R_{\text{wp}}$ ,  $R_{\text{bragg}}$ , and  $\chi^2$ ) typically improve from *model 2* to *model 1* to *model 3* (see Tables SII–SIV of the SI), which can be explained by the increasing amount of freely refined parameters (see comparison in Table SV of the SI). Since the results from *model 1* were in some cases not physically sound and since the monoclinic extension of *model 3* aims primarily at the in-plane Li/TM ordering (which further might get lost within the first cycles<sup>45,46</sup>), we think that the rhombohedral *model 2* (with the constraints  $u_{\text{Li}} \geq 0$  and  $w_{\text{O}} = 1$ ) is the simplest and most robust approach to determine  $\text{Ni}_{\text{Li}}$  in this study. In the following, we want to systematically compare the amount of migrated  $\text{Ni}_{\text{Li}}$  from *model 2* in the second cycle (highlighted in gray in Fig. 9). After activation, this cycle is characterized by a quasi-reversible hysteresis of the OCV and the lattice parameters as a function of SOC. Table III contrasts the results from the harvested electrodes of the second cycle according to their SOC, OCV, unit cell volume  $V$ , and migrated  $\text{Ni}_{\text{Li}}$  amount. As discussed in Fig. 6, the charge/discharge pairs have either the same SOC (③ $\leftrightarrow$ ⑦), essentially the same OCV and unit cell volume  $V$  (④ $\leftrightarrow$ ⑦ and ⑤ $\leftrightarrow$ ⑥), or they differ for all of the three parameters (④ $\leftrightarrow$ ⑥). On the other hand, the  $\text{Ni}_{\text{Li}}$  amount deviates by  $\approx 0.5\%$ – $1.2\%$  (absolute) for each pair (see last column in Table III), which is quite a lot with regards to the maximally observed difference of  $\approx 2.4\%$  (between the samples ② and ③; see Fig. 9d). Consequently, we could not prove a causal relationship between the extent of TM migration, in particular  $\text{Ni}_{\text{Li}}$ , to the electrochemical (SOC, OCV) and lattice parameter data (for none of the tested models), as we would have intuitively expected based on the  $\text{TM}_{\text{Li}}$  hysteresis reported by Mohanty et al.<sup>29</sup> and Gent et al.<sup>30</sup> in comparison to the here examined hysteresis of the OCV and lattice dimensions. Comparing all samples, we see an increase of the average  $\text{Ni}_{\text{Li}}$  level in *model 2* from the low/mid-SOC range of the first charge ( $\approx 2.1\%$ – $2.8\%$  for the samples ①–③) to the low/mid-SOC range of the second charge ( $\approx 3.3\%$ – $3.9\%$  for ④+⑤) to the mid/high-SOC range of the second discharge ( $\approx 4.4\%$ – $4.5\%$  for ⑥+⑦). This trend is in line with the irreversible increase of  $\text{TM}_{\text{Li}}$ , which is frequently reported in other studies and amounts there to  $\Delta\text{TM}_{\text{Li}}^{\text{irrev}} \approx 1.3\%$ – $1.9\%$  after the first activation cycle and to  $\approx 2.8\%$ – $2.9\%$  after 15–25 cycles ( $\Delta\text{TM}_{\text{Li}}^{\text{irrev}}$  analyzed as the difference of the discharged state relative to the pristine material).<sup>30,36,40</sup> On the other hand, our data do not entirely contradict a partially reversible intra-cycle TM migration within the second cycle; however, this hysteresis would be significantly smaller than the  $\Delta\text{TM}_{\text{Li}}^{\text{rev}} \approx 3.6\%$  reported by Gent et al. for the first activation cycle ( $\Delta\text{TM}_{\text{Li}}^{\text{rev}}$  analyzed as the difference between the charged and discharged state).<sup>30</sup> To prove such a small tendency (probably smaller than the overall increase of 2.4% in this study), one certainly needs more data points (including samples in the completely discharged and charged state, which should represent the limit values of  $\text{Ni}_{\text{Li}}$  within a cycle, and low-SOC samples during the second discharge, where  $\text{Ni}_{\text{Li}}$  would have to go down again).

DFT simulations of the fully charged structure raise further doubts on a correlation between the TM migration and the voltage hysteresis. Although  $x_{\text{Li}}$  in reality does not fall below 0.1 at the end

**Table III.** Comparison of mid-lithium LMR-NCM electrode samples harvested in the second cycle (shown in blue in Fig. 6) with respect to their SOC, OCV, unit cell volume  $V$ , and migrated  $\text{Ni}_{\text{Li}}$  amount (according to the rhombohedral *model 2*). The relation of the charge/discharge pairs is either classified as identical ( $=$ ), similar ( $\approx$ ), or different ( $\neq$ ). The respective difference is given as  $\Delta = \text{DIS} - \text{CHA}$ . The maximum differences from the completely discharged (2.0 V) to charged state (4.8 V) in the second cycle are:  $\Delta\text{SOC} \approx 270 \text{ mAh g}^{-1}$ ,  $\Delta\text{OCV} \approx 1.5 \text{ V}$ , and  $\Delta V \approx 3.1 \text{ \AA}^3$ .

Samples		SOC [mAh/g]		OCV [V vs. Li <sup>+/</sup> Li]		$V [\text{\AA}^3]$		$\text{Ni}_{\text{Li}} [\%]$			
CHA	DIS	Relation	$\Delta$	Relation	$\Delta$	Relation	$\Delta$	Relation	CHA	DIS	$\Delta$
⑤	⑦	=	0	$\neq$	-0.30	$\neq$	+0.63	$\neq$	3.29(9)	4.44(9)	+1.15
④	⑦	$\neq$	+100	$\approx$	+0.05	$\approx$	+0.09	$\neq$	3.93(8)	4.44(9)	+0.51
⑤	⑥	$\neq$	+60	$\approx$	+0.04	$\approx$	-0.02	$\neq$	3.29(9)	4.48(11)	+1.19
④	⑥	$\neq$	+160	$\neq$	+0.39	$\neq$	-0.55	$\neq$	3.93(8)	4.48(11)	+0.55

of charge (see Fig. 6), we assume  $x_{\text{Li}} = 0$  for the DFT calculation (i.e.,  $\text{Li}_0\text{Ni}_{12}\text{Co}_6\text{Mn}_{30}\text{O}_{120}$ ), thereby removing the combinatorial complexity due to the Li distribution and greatly reducing the computational effort. A structure where 10 Mn moved to tetrahedral positions in the TM layer (see 4th row from the bottom of Table SVI in the SI) is 50 meV  $\text{atom}^{-1}$  more stable than a perfectly layered model with every TM in octahedral sites (bottom row of Table SVI). We found several structural candidates where the diffusion of Ni into octahedral sites of the Li layer further lowered the total energy of the system. In many instances we also observed the concomitant formation of  $\text{O}-\text{O}^{2-}$  dimers in the TM layer from which the diffusing atom(s) originated (see second to last column in Table SVI).<sup>30</sup> All these structures for  $\text{Li}_0\text{Ni}_{12}\text{Co}_6\text{Mn}_{30}\text{O}_{120}$  are within 13 meV  $\text{atom}^{-1}$  (see last 9 rows in Table SVI), which is well below the value of  $k_{\text{B}}T$  at 300 K (25 meV  $\text{atom}^{-1}$ ), and at least 43 meV  $\text{atom}^{-1}$  lower in energy than the perfectly layered structure without migrated TMs. This result highlights the complexity of the potential energy surface, where many local minima, even with very different structural features, coexist within an energy range comparable with the thermal energy at room temperature. Therefore, the completely delithiated structure appears to be a very “fluxional” system where many processes can happen at virtually no energetical cost.

We now raise the question of what happens when we reinsert Li into the structure with migrated Ni. The expectation is that, after the first charge, we should generally end up at lower voltages (i.e., energies) than before. Instead, every calculated structure containing 1–2 Ni in the lithium layer at  $x_{\text{Li}} = 0.5$  (i.e., for  $\text{Li}_{30}\text{Ni}_{12}\text{Co}_6\text{Mn}_{30}\text{O}_{120}$ ) is consistently higher in energy (by 9–27 meV  $\text{atom}^{-1}$ ; see Table SVI) than the counterpart where the TMs reside solely in the TM layer. This contradicts our expectation based on the lattice parameter results, where we learned that the structural changes (e.g., TM migration) occur mainly at the end of the charge process. Therefore, we would have expected that the lower voltages/energies of the partially lithiated structure with a lithium content of  $x_{\text{Li}} = 0.5$  that lies in the voltage plateau region would correlate with a significant number of TMs migrated into the lithium layer.

Based on our calculations, which however do not comprise an exhaustive screening, we can say that TM migration is only at the fully charged state energetically degenerated. The data do not provide any hint for the lower voltages/energies between the charge and discharge process caused by nickel migration because the TM movements stays unfavorable with increasing lithium content. This means that there is no driving force to energetically maintain a possibly moved TM in the lithium layer after charging the material.

Finally, let us comment on the accuracy of the  $\text{Ni}_{\text{Li}}$  amount from our joint Rietveld refinements. Using the example of *model 2*, all correlations of  $\text{Ni}_{\text{Li}}$  are below  $\approx 55\%$  and thus minor for most of the samples (①–④). The level of correlations rises with increasing SOC, reaching up to  $\approx 70\%$  to the L-XPD scale factor and  $\approx 60\%$  to the atomic displacement parameter of the Li layer,  $b_{3a,\text{Li}}$ , for the high-

SOC sample ⑥. In general, the ADPs are in a reasonable range for layered oxides ( $0.5 < b_{3a,\text{Li}} < 2.1$ ,  $0.1 < b_{3b,\text{TM}} < 0.3$ ,  $0.8 < b_{6c,\text{O}} < 1.2$ , all in  $\text{\AA}^2$ ; see Table SIII in the SI),<sup>39,89</sup> but  $b_{3a,\text{Li}}$  and  $b_{3b,\text{TM}}$  run into the lower limit of 0 for sample ⑥. Fixing them intentionally to 1.0 and 0.25  $\text{\AA}^2$ , respectively, changes the  $\text{Ni}_{\text{Li}}$  amount in *model 2* from 4.48(11)% to 4.90(9)%. This difference is undesirably large and thus emphasizes the strong dependence of SOFs on ADPs. The accurate determination of ADP values needs high- $Q$  diffraction data in the range of  $\approx 10\text{--}20 \text{ \AA}^{-1}$ , as they could be obtained from S-XPD and time-of-flight NPD (TOF-NPD would be most qualified, because the neutron scattering length does not fall off with increasing  $Q$ ).<sup>39,89</sup>

By applying high-quality S-XPD and TOF-NPD data separately to a series of twelve pristine NCM materials, Yin et al. achieved an absolute agreement of 0.1% for the paired anti-site  $\text{Ni}_{\text{Li}}/\text{Li}_{\text{TM}}$  defect between both Rietveld fits (with partially constrained ADP values).<sup>89</sup> In a similar manner, we also tested *model 2* individually against every L-XPD, S-XPD, and NPD pattern of the seven co-refined samples (by combining all available data from Figs. 5 and 9). The comparison of the structural parameters in Fig. S9 of the SI shows that  $z_{6c,\text{O}}$  is fairly invariant among the different datasets,<sup>39</sup> while  $\text{Ni}_{\text{Li}}$  and  $b_{3a,\text{Li}}$  have a significant scatter. The steady increase of  $\text{Ni}_{\text{Li}}$  over the course of the two charge/discharge cycles is reflected, on average, in all datasets, but the variation of the  $\text{Ni}_{\text{Li}}$  amount for a given sample ranges from 0.2% to 3.8%. We thus think that an accuracy of 0.1% is extremely difficult, if not impossible, to accomplish in our work and related studies about Li- and Mn-rich layered oxides. This type of CAMs is crystallographically more challenging than regular NCMs without over-lithiation, because lithium also resides in the TM layer, where it causes an (imperfect) Li/TM ordering. Both the lithium occupation and the in-plane ordering change upon electrochemical cycling. Furthermore, the atoms of the layered oxides go through different oxidation states during cycling, involving both cationic and anionic redox activities in LMR-NCMs.

This electronic aspect raises the question about the proper choice of X-ray atomic form factors. We applied neutral atoms because they ensure charge neutrality for any (cycled) sample. Using ions, namely  $\text{Li}^+$ ,  $\text{Ni}^{2+}$ ,  $\text{Co}^{3+}$ ,  $\text{Mn}^{4+}$ , and  $\text{O}^{2-}$ , would yield consistently lower  $\text{Ni}_{\text{Li}}$  values by 0.5%–0.9% (see Fig. S10 of the SI). Yin et al. proposed alternatively the combination of neutral metal species with ionic  $\text{O}^{2-}$ .<sup>89</sup> As the oxidation states are different, but not exactly known at any given SOC, they add an unavoidable bias to the refined  $\text{Ni}_{\text{Li}}$  amount of cycled samples. For this reason, Liu et al. proposed to exclude low- $Q$  values from XPD refinements, because different oxidation states have the biggest impact there.<sup>39</sup> Following their suggestion, we tested *model 2* again with  $Q_{\text{min}}^{\text{L-XPD}} = 2.9 \text{ \AA}^{-1}$ , which ignores the rhombohedral reflections (003), (101), (006), and (102). The comparison of the refinements using atomic form factors with either full or limited  $Q^{\text{L-XPD}}$  range is also provided in Fig. S10 of the SI, yielding by 0.2%–1.1% smaller  $\text{Ni}_{\text{Li}}$  values for the latter.

Since these variations are within the magnitude which is often discussed in the literature as a meaningful difference when analyzing different CAMs, it is essential to report all these refinement details to enable a minimum of comparability between different publications.

Even though the purpose of Rietveld refinements of diffraction data from Li- and Mn-rich layered oxides is to determine  $Ni_{Li}$  and site occupancy factors, their quantification is clearly subject to much uncertainty. As there is no generally accepted agreement yet in the literature about the proper choice of instrumentation (e.g., synchrotron vs laboratory diffractometer), X-ray atomic form factors, and structural models, all these uncertainties clamor in our opinion for a systematic study, as it was done for regular layered oxides by Liu et al.<sup>39</sup> and Yin et al.<sup>89</sup> Comparing high-quality diffraction data, preferably S-XPD and TOF-NPD, of over-lithiated CAMs at different SOC levels might show a path towards the precise quantification of TM migration. The current efforts to synthesize Co-free LMR-NCM<sup>6,94</sup> would additionally reduce the compositional complexity in diffraction experiments. We hope that this work can serve as a starting point in this respect.

### Conclusions

In this work, we investigated the well-known open circuit voltage (OCV) hysteresis in Li- and Mn-rich layered oxides (LMR-NCMs, i.e.,  $Li[LixTM_{1-x}]O_2$  with  $0.1 < x < 0.2$  and TM = Ni, Co, Mn) on a structural level, using a combination of diffraction techniques and DFT simulations. In the first part, the lattice parameter evolution of a mid-lithium LMR-NCM with  $\delta = 0.17$  was monitored within the initial cycles by in-situ X-ray powder diffraction on a laboratory instrument (L-XPD). After passing the activation voltage plateau during the first charge, the lattice parameters  $a$  and  $c$  as well as the unit cell volume  $V$ , from which  $c$  can be further divided into the layer heights  $h_{Li}$  and  $h_{TM}$ , resemble the quasi-reversible hysteresis of the OCV. Here, changes of  $a$  and  $h_{TM}$  are determined by the cationic redox of the transition metals, while  $h_{Li}$  and the overall shape of  $c$  are a measure of the anionic redox,  $O^{2-}/O^{n-}$  with  $n < 2$ . These assignments are derived from the literature about stoichiometric NCMs with  $\delta$  being close to 0, and could be further verified by the comparison of three LMR-NCM with different extents of over-lithiation (ranging from  $\delta = 0.14$  to 0.20) with a regular NCM-811. The hysteresis does not occur when LMR-NCMs are cycled in their pre-activated state before the first charge plateau at  $\approx 4.5$  V, but it can also be diminished afterwards by narrowing the effective SOC window, as was shown by window opening experiments. When correlated to the OCV instead of the SOC, the path dependence of the lattice parameters  $c$  remains for the activated LMR-NCMs, but gets really small for the lattice parameter  $a$ . On the other hand, the path dependence of the unit cell volume vanishes completely and gives a linear correlation with OCV with a slope of ca.  $-2 \text{ \AA}^3 \text{ V}^{-1}$ , independent of the extent of over-lithiation. Therefore, the V-OCV relationship can be seen as universal property, which applies to all here investigated LMR-NCMs.

In the second part, we aimed at quantifying the amount of migrating transition metals (TMs) in the bulk by a joint Rietveld refinement approach of ex-situ L-XPD and neutron powder diffraction (NPD) data of the mid-lithium material. It is often believed in the literature that the reversible TM migration between their native TM layer,  $TM_{TM}$ , and the Li layer,  $TM_{Li}$ , causes the reversible hysteresis phenomena in LMR-NCMs, whereas the irreversible capture of TMs in the Li layer is attributed to the voltage fade during long-term cycling.<sup>27,30</sup> Due to limitations with regards to the measurement time and the large amount of sample that is required for NDP, we could only look at a few samples within the first two cycles and could hence not resolve an intra-cycle hysteresis loop of  $TM_{Li}$ . Furthermore, with the four samples of the second cycle, we could not observe any correlation of the refined  $Ni_{Li}$  amount to the electrochemical and lattice parameter data. Using a simplified rhombohedral model for which the amount of lithium in the TM layer,  $Li_{TM}$ , was constrained and that did not allow for

oxygen vacancies (referred to as *model 2*), the maximum difference of  $Ni_{Li}$  was 2.4% (absolute) among the investigated samples. In view of all the assumptions and uncertainties associated with the Rietveld refinement of LMR-NCMs, it is in our opinion difficult and speculative to discuss even smaller differences within a subgroup of samples.

A huge variety of structural models is used in the literature, spanning from rhombohedral to monoclinic to composite models, from which we tested the first two under various assumptions. For none of them we observed the hoped-for correlation between voltage hysteresis and TM migration. The error of the refined  $Ni_{Li}$  values is estimated to be on the order of  $\pm 0.5\%$ . Since the maximum difference between the four samples of the second cycle is less than 2% for any of the tested models (using the joint Rietveld refinement approach), we thus assume the reversible intra-cycle  $\Delta N_{Li}$  to be smaller than 3%. Even though our DFT simulations did also not find any hint that TM migration causes the observed OCV hysteresis, it is actually not known in the literature how much migrated  $Ni_{Li}$  would be needed to explain the separation of the charge/discharge curves by hundreds of mV. If  $\leq 3\%$  are indeed sufficient, Rietveld refinements are in our opinion not fully established yet to resolve TM migration in LMR-NCMs, but further in-depth work might bring us to the point.

### Acknowledgments

We want to acknowledge BASF SE for the support through its Scientific Network on Electrochemistry and Batteries and the BMBF (Federal Ministry of Education and Research, Germany) for its financial support within the ExZellTUM II project (grant no. 03XP0081). We also thank the Heinz Maier-Leibnitz Zentrum (MLZ) for granting beamtime at FRM II (proposal no. 14350 and 14839). Beyond that, we wish to acknowledge the beamline scientist Nicola Casati (Material Science beamline MS-X04SA, Swiss Light Source) for his support during sample preparation, data collection, and data analysis of the ex-situ S-XPD data. Further gratitude is expressed to Franziska Friedrich and Rebecca Wilhelm for their help with the in-situ L-XPD measurements and during the NPD beamtime preparation, respectively.

### ORCID

Benjamin Strehle  <https://orcid.org/0000-0001-8878-1160>  
 Tanja Zünd  <https://orcid.org/0000-0002-1650-3636>  
 Hubert A. Gasteiger  <https://orcid.org/0000-0001-8199-8703>

### References

1. D. Andre, S.-J. Kim, P. Lamp, S. F. Lux, F. Maglia, O. Paschos, and B. Stiaszny, *J. Mater. Chem. A*, **3**, 6709 (2015).
2. O. Gröger, H. A. Gasteiger, and J.-P. Suchsland, *J. Electrochem. Soc.*, **162**, A2605 (2015).
3. Y. Ding, Z. P. Cano, A. Yu, J. Lu, and Z. Chen, *Electrochem. Energy Rev.*, **2**, 1 (2019).
4. P. Liu, R. Ross, and A. Newman, *MRS Energy Sustain.*, **2**, E12 (2015).
5. USCAR (2020), USABC Goals for Advanced High-Performance Batteries for Electric Vehicle (EV) Applications, <http://uscar.org/usabc>.
6. J. Helbig, T. Beuse, V. Sizios, T. Placke, M. Winter, and R. Schmuch, *J. Electrochem. Soc.*, **167**, 060519 (2020).
7. N. Leifer, T. Penki, R. Nanda, J. Grinblat, S. Luski, D. Aurbach, and G. Goobes, *Phys. Chem. Chem. Phys.*, **22**, 9098 (2020).
8. R. Jung, M. Metzger, F. Maglia, C. Stinner, and H. A. Gasteiger, *J. Electrochem. Soc.*, **164**, A1361 (2017).
9. S.-K. Jung, H. Gwon, J. Hong, K.-Y. Park, D.-H. Seo, H. Kim, J. Hyun, W. Yang, and K. Kang, *Adv. Energy Mater.*, **4**, 1300787 (2014).
10. M. M. Thackeray, S.-H. Kang, C. S. Johnson, J. T. Vaughey, R. Benedek, and S. A. Hackney, *J. Mater. Chem.*, **17**, 3112 (2007).
11. P. Rozier and J. M. Tarascon, *J. Electrochem. Soc.*, **162**, A2490 (2015).
12. J. Hong, H. Gwon, S.-K. Jung, K. Ku, and K. Kang, *J. Electrochem. Soc.*, **162**, A2447 (2015).
13. T. Teuffl, B. Strehle, P. Müller, H. A. Gasteiger, and M. A. Mendez, *J. Electrochem. Soc.*, **165**, A2718 (2018).
14. A. T. S. Freiberg, M. K. Roos, J. Wandt, R. de Vivie-Riedle, and H. A. Gasteiger, *J. Phys. Chem. A*, **122**, 8828 (2018).
15. T. Teuffl, D. Pritzl, P. Krieg, B. Strehle, M. A. Mendez, and H. A. Gasteiger, *J. Electrochem. Soc.*, **167**, 110505 (2020).

16. D. Schreiner et al., *J. Electrochem. Soc.*, **168**, 030507 (2021).
17. T. Teufl, D. Pritzl, S. Solchenbach, H. A. Gasteiger, and M. A. Mendez, *J. Electrochem. Soc.*, **166**, A1275 (2019).
18. J. R. Croy, M. Balasubramanian, K. G. Gallagher, and A. K. Burrell, *Acc. Chem. Res.*, **48**, 2813 (2015).
19. L. Kraft, T. Zünd, D. Schreiner, R. Wilhelm, F. J. Günter, G. Reinhart, H. A. Gasteiger, and A. Jossen, *J. Electrochem. Soc.*, **168**, 020537 (2021).
20. S. Susanna, B. R. Dewangga, O. Wahyungoro, and A. I. Cahyadi, *2019 International Conference on Information and Communications Technology (ICOIACT)*, Piscataway, NJ (IEEE) p. 738 (2019).
21. L. Wang, D. Lu, Q. Liu, L. Liu, and X. Zhao, *Electrochim. Acta*, **296**, 1009 (2019).
22. Z. Lu, L. Y. Beaulieu, R. A. Donaberger, C. L. Thomas, and J. R. Dahn, *J. Electrochem. Soc.*, **149**, A778 (2002).
23. J. R. Croy, K. G. Gallagher, M. Balasubramanian, Z. Chen, Y. Ren, D. Kim, S.-H. Kang, D. W. Dees, and M. M. Thackeray, *J. Phys. Chem. C*, **117**, 6525 (2013).
24. G. Assat, D. Foix, C. Delacourt, A. Iadecola, R. Dedryvère, and J.-M. Tarascon, *Nat. Commun.*, **8**, 2219 (2017).
25. H. Konishi, T. Hirano, D. Takamatsu, A. Gunji, X. Feng, S. Furutsuki, T. Okumura, S. Terada, and K. Tamura, *J. Solid State Chem.*, **262**, 294 (2018).
26. H. Koga, L. Croguennec, M. Ménétrier, P. Mannesiez, F. Weill, C. Delmas, and S. Belin, *J. Phys. Chem. C*, **118**, 5700 (2014).
27. K. G. Gallagher, J. R. Croy, M. Balasubramanian, M. Bettge, D. P. Abraham, A. K. Burrell, and M. M. Thackeray, *Electrochem. Commun.*, **33**, 96 (2013).
28. F. Dogan, B. R. Long, J. R. Croy, K. G. Gallagher, H. Iddir, J. T. Russell, M. Balasubramanian, and B. Key, *J. Am. Chem. Soc.*, **137**, 2328 (2015).
29. D. Mohanty, J. Li, D. P. Abraham, A. Huq, E. A. Payzant, D. L. Wood, and C. Daniel, *Chem. Mater.*, **26**, 6272 (2014).
30. W. E. Gent et al., *Nat. Commun.*, **8**, 2091 (2017).
31. R. A. House, G. J. Rees, M. A. Pérez-Osorio, J.-J. Marie, E. Boivin, A. W. Robertson, A. Nag, M. Garcia-Fernandez, K.-J. Zhou, and P. G. Bruce, *Nat. Energy*, **5**, 777 (2020).
32. L. de Biasi, A. O. Kondrakov, H. Geßwein, T. Brezesinski, P. Hartmann, and J. Janek, *J. Phys. Chem. C*, **121**, 26163 (2017).
33. A. O. Kondrakov et al., *J. Phys. Chem. C*, **121**, 24381 (2017).
34. Z. W. Lebens-Higgins et al., *Mater. Horizons*, **6**, 2112 (2019).
35. L. Yin et al., *Chem. Mater.*, **32**, 1002 (2020).
36. K. Kleiner, B. Strehle, A. R. Baker, S. J. Day, C. C. Tang, I. Buchberger, F.-F. Chesneau, H. A. Gasteiger, and M. Piana, *Chem. Mater.*, **30**, 3656 (2018).
37. P. S. Whitfield, I. J. Davidson, L. M. D. Cranswick, I. P. Swainson, and P. W. Stephens, *Solid State Ionics*, **176**, 463 (2005).
38. P. S. Whitfield, I. J. Davidson, P. H. J. Mercier, Y. Le Page, L. D. Mitchell, P. W. Stephens, L. M. D. Cranswick, and I. P. Swainson, *Powder Diffr.*, **21**, 172 (2006).
39. H. Liu, H. Liu, S. H. Lapidus, Y. S. Meng, P. J. Chupas, and K. W. Chapman, *J. Electrochem. Soc.*, **164**, A1802 (2017).
40. P. M. Csernica et al., *Nat. Energy*, **6**, 642 (2021).
41. F. Friedrich, B. Strehle, A. T. S. Freiberg, K. Kleiner, S. J. Day, C. Erk, M. Piana, and H. A. Gasteiger, *J. Electrochem. Soc.*, **166**, A3760 (2019).
42. P. R. Willmott et al., *J. Synchrotron Radiat.*, **20**, 667 (2013).
43. M. Hoelzel, A. Senyshyn, N. Juenke, H. Boysen, W. Schmahl, and H. Fuess, *Nucl. Instruments Methods Phys. Res. Sect. A Accel. Spectrometers, Detect. Assoc. Equip.*, **667**, 32 (2012).
44. D. Mohanty, A. Huq, E. A. Payzant, A. S. Sefat, J. Li, D. P. Abraham, D. L. Wood, and C. Daniel, *Chem. Mater.*, **25**, 4064 (2013).
45. H. Yu et al., *J. Am. Chem. Soc.*, **140**, 15279 (2018).
46. M. Jiang, B. Key, Y. S. Meng, and C. P. Grey, *Chem. Mater.*, **21**, 2733 (2009).
47. 2011 WinXP0W V3.0.2.1, STOE & Cie GmbH, Darmstadt, Germany.
48. 2016 TOPAS-Academic V6, Coelho Software, Brisbane, Australia.
49. Z. Lu and J. R. Dahn, *J. Electrochem. Soc.*, **149**, A815 (2002).
50. D. Mohanty, S. Kalnaus, R. A. Meisner, K. J. Rhodes, J. Li, E. A. Payzant, D. L. Wood, and C. Daniel, *J. Power Sources*, **229**, 239 (2013).
51. G. Kresse and J. Hafner, *Phys. Rev. B*, **47**, 558 (1993).
52. G. Kresse and J. Hafner, *Phys. Rev. B*, **49**, 14251 (1994).
53. G. Kresse and J. Furthmüller, *Comput. Mater. Sci.*, **6**, 15 (1996).
54. G. Kresse and J. Furthmüller, *Phys. Rev. B*, **54**, 11169 (1996).
55. P. E. Blöchl, *Phys. Rev. B*, **50**, 17953 (1994).
56. G. Kresse and D. Joubert, *Phys. Rev. B*, **59**, 1758 (1999).
57. H. Peng, Z.-H. Yang, J. P. Perdew, and J. Sun, *Phys. Rev. X*, **6**, 041005 (2016).
58. K. Okhotnikov, T. Charpentier, and S. Cadars, *J. Cheminform.*, **8**, 17 (2016).
59. B. Strehle, K. Kleiner, R. Jung, F. Chesneau, M. Mendez, H. A. Gasteiger, and M. Piana, *J. Electrochem. Soc.*, **164**, A400 (2017).
60. X. Zhang, A. Mauger, Q. Lu, H. Groult, L. Perrigaud, F. Gendron, and C. M. Julien, *Electrochim. Acta*, **55**, 6440 (2010).
61. K. Luo et al., *Nat. Chem.*, **8**, 684 (2016).
62. G. Assat, A. Iadecola, D. Foix, R. Dedryvère, and J.-M. Tarascon, *ACS Energy Lett.*, **3**, 2721 (2018).
63. A. O. Kondrakov, A. Schmidt, J. Xu, H. Geßwein, R. Mönig, P. Hartmann, H. Sommer, T. Brezesinski, and J. Janek, *J. Phys. Chem. C*, **121**, 3286 (2017).
64. D.-H. Seo, J. Lee, A. Urban, R. Malik, S. Kang, and G. Ceder, *Nat. Chem.*, **8**, 692 (2016).
65. D.-H. Seo, A. Urban, and G. Ceder, *Phys. Rev. B*, **92**, 115118 (2015).
66. H. Liu, Y. Chen, S. Hy, K. An, S. Venkatchalam, D. Qian, M. Zhang, and Y. S. Meng, *Adv. Energy Mater.*, **6**, 1502143 (2016).
67. H.-H. Ryu, K.-J. Park, C. S. Yoon, and Y.-K. Sun, *Chem. Mater.*, **30**, 1155 (2018).
68. P. Yan, J. Zheng, M. Gu, J. Xiao, J.-G. Zhang, and C.-M. Wang, *Nat. Commun.*, **8**, 14101 (2017).
69. S. Oswald, D. Pritzl, M. Wetjen, and H. A. Gasteiger, *J. Electrochem. Soc.*, **167**, 100511 (2020).
70. H. Li, A. Liu, N. Zhang, Y. Wang, S. Yin, H. Wu, and J. R. Dahn, *Chem. Mater.*, **31**, 7574 (2019).
71. H. Komatsu et al., *J. Phys. Chem. C*, **122**, 20099 (2018).
72. R. A. House et al., *Nature*, **577**, 502 (2020).
73. G. Assat, S. L. Glazier, C. Delacourt, and J.-M. Tarascon, *Nat. Energy*, **4**, 647 (2019).
74. N. Yabuuchi, K. Yoshii, S.-T. Myung, I. Nakai, and S. Komaba, *J. Am. Chem. Soc.*, **133**, 4404 (2011).
75. C. R. Fell, D. Qian, K. J. Carroll, M. Chi, J. L. Jones, and Y. S. Meng, *Chem. Mater.*, **25**, 1621 (2013).
76. N. Ishida, N. Tamura, N. Kitamura, and Y. Idemoto, *J. Power Sources*, **319**, 255 (2016).
77. C. Genevois, H. Koga, L. Croguennec, M. Ménétrier, C. Delmas, and F. Weill, *J. Phys. Chem. C*, **119**, 75 (2015).
78. A. Boulineau, L. Simonin, J.-F. Colin, C. Bourbon, and S. Patoux, *Nano Lett.*, **13**, 3857 (2013).
79. P. Yan et al., *Nano Lett.*, **15**, 514 (2015).
80. I. Takahashi et al., *J. Phys. Chem. C*, **120**, 27109 (2016).
81. P. Yan et al., *Chem. Mater.*, **27**, 5393 (2015).
82. J. Ma, S.-H. Bo, L. Wu, Y. Zhu, C. P. Grey, and P. G. Khalifah, *Chem. Mater.*, **27**, 2387 (2015).
83. C.-J. Chen et al., *J. Am. Chem. Soc.*, **138**, 8824 (2016).
84. H. Liu et al., *J. Mater. Chem. A*, **6**, 4189 (2018).
85. J. M. Joubert, R. Cerný, M. Latroche, A. Percheron-Guégan, and K. Yvon, *J. Appl. Crystallogr.*, **31**, 327 (1998).
86. H. Koga, L. Croguennec, P. Mannesiez, M. Ménétrier, F. Weill, L. Bourgeois, M. Duttine, E. Suard, and C. Delmas, *J. Phys. Chem. C*, **116**, 13497 (2012).
87. J. Liu, L. Yin, L. Wu, J. Bai, S.-M. Bak, X. Yu, Y. Zhu, X.-Q. Yang, and P. G. Khalifah, *Inorg. Chem.*, **55**, 8478 (2016).
88. T. Ohzuku, *J. Electrochem. Soc.*, **140**, 1862 (1993).
89. L. Yin et al., *Rev. Sci. Instrum.*, **89**, 093002 (2018).
90. G. Liang, C. Didier, Z. Guo, W. K. Pang, and V. K. Peterson, *Adv. Mater.*, **1904528**, 1 (2019).
91. P. Yan, J. Zheng, Z.-K. Tang, A. Devaraj, G. Chen, K. Amine, J.-G. Zhang, L.-M. Liu, and C. Wang, *Nat. Nanotechnol.*, **14**, 602 (2019).
92. S. Ahmed et al., *ACS Nano*, **13**, 10694 (2019).
93. J. Bréger, M. Jiang, N. Dupré, Y. S. Meng, Y. Shao-Horn, G. Ceder, and C. P. Grey, *J. Solid State Chem.*, **178**, 2575 (2005).
94. W.-C. Chen, Y.-F. Song, C.-C. Wang, Y. Liu, D. T. Morris, P. A. Pianetta, J. C. Andrews, H.-C. Wu, and N.-L. Wu, *J. Mater. Chem. A*, **1**, 10847 (2013).



---

## 4.4 SOC-dependent Heat Release Associated with the OCV-hysteresis

The newest article is named “Classification of Heat Evolution Terms in Li-ion Batteries regarding the OCV Hysteresis in a Li- and Mn-Rich NCM Cathode Material in Comparison to NCA”. The manuscript was submitted in February 2022 and published in April 2022 as a peer-reviewed publication in the Journal of the Electrochemical Society. It is available as an “open access” article and distributed under the terms of the Creative Commons Attribution 4.0 License ([CC BY-NC-ND](https://creativecommons.org/licenses/by-nc-nd/4.0/)). The permanent web link to this article can be found under: <https://iopscience.iop.org/article/10.1149/1945-7111/ac6541/meta>

The hysteresis phenomena of LMR-NCMs were intensively studied regarding its origin and its correlation to the SOC and OCV. As already discussed in Section 4.2, the OCV-hysteresis is not only mechanistically interesting, but has also practical impact on battery operation. The energy round trip efficiency ( $\Delta E_{\text{DCHA}}/\Delta E_{\text{CHA}}$ ) at low C-rates is only  $\approx 88\%$  for LMR-NCM cells, significantly lower than for NCA cells with  $\approx 98\%$ . For the design of battery systems and, in particular, their cooling unit, it is essential to know the overall amount of energy that is released as heat and, perhaps even more critical, to know the heat flux as a function of SOC.

In this study, a comparison was made for LMR-NCM and NCA cells with regard to the heat fluxes during cycling using calorimetry. Here, NCA served as a reference cathode active material that does not exhibit an OCV-hysteresis (like all stoichiometric NMCs). In OCV-hysteresis-free materials (such as NCA), the SOC-resolved heat release can be described adequately by the SOC dependence of the cell resistance; it therefore scales with the applied current and can be determined by intermittent cycling or impedance measurements. For LMR-NCMs that show a substantial OCV-hysteresis, however, the energy loss corresponding to the OCV-hysteresis is up to 55% of the total energy loss and is current-independent, meaning it does not simply scale with the cell impedance. For this reason, the heat flux due to the OCV-hysteresis cannot be directly assigned to the charge or discharge process.

In this work, it was suggested that the combination of calorimetry and resistance measurements is needed to accomplish a quantification of the heat flux caused by

the OCV-hysteresis. By isothermal micro-calorimetry, the SOC-resolved total energy loss at different C-rates in LMR-NCM and NCA cells was quantified. In combination with *in situ* techniques to determine the cell resistance, such as OCV-intermittent cycling and impedance spectroscopy, it was possible to differentiate between the generally observed heat release due to current-dependent overpotentials and the heat released by the OCV-hysteresis. The non-hysteresis generated heat as a function of SOC was further deconvoluted into the cathode charge transfer resistance, the low frequency resistance (LFR), and a residual kinetic resistance (corresponding to the difference of the resistance determined by intermittent cycling plus the high frequency resistance (HFR)).

By measuring the heat release at different C-rates, it was possible to show the change from an OCV-hysteresis-dominated heat release (low C-rates) to an overpotential-dominated heat release (high C-rates). Reversible heat terms (due to entropy changes) were also included into the energetic considerations, and a quantitative overall comparison was shown. In the work it was shown that the individual, SOC-dependent heat terms differ significantly between the LMR-NCM and NCA-based cells. By considering also the very low heat fluxes in the case of NCA cells, the limitation of the method was critically discussed as well as the usually negligible contribution of parasitic reactions. The quantification of the SOC-dependent heat release terms will enable the development of a thermal battery model for active materials that exhibit an OCV-hysteresis. Such a heat flux-based modelling was subsequently applied by several collaborators in order to simulate the thermal behaviour of batteries with different cell formats examining different cooling schemes and operation conditions.<sup>71</sup>

#### Author contributions

F.F. and T.Z. conducted electrochemical experiments and analysed the data. A.H. was responsible for the calorimetric measurements. The results of the experiments were analysed and interpreted by F.F. and T.Z. The manuscript was written by F.F. and T.Z., and further revised by the co-authors. All authors discussed the data and commented on the results. F.F. and T.Z. contributed equally to this work as co-sharing first authors.



# Classification of Heat Evolution Terms in Li-Ion Batteries Regarding the OCV Hysteresis in a Li- and Mn-Rich NCM Cathode Material in Comparison to NCA

Franziska Friedrich,<sup>1,=z</sup>  Tanja Zünd,<sup>1,=</sup>  Alexander Hoefling,<sup>2</sup> Jens Tübke,<sup>3</sup> and Hubert A. Gasteiger<sup>1</sup> 

<sup>1</sup>Chair of Technical Electrochemistry, Department of Chemistry and Catalysis Research Center, Technical University of Munich, Munich, Germany

<sup>2</sup>Helmholtz Institute Ulm, Electrochemical Energy Storage, Ulm, Germany

<sup>3</sup>Karlsruhe Institute of Technology, Karlsruhe, Germany

We investigate the heat release of Li- and Mn-rich NCM (LMR-NCM) and NCA half-cells during cycling at different C-rates and quantify the individual contributions to the overall heat flow using a combination of isothermal micro-calorimetry and electrochemical methods. The paper focuses in particular on the open-circuit voltage (OCV) hysteresis of the LMR-NCM material, which results in a significant reduction in energy round-trip efficiency ( $\approx 90\%$  for LMR-NCM/Li cells vs  $\approx 99\%$  for NCA/Li cells at C/10) and therefore in an additional source of heat that has to be considered for the thermal management of the cell. The total heat release of the LMR-NCM/Li cells is found to be nine times higher than that of the corresponding NCA/Li cells (at C/10). In the case of the LMR-NCM cathode, the heat due to OCV hysteresis is responsible for up to 55% of the total energy loss. Using the applied approach, the OCV hysteresis heat is separated into its share during charge and discharge and is furthermore presented as a function of SOC. Additional sources of heat, such as reversible entropic heat, parasitic effects, and measurement limitations, are discussed in terms of their contribution to the overall energy balance of the two cell chemistries.

© 2022 The Author(s). Published on behalf of The Electrochemical Society by IOP Publishing Limited. This is an open access article distributed under the terms of the Creative Commons Attribution Non-Commercial No Derivatives 4.0 License (CC BY-NC-ND, <http://creativecommons.org/licenses/by-nc-nd/4.0/>), which permits non-commercial reuse, distribution, and reproduction in any medium, provided the original work is not changed in any way and is properly cited. For permission for commercial reuse, please email: [permissions@iopublishing.org](mailto:permissions@iopublishing.org). [DOI: 10.1149/1945-7111/ac6541]



Manuscript submitted February 4, 2022; revised manuscript received March 27, 2022. Published April 25, 2022.

Lithium-ion batteries (LIB) for use in portable electronic devices and in battery electric vehicles (BEVs) dominate the battery market. For the latter application, high-energy density batteries are required ( $> 350 \text{ Wh kg}_{\text{cell}}^{-1}$ ),<sup>1</sup> so that a significant challenge is to create a suitable thermal management system, since the reduced surface area to volume ratio in large batteries can result in insufficient heat transfer from the cells to the surroundings.<sup>2</sup> Thus, the design of large batteries requires an accurate prediction of the heat flow rate from the LIB for the current loads applied.

Heat is produced and absorbed through various processes during electrochemical cycling of a battery. These processes generally include reversible entropic heat, irreversible heat due to the effects of polarization, heat from side reactions, and heat of mixing caused by the effects of the relaxation of lithium ion concentration gradients after interruption of the current. This study does not take into account the heat generation from side reactions because after several formation cycles and compared to the other sources of heat, it is typically negligible for cells that can be reversibly cycled.<sup>3,4</sup> Heat evolution due to mixing was also neglected, since it is a diffusional effect after current interruption, which is only significant for electrodes with large active material particles and at high current densities.<sup>5</sup> In the isothermal calorimetric measurements applied here, the heat absorbed by the cell remains close to zero, since the cell is maintained at a constant temperature. This means that only entropic and polarization effects contribute to the total heat generation. Usually, the heat flow rate of a LIB is dominated by irreversible heat at high current densities, while at lower currents, reversible heat can make a significant contribution. A recently published study, comparing the cycling behavior of 7 Ah pouch full-cells with Li- and Mn-rich layered oxide (LMR-NCM) cathodes to that of NCA cathodes, points out an additional significant heat evolution term for LMR-NCM cathode active materials (CAMs) that is caused by its large open-circuit voltage hysteresis (OCV hysteresis) and that largely affects thermal management.<sup>6,7</sup> Hence, apart from the applied current, the heat generation is also closely related to the

cell chemistry and for active materials with a significant voltage hysteresis like Li- and Mn-rich NCMs and silicon, an additional heat term due to the OCV hysteresis needs to be considered. The thermal properties of electrode active materials are therefore critical for the design of large-scale high-energy density batteries. These thermodynamic data are essential input parameters in the modeling and development of thermal management systems.

The aim of the present study is therefore to enable a thorough understanding of the heat generation processes taking place in cells with an LMR-NCM ( $\text{Li}_{1.14}\text{Ni}_{0.26}\text{Co}_{0.14}\text{Mn}_{0.6}\text{O}_{2}$ ) CAM that exhibits a significant OCV hysteresis in comparison to cells with NCA ( $\text{LiNi}_{0.81}\text{Co}_{0.15}\text{Al}_{0.04}\text{O}_{2}$ ). We will compare these two CAMs cycled in half-cells with a lithium anode, whereby NCA serves as a reference CAM with a negligible OCV hysteresis that has been commercialized by Tesla in its electric vehicles and is incorporated in projections for grid-connected applications.<sup>8</sup> The scientific focus of this study is on LMR-NCM, which has a high gravimetric capacity ( $\approx 250 \text{ mAh g}_{\text{CAM}}^{-1}$ ) and a low material cost compared to other state-of-the-art CAMs, as it has a high manganese content instead of cobalt and nickel. However, issues such as oxygen evolution, gradual voltage fade during cycling, and a large OCV hysteresis still hamper the commercialization of LMR-NCM.<sup>9–11</sup> As mentioned by Kraft et al.,<sup>6</sup> its OCV hysteresis, which is largely independent of the applied current and thus a material-specific property, negatively affects the round-trip efficiency of LMR-NCM based cells when compared to NCA based cells. At low C-rates, the energy round-trip efficiency for LMR-NCM/Li cells is  $\approx 90\%$ , while it is  $\approx 99\%$  for NCA/Li cells. If this energy inefficiency is dissipated as heat, it not only constitutes an additional source of heat in the overall energy balance, but it is also a challenge for the development of a thermal management system of such batteries. Hence, the following questions need to be addressed for materials like LMR-NCM that have a pronounced OCV hysteresis: (i) Is the energy loss due to the OCV hysteresis dissipated as heat? (ii) In what proportions is this heat dissipated in charge and discharge? (iii) At what point during charge and discharge is the heat evolved? (iv) What conclusions can be drawn from the heat evolution profiles with regard to the underlying thermodynamic mechanisms behind voltage hysteresis?

<sup>=</sup>These authors contributed equally to this work.

<sup>z</sup>E-mail: [franziska.friedrich@tum.de](mailto:franziska.friedrich@tum.de)

The current independent OCV hysteresis of LMR-NCM has previously been studied from several perspectives. Literature reports show correlations between OCV hysteresis, impedance response,<sup>12</sup> lattice parameters,<sup>13</sup> entropy,<sup>14</sup> and oxygen redox behavior.<sup>15,16</sup> Shi et al. showed that the entropy and overpotential behavior of LMR-NCM is unique compared to that of regular layered oxide materials.<sup>17</sup> Using only electrochemical methods, their study mainly correlates the gradual voltage decay (shown to be  $\approx 100$  mV over 100 cycles by Kraft et al.<sup>6</sup>) with the entropy change within the material, whereas we focus on the OCV hysteresis between the charge and discharge voltage curve of a single cycle ( $\approx$  up to 300 mV), which has a significant impact on the thermal behavior of the cell. The application of isothermal micro-calorimetry (IMC) in the precise thermal analysis of batteries was demonstrated long ago with the measurement of parasitic reactions in LIBs.<sup>18</sup> In a similar approach to ours, Housel et al.<sup>19</sup> analyzed the heat evolution of silicon anodes by combining IMC with the measurement of polarization induced and entropic heat flows. A recent study by Assat et al.<sup>20</sup> addressed some of our questions for an LMR-NCM model system (viz.,  $\text{Li}_2\text{Ru}_{0.75}\text{Sn}_{0.25}\text{O}_3$ ) and showed how the thermal characterization of a cathode active material with a pronounced OCV hysteresis could be accomplished with the help of isothermal micro-calorimetry (IMC). Chevrier et al.<sup>21</sup> used IMC in a similar manner to study silicon as an anode material, which also shows a path dependent behavior and heat generation for zero-current hysteresis.

The present study uses isothermal micro-calorimetry to analyze the thermal behavior during cycling of NCA/Li and LMR-NCM/Li half-cells at different C-rates. The data obtained relating to the generated heat are complemented by measurements of reversible and irreversible heat in order to quantify the different heat sources measured by IMC. Reversible heat is determined by entropy measurements,<sup>14</sup> while irreversible heat is calculated using impedance spectroscopy and overpotential data from an intermittent cycling protocol (constant-current charge intervals followed by OCV periods). In the case of LMR-NCM, the combination of all data sets enables the quantification of the evolved heat due to OCV hysteresis during charge and discharge, along with the calculation of a respective heat evolution profile.

### Theoretical Considerations

**Derivation of total heat generation in a battery.**—The heat flow ( $\dot{Q}$ ) generated by an electrochemical cell is described by Eq. 1. The interpretation of IMC data is based on the thermodynamics of a battery. A detailed derivation of Eq. 1 is provided by Housel et al.<sup>19</sup> in their Supporting Information.

$$\dot{Q} = I \cdot (E_{load} - E_{eq}) + T \cdot I \cdot \frac{\partial E_{eq}}{\partial T} \quad [1]$$

The first term on the right-hand side of Eq. 1 denotes irreversible heat generation ( $\dot{Q}_{irrev}$ ), which originates from the polarization processes that cause the measured cell potential under load ( $E_{load}$ ) to deviate from the thermodynamic equilibrium potential ( $E_{eq}$ ). The difference between  $E_{load}$  and  $E_{eq}$  is generally called overpotential ( $\eta$ ). It is further illustrated in Fig. 3 (whereby  $E_{OC}$  is used instead of  $E_{eq}$  as explained below). Note here, that  $E_{load}$  is a function of the applied current ( $I$ ).  $\dot{Q}_{irrev}$  is always exothermic. The second term is the reversible heat generation ( $\dot{Q}_{rev}$ ) caused by an entropic heat flow arising from changes in entropy as a result of the electrochemical reaction.  $\dot{Q}_{rev}$  can be calculated based on the change in  $E_{eq}$  with temperature. Entropic heat flow is reversible, hence it has different signs in the charge and discharge directions and should, by definition, have a zero contribution if a complete charge/discharge cycle is considered. In addition to these conventional heat flows, another term might be added to Eq. 1 to describe the parasitic heat flow ( $\dot{Q}_{par}$ ) caused by any side or parasitic reactions, such as

electrolyte decomposition<sup>22</sup> or SEI formation.<sup>19</sup> Although the contribution from parasitic heat flow is not equal to zero, it is not further analyzed in the present study, because it can be assumed to be small in comparison to the other sources of heat for a reversibly cycling cell, as will be shown later. As outlined in the Experimental section, a correction for minor parasitic heat flow is applied similar to what is reported by Assat et al.<sup>20</sup> Other non-Faradaic heat sources include the heat of mixing and the heat absorbed by the cell from the surroundings. As the measurements are conducted in an isothermal environment, the latter heat term is considered to be close to zero. The heat of mixing is reported to be only important at high current densities ( $>2\text{C}$ ) and for electrodes with large particles ( $d \approx 40 \mu\text{m}$ ),<sup>5</sup> which is not the case in the present paper (max. 1C and particles with  $d \approx 10\text{--}15 \mu\text{m}$ ).

However, particularly in the case of LMR-NCM, heat generation is not adequately described by Eq. 1. This is due to the hysteresis of the open-circuit voltage between charge and discharge. For a given state-of-charge (SOC), a cell with an LMR-NCM cathode has different OCVs upon charge and discharge, meaning that the OCV is path-dependent. The OCV hysteresis thus translates into a yet undescribed energy loss term. The whole situation thus becomes more complicated, and Eq. 1 has to be extended. To adapt the commonly used energy balance established above to a system with an OCV hysteresis, the voltage measured under open-circuit conditions will not be considered as a reversible equilibrium potential ( $E_{eq}$ ) but as  $E_{OC}$ . Consequently, a similar situation to that of the polarization effect is created by establishing a difference ( $\Delta E$ ) between a (hypothetical) equilibrium potential ( $E_{eq}$ ) without hysteresis and the measurable potential under open-circuit conditions ( $E_{OC}$ ). To account for this conceptually, the first term in Eq. 1 can be expanded into two separate terms, one describing nominally the heat evolution term due to a current induced polarization ( $\equiv \dot{Q}_{irrev}$ , first term in Eq. 2) and one describing nominally the heat evolution induced by the OCV hysteresis ( $\equiv \dot{Q}_{hys}$ , first term in Eq. 2), whereby the true reversible voltage ( $E_{eq}$ ) is unknown:

$$\begin{aligned} \dot{Q} &= I \cdot (E_{load} - E_{OC}) + I \cdot (E_{OC} - E_{eq}) + T \cdot I \cdot \frac{\partial E_{eq}}{\partial T} \\ &= \dot{Q}_{irrev} + \dot{Q}_{hys} + \dot{Q}_{rev} \end{aligned} \quad [2]$$

We want to underline that, unlike in classical intercalation materials, the position of  $E_{eq}$  cannot simply be assumed to be halfway between the charge and discharge  $E_{OC}$  because  $E_{OC}$  is highly path-dependent. The position of  $E_{eq}$  is thus not directly accessible by experimental methods. Instead of the equilibrium potential, Assat et al.<sup>20</sup> and Chevrier et al.<sup>21</sup> constructed the so-called enthalpy potential based on calorimetric data. In the usual case with active materials that show no OCV hysteresis, i.e., where  $E_{OC} = E_{eq}$  (as for NCA/Li cells), Eq. 2 again simplifies to the form of Eq. 1. Note that there is an important difference between the calculation of  $\dot{Q}_{irrev}$  and  $\dot{Q}_{hys}$  although in both cases, the heat flow is based on the product of current and a potential difference. However,  $\dot{Q}_{irrev}$  becomes very small when the current is reduced because  $E_{load}$  is a function of the applied current and approaches  $E_{OC}$  for small currents, thus  $\Delta E(I) = E_{load}(I) - E_{OC} \approx 0$  for small  $I$ . In contrast, since both  $E_{OC}$  and  $E_{eq}$  are a material specific property, their potential difference  $\Delta E = E_{OC} - E_{eq}$  is independent of the applied current and hence leads to a significant contribution even at low currents. Strictly speaking, the entropic heat for LMR-NCM is also determined from the change in  $E_{OC}$  with temperature, since the (hypothetical)  $E_{eq}$  is not accessible. However, this is more of a theoretical problem, and since the contributions from entropic heat flow are minor in the case of LMR-NCM, it will not be discussed further here. The interested reader is referred to a detailed discussion of the entropy of LMR-NCM by Friedrich et al.<sup>14</sup> The essential conclusion from Eq. 2 is that the heat flow due to OCV hysteresis

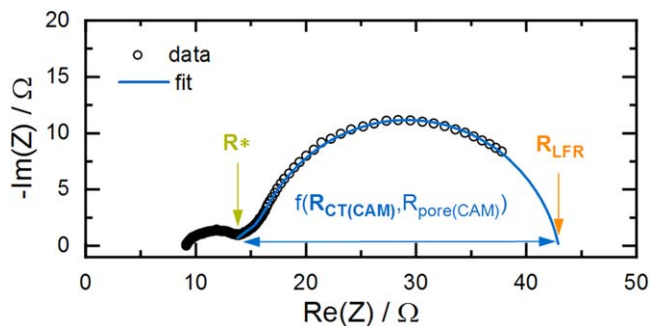


**Figure 1.** Exemplary impedance spectrum of an LMR-NCM/Li cell at a nominal SOC of  $\approx 260$  mAh/g<sub>CAM</sub> during a C/10 charge, with data depicted as black circles and the applied fit as a blue line. Only the low-frequency semi-circle was fitted by the equivalent circuit  $R^* + TLM(R_{pore} + R_{CT(CAM)})/Q$ . From this spectrum, the pore resistance of this cell was determined as 12.2  $\Omega$  cm<sup>2</sup>. The arrows mark the parameters extracted from the fit: (i)  $R^*$ , which includes the high frequency resistance of the cell, contact resistances, and contributions of the Li anode impedance; (ii) the charge transfer resistance of the cathode,  $R_{CT(CAM)}$ , which was extracted from the transmission line model; and, (iii) the low frequency resistance  $R_{LFR}$ , as described above. The high frequency semi-circle was not taken into account for fitting.

( $\dot{Q}_{hys}$ ) can be calculated from the difference between the total heat flow  $\dot{Q}$  measured by IMC and the sum of the reversible ( $\dot{Q}_{rev}$ ) and irreversible heat flow terms ( $\dot{Q}_{irrev}$ ).

We want to make clear that the current ( $I$ ) in Eq. 1 is defined to be positive in the discharge direction (voluntary process, lithiation of the cathode) and negative in the charge direction. By this definition, a positive  $\dot{Q}$  represents heat absorbed by the cell (endothermic), while a negative  $\dot{Q}$  means that heat is generated by the cell (exothermic). It should be noted, however, that in contrast to this thermodynamic definition, the sign convention used in this study is based on the perspective of the calorimeter, as is common in the literature. Thus, if the IMC measures heat generated by the cell (exothermic reaction) the heat flow has a positive sign, while it takes a negative value for heat absorbed by the cell (endothermic process).

**Contributions to irreversible heat.**—Irreversible heat arises from the internal battery resistance and is calculated either as the current multiplied by the polarization induced overpotential ( $\eta$ ) or as the product of the current squared and the total cell resistance ( $R_{tot}$ ).

$$\dot{Q}_{irrev} = I \cdot (E_{load} - E_{OC}) = I \cdot \eta = I^2 \cdot R_{tot} \quad [3]$$

The full voltage relaxation during the applied intermittent cycling protocol (constant-current charge intervals followed by OCV periods; Experimental section) gives the polarization induced overpotential  $\eta$  for each relaxation phase at this specific current (see Fig. 3), from which the total irreversible heat flow ( $\dot{Q}_{irrev}$ ) can be calculated.

The contributions to the total cell resistance can be further analyzed by impedance spectroscopy. As shown in Fig. 1, the impedance spectra in this study were fitted with a simplified transmission line model. The fitted equivalent circuit is described by  $R^* + TLM(R_{pore} + R_{CT(CAM)})/Q$ . Hereby,  $R^*$  represents the sum of several contributions: (i) the high frequency resistance, which includes the ionic resistance of the separator and the electrical resistance of the external cell contacts; (ii) the resistance of the Li anode; and, (iii) the contact resistance between the cathode and the Al current collector. As can be seen from the example in Fig. 1,  $R^*$  is defined as being at the end of the high-frequency semi-circle. The low-frequency semi-circle corresponds to a complex convolution of the pore resistance due to the lithium ion conduction across the

porous cathode ( $R_{pore}$ ) and the cathode charge transfer resistance ( $R_{CT(CAM)}$ ). In case of the LMR-NCM/Li cells, the low-frequency semi-circle was fitted by a transmission line model.<sup>23</sup> The assignment of the fitting parameters to the semi-circles is verified by experiments with a micro-reference electrode (not shown here) and by comparison to literature reports.<sup>12</sup> In the case of NCA/Li cells, the pore resistance could not be clearly distinguished. In this case, the second semi-circle was fitted by a simplified  $R_{CAM}/Q_{CAM}$  element where  $R_{CAM}$  includes  $R_{CT(CAM)}$  and  $R_{pore}$ . More details on the analysis and fitting of the impedance data can be found in the Experimental section. Since  $R_{pore}$  is assumed to be constant and independent of the SOC, we will focus on the analysis of  $R^*$  and  $R_{CT}$ . However, to compare the results of the impedance analysis to those of intermittent cycling, the low frequency resistance  $R_{LFR}$  needs to be calculated from the fitting parameters:<sup>23</sup>

$$R_{LFR} = R^* + 1/3 R_{pore} + R_{CT(CAM)} \quad [4]$$

Equation 4 was applied for the impedance spectra of the LMR-NCM/Li cells within its validity criteria.<sup>24</sup> For NCA,  $R_{LFR}$  is calculated from the sum of  $R^*$  and  $R_{CAM}$ . Both,  $R^*$  and  $R_{CAM}$ , are only shown for NCA where they were clearly distinguishable (at high and low SOC). The difference between  $R_{LFR}$  and the total resistance determined by the intermittent cycling ( $R_{tot}$ ) is a result of diffusion limitations. For a more advanced impedance analysis of cells with LMR-NCM cathodes, the reader is referred to the work by Teuffl et al.<sup>12</sup> However, the aim of this study is not to conduct a detailed impedance analysis, but to deconvolute the different sources of irreversible heat, in particular the contributions of the cathode, which justifies the applied simplification.

**Thermal energy per cycle.**—So far, only heat flows, i.e., the evolution of heat over time, have been discussed. However, the total heat generated during a complete charge/discharge cycle, the thermal energy per cycle, can be obtained from them. This parameter can be accessed by various means: (i) as the sum of the integration of all calculated heat flow terms over time; (ii) as the integration of the voltage curve over a whole cycle; and, (iii) as the sum of the integrated heat evolution during a charge/discharge cycle measured by IMC. Therefore, the contributions of different heat sources can be quantified by calculating (i) and (ii) and then comparing it to the thermal energy measured by IMC (iii). An essential requirement for the validity of this analysis is that the total thermal energy per cycle calculated by all three methods is equal. This means that the electrical energy lost according to the voltage curve is fully converted into heat and that there are no other (non-Faradaic) heat sources.

For calculation method (i), the heat generated during charge  $Q_{cha}$  (during discharge  $Q_{dis}$ ) is integrated from time  $t_0$ , where the charge (discharge) commenced, to  $t_c$  ( $t_d$ ), where the charge (discharge) half-cycle ends. The sum of the heat generated during charge and discharge gives the total heat generated per cycle,  $Q_{cycle}$ . Since reversible heat has opposite signs on charge and discharge, it cancels out and thus does not contribute to the thermal energy per cycle.

$$Q_{cycle} = \int_{t_0}^{t_c} \dot{Q}_{cha} dt + \int_{t_0}^{t_d} \dot{Q}_{dis} dt = Q_{irrev,cha} + Q_{irrev,dis} + Q_{hys,cha} + Q_{hys,dis} \quad [5]$$

Thus, only the irreversible heat and the energy loss due to hysteresis (in the case of LMR-NCM), both separated into their charge and discharge components, contribute to the thermal energy per cycle.

Using calculation method (ii), the integration over the voltage curve on load, only one value, which is the sum of all heat sources, can be obtained:

$$Q_{cycle} = \int_{t_0}^{t_c} I_{cha} \cdot E_{load,cha} dt - \int_{t_0}^{t_d} I_{dis} \cdot E_{load,dis} dt \quad [6]$$

However, when applying intermittent charging, the voltage under load can be distinguished from that under open-circuit conditions. This enables the quantification of individual contributions to the thermal energy per cycle. The generated irreversible heat can be calculated for the charge ( $Q_{irrev,cha}$ ) and discharge ( $Q_{irrev,dis}$ ). For example, the energy loss caused by the effects of polarization during charge is the integrated area between the upper voltage curve under load and the upper OCV curve (analogously for the discharge):

$$Q_{irrev,cha} = \int_{t_0}^{t_c} I_{cha} (E_{load,cha} - E_{OC,cha}) dt \quad [7]$$

The energy loss caused by OCV hysteresis is calculated by integrating the area enclosed by the OCV points upon charge and discharge. Only the sum of the charge and discharge contributions to  $Q_{hys}$  is accessible from integration of the OCV data.

$$Q_{hys} = \oint_{t_0}^{t_d} I \cdot (E_{OC,cha} - E_{OC,dis}) dt \quad [8]$$

It is important to keep in mind that the integration over the whole charge/discharge voltage curve is not a closed loop due to the coulombic inefficiency of the cell. When Eq. 6 is thus strictly applied,  $Q_{cycle}$  is overestimated as compared to reconstructing  $Q_{cycle}$  according to Eq. 5 from  $Q_{irrev,cha}$ ,  $Q_{irrev,dis}$  and  $Q_{hys}$  calculated according to Eqs. 7 and 8. The resulting inaccuracy of the analysis and how to best minimize it will be discussed later in the Results section.

For method (iii), the heat flow signal measured by IMC is integrated over time to give the total generated heat. When a sufficiently long OCV phase is applied at the end of each charge/discharge half-cycle, the total heat generated during charge can be separated from that during discharge. The heat evolution is measured by IMC both during current flow and the consecutive OCV phase, in which the heat signal levels off while the cell cools down. When comparing with calculated heat flows, only the signal during current flow is considered, while for the calculation of the total heat generation, the heat evolution at zero current also needs to be taken into account. However, for this part of the IMC signal, the time delay of the instrument needs to be taken into consideration, in order to determine a reasonable time frame during which the IMC signal at open-circuit conditions is included in the integration. The applied method is explained in more detail in the Experimental section.

The combination of all three methods enables the differentiation and identification of the different sources of heat contributing to the experimental IMC data. In particular, when the irreversible heat calculated by Eq. 7 is subtracted from the calorimetric data of the respective half-cycle,  $Q_{hys}$  can be determined for the charge and discharge half-cycles. However, when calculating  $Q_{hys}$  with this method, the reversible heat,  $Q_{rev}$ , cannot be neglected, although the fact that  $Q_{rev}$  cancels out in Eq. 5 might give this impression. This is because, unlike a whole cycle, the reversible heat during a half-cycle, e.g.,  $Q_{rev,cha}$  during charge, contributes to the heat evolution measured by IMC. However, when calculating the heat evolution of a half-cycle by method (ii), the reversible heat is not included because it cannot be calculated from the voltage data collected during intermittent cycling. Thus, when comparing both values, the inconsistency with regard to  $Q_{rev}$  constitutes an error source for determining the share of  $Q_{hys}$  for individual half-cycles. Therefore, we use the term  $Q_{residual}$  instead of  $Q_{hys}$  (see Fig. 10) to make it more clear that what is determined by method (ii) is the residual heat for each charge/discharge half-cycle. In other words,  $Q_{residual}$  only

equals  $Q_{hys}$  if  $Q_{rev}$  were zero. This will be discussed in more detail in the Results section.

## Experimental

**Battery assembly and cycling.**—LMR-NCM of the composition  $\text{Li}_{1.14}(\text{Ni}_{0.26}\text{Co}_{0.14}\text{Mn}_{0.6})_{0.86}\text{O}_2$ , which corresponds to the nomenclature  $0.33 \text{Li}_2\text{MnO}_3 \cdot 0.67 \text{LiNi}_{0.38}\text{Co}_{0.21}\text{Mn}_{0.41}\text{O}_2$  as used by Teuff et al.<sup>9</sup> and NCA of the composition  $\text{LiNi}_{0.81}\text{Co}_{0.15}\text{Al}_{0.04}\text{O}_2$  were obtained from BASF SE (Germany). For electrode preparation, inks of the cathode active material (CAM) were prepared by mixing 92.5 wt% CAM (NCA or LMR-NCM), 3.5 wt% polyvinylidene-fluoride binder (PVdF, Solef 5130, Solvay, Belgium), and 4 wt% conductive carbon (Super-C65, Timcal, Switzerland) with N-methyl pyrrolidine (NMP, anhydrous, Sigma-Aldrich, Germany). The dispersion was mixed in a planetary orbital mixer (solid content  $\approx 58$  wt%; Thinky, USA). The resulting ink was coated onto aluminum foil ( $\approx 15 \mu\text{m}$ , MTI, USA) and the dried coatings were calendered (GK 300 L, Saueressig, Germany) to a porosity of  $\approx 42\%$ – $45\%$ . For electrochemical testing, the electrodes were dried for a minimum of 12 h at  $120^\circ\text{C}$  under dynamic vacuum (Büchi, Switzerland). The loading of the LMR-NCM electrodes was  $\approx 12 \text{ mg cm}^{-2}$ , which corresponds to  $\approx 3 \text{ mAh cm}^{-2}$ , (based on a nominal reversible capacity of  $250 \text{ mAh g}_{\text{LMR-NCM}}^{-1}$ ). The NCA electrode loading was  $\approx 13 \text{ mg cm}^{-2}$ , which corresponds to  $\approx 2.6 \text{ mAh cm}^{-2}$ , (based on a nominal reversible capacity of  $200 \text{ mAh g}_{\text{NCA}}^{-1}$ ).

Coin cells (type CR2032) were assembled in an argon-filled glovebox ( $\text{O}_2$ ,  $\text{H}_2\text{O} < 0.1$  ppm, MBraun, Germany) with the manufactured cathodes (14 mm diameter), two glass fiber separators (17 mm diameter, glass microfiber #691, VWR, Germany), and a Li counter electrode (15 mm diameter,  $450 \mu\text{m}$  thickness, 99.9%, Rockwood Lithium, USA). A volume of  $100 \mu\text{l}$  of electrolyte was added, composed of 1 M  $\text{LiPF}_6$  in a FEC:DEC-based (12:64 v:v) solvent with 24 vol% of an additional fluorinated co-solvent (BASF SE, Germany). Electrochemical testing was performed at  $25^\circ\text{C}$  in a temperature-controlled oven (Binder, Germany) using a potentiostat (VMP300, Biologic, France). First, a formation cycle at a C-rate of C/15 (voltage cutoffs for LMR-NCM were 2.0–4.8 V and for NCA 3.0–4.4 V; all voltages reported vs  $\text{Li}^+/\text{Li}$ ) and two stabilization cycles at C/10 (2.0–4.7 V for LMR-NCM and 3.0–4.4 V for NCA) were conducted. All C-rates reported here refer to the above stated nominal capacities of the CAMs. The cells analyzed in this study can be divided into two groups: (i) those used for the IMC measurements (red box in Fig. 2); and (ii) those used to determine the irreversible heat (blue box in Fig. 2).

**Isothermal micro-calorimetry measurements.**—Following the initial formation cycles, which were conducted in-house, the calorimeter cells were transferred to an isothermal micro-calorimeter at the Helmholtz Institute Ulm to record the heat generation during cycling. A TAM IV calorimeter equipped with a 20 ml micro-calorimeter (stability  $\pm 50 \mu\text{K}$ , accuracy  $\pm 300 \text{ nW}$ , precision  $\pm 100 \text{ nW}$ , TA Instruments, USA) was used for this purpose. All measurements were performed at  $25^\circ\text{C}$  under isothermal conditions, following internal gain calibration. During the course of the experiments, the baseline drift did not exceed  $700 \text{ nW}$ . The step response of the heat flow is of second order, and the two characteristic time constants are  $T_1 = T_2 = 158 \pm 1 \text{ s}$ . This results in a time delay of  $\approx 1050 \text{ s}$  until 99% of the heat flow signal is detected. Here, a positive sign in the observed heat flow indicates that heat is generated by the cell.

The cells were cycled in a custom-made coin cell holder, which was connected by Cu-P bronze wires (36 AWG, Lakeshore, USA) to a potentiostat (VSP, BioLogic, France). Galvanostatic cycling was conducted, as shown in the red box in Fig. 2, at a number of current levels (C/10, C/5, C/2, 1C). For each C-rate, one first continuous charge/discharge cycle was performed and ended by a 6 h equilibration phase in the discharged state under open-circuit conditions. This

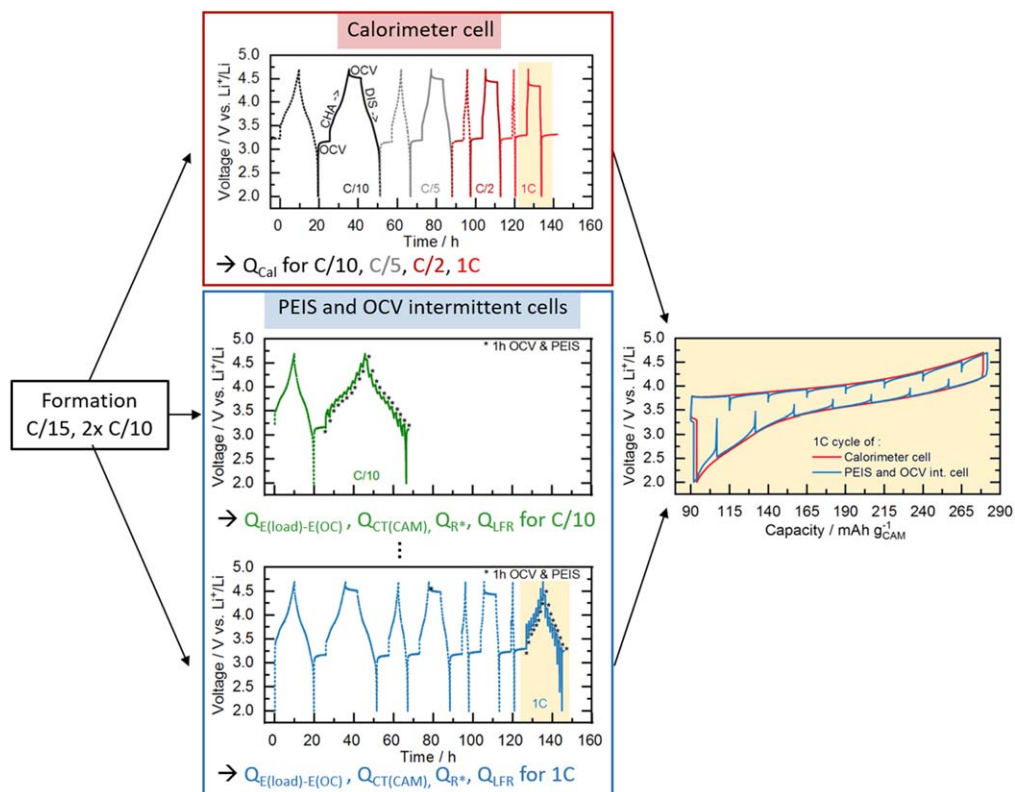


**Figure 2.** Graphic representation of the cycling procedures used in this study, with the initial formation cycle at C/15 (2.0–4.8 V for LMR-NCM/Li and 3.0–4.4 V for NCA/Li) and two stabilization cycles at C/10 (2.0–4.7 V for LMR-NCM/Li and 3.0–4.4 V for NCA/Li) conducted in-house (black box, left). The subsequent actual test protocols differ for the two types of experiments: (i) for the IMC measurements (red box), cells were cycled inside the calorimeter with a loop of one stabilization cycle and one cycle with 6 h rest phases at the beginning and end of each half-cycle, repeated for each applied C-rate (C/10, C/5, C/2, 1C); (ii) for the determination of the different sources of heat (blue box), an intermittent cycling protocol with 10% SOC steps and 1 h OCV phases was applied. For each C-rate, two identical cells were cycled with the same protocol as the IMC cells but for the C-rate of interest, where the intermittent cycling was applied (see example for C/10 and 1C in the blue box). The panel on the right presents a comparison of the data at 1C for a calorimeter cell and the cell with intermittent cycling.

first cycle was intended for the purpose of adapting to a new C-rate, and the heat generated during this process was not considered. The heat flows were determined from the second cycle, commencing with a constant-current charge to the respective upper cutoff voltage (4.7 V for LMR-NCM and 4.4 V for NCA) at the particular C-rate, followed by a further 6 h equilibration phase to enable separation of the heat flow during charge and discharge, and finally discharging to the respective lower cutoff voltage (2.0 V for LMR-NCM and 3.0 V

for NCA). The discharge was followed by a 6 h open-circuit phase before the whole loop of two cycles was repeated for the next C-rate. Two identical cells were measured for each CAM. A constant baseline was used for integration of the data, which was determined as the minimum heat flow at each C-rate section. By subtraction of this constant background signal, a correction for minor parasitic heat flows is achieved.<sup>20</sup> However, it must be kept in mind this is not the true value of the parasitic heat of this cell, which depends on complex relationships among all cell components, the SOC and voltage of the cell and its cycling history. This simplification is acceptable for the scope of this study but it does not describe the nature of the parasitic heat flow. Due to the time delay, the integration of the heat flow of an individual charge or discharge half-cycle includes not only the heat signal during current flow, but also that during the subsequent relaxation phase. Of the applied 6 h relaxation phase, we only included the first 1.5 h into the calculation, which is sufficient to obtain most of the actual heat signal, considering the time delay of  $\approx 18$  min (until 99% of the signal is detected), while being short enough to minimize contributions from parasitic heat flows.

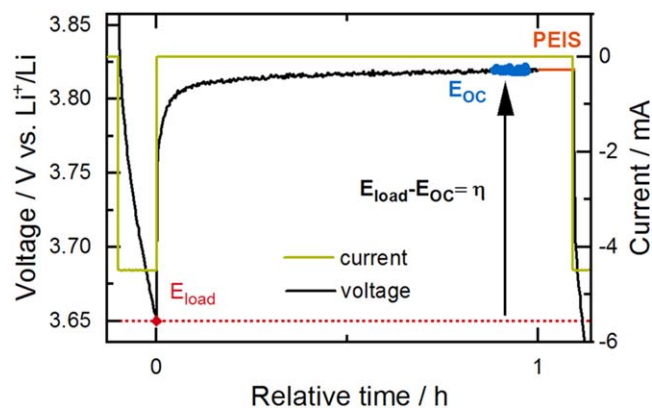


**Figure 3.** Application of intermittent cycling to determine the polarization induced overpotential  $\eta = E_{load} - E_{OC}$ . The current (green) and voltage (black) during a 1C discharge ( $\Delta SOC = 10\%$ ) and a consecutive 1 h OCV phase are shown.  $E_{OC}$  is determined by averaging over the final 300 s of the OCV phase (data marked in blue). After relaxation, a PEIS measurement is conducted, whose duration is only shown schematically here (orange).

**Determination of irreversible heat by intermittent cycling and impedance analysis.**—As shown in Eq. 3, the irreversible heat generation rate ( $\dot{Q}_{irrev}$ ) is a function of the voltage difference  $\eta$  between the voltage on load ( $E_{load}$ ) and after relaxation at open-circuit conditions ( $E_{OC}$ ). During intermittent cycling,  $\eta$  is determined after a certain time  $t$  of the intermittent relaxation phase, as shown in Fig. 3. The applied cycling protocol was similar to a galvanostatic intermittent titration and included (dis)charging steps of  $\Delta SOC = 10\%$  followed by a relaxation phase of  $t = 1$  h. This was repeated

until the upper (lower) voltage cutoff was reached. To determine  $\eta$  for the first SOC point during charging, the method shown in Fig. 3 is not applicable, because there is no preceding voltage relaxation in the charge direction. Therefore, for this data point, it was only possible to determine the instantaneous voltage jump upon applying the charging current. The same holds for the first point on discharge. The underlying resistance to this instantaneous voltage change was calculated using Ohm's law, and it was observed that it agrees well with the low-frequency resistance calculated from the impedance analysis. Hence, for the first SOC point of each half-cycle, the intermittent technique complies with the impedance and does not include any effects of diffusion, as is the case if  $\eta$  can be determined from full voltage relaxation.

The intermittent cycling, shown in the blue box in Fig. 2, was conducted with identical cells, as used in the IMC measurement with two cells for each C-rate. To ensure applicability of the herein determined irreversible heat to the data obtained from IMC experiments, the intermittent cycling protocol mimics the cycling protocol for the IMC. This means that to determine  $\eta$  at a specific C-rate, the cell first underwent the same loop of continuous cycling and charging/discharging with a 6 h rest phase in between at each C-rate preceding the C-rate of interest, such that the irreversible heat data are from the exact same cycle with the same cycling history as the heat data from the IMC (illustrated in the bottom panel of Fig. 2 for acquiring intermittent cycling data at 1C). Furthermore, the OCV data shown in this paper were determined by a Matlab script averaging over the final 300 s of the intermittent relaxation phase (see data given in blue in Fig. 3).

In addition to determining the overpotential by intermittent cycling, the cell resistance was further analyzed by means of impedance spectroscopy. As marked in Fig. 3, an impedance measurement (PEIS) was conducted at the end of each 1 h intermittent relaxation phase of the protocol described above. A potentiostat (VMP300, Biologic, France) was used in a frequency range of 200 kHz to 100 mHz with an AC voltage perturbation of 10 mV (taking 20 data points per decade and 3 period repetitions). As explained in the Theoretical Considerations above, data were fitted by the equivalent circuit  $R^* + TLM(R_{pore} + R_{CT(CAM)}/Q)$ . Here,  $R^*$  includes the high frequency resistance of the cell, the impedance of the Li anode, and the contact resistance of the cathode. The data of the high-frequency semi-circle was not taken into account for the fit, and  $R^*$  was set to the end of the first semi-circle, as shown in Fig. 1. The low-frequency semi-circle was fitted by the transmission line model, including contributions from the pore resistance,  $R_{pore}$ , and the charge transfer resistance of the cathode,  $R_{CT(CAM)}$ . The pore resistance of the LMR-NCM/Li cells was extracted from a fit of an impedance spectrum at high SOC during

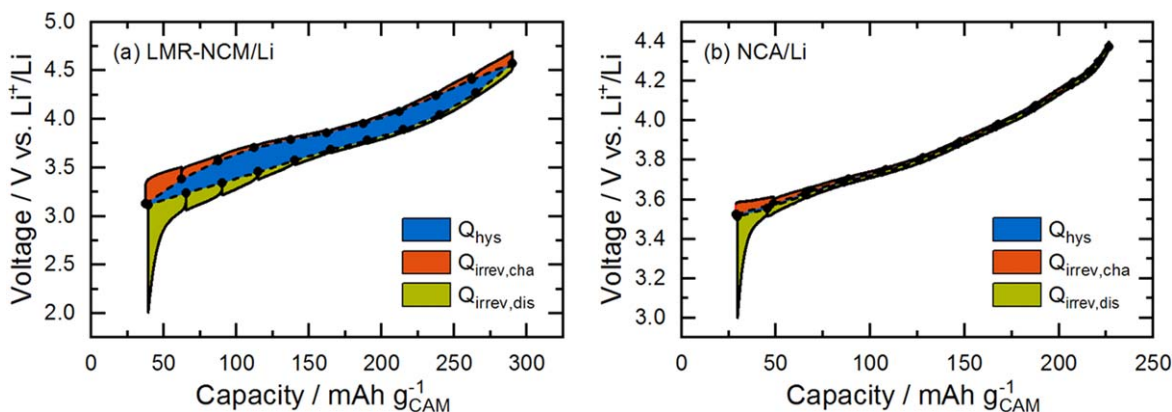
charge, in which the characteristic 45° line<sup>23</sup> was clearly observable and kept constant for all other impedance fits of this cell. In the case of NCA/Li cells, the pore resistance could not be clearly distinguished and is therefore a part of  $R_{CT(CAM)}$ . Furthermore, we only show  $R^*$  and the sum of  $R_{CT(CAM)}$  and  $R_{pore}$  for NCA where they were clearly distinguishable (at high and low SOC) and otherwise report  $R_{LFR}$ . Due to the generally much smaller  $R_{CT(CAM)}$  of NCA/Li cells compared to LMR-NCM/Li cells, the impedance contribution of the lithium counter electrode in the mid-SOC region is of a similar order as  $R_{CT(CAM)}$ , which results in the two semi-circles merging. Hence, for the respective spectra,  $R_{CT(CAM)}$  cannot be assigned unambiguously.

Figure 1 shows an example of an impedance spectrum for an LMR-NCM/Li cell. Unfortunately, we did not collect any data under blocking conditions, as would usually be performed to determine  $R_{pore}$ .<sup>23</sup> The results for  $R_{pore}$  are 12.2  $\Omega \text{ cm}^2$  and 10.1  $\Omega \text{ cm}^2$  for the two nominally identical LMR-NCM/Li cells at C/10. The charge transfer resistance of the cathode was extracted from the transmission line model. It was verified by impedance experiments using a gold wire micro-reference electrode (not shown here), which, furthermore, correspond with the data in the literature.<sup>12</sup> The difference between the irreversible heat calculated from the polarization induced overpotential  $\eta = E_{load} - E_{OC}$  and that calculated from the low-frequency resistance ( $R_{LFR}$ ) determined from the PEIS data is due to the mass-transport limitations within the electrolyte and the porous electrode, which are not captured by the PEIS measurements in the applied frequency range.

**Determination of reversible heat.**—As shown in Eq. 2, reversible heat is calculated as a product of the current, temperature and temperature-dependent OCV value,  $\frac{\partial E_{eq}}{\partial T}$ . The latter was measured as a function of SOC after (dis)charging the cell to a certain SOC point and allowing it to relax until the change in OCV over time was less than 0.2 mV/h. After this relaxation,  $\frac{\partial E_{eq}}{\partial T}$  was determined by linearly varying the temperature of the cell between 5 °C and 35 °C in an Espec temperature chamber (LU114, Espec, Japan), while recording the respective OCV variation (VMP300, Biologic, France). A detailed description of the method applied is reported elsewhere.<sup>14</sup> The obtained values for  $\frac{\partial E_{eq}}{\partial T}$  are shown in the appendix (Figure A-1).

## Results and Discussion

**Lost electrical energy.**—Lost electrical energy is the difference between the charge and the discharge energy of one cycle, and is expected to dissipate as waste heat. The two cathode active materials



**Figure 4.** Voltage vs SOC charge/discharge curves of (a) LMR-NCM/Li and (b) NCA/Li in the 5th cycle at C/10 obtained during intermittent cycling with 1 h OCV holds at every 10% SOC interval. The charge curve is shown as a black solid line and the OCV points are shown as black circles connected by a dashed line. The integral of the whole curve is the total lost electrical energy, which can be separated into three parts: irreversible losses during charge (orange) and discharge (green) due to polarization induced overpotential, and the lost energy due to OCV hysteresis (blue).

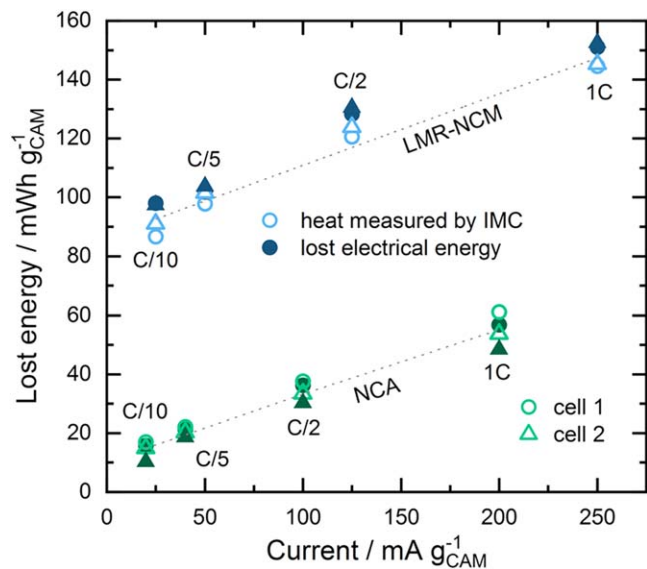


**Figure 5.** Comparison of the lost electrical energy calculated from the voltage vs SOC curve (dark, filled symbols) and the heat measured by IMC (pale, empty symbols) for two identical LMR-NCM/Li cells (blue) and NCA/Li cells (green) for different mass-specific current densities (corresponding to the C-rates indicated in the figure). The dashed lines represent a linear fit through the average of all data points of one cell chemistry at each C rate.

of interest, LMR-NCM and NCA, exhibit considerably different energy efficiencies. While an LMR-NCM/Li cell has an energy efficiency of  $\approx 90\%$  in the 5th cycle at C/10, that of an NCA/Li cell reaches  $\approx 99\%$ . Figure 4 shows a voltage vs SOC charge/discharge curve for both cell types in a C/10 cycle. According to Eq. 6, the total energy loss corresponds to the integration of the geometrical area enclosed by the charge and discharge voltage curve (sum of orange, blue, and green shaded areas in Fig. 4). This total energy loss can be further separated into three parts: (i) the irreversible energy loss during charge ( $Q_{irrev,cha}$ ), i.e., the difference between the voltage curve on load and the OCV curve during charge (orange shaded area), as described by Eq. 7; (ii) the irreversible losses during discharge ( $Q_{irrev,dis}$ ; green shaded area); and, (iii) the energy loss due to OCV hysteresis ( $Q_{hys}$ ; blue shaded area), as described by Eq. 8.

Note here, that the coulombic inefficiency of the cell means that the end of the discharge curve does not meet the start of the charge curve. For clarity, the resulting “gap” is not colored in Fig. 4. The deconvolution of these different energy loss terms as a function of the C-rate is shown in Table I for LMR-NCM and NCA half-cells. Thereby, the values for  $Q_{irrev}$  for charge and discharge were calculated by applying Eq. 7. The calculation of  $Q_{hys}$  was based on Eq. 8. However, the last  $E_{OC}$  value upon discharge did not agree with the first  $E_{OC}$  on charge due to the coulombic inefficiency of the cell. If Eq. 8 were exactly applied, this would lead to an obvious overestimation of  $Q_{hys}$ , which is physically not meaningful. In other words, the blue area in Fig. 4 would extend down to zero volts because there is no matching discharge voltage curve. Instead, we applied a small correction, so that the last  $E_{OC,dis}$  value agrees with the first  $E_{OC,cha}$  value.  $Q_{hys}$  is thus calculated by integrating over a closed OCV hysteresis curve. This assumption minimizes the error of the coulombic inefficiency but does not exclude it all together. The resulting implications will be discussed throughout this work. For an absolutely accurate calculation the error introduced by the coulombic inefficiency should be ruled out by the design of the experiment using capacity limited cycling procedures (instead of voltage limited), so that the discharge capacity is equal to the charge capacity. This might be a starting point for future research activities striving for the exact quantification of individual heat terms.

As outlined in the Theory section, irreversible energy losses due to overpotential ( $Q_{irrev}$ ) are dependent on the applied current, while the hysteresis of the OCV is expected to be independent of the C-rate. As expected, the polarization induced overpotential losses in Table I increase with increasing current for both cell chemistries. In the case of LMR-NCM, the irreversible heat during discharge is larger than during charge and becomes more and more dominant for increasing current values, until it reaches 50% of total heat generation at 1C. In Fig. 4a, it can be seen that the potential difference between the voltage curve on load and the OCV curve increases drastically at the end of the discharge (to a lesser degree also at the end of the charge). Hence, the end of the lithiation process of the cathode active material seems to be accompanied by significant kinetic limitations, leading to high overpotentials and, in turn, to high irreversible heat evolution. The asymmetry of the LMR-NCM cathode resistance between the charge and discharge direction was previously demonstrated by Teufl et al.<sup>12</sup>

Energy loss due to overpotential is significantly smaller for NCA, as can be clearly seen in Fig. 4b and Table I. Still, the resistance behavior of NCA at low SOC during discharge is similar to that of LMR-NCM, with a steep increase at the end of the discharge. This was attributed to an increase in the charge transfer resistance, as reported by Weber et al.<sup>25</sup> More important is the OCV hysteresis comparison, since there is no significant contribution from this term for NCA/Li cells and the determined contribution of the OCV hysteresis to the overall energy loss of 0.1%–0.3% (see last row in Table I) are most probably due to the fact that the  $E_{OC}$  is not yet exactly equal to  $E_{eq}$  after the 1 h rest phase. In contrast, the cells with an LMR-NCM cathode suffer a considerable energy loss due to OCV hysteresis of up to 55% of the total energy loss at C/10. At first sight surprising is the observation that the energy loss due to the OCV hysteresis of the LMR-NCM/Li cells decreases with increasing C-rate. The reason for this is that the applied cycling protocol is voltage-limited, meaning that a smaller overall SOC range is accessed when cycling at higher C-rates, and therefore only a smaller part of the OCV hysteresis is observable. We have shown elsewhere (see Fig S6 (available online at [stacks.iop.org/JES/169/040547/mmedia](https://stacks.iop.org/JES/169/040547/mmedia)) in Ref. 14) that when applying a capacity-limited cycling procedure, the OCV hysteresis is independent of the C-rate. The energy loss due to OCV hysteresis results in an undesirable energy inefficiency, which is presumably dissipated as heat. To clarify this, IMC measurements were conducted to analyze the different sources of heat, particularly the heat due to OCV hysteresis in such materials and to compare it to the thermal behavior of a classical CAM such as NCA.

**Accuracy of the isothermal micro-calorimeter.**—In order to establish a quantitative correlation between the lost electrical energy calculated from the voltage vs SOC curve by method (ii), as described in the Theory section, and the heat measured by IMC (method (iii)), the accuracy of the calorimetric measurement first has to be validated. For this purpose, the heat evolution from the IMC data (pale, empty symbols) and that calculated from the respective voltage curves (dark, filled symbols) are contrasted in Fig. 5. Ideally, both data sets should show perfect agreement, which is indicated by the dashed lines that represent linear regression lines through all the data. For the LMR-NCM/Li cell, the deviation is between  $-2\%$  and  $-6\%$ , with one outlier of  $-12\%$  for the LMR-NCM/Li cell for one of the two cells (cell number 1) at C/10. This means that the measured heat by calorimetry is generally slightly below the expected value, which may be due to instrument errors such as the loss of heat through the cables connecting the coin cell holder with the potentiostat. Also, it should be noted that if the integration of the calorimeter heat signal in the 6 h OCV rest phase at the end of discharge had been chosen to be longer than 1.5 h, the deviations would become smaller. However, since the estimated time delay for detection of 99% of the heat signal is  $\approx 18$  min, any extension of the

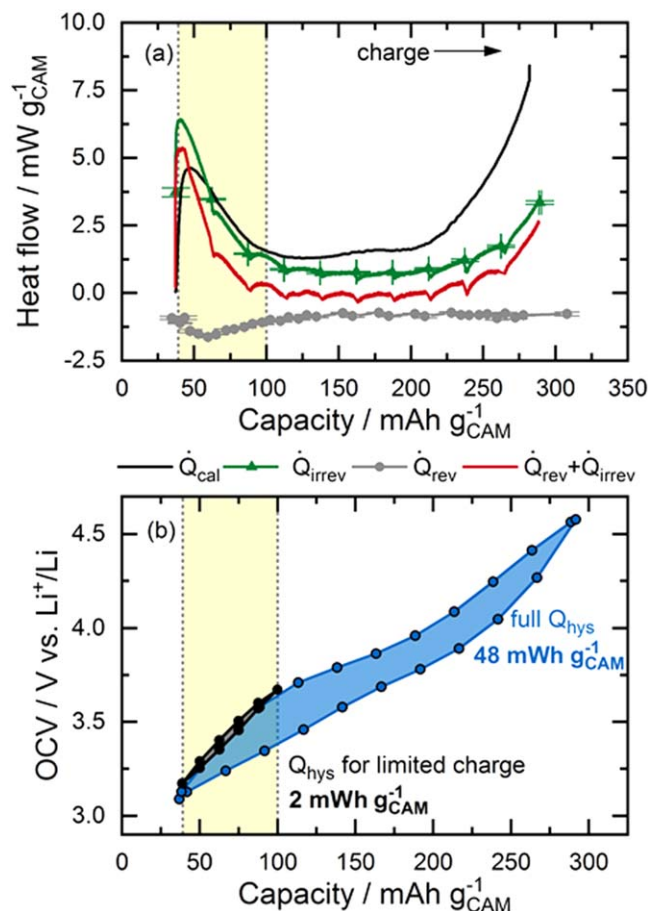


**Figure 6.** (a) Heat flow of an LMR-NCM/Li cell in charge at C/10 as a function of SOC. The heat flow measured by IMC (black) for cell 2 is compared to the calculated profiles of  $\dot{Q}_{irrev}$ , based on the polarization induced overpotential (green, error bars from two measurements; the green line representing a linear interpolation of the OCV data points), and  $\dot{Q}_{rev}$ , as determined from entropy measurements (gray, error bars from the calculation). The sum of  $\dot{Q}_{irrev}$  and  $\dot{Q}_{rev}$  is shown in red. (b) OCV curve at C/10 of a complete cycle (blue) and a cycle limited to a nominal capacity of 100 mAh  $g_{CAM}^{-1}$  during charge (black). The yellow shaded area highlights the SOC range in which no significant OCV hysteresis is expected (thus,  $\dot{Q}_{hys} \approx 0$ ).

integration window would increase the risk of including contributions from non-faradaic heat (e.g., through parasitic side reactions). In the case of NCA, the deviations are between +4% and +10%, i.e., the heat measured by calorimetry is more than that obtained by the integration of the voltage vs SOC curves. One of the two NCA/Li cells (cell number 2) showed an outlier of +45% at C/10, but since a fluctuation in the applied electrical current was detected, we did not include this data point in our calculations. Due to the much smaller absolute amount of produced heat in case of the NCA/Li cell, any contributions from undesired side reactions and parasitic heat terms result in a much higher relative error, which might be the reason why the integrated IMC signal is higher than expected. Nevertheless, since the deviations between the expected and measured heat are below  $\pm 10\%$  (with the exception of the two above mentioned cases) for both cell chemistries, our original assumption that the lost electrical energy is converted into heat and that parasitic side reactions play no major role is confirmed within the error of the measurements. Another conclusion that can be drawn from Fig. 5 is that the experiments are reproducible, since the energy losses for both cells correspond fairly well (the deviation between two repeat cells at the same C-rate is less than 6% in all cases, except for the two instances mentioned above). For all further calculations, we considered LMR-NCM/Li cell 2 and NCA/Li cell 1.

When comparing the total electrical energy loss/heat production measured by the continuous constant-current (CC) cycling protocol used in the calorimeter experiments (data in Fig. 5) with the total electrical energy loss measured in the intermittent cycling protocol (first row in Table I), it becomes apparent that there is a reasonably good agreement at the low C-rate of C/10, with the intermittent cycling yielding slightly lower energy losses, but that at higher C-rates, this deviation increases substantially, so that at 1C the intermittent cycling procedure results in a  $\approx 25\%$ – $35\%$  lower total energy loss. This is mainly due to three factors. First, the CC-cycling procedure, particularly at higher C-rates, leads to a higher overall voltage polarization compared to the intermittent cycling procedure, for which the intermittent OCV holds allow for a repeated relaxation of the concentration gradients in the liquid and solid phase. This can be seen by the comparison of the resulting voltage vs SOC curves shown in the right-hand panel of Fig. 2. Thus, integrating a voltage vs SOC curve from an intermittent cycling protocol always resulted in a smaller value compared to that from a CC-cycling protocol, meaning that the energy losses from intermittent cycling are slightly lower (by  $\approx 4\%$ – $7\%$  for the LMR-NCM/Li cells and by up to  $\approx 25\%$  for NCA/Li cells). The second reason is that the Coulombic efficiency of each cycle is slightly less than 100%. This irreversible capacity leads to a small ‘gap’ between the charge and the discharge voltage curves, so that the integration of the voltage vs SOC curve cannot be performed 100% accurately. The calculation of total electrical energy loss from the voltage vs SOC curves of the cells tested in the calorimeter energy loss caused by the integration of the gap. For the cells from the intermittent cycling, the electrical energy loss is calculated based on Eq. 6. This mathematical approach, however, does not include the integration of the ‘gap’ since it can neither be ascribed to  $\dot{Q}_{irrev}$  during charge or discharge, nor to  $\dot{Q}_{hys}$ . Thus, the calculated electrical energy loss is lower in case of the cells from intermittent cycling due to the integration of the voltage vs SOC curve. The third reason is the slightly higher contact resistance of the custom-made coin cell holder for the experiments conducted in the calorimeter ( $\approx 9 \Omega$ ). As these three factors yield reasonably small differences in the total lost electrical energy determined from the voltage vs SOC curves obtained by the two different cycling protocols at C/10, but yield increasingly large differences at higher C-rates, the analysis in the following sections for which both cycling protocols are required will be limited to C/10.

Although the limits of the applied IMC method become clear from Fig. 5, it also provides an answer to the first question in the introduction to this paper: the energy loss due to the OCV hysteresis in LMR-NCM is indeed dissipated as heat (note that another, albeit unlikely possibility would have been that the OCV hysteresis presents a continuous chemical conversion of the bulk of the LMR-NCM material). Moreover, there is an important difference between the two cell chemistries, which is visualized in Fig. 5: the y-axis intercepts of the linear relationship between lost electrical work and measured heat vs mass-specific current density (dashed lines in Fig. 5) is rather small for the NCA/Li cells ( $\approx 12.1 \text{ mWh } g_{CAM}^{-1}$  and  $\approx 12.4 \text{ mWh } g_{CAM}^{-1}$  for cell 1), while it is quite large ( $\approx 93.1 \text{ mWh } g_{CAM}^{-1}$  and  $\approx 88.9 \text{ mWh } g_{CAM}^{-1}$  for cell 2) for the LMR-NCM/Li cells, caused by the quasi-static OCV hysteresis, as discussed by Assat et al.<sup>20</sup> for the  $\text{Li}_2\text{Ru}_{0.75}\text{Sn}_{0.25}\text{O}_3$  model compound. Chevrier et al.<sup>21</sup> also report a significant heat production at zero current for silicon anodes, and thereby correlate their observation to the current independent nature of the voltage hysteresis. We conclude that even at very low rates, there is significant hysteresis between the OCV curve on charge and discharge, indicating that the underlying processes are far from the thermodynamic equilibrium. The fact that the intercept for the NCA/Li measurement results is not zero, however, underlines the limits of the applied IMC method especially at such small observable heat signals. One would have expected the intercept to be zero because both contributions of reversible and irreversible heat should ideally vanish to zero at infinitesimally small currents. Apart from the accuracy of the method at such small heat

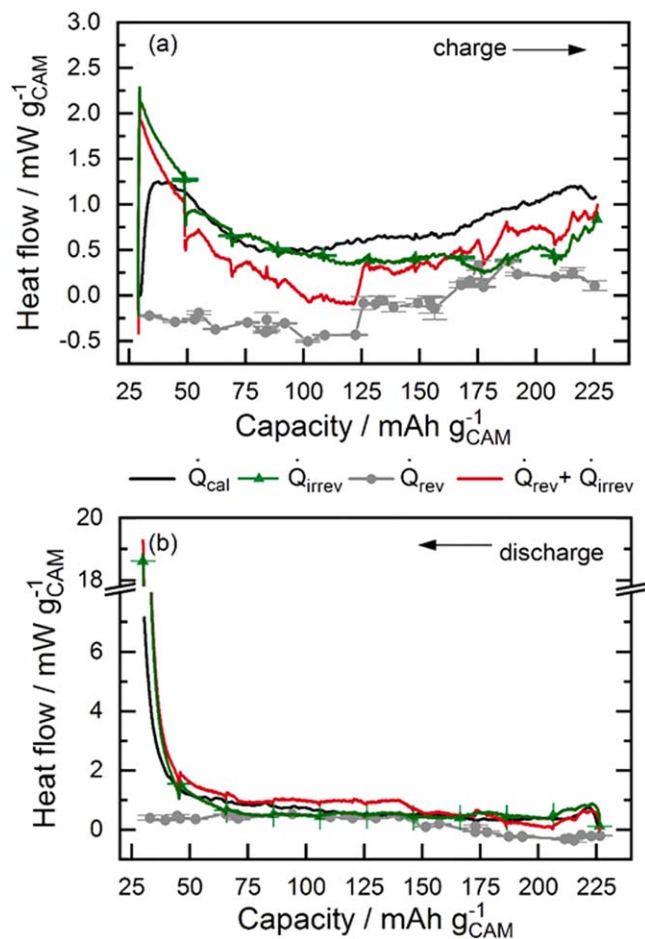


**Figure 7.** (a) Heat flow of an NCA/Li cell in charge at C/10 as a function of SOC. The heat flow measured by IMC (black) for cell 1 is compared to the calculated profiles of  $\dot{Q}_{irrev}$ , based on the polarization induced overpotential (green, error bars from two measurements), and  $\dot{Q}_{rev}$  as determined from entropy measurements (gray, error bars from the calculation). The sum of  $\dot{Q}_{irrev}$  and  $\dot{Q}_{rev}$  is shown in red. In panel (b) the same analysis is shown for the discharge process.

signal amplitudes, any assumptions and simplifications made during the calculation (e.g. correction for  $Q_{par}$ , integrating the voltage curve although the coulombic efficiency is less than 100%, etc.) are possible error sources, which might lead to the observed deviation from zero.

**Conventional contributions to the heat flow profile.**—In addition to the integration of the IMC heat signal to a total heat value, it is also possible to analyze the heat flow profile as a function of the SOC. This analysis involves calculating different heat sources, as outlined in the Theory section of the paper. Figs. 6 and 7 show the heat flow signal measured by IMC (black) together with various heat flow profiles calculated as a function of SOC for LMR-NCM/Li and NCA/Li, respectively. According to Eq. 2, three contributions to the total heat flow can be identified: irreversible heat ( $\dot{Q}_{irrev}$ ), reversible heat ( $\dot{Q}_{rev}$ ) and heat due to OCV hysteresis ( $\dot{Q}_{hys}$ ); while the first two terms can be observed for any electrode material, the latter is only observable in materials with a pronounced OCV hysteresis, such as LMR-NCM. The discussion in this section will focus on the conventional sources of heat,  $\dot{Q}_{irrev}$  and  $\dot{Q}_{rev}$ .

To compare the measured heat flow with the calculated values, two assumptions have to be made: (i) only the heat signal during current flow is analyzed, which means that heat dissipated after the current is removed is disregarded; (ii) the time delay of the IMC is

assumed to be virtually negligible, so the heat flow profile measured as a function of time can be directly translated to the SOC. Since both the time resolution and the heat dissipation after switching off the current increase with increasing C-rates, this heat flow analysis is only reliable for low currents. For example, with a C-rate of 1C, a time delay of  $\approx 18$  min already corresponds to a deviation of  $\approx 30\%$  SOC, which substantially falsifies the translation of the time axis into an SOC axis, whereas for a C-rate of C/10, this time delay only represents a deviation of 3%. Furthermore, with a C-rate of C/10, the heat evolved after switching off the current at the end of charge is  $\approx 12\%$  of the total heat measured for the charge half-cycle of an LMR-NCM/Li cell ( $\approx 4\%$  for NCA). In the discharge direction,  $\approx 7\%$  of the total heat is evolved at zero current for both cells. In contrast, for the cycle at 1C, these terms increase to  $\approx 19\%$  for the charge and  $\approx 27\%$  for the discharge in case of LMR-NCM/Li ( $\approx 11\%$  and  $\approx 22\%$  for NCA), which would clearly not lead to a meaningful analysis. However, even with the slowest C-rate, it is important to bear in mind that measured heat flow profiles are never completely accurate.

**Reversible heat contributions to the overall heat flow.**—As mentioned above, the reversible heat is included in the calorimetric signal but cannot be calculated from the voltage curve. As shown in Eq. 2,  $\dot{Q}_{rev}$  is determined on the basis of the variation of OCV with temperature. These measurements were conducted with the same cathode active material but the OCV was measured against a Li reference electrode, which did not undergo any electrochemical cycling as the Li counter electrode used in this study. Details of the experiment and a discussion of the entropy profile of LMR-NCM are reported elsewhere,<sup>14</sup> but the results from the entropy measurements of the two cathode active materials are plotted in the appendix. For the present study, the most important aspect of our previous publication is that the reversible heat of LMR-NCM/Li cells cannot be calculated from the measured partial molar entropy data because of the path dependence of the entropy curve as a function of SOC. Its integration would include non-reversible pathways, as is generally the case for material that shows a hysteresis in the partial molar entropy vs SOC. This means that a theoretical  $\dot{Q}_{rev}$  curve calculated from the entropy data would include an unknown contribution of entropy production in the material. Hence, although mathematically possible, this would not produce a physically meaningful result for the reversible heat flow as a function of SOC. However, this means that we cannot determine what share of the theoretical  $\dot{Q}_{rev}$  curve corresponds to the heat term that is reversibly evolved as a function of SOC.

Yet, with the IMC data we can estimate what effect neglecting  $\dot{Q}_{rev}$  has on the total heat evolution within a limited SOC range. For this purpose, Fig. 6 shows the IMC heat signal ( $\dot{Q}_{cal}$ , black) together with the irreversible heat calculated from the difference between the voltage vs SOC curve on load and under OCV conditions ( $\dot{Q}_{irrev}$ , green) and the theoretical reversible heat, which was calculated from the entropy data as explained in Eq. 2, although we already know that this is physically not meaningful (gray). Nevertheless, we will use these calculated data sets in our approach and focus on the heat flow in the low SOC region ( $< 100 \text{ mAh g}_{CAM}^{-1}$ ) during charge. There are two reasons why this SOC region is of special interest: (i) the theoretically calculated reversible heat flow profile exhibits a peak at around  $\approx 60 \text{ mAh g}_{CAM}^{-1}$  meaning that in the low SOC region, the contribution of  $\dot{Q}_{rev}$  is expected to be most significant; (ii) from cycling experiments it is known that when LMR-NCM is only charged to  $\approx 100 \text{ mAh g}_{CAM}^{-1}$  and then discharged again, there is no significant OCV hysteresis (see black data points in Fig. 6b), which means that the heat measured by IMC is exclusively attributable to  $\dot{Q}_{irrev}$  and  $\dot{Q}_{rev}$ , from which the first one can be easily determined. Figure 6b shows the OCV curve of a cell charged to  $100 \text{ mAh g}_{CAM}^{-1}$  together with an OCV curve that is obtained for a full charge/discharge. As is also known from window-opening

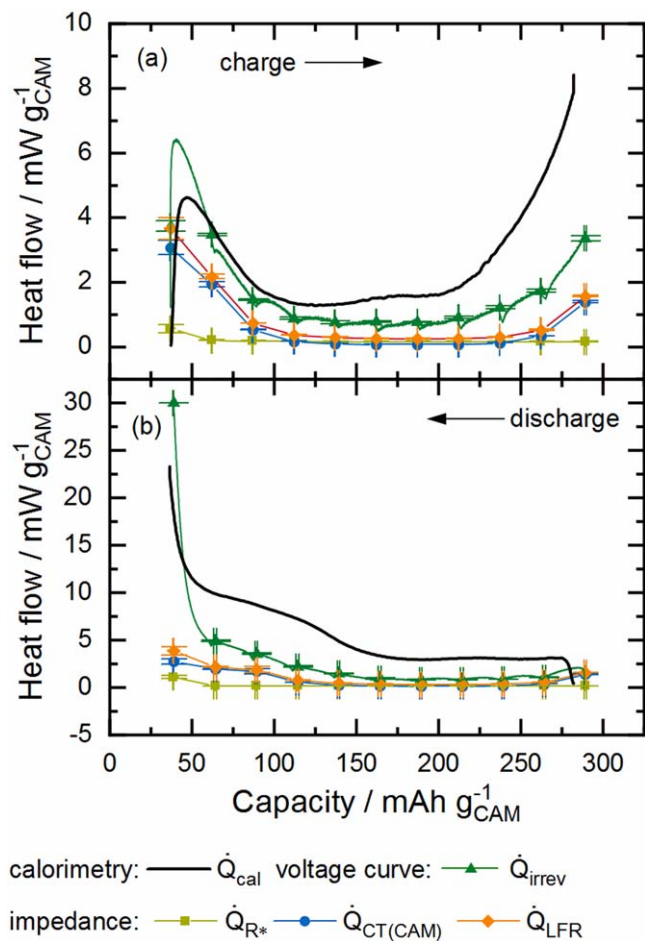


**Figure 8.** Heat flow during (a) charge and (b) discharge of the LMR-NCM/Li cell (number 2) at C/10 as a function of SOC. The heat flow measured by IMC (black) is compared to calculated heat flow profiles based on data from identical cells. Calculated heat flows are based on the voltage drop measured during intermittent cycling ( $\dot{Q}_{irrev}$ , green triangles), and impedance measurements including the LFR (orange), the  $R_{CT(CAM)}$  (blue) and the “ohmic” resistance  $R^*$  (light green). Error bars are shown for two measurements. The line connecting the voltage drop points (green triangles) results from the subtraction of the OCV curve from the voltage curve on load for the respective half-cycle.

experiments in the literature,<sup>26</sup> the OCV hysteresis of LMR-NCM is not pronounced if the charge window is not opened up to higher SOC. Thus, Eq. 2 simplifies, since  $\dot{Q}_{hys} = 0$ . This means that any difference between the heat flow measured by IMC and the irreversible heat generation determined from the polarization induced overpotential has to be caused by  $\dot{Q}_{rev}$ . However, as shown in Fig. 6a, the measured heat flow (black line) in the yellow shaded region, for which  $\dot{Q}_{hys} = 0$ , corresponds very closely with the irreversible heat generation (green line and symbols), indicating that the contribution from  $\dot{Q}_{rev}$  is not significant. The only deviation between the two heat signals is at the very beginning of charge, when the calculated irreversible heat exceeds the measured signal. This might be an artifact which comes from the fact that  $\dot{Q}_{irrev}$  is determined by interpolating between the first and the second OCV points whereby the first OCV point is obtained differently from the subsequent OCV points, as outlined in the Experimental part. The interpretation of this apparent overshoot should be considered carefully. Another reason for the observed mismatch between  $\dot{Q}_{irrev}$  and  $\dot{Q}_{cal}$  at the beginning of charge might be the above-mentioned time lag of the IMC signal detection. Another possibility is that at the beginning of charge, the endothermic reversible heat

indeed makes a contribution and hence partly compensates for the irreversible heat. However, when the heat flow calculated from the sum of the exothermic irreversible heat and the endothermic reversible heat (red curve in Fig. 6a) is compared to the measured data, no agreement is observed. This further underlines the conclusion drawn by Friedrich et al.<sup>14</sup> that the entropy measurements for LMR-NCM cannot be directly translated into a heat flow curve. The observation that the entropy does not significantly contribute to the measured heat flow profile in the low SOC range, where its values are maximum indicates that also for the rest of the cycle, its contribution can be neglected. Further IMC studies are required to quantify the reversible heat in this type of material. For the investigation conducted here, the reversible heat flow was neglected. Still, we want to emphasize that this simplification is a possible error source regarding the quantification of  $\dot{Q}_{hys}$ . What we report here as  $\dot{Q}_{hys}$  hence includes an unknown but comparably small contribution of the reversible heat.

The rather complicated discussion regarding the LMR-NCM material becomes simpler with a regular cathode active material, such as NCA, where no hysteresis is present and  $\dot{Q}_{rev}$  can be directly calculated from the measurement of  $\frac{\partial E_{eq}}{\partial T}$ , as explained in the Theory and Experimental sections. Since there is virtually no heat due to OCV hysteresis, Eq. 2 simplifies to  $\dot{Q} = \dot{Q}_{irrev} + \dot{Q}_{rev}$ . As discussed above, neglecting the SOC dependence of  $\dot{Q}_{par}$  results in a rough simplification of the energy balance for NCA. However, as can be seen in Fig. 7, this simplification is acceptable for a semi-quantitative analysis of heat flow as a function of SOC. In Fig. 7, the IMC signal (black) is shown together with the irreversible heat flow calculated from the intermittent cycling (green), the reversible heat calculated from entropy measurements (grey), and the sum  $\dot{Q}_{irrev} + \dot{Q}_{rev}$  (red). For the charge half-cycle in Fig. 7a, the irreversible heat is slightly higher than the measured heat at low SOC, while it is clearly smaller at a high SOC. By adding the reversible and irreversible heat, the calculated curve (red) moves closer to the measured one. However, there is still a gap, especially at a high SOC, between the measured signal and the calculated heat flow, which might be attributable to parasitic heat, or simply the inaccuracy of calculating and scaling such small heat flows. For the discharge direction, shown in Fig. 7b, the agreement of the calculated and measured heat flow is similar to that of the charge direction. However, it should be stressed that the absolute signal amplitude is nearly seven times higher, especially at the end of discharge, which makes a direct comparison of the two figure panels difficult.

Based on the data discussed, we conclude that the effect of reversible heat on total heat flow is a source of error, in particular for NCA/Li cells. While it is acceptable to assume a minor contribution of  $\dot{Q}_{rev}$  for the LMR-NCM/Li cell due to the comparably very high contribution from the OCV hysteresis heat,  $\dot{Q}_{rev}$  has a more significant effect on the overall heat flow for the NCA/Li cell, in which the measurement uncertainties are of the same order of magnitude as  $\dot{Q}_{rev}$ . Nevertheless, we want to stress that the exact contribution of  $\dot{Q}_{rev}$  was not quantified for either one of the two cells in this study, meaning that it is still contained in the additional heat term,  $\dot{Q}_{hys}$ , which will be discussed in the following. Since the significance of  $\dot{Q}_{rev}$  was shown to be rather minor for LMR-NCM/Li cells, its contribution to  $\dot{Q}_{hys}$  is not considered to be falsifying the analysis.

**Irreversible heat.**—So far, only the irreversible heat calculated from the potential drop during intermittent cycling has been shown. However, the resistances due to overpotential induced polarization can be further analyzed, using the impedances obtained by EIS analysis. Figures 8a and 8b show the heat flow profiles measured by

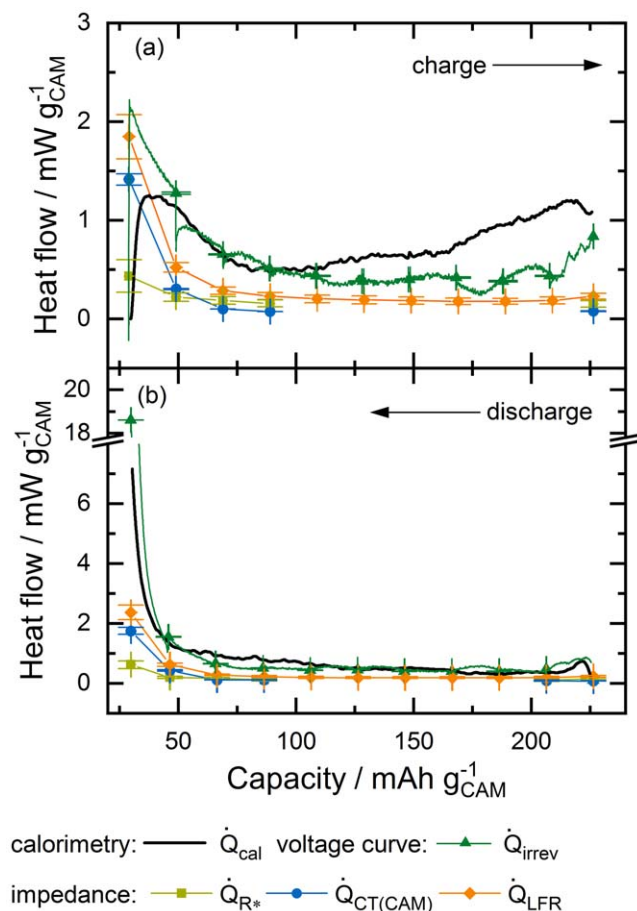


**Figure 9.** Heat flow during (a) charge and (b) discharge of NCA/Li cells at C/10 as a function of SOC. The heat flow measured by IMC (black) for cell 1 is compared to calculated profiles based on data from identical cells. Calculated heat flows are based on the voltage drop ( $\dot{Q}_{irrev}$ , green), and data calculated from impedance measurements including the LFR (orange), the  $R_{CT(CAM)}$  (blue) and the “ohmic” resistance  $R^*$  (light green). Error bars are shown for two measurements. The line connecting the voltage drop points (green triangles) results from the subtraction of the OCV curve from the voltage curve on load for the respective half-cycle.

IMC for the LMR-NCM/Li cell (black), together with those calculated from the impedance data based on Eq. 3 but using  $R_{LFR}$  instead of  $R_{tot}$  (orange). Figure 8 also includes the heat flow curves calculated from the individual components of  $R_{LFR}$ , namely  $R_{CT(CAM)}$  (blue) and  $R^*$  (light green) as explained by Eq. 4 and the polarization induced overpotentials (i.e.,  $E(load) - E(OC)$ ) determined by the intermittent cycling protocol, using the first part of Eq. 3 ( $\dot{Q}_{irrev}$ , green triangles).

In a first comparison of the calorimetric data (black), a clear asymmetry between the charge and discharge heat flow profiles can be observed (see Figs. 8a and 8b). At the beginning of charge cycle, there is a peak in the heat evolution, with a maximum at  $\approx 55 \text{ mAh g}_{CAM}^{-1}$ , which levels off at around  $100 \text{ mAh g}_{CAM}^{-1}$ , after which a plateau is observed. At around  $225 \text{ mAh g}_{CAM}^{-1}$ , the heat flow increases again and reaches a maximum at the end of charge. For the charge half-cycle, the heat flow values over most of the charge are in a range of  $1.3 \text{ mW g}_{CAM}^{-1}$  to  $8 \text{ mW g}_{CAM}^{-1}$ , while for the discharge, these values are much larger, varying between  $3 \text{ mW g}_{CAM}^{-1}$  and  $36 \text{ mW g}_{CAM}^{-1}$ . Besides the absolute values, the profile shape between charge and discharge also differs. During discharge, the heat flow is constant in the high SOC region but starts to increase when discharging below  $\approx 170 \text{ mAh g}_{CAM}^{-1}$ . Following a steady increase in heat flow in this lower SOC region, a sharp increase is observed when discharging below  $\approx 65 \text{ mAh g}_{CAM}^{-1}$ .

Irreversible heat flow can be calculated with Eq. 3 based on the voltage drop occurring when the current is switched off during an intermittent cycling, as indicated by the green triangles in Fig. 8. In addition, the OCV curve of a charge/discharge half-cycle (linear interpolation between OCV points) can be subtracted from the respective voltage curve on load (green curve, which is identical with that shown in Fig. 6a), which in principle should give the same results as the data based on the potential drop after one hour of OCV. As a matter of fact, both data sets agree except for the first point during charge, at which the calculation of the voltage drop is based on the instantaneous voltage jump upon connecting the current, as described in the Experimental section. Thus, for the first 10% SOC range, the subtraction line is a better measure for the irreversible heat.

Since the generation of irreversible heat is based on the resistances within a battery cell, impedance spectroscopy is a complementary tool that can be used to further distinguish the underlying resistive phenomena that cause irreversible heat flow. The applied equivalent circuit model includes the charge transfer resistance of the cathode ( $R_{CT(CAM)}$ , shown in blue in Fig. 8), the low-frequency resistance (LFR, orange) and a so-called  $R^*$  (light green), which includes contributions from the high frequency resistance, cathode contact resistance, and anode impedance, as discussed in the Theory and Experimental sections. An example impedance spectrum is shown in Fig. 1. These resistances were translated into a heat flow with Eq. 3. As can be seen in Fig. 8, the profile of the total irreversible heat flow  $\dot{Q}_{irrev}$  as determined from the voltage drop agrees with the shape of that calculated from impedance data,  $\dot{Q}_{LFR}$ . Both exhibit a U-shape as a function of SOC during charge, which is typical for this type of material.<sup>12</sup> Furthermore, the impedance measurements prove that the dominating contribution to the irreversible heat flow is the charge-transfer resistance,  $\dot{Q}_{CT(CAM)}$ , while all other resistances, summarized as  $\dot{Q}_{R^*}$ , make only minor contributions. The offset between the irreversible heat calculated from the voltage drop ( $\dot{Q}_{irrev}$ ) and the heat obtained from the impedance data ( $\dot{Q}_{LFR}$ ) is due to diffusion limitations, which are not captured in the impedance experiment with a lower frequency limit of 0.1 Hz but are included in the voltage drop. These limitations include liquid and solid diffusion, which seem to be rather constant in the middle of the SOC window, with increasing values at low and high SOC. The overall diffusion resistance can be estimated from the difference of the two heat profiles by translating the respective heat flow into an apparent resistance based on Eq. 3. In the constant region, it is around  $\approx 60 \Omega \text{ cm}^2$  while at high SOC during charge, it increases to  $\approx 140 \Omega \text{ cm}^2$  and at low SOC during discharge up to  $\approx 215 \Omega \text{ cm}^2$ , with an extremely high value at the end of discharge in the k $\Omega$ -range.

We performed a similar analysis for the NCA/Li cells, shown in Figs. 9a and 9b. The heat flow measured by IMC ( $\dot{Q}_{cal}$ , black) displays some interesting differences to that of the LMR-NCM/Li cells. Most strikingly, the overall measured heat flow (black curve) is significantly lower. The curve of the IMC signal during charge has its maximum of  $\approx 1.2 \text{ mW g}_{CAM}^{-1}$  at the beginning of charge, after which the heat flow levels off until  $\approx 75 \text{ mAh g}_{CAM}^{-1}$  and gradually increases again until the end of the half-cycle. Overall, the heat flow curve during charge of the NCA/Li cell is rather flat compared to that of the LMR-NCM/Li cell. The IMC signal of the NCA/Li cell during discharge, shown in Fig. 9b, has a similarly flat shape as during charge, and its absolute values are of the same order of magnitude until the cell is discharged below  $\approx 50 \text{ mAh g}_{CAM}^{-1}$ , at which point the heat signal displays a steep increase up to  $\approx 7 \text{ mW g}_{CAM}^{-1}$ . The deviation between the irreversible heat flow ( $\dot{Q}_{irrev}$ , green curve) and the measured signal (black curve), which is especially prominent at the end of the charge process, was discussed above and arises from a combination of reversible heat and measurement inaccuracy. The diffusion limitations causing the difference between  $\dot{Q}_{irrev}$  (green) and  $\dot{Q}_{LFR}$  (orange) cover  $\approx 50\%$

**Table I.** Lost electrical energy for LMR-NCM and NCA half-cells calculated from the voltage vs SOC charge/discharge curve as a function of C-rate, using an intermittent cycling protocol. The total energy loss is shown in absolute numbers and relative to the charge energy of the respective cycle. The different energy terms as defined by Eqs. 7 and 8 are shown as absolute numbers and relative shares of  $Q_{total}$ .

Electrical energy loss	C/10		C/5		C/2		1C	
	LMR-NCM	NCA	LMR-NCM	NCA	LMR-NCM	NCA	LMR-NCM	NCA
$Q_{total}$ [mWh/g <sub>CAM</sub> ]	84.1	9.3	88.1	14	99.7	23.8	114.6	34.8
% of charge energy	8%	1.2%	9%	1.9%	12%	3.4%	15%	5.2%
$Q_{irrev,cha}$ [mWh/g <sub>CAM</sub> ]	15.0	3.1	19.8	4.9	28.7	10.6	37.7	15.6
% of $Q_{total}$	18%	33%	23%	35%	29%	45%	33%	45%
$Q_{irrev,dis}$ [mWh/g <sub>CAM</sub> ]	23.0	4.8	31.2	7.2	42.6	12.5	57.6	18.4
% of $Q_{total}$	27%	52%	35%	51%	43%	53%	50%	53%
$Q_{hys}$ [mWh/g <sub>CAM</sub> ]	46.1	1.4	37.1	1.9	28.4	0.7	19.4	0.8
% of $Q_{total}$	55%	15%	42%	14%	28%	3%	17%	2%

of the irreversible heat flow. They translate into diffusion resistances similar to those found for the LMR-NCM/Li cells of around  $50 \Omega \text{ cm}^2$  in the mid-SOC region with increasing values at the end of charge ( $120 \Omega \text{ cm}^2$ ) and discharge ( $>200 \Omega \text{ cm}^2$ ). The cathode related resistance ( $R_{CAM}$ ) dominates the impedance response in the lower SOC region, with values of up to  $250 \Omega \text{ cm}^2$ . In contrast to the impedance spectra of the LMR-NCM/Li cells (see Fig. 1), the two semi-circles of the NCA spectra, from which  $R^*$  and  $R_{CAM}$  were determined, are merged together in the middle SOC range ( $40 \text{ mAh g}_{CAM}^{-1} < \text{SOC} < 200 \text{ mAh g}_{CAM}^{-1}$ ). This means that the two resistances could not be deconvoluted using the transmission line model. This is why, in this SOC region, only the LFR was

determined from the impedance spectra of NCA. Another difference to the impedance response of LMR-NCM is that, at the end of charge,  $R_{CAM}$  of NCA does not increase significantly, due to the simple fact that the cut-off potential for the NCA cells is lower and a larger amount of cyclable lithium is still available in the material at the end of the charge process.

As outlined in Eq. 2, another heat generation term exists for materials with an OCV hysteresis, such as LMR-NCM, which is  $Q_{hys}$ , i.e., the heat due to OCV hysteresis. This will be discussed in more detail in the following.

**Deconvolution of energy losses.**—Valuable information on the allocation of heat due to OCV hysteresis ( $Q_{hys}$ ) to a charge and discharge half-cycle can be gained by comparing the heat measured by IMC with the electrical energy loss terms. In Fig. 10, this analysis is conducted for the lowest C-rate of C/10 with the integrated calorimetric heat signal shown in the left-hand column (charge and discharge heat stacked) and the electrical energy losses in the right-hand column for both the LMR-NCM/Li and the NCA/Li cell. The analysis is based on the combination of electrochemical and calorimetric data visualized in Fig. 2. Thereby, the IMC signal is integrated over the charge or discharge half-cycle including the first 1.5 h of the consecutive relaxation phase at zero current as described above. In contrast to the heat flow data ( $\dot{Q}_{cal}$  in  $\text{mW/g}_{CAM}$ ) shown in Figs. 6 to 9, the integration over time leads to the amount of evolved heat  $Q_{cal}$  (in  $\text{mWh/g}_{CAM}$ ). For example, from IMC, the evolved heat during charge ( $Q_{cal,cha}$ ) is accessible, which is a sum of the following terms:

$$Q_{cal,cha} = Q_{irrev,cha} + Q_{hys,cha} + |Q_{rev,cha}| \quad [9]$$

Solving for  $Q_{hys,cha}$ , this yields:

$$Q_{hys,cha} = Q_{cal,cha} - Q_{irrev,cha} - |Q_{rev,cha}| \quad [10]$$

$Q_{irrev,cha}$  is calculated from the electrochemical measurements by integrating over the voltage curve as shown in Fig. 4 and Table I. To obtain values for  $Q_{hys,cha}$ , one has to assume that the contribution of  $Q_{rev,cha}$  is negligible since the moment  $Q_{rev,cha}$  becomes comparable

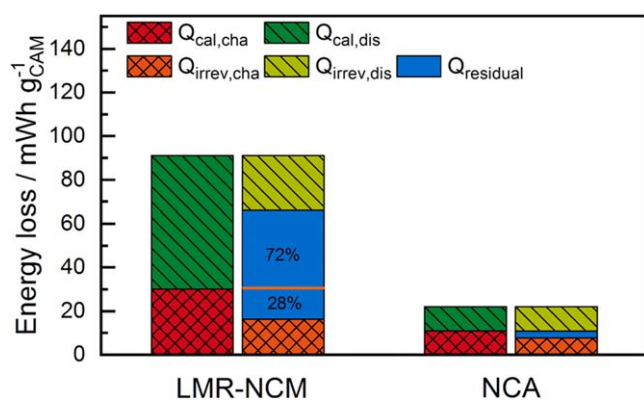


**Figure 10.** Allocation of different sources of heat according to the results from intermittent cycling to the heat measured by IMC for the lowest C-rate of C/10 for the LMR-NCM/Li cell (number 2) and for the NCA/Li cell (number 1). For each cell, the left-hand column contains the stacked IMC heat data from the charge (red) and discharge (green) half-cycle. The expected electrical energy loss determined from intermittent cycling is shown for each cell by the right-hand column. Thereby, the relative shares for the polarization induced overpotential in charge (orange) and discharge (light green) are shown (see Table I) together with the residual energy loss ( $Q_{residual}$ , blue). In case of LMR-NCM/Li, this corresponds to the OCV hysteresis. The orange line and relative numbers indicate its share in charge and discharge.

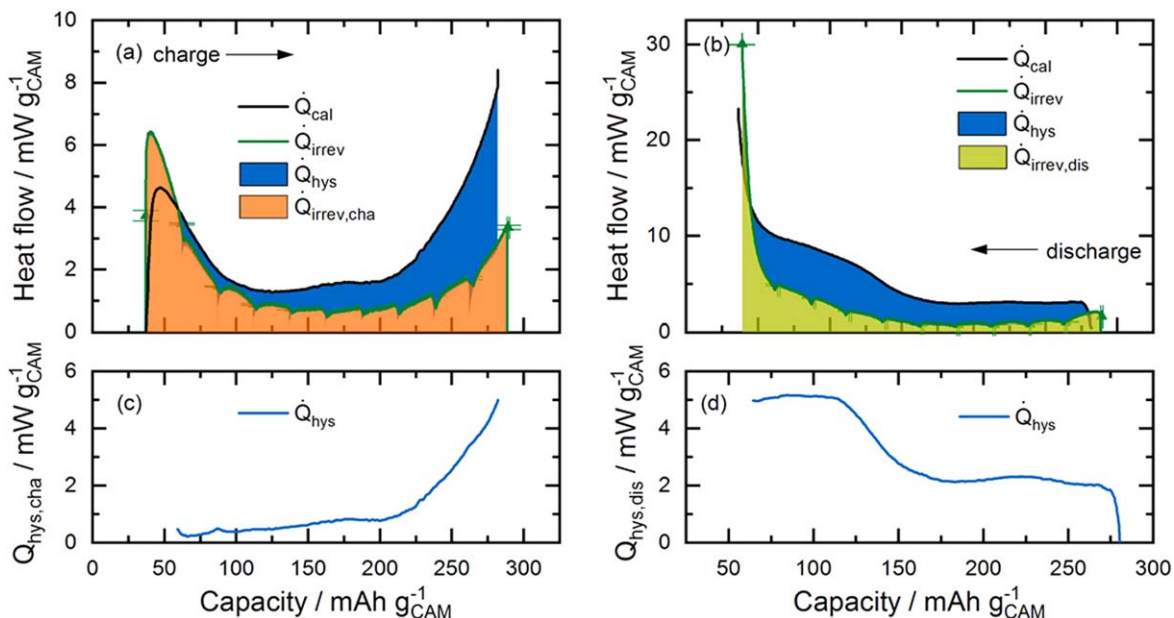


**Figure 11.** Heat flow during (a) charge and (b) discharge of the LMR-NCM/Li cell (cell number 2) at C/10 as a function of SOC. The heat flow measured by IMC (black) is compared to the irreversible heat generation calculated from the difference between the voltage at load and the OCV curve obtained by the intermittent cycling protocol (green line, error bars from two measurements). The shaded areas correspond to the irreversible heat in charge (orange) and discharge (green) and the heat due to OCV hysteresis (blue). The heat flow of  $\dot{Q}_{hys}$  in (c) charge and (d) discharge is calculated by  $\dot{Q}_{cal} - \dot{Q}_{irrev}$  (only exothermic signal is shown).

to any of the other heat terms, independent values for  $Q_{hys,cha}$  cannot be obtained by this approach anymore. For the analysis shown in Fig. 10, we therefore deliberately use the term  $Q_{residual}$  instead of  $Q_{hys}$  to make the difference between both values more clear. The effect on the accuracy of the results will be discussed below. For the discharge, an equivalent derivation can be made.

The results from the IMC measurements ( $Q_{cal,cha}$  and  $Q_{cal,dis}$ ) are shown by the left-hand column for both the LMR-NCM/Li and the NCA/Li cell. The right-hand column for each cell marks the expected total electrical energy loss. To allocate the different sources of heat, determined by intermittent cycling, to the heat measured by IMC, the relative shares, as shown in Table I, were applied to the calorimeter signal. Note that by this definition, the height of the right-hand column agrees with that of the left-hand column since it simply illustrates the relative distribution of heat sources. For example, it is known from the intermittent cycling at C/10 that 18% of the total energy loss is attributable to  $Q_{irrev,cha}$  and 27% to  $Q_{irrev,dis}$ . Hence, the remaining heat, which is measured by IMC ( $Q_{residual}$  in Fig. 10), can be allocated to the OCV hysteresis and can furthermore be separated into its shares during the charge and discharge half-cycles, respectively. This is illustrated by the orange line in Fig. 10 and the percentage values in the blue section.

The left part of Fig. 10 shows the allocation of the different sources of heat to the IMC signal for the LMR-NCM/Li cell, indicating that the heat measured by IMC during charge (red column) is only about half of that measured during discharge (green column). As can be seen in the right-hand column for the LMR-NCM/Li cell in Fig. 10, the polarization induced overpotential losses during discharge ( $Q_{irrev,dis}$ , light green) are larger than during charge ( $Q_{irrev,cha}$ , orange), which means that more irreversible heat is evolved during discharge. The heat caused by these overpotential losses is directly attributable to the respective charge and discharge IMC heat signal. The additional heat, which is observed by IMC for each half-cycle ( $Q_{residual}$ ), is assigned to the OCV hysteresis. It can be seen that the ratio between discharge and charge is around 70:30, meaning that most of the heat due to OCV hysteresis is evolved in the discharge process. Together with the higher irreversible heat

evolved during discharge, this leads to a considerable asymmetric heat evolution between the two half-cycles.

As mentioned above, this analysis is somewhat compromised by the reversible heat due to entropic changes, which is assumed to be negligible for the construction of  $Q_{residual}$  in Fig. 10. It needs to be noted, however, that any contribution of the reversible heat is recorded by the calorimeter but cannot be observed in the voltage vs SOC curve. Hence, this heat term contributes to the overall heat observed by IMC (left-hand columns in 10) but is not considered for the construction of the right-hand ones. As explained in the Theory section, reversible heat has opposite signs on charge and discharge and is therefore, by definition, equal to zero for a whole cycle. This means that both the total heat measured by IMC and the electrical energy loss have no net contribution from  $Q_{rev}$ . However,  $Q_{rev}$  influences the respective half-cycles by adding another exothermic heat source to one direction (discharge in the case of the LMR-NCM)<sup>14</sup> and an endothermic source to the other one (charge for the LMR-NCM).<sup>14</sup> The reversible heat can be determined from entropy measurement. However, in the case of LMR-NCM, these experiments revealed that the entropy is path-dependent between charge and discharge, which suggests that the integration of  $Q_{rev}$  would include non-reversible pathways, and hence would not give a meaningful value for  $Q_{rev}$ .<sup>14</sup> Rather, we assume that the entropy curve indicates that entropy production is being observed.<sup>14</sup> For a detailed discussion on the entropy and reversible heat in LMR-NCM and the implications of non-reversible pathways, the interested reader is referred to our previous work (in particular the discussion of Eq. 17 in Friedrich et al.<sup>14</sup>). However, the effect of the reversible heat can be analyzed when the heat flow is considered instead of the total integrated heat. As is shown in Fig. 6, the reversible heat can be assumed to be negligible in the case of the LMR-NCM/Li cell investigated here, so that the analysis shown in Fig. 10 should be reasonably accurate.

Figure 10 also shows the IMC results of the NCA/Li cell, comparing them with the energy loss data expected from the intermittent cycling (Table I and Fig. 5) in the same way as for the LMR-NCM/Li cell. The generated heat of the NCA/Li cell is clearly less than for the LMR-NCM/Li cell. For the results from

calorimetry, a symmetrical heat release between charge and discharge is observed. The electrochemical data, however, suggest that the irreversible heat in charge direction should be slightly smaller than the heat determined by calorimetry, while for the discharge direction it should be slightly larger. The mismatch between the heat measured by IMC and the calculated heat in charge and discharge is most likely attributable to the simplifications made with the calculation of the different heat terms. As mentioned above, the irreversible capacity loss results in a relatively large error when calculating the total electrical energy loss in the case of NCA, because of the rather small absolute heat flow signal. When the relative shares of the energy terms calculated from the intermittent cycling are then applied to deconvolute the different contributions to the IMC signal, this additional heat term is evenly distributed between  $Q_{irrev,cha}$ ,  $Q_{irrev,dis}$  and  $Q_{residual}$ . However, it seems that by doing so,  $Q_{irrev,dis}$  is overestimated while  $Q_{irrev,cha}$  is underestimated. For materials with small absolute heat signals, such as NCA, neglect of this energy loss term is not justified when aiming at a quantitative analysis. We therefore recommend determining this heat term separately so as to be able to allocate it to the charge or discharge direction or analyze the heat flow signal as a function of SOC.

**Heat evolution due to OCV hysteresis of LMR-NCM.**—Figure 8 shows the various sources of irreversible heat, while Fig. 6 elucidates the rather minor contribution of reversible heat for LMR-NCM. The lost electrical energy, which can be calculated by integrating the OCV curve, as shown in Fig. 4a and Table I, is an additional source of heat for cells with LMR-NCM compared to normal cathodes like NCA. In Fig. 10, we discussed what share of this heat is evolved in each charge and discharge half-cycle at C/10 of LMR-NCM/Li cells. Besides absolute numbers, another interesting question, which we posed at the beginning of the paper, is how  $\dot{Q}_{hys}$  is evolved as a function of the SOC. To answer it, we will compare the heat evolution measured by IMC with the total irreversible heat flow determined from the intermittent cycling protocol, as shown in Figs. 11a and 11b. The data are the same as in Fig. 8, but focus only on the two sources of heat that are essential for determining  $\dot{Q}_{hys}$ , i.e., ignoring the minor contribution from reversible heat. The difference between the measured heat flow ( $\dot{Q}_{cal}$ , black curve) and the expected irreversible heat flow ( $\dot{Q}_{irrev}$ , green curve) is a measure of the evolution of  $\dot{Q}_{hys}$  (blue shaded area). The difference curve,  $\dot{Q}_{cal} - \dot{Q}_{irrev}$ , is shown in Figs. 11c and 11d for the charge and discharge half-cycle, respectively.

As can be seen from the difference plot in Fig. 11c for the charge half-cycle, the heat flow due to the OCV hysteresis is small up to an SOC of  $\approx 200$  mAh  $g_{CAM}^{-1}$ , after which it increases steadily. At the beginning of charge, however, the irreversible heat flow is greater than the measured signal. This apparent overshoot in the green curve is most likely due to the way how  $\dot{Q}_{irrev}$  is constructed by linear interpolation between the OCV points as mentioned above. This is supported by the observation that the two first data points (green triangles; direct result of taking the difference between  $E_{load}$  and at this SOC) agree rather well with the IMC heat flow curve (black line). Other sources of errors include the time delay of the measurement setup and the inaccuracy in the determination of  $\dot{Q}_{irrev,cha}$ . Since this deviation is considered to be an artifact from the calculation, no endothermic  $\dot{Q}_{hys}$  signal is shown in Fig. 11c. A more detailed analysis of this lower SOC range, for instance with a smaller  $\Delta$ SOC spacing in the intermittent cycling, could shed further light on the thermal effects at the beginning of charge. During discharge,  $\dot{Q}_{hys}$  is evolved over the whole SOC window with a constant value of  $\approx 2$  mW  $g_{CAM}^{-1}$  during the initial discharge and an increasing heat flow when the cell is discharged below  $\approx 170$  mAh  $g_{CAM}^{-1}$ ; this forms a plateau at  $\approx 5$  mW  $g_{CAM}^{-1}$  towards the end of discharge, where the irreversible heat strongly dominates the total heat flow. A comparison with the total heat flow of NCA serves to

classify the magnitude of the evolution of  $\dot{Q}_{hys}$ . While for the NCA/Li cells the total measured IMC signal is between 0.5 mW  $g_{CAM}^{-1}$  and 2 mW  $g_{CAM}^{-1}$  for most of the SOC range, the heat evolution only due to the OCV hysteresis for the LMR-NCM/Li cells is between 0.5–5 mW  $g_{CAM}^{-1}$  in charge and between 2–5 mW  $g_{CAM}^{-1}$  in discharge. Hence, for LMR-NCM/Li cells, the material-specific  $\dot{Q}_{hys}$ , is of the same order of magnitude (or even greater) as the total heat flow of the reference material NCA.

The profile of the total heat evolution of LMR-NCM in charge is dominated by the shape of the irreversible heat flow (up to  $\approx 100$  mAh  $g_{CAM}^{-1}$ ), while in the discharge direction,  $\dot{Q}_{hys}$  makes a significant contribution to the heat flow profile, especially in the SOC range between  $\approx 250$  mAh  $g_{CAM}^{-1}$  and  $\approx 65$  mAh  $g_{CAM}^{-1}$ . The SOC ranges at which  $\dot{Q}_{hys}$  is mainly evolved in charge and discharge (see Figs. 11c and 11d) suggest that the underlying phenomena for OCV hysteresis in LMR-NCM occur particularly at high SOC during charge ( $>200$  mAh  $g_{CAM}^{-1}$ ) and at low SOC during discharge ( $<170$  mAh  $g_{CAM}^{-1}$ ). From window-opening experiments, it is known that the hysteresis of the OCV curve,<sup>26,27</sup> the lattice parameters,<sup>13</sup> and the entropy profile<sup>14</sup> grow gradually, becoming more and more pronounced as the charge or discharge window are continuously opened. The evolution of  $\dot{Q}_{hys}$  reflects the behavior of these other properties and hence indicates that the underlying processes leading to the reported hysteresis phenomena cause waste heat, which is observed at high SOC in charge and at low SOC during discharge. However, as discussed above, the accuracy of this analysis method is limited due to the time-delay of the calorimeter, and we can therefore only report a trend in  $\dot{Q}_{hys}$  evolution as a function of SOC. In an extreme case, a pronounced time lag would lead to a relative shift on the SOC axis, meaning that the SOC for the  $\dot{Q}_{hys}$  evolution in charge is generally overestimated, while in discharge it is underestimated. For the data shown in Fig. 11, this potential error is rather small, as outlined above (i.e., the time lag  $\approx 18$  min until 99% of the heat signal is detected corresponds to a  $\Delta$ SOC of  $\approx 3\%$ ). However, as mentioned above, there is still some heat flow present after removing the current, and there is also an excess of irreversible heat at the beginning of charge. This means that not all heat is detected at the moment of its production. The heat evolution towards the end of each half-cycle might therefore include some share of the heat produced at lower SOC, leading to an overestimation of the heat flow at high SOC. As mentioned above for Figs. 6 and 8, the heat signal after disconnecting the current was also neglected in the analysis shown in Fig. 11. Moreover, the heat flow observed by IMC might contain contributions from parasitic heat sources, such as electrolyte decomposition, leading to an overestimation of  $\dot{Q}_{hys}$ . Probably the most significant source of error is the unknown but evidentially minor contribution of  $\dot{Q}_{rev}$  to the herein determined  $\dot{Q}_{hys}$ , which might lead to an overestimation of  $\dot{Q}_{hys}$  in case of an exothermic  $\dot{Q}_{rev}$  (and an underestimated for an endothermic  $\dot{Q}_{rev}$ ). In conclusion, we wish to emphasize that what is reported here is a semi-quantitative trend in the evolution of  $\dot{Q}_{hys}$  in charge and discharge and that further measurements are required for a more accurate quantitative analysis.

## Conclusions

We conducted a comparative study comprising an investigation of the heat release of LMR-NCM/Li and NCA/Li coin cells at different C-rates using isothermal micro-calorimetry. Impedance spectroscopy and an intermittent cycling protocol were applied as complementary methods to analyze the various heat sources. The focus of this study is on the LMR-NCM cathode active material (CAM), which has a unique OCV hysteresis. The electrochemical and calorimetric data sets were analyzed employing two different approaches: (i) integrating the heat flow for an individual half-cycle

to get the total generated heat for the respective charge or discharge direction (in  $\text{mWh g}_{\text{CAM}}^{-1}$ ), and (ii) converting the heat flow over time to a heat flow as a function of SOC (in  $\text{mW g}_{\text{CAM}}^{-1}$ ). Using the first approach, we observed that the total heat generation for LMR-NCM is much higher than for NCA (decreasing from a factor of 9 to 3 for increasing the C-rate from C/10 to 1C), leading to a lower energy round-trip efficiency. For both CAMs, the overall released heat shows a linear correlation with the applied C-rate. However, while the heat release extrapolated to a zero C-rate is rather small for the NCA/Li cells, it is significantly higher for the LMR-NCM/Li cells due to the quasi-static OCV hysteresis being a material-specific property present even under zero current conditions.

The OCV hysteresis was further analyzed by intermittent cycling, in which a 1 h rest phase was applied after each 10% SOC step to collect OCV points during charging and discharging at different C-rates. These electrochemical measurements indicate that the OCV hysteresis of the LMR-NCM material is responsible for up to 55% of the total electrical energy loss of LMR-NCM/Li cells at C/10. The irreversible heat generated during charge and discharge was also calculated by this method. The share of the heat generation due to OCV hysteresis was attributed to either the charge or discharge direction on the basis of the calculated heat terms and the heat measured by IMC for the individual half-cycles assuming that the reversible heat due to entropy is negligible. We found that most of the heat due to OCV hysteresis in the LMR-NCM/Li cells is dissipated during discharge (72% for C/10).

Using approach (ii) above, we compared the measured heat flow signal with the profile calculated from electrochemical data. For the NCA/Li cells, the sum of the irreversible heat determined by intermittent cycling and the reversible heat calculated from entropy measurements corresponded well with the heat flow measured by IMC. The heat flow is clearly dominated by irreversible heat while the reversible heat serves more as a small correction for the calculated curve. However, the very small absolute level of the heat flow signal for the NCA material means that the limit of the applied approach's accuracy is reached, especially with regard to the combination of the measurement results from different cells and methods with an irreversible capacity leading to a source of error, which is in the order of the measured data. In contrast, due to the higher absolute signal for LMR-NCM/Li cells ( $\approx 4$  times), the analysis is more accurate in this case. Using impedance spectroscopy, the irreversible heat determined from intermittent cycling was further differentiated into the underlying resistive phenomena, which lead to the observed potential drop. We found that for both cathode active materials, the charge transfer resistance of the cathode dominates the irreversible heat flow curve. For LMR-NCM, the  $R_{\text{CT}(\text{CAM})}$  shows a characteristic U-shape as a function of SOC and

further contributions from diffusional limitations are rather small. For the NCA/Li cells, the diffusion resistances are very similar, while the charge transfer resistance is generally much smaller and covers only  $\approx 50\%$  of the overpotential losses. The contribution of the Li anode is included in the fitting parameters but makes only a minor contribution to the low frequency resistance at very low and high SOC.

With LMR-NCM/Li cells, the analysis of the heat flow profiles provides detailed information about the OCV hysteresis. The heat evolution due to OCV hysteresis is determined as a function of SOC by subtracting the calculated irreversible heat flow from the measured heat signal. During charge,  $\dot{Q}_{\text{hys}}$  is mainly evolved at a high SOC ( $>200 \text{ mAh g}_{\text{CAM}}^{-1}$ ), while during discharge, it is released over the whole SOC range at a constant evolution rate until  $170 \text{ mAh g}_{\text{CAM}}^{-1}$  and an increasing rate below that. The heat evolved due to OCV hysteresis in LMR-NCM is of the same order of magnitude as the total heat release of the reference material NCA, which underlines the importance of the analysis of this heat source.

To revisit the questions raised at the beginning of this paper, we found that (i) the energy loss due to OCV hysteresis is fully dissipated as heat and (ii) the majority is evolved during discharge. The fact that (iii) the heat due to OCV hysteresis is mainly generated at high SOC during charge and at low SOC during discharge indicates that (iv) the underlying processes leading to the hysteresis phenomena in LMR-NCM occur in these SOC ranges, which agrees with observations from literature reports on parameters, such as the LMR-NCM lattice parameters.

### Acknowledgments

We want to acknowledge BASF SE for the support within its Scientific Network on Electrochemistry and Batteries and the German Federal Ministry of Education and Research (BMBF) for its financial support within the ExZellTUM II project (grant no. 03XP0081). We gratefully thank See Tow Wei Hao for his contribution to the entropy measurements of NCA and Viola Knödler for her support with the NCA/Li cell building.

### Appendix

As shown in Eq. 2, reversible heat is calculated as a product of the current, temperature and temperature-dependent OCV value,  $\frac{\partial E_{\text{eq}}}{\partial T}$ . The latter was determined for both LMR-NCM/Li and NCA/Li cells as described in the Experimental section. A detailed discussion of the method and the results for LMR-NCM/Li cells is reported elsewhere.<sup>14</sup> The obtained  $\frac{\partial E_{\text{eq}}}{\partial T}$  values are shown in Figure A.1.

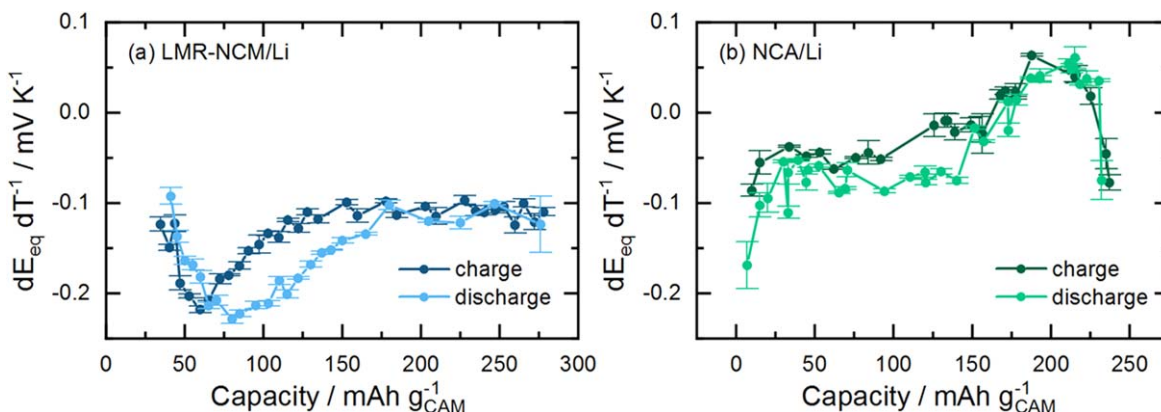


**Figure A.1.** Temperature-dependent OCV value,  $\frac{\partial E_{\text{eq}}}{\partial T}$ , for (a) LMR-NCM/Li and (b) NCA/Li cells during charge and discharge as a function of specific capacity. The variation of the OCV with temperature was measured as described above and discussed by Friedrich et al.<sup>14</sup>

## ORCID

Franziska Friedrich  <https://orcid.org/0000-0001-9400-1212>  
 Tanja Zünd  <https://orcid.org/0000-0002-1650-3636>  
 Hubert A. Gasteiger  <https://orcid.org/0000-0001-8199-8703>

## References

1. R. Schmuck, R. Wagner, G. Hörpel, T. Placke, and M. Winter, *Nat. Energy*, **3**, 267 (2018).
2. K. Onda, T. Ohshima, M. Nakayama, K. Fukuda, and T. Araki, *J. Power Sources*, **158**, 535 (2006).
3. H. Bang, H. Yang, Y. K. Sun, and J. Prakash, *J. Electrochem. Soc.*, **152**, A421 (2005).
4. H. Yang and J. Prakash, *J. Electrochem. Soc.*, **151**, A1222 (2004).
5. K. E. Thomas and J. Newman, *J. Electrochem. Soc.*, **150**, A176 (2003).
6. L. Kraft, T. Zünd, D. Schreiner, R. Wilhelm, F. Günter, G. Reinhart, H. A. Gasteiger, and A. Jossen, *J. Electrochem. Soc.*, **168**, 020537 (2021).
7. L. Kraft, A. Hoeffling, T. Zünd, A. Kunz, M. Steinhardt, J. Tübke, and A. Jossen, *J. Electrochem. Soc.*, **168**, 053505 (2021).
8. G. Zubi, R. Dufo-López, M. Carvalho, and G. Pasaoglu, *Renew. Sustain. Energy Rev.*, **89**, 292 (2018).
9. T. Teuff, B. Strehle, P. Müller, H. A. Gasteiger, and M. A. Mendez, *J. Electrochem. Soc.*, **165**, A2718 (2018).
10. K. G. Gallagher, J. R. Croy, M. Balasubramanian, M. Bettge, D. P. Abraham, A. K. Burrell, and M. M. Thackeray, *Electrochem. Commun.*, **33**, 96 (2013).
11. J. R. Croy, D. Kim, M. Balasubramanian, K. Gallagher, S.-H. Kang, and M. M. Thackeray, *J. Electrochem. Soc.*, **159**, A781 (2012).
12. T. Teuff, D. Pritzl, S. Solchenbach, H. A. Gasteiger, and M. A. Mendez, *J. Electrochem. Soc.*, **166**, A1275 (2019).
13. B. Strehle, T. Zünd, S. Siculo, A. Kiebling, V. Baran, and H. A. Gasteiger, *J. Electrochem. Soc.*, **169**, 020554 (2022).
14. F. Friedrich, S. Pieper, and H. A. Gasteiger, *J. Electrochem. Soc.*, **168**, 120502 (2021).
15. G. Assat, D. Foix, C. Delacourt, A. Iadecola, R. Dedryvère, and J.-M. Tarascon, *Nat. Commun.*, **8**, 2219 (2017).
16. W. E. Gent et al., *Nat. Commun.*, **8**, 2091 (2017).
17. W. Shi, J. Zheng, J. Xiao, X. Chen, B. J. Polzin, and J.-G. Zhang, *J. Electrochem. Soc.*, **163**, A571 (2016).
18. L. J. Krause, L. D. Jensen, and J. R. Dahn, *J. Electrochem. Soc.*, **159**, A937 (2012).
19. L. M. Housel et al., *ACS Appl. Mater. Interfaces*, **11**, 37567 (2019).
20. G. Assat, S. L. Glazier, C. Delacourt, and J.-M. Tarascon, *Nat. Energy*, **4**, 647 (2019).
21. V. L. Chevrier, Z. Yan, S. L. Glazier, M. N. Obrovac, and L. J. Krause, *J. Electrochem. Soc.*, **168**, 030504 (2021).
22. L. E. Downie, S. R. Hyatt, A. T. B. Wright, and J. R. Dahn, *J. Phys. Chem. C*, **118**, 29533 (2014).
23. J. Landesfeind, D. Pritzl, and H. A. Gasteiger, *J. Electrochem. Soc.*, **164**, A1773 (2017).
24. R. Morasch, J. Keilhofer, H. A. Gasteiger, and B. Suthar, *J. Electrochem. Soc.*, **168**, 080519 (2021).
25. R. Weber, A. J. Louli, K. P. Plucknett, and J. R. Dahn, *J. Electrochem. Soc.*, **166**, A1779 (2019).
26. J. R. Croy, K. G. Gallagher, M. Balasubramanian, Z. Chen, Y. Ren, D. Kim, S.-H. Kang, D. W. Dees, and M. M. Thackeray, *J. Phys. Chem. C*, **117**, 6525 (2013).
27. J. R. Croy, K. G. Gallagher, M. Balasubramanian, B. R. Long, and M. M. Thackeray, *J. Electrochem. Soc.*, **161**, A318 (2014).

## 5 Conclusions and Outlook

The overarching goal of this PhD thesis was to produce performance-optimized multilayer pouch cells with cathodes based on the promising next-generation lithium- and manganese-rich NCM cathode active material. This was done by first preparing and studying laboratory-scale coin half-cells to find the cathode electrode specifications (CAM loading, electrode porosity, electrode composition, etc.) that would yield the best compromise between rate capability and the projected energy density of multilayer pouch cells that were subsequently produced on a semi-automatic pilot line. While in pure material-based research the focus is predominantly put on achieving high specific capacity (normalized to the cathode active material) at reasonable C-rates, this work tries to also include other aspects that are critical for large-scale cells, namely the energy efficiency, the volumetric and gravimetric energy densities (related to weight and volume of the inactive cell components), and the thermal behaviour of large-format cells. The challenges during the scale-up process were investigated and analysed with regard to the specific material properties. By comparing the cell performance of multilayer LMR-NCM pouch cells with that of regular NCA cells, the difference in cell temperature at high C-rates was correlated with the poor energy efficiency and the voltage hysteresis of the LMR-NCM material. These findings led to in-depth studies of the structural origin of the voltage hysteresis by diffraction methods (X-ray and neutron powder diffraction) and a heat flow analysis by calorimetry.

In Section 4.1, it was shown how half-cell based material performance data can be used to predict the performance of large-format cells. As part of the steps undertaken to validate these performance predictions, the challenges faced in the semi-automatic production of LMR-NCM cathode electrodes were shown. To distinguish between setup and scale-up related effects of the cell performance, as discussed in Section 3.1, it was explained how and when it was important to carefully choose the counter electrode, the electrolyte as well as the separator and cell format. Overall, it can be stated that it is a reasonable approach to utilize the data from easily prepared coin half-cells to project the achievable initial energy

density of large-format cells. By considering some of the obvious differences between half-cells and full-cells, a simple Excel based cell configuration tool was developed that predicts the cell performance of multilayer pouch cells based on the half-cell performance of previously measured coin half-cells. At the same time, some weaknesses of such projections (particularly at higher C-rates this is different for coin versus large-format cells) calculations were also revealed, such as for example the influence of cell temperature on rate capability and cell aging. Regarding the production steps for the multilayer pouch cells, two steps were found to be crucial when using the LMR-NCM material. One is the calendaring of the electrode, which determines the final density as well as the ionic and electrical conductivity of the electrode. While the densification of the LMR-NCM cathode to a porosity of  $\approx 30\%$  could be easily achieved for coin cell electrodes, namely by compress small area electrodes in a press, the roll-to-roll processing with a calender could not achieve the same electrode densification. As no such problem was encountered for the NCA electrodes, this different behaviour of the LMR-NCM material was investigated in more detail. In this context, a direct correlation was found between the pore size distribution determined by Hg-porosimetry and the maximum densification that could be achieved by calendaring. This finding enables a materials-based prediction for electrode densification of new materials. The other crucial step is related to the formation of large-format cells with LMR-NCM cathodes. Here, the extensive gassing of the LMR-NCM cathode active material was discussed for the first time from the perspective of conducting the formation of large-format cells. Based on OEMS-measurements, it was found that it was best to do the formation of LMR-NCM cells at elevated temperature and to add a second degassing to the formation process in order to minimize the build-up of internal cell pressure during the subsequent cycle life tests.

In the second part (Section 0), the cell performance results of the LMR-NCM and NCA multilayer pouch cells are discussed and compared to coin full-cells. Driven by different cell temperatures, the energy efficiency of the two materials was compared regarding their overpotential as well as the so-called OCV-hysteresis related losses. The latter phenomena is negligible for regular NCMs and NCAs, but lowers the energy efficiency by 10-12% for the case of LMR-NCM cells. However, comparing the overall cell performance, LMR-NCM cells delivered an around 30%

higher specific capacity with regard to the active material. Despite the lower discharge potential of the LMR-NCM material, LMR-NCM cells still delivered an around 11 % higher energy density on the cell level. In the end, this energy density benefit of LMR-NCM vs. NCA cells is maintained for around 210 cycles, until the stronger capacity fading of the LMR-NCM cells results in an inferior energy density compared to the NCA cells.

While in the previous sections strategies were suggested on how LMR-NCM based electrodes can be up-scaled to build multilayer pouch cells, the voltage hysteresis and the resulting energy inefficiency cause serious problems. This phenomenon has its origin in the LMR-NCM bulk structure and was thus studied by diffraction methods, as reported in Section 4.3. By using *in situ* laboratory XPD, the lattice parameters were monitored within the initial cycles as a function of SOC and OCV for three different over-lithiated LMR-NCM materials. When plotted versus the state of charge, the lattice parameters experienced an analogous hysteresis between the charge and discharge direction like the measured OCV. This suggests there to be a structural OCV path dependence of the underlying redox processes. Furthermore, the extent of the OCV and cell volume hysteresis depends on the SOC window. The hysteresis enclosed area in the OCV motile enlarges above 4.2 V and increases rapidly towards the end of the charging process. In the discharge process, the behaviour is inverse below 3.7 V. Surprisingly, the hysteresis of the unit cell vanishes when it is correlated to the OCV and results in a universal linear relation, regardless of the original lithium content of the material. By using *ex situ* XPD of cycled LMR-NCM material it was further possible to show that the hysteresis of the TM-TM distance correlates directly with the OCV-hysteresis of the material. As this finding does not allow to distinguish between the two commonly discussed mechanistic origins for the OCV- hysteresis, joint Rietveld refinements of *ex situ* XPD and NPD data were carried out to clarify the role of transition metal migration. As part of the critical discussion of the structural models used in the literature, it was decided to compare three different refinement models and discuss their implications. From the obtained data, no correlation could be revealed between the OCV-hysteresis and the Ni migration. However, a maximum difference of  $\approx 2.4$  % migrated Ni was found between the charge and discharge direction, what is close to the uncertainty range (1-2%). Therefore, it can only be stated that there is either no

correlation between Ni migration and the OCV-hysteresis or that already a very small amount of Ni migration (<2%) would result in the pronounced OCV-hysteresis.

In Section 4.4, an attempt was made to assign the different energy losses between the charge and discharge direction either to overpotential driven losses or to OCV-hysteresis losses. *In situ* micro-calorimetry, impedance spectroscopy, and intermittent cycling were combined to verify that almost all energy inefficiency is released as heat. The analysis was carried out for different C-rates. For a low C-rates, the major fraction of the LMR-NCM energy was found to be lost as OCV-hysteresis heat during the discharge process (around 9 times the energy loss of NCA). On the other hand, at the higher rate of 1C, the overpotential driven heat release dominates for both materials, but generates still three times less heat for NCA based cells.

In summary, starting with this research with the quite new and highly promising LMR-NCM material in 2017, different limitations of the material were encountered. The challenges faced when trying to calender LMR-NCM electrodes to commonly employed porosities of  $\approx 30\%$  could be ascribed to the substantial inner porosity of the secondary LMR-NCM particles. It can only be addressed by synthesizing LMR-NCMs with a different morphology. Similarly, the extensive gassing of LMR-NCMs during the first cycle can be addressed by a modified cell formation process, a modification of the active material and/or the electrolyte should be pursued to reduce gassing.

Over the course of the last few years, the LMR-NCM material development also advanced and the currently available materials have fewer intrinsic problems. A development in the direction of single crystals like for Ni-rich materials<sup>120,121</sup> would probably be accompanied with less gassing thanks to the reduced specific surface. Moreover, electrode densities of  $> 3 \text{ g/cm}^3$  would then be possible in the absence of inner particle porosities. The reactivity of singlet oxygen<sup>114</sup> and surface impurities<sup>74</sup> at elevated voltages remains a difficult challenge. However, as shown in Section 2.5, there are already different approaches to handle the reactivity of the particle/electrolyte interface. This can be done either by substituting carbonate-based electrolytes or by the use of proton-scavenging electrolyte additives.

Furthermore, the dependence of the performance of LMR-NCM cells on the separator was also investigated, and its cycle life improvements might be addressed by enhancing the HF-scavenging properties of the ceramic particles that are already used for safety reasons. In addition, the intensively pushed development of all-solid-state batteries (ASSB) could open an interesting application for LMR-NCM material. If the issue of gassing, inner porosity, and electrolyte stability at the high upper cut-off potential of LMR-NCMs can be resolved, the relatively low volume change of LMR-NCM during the lithiation process compared to regular NCMs would be advantageous. In the end, the material remains exciting with all its peculiarities and a possible industrial application depends highly on the development of all other cell components.



---

## 6 References

1. Zhao, Y., Pohl, O., Bhatt, A. I., Collis, G. E., Mahon, P. J., Rüther, T. & Hollenkamp, A. F. A Review on Battery Market Trends, Second-Life Reuse, and Recycling. *Sustain. Chem.* **2**, 167–205 (2021).
2. Zhao, S., Guo, Z., Yan, K., Wan, S., He, F., Sun, B. & Wang, G. Towards high-energy-density lithium-ion batteries: Strategies for developing high-capacity lithium-rich cathode materials. *Energy Storage Mater.* **34**, 716–734 (2021).
3. Schmuch, R., Wagner, R., Hörpel, G., Placke, T. & Winter, M. Performance and cost of materials for lithium-based rechargeable automotive batteries. *Nat. Energy* **3**, 267–278 (2018).
4. Nishi, Y. The Dawn of Lithium-Ion Batteries. *Interface Mag.* **25**, 71–74 (2016).
5. Ligen, Y., Vrubel, H. & Girault, H. Mobility from Renewable Electricity: Infrastructure Comparison for Battery and Hydrogen Fuel Cell Vehicles. *World Electr. Veh. J.* **9**, 1–12 (2018).
6. Albatayneh, A., Assaf, M. N., Alterman, D. & Jaradat, M. Comparison of the Overall Energy Efficiency for Internal Combustion Engine Vehicles and Electric Vehicles. *Environ. Clim. Technol.* **24**, 669–680 (2020).
7. Zuccari, F., Orecchini, F., Santiangeli, A., Suppa, T., Ortenzi, F., Genovese, A. & Pede, G. Well to wheel analysis and comparison between conventional, hybrid and electric powertrain in real conditions of use. *AIP Conf. Proc.* **2191**, 1–10 (2019).
8. Lund, C. & Biswas, W. A Review of the Application of Lifecycle Analysis to Renewable Energy Systems. *Bull. Sci. Technol. Soc.* **28**, 200–209 (2008).
9. Li, M., Zhang, X. & Li, G. A comparative assessment of battery and fuel cell electric vehicles using a well-to-wheel analysis. *Energy* **94**, 693–704 (2016).
10. An, F. & Santini, D. Assessing Tank-to-Wheel Efficiencies of Advanced Technology Vehicles. in *SAE Technical Papers* vol. **724**, 1–23 (2003).
11. Hjelkrem, O. A., Arnesen, P., Aarseth Bø, T. & Sondell, R. S. Estimation of tank-to-wheel efficiency functions based on type approval data. *Appl. Energy* **276**, 1–8 (2020).
12. Decock, G. *Electrofuels? Yes, we can ... if we're efficient*, *Transport & Environment* **12**, 1–35 (2020).
13. Bezergianni, S. & Dimitriadis, A. Comparison between different types of renewable diesel. *Renew. Sustain. Energy Rev.* **21**, 110–116 (2013).
14. Hydrogen Fuel Cell Engines and Related Technologies. Module 1: Hydrogen Properties. *Hydrog. Fuel Cell Engines* **12**, 1–41 (2001).

15. Umweltbundesamt Energieverbrauch Deutschland, accessed 27/12/2021, <https://www.umweltbundesamt.de/daten/energie/energieverbrauch-nach-energetraegern-sektoren#entwicklung-des-endenergieverbrauchs-nach-sektoren-und-energetragern>.
16. European energy demand for transport sector, accessed 27/12/2021, <https://www.eea.europa.eu/data-and-maps/figures/consumption-by-mode-eu-2>.
17. Renewable energy in germany, accessed 27/12/2021, <https://www.bmwi.de/Redaktion/DE/Dossier/erneuerbare-energien.html>.
18. Renewable energy germany timeline, accessed 27/12/2021, [https://www.erneuerbare-energien.de/EE/Navigation/DE/Service/Erneuerbare\\_Energien\\_in\\_Zahlen/Entwicklung/entwicklung-der-erneuerbaren-energien-in-deutschland.html](https://www.erneuerbare-energien.de/EE/Navigation/DE/Service/Erneuerbare_Energien_in_Zahlen/Entwicklung/entwicklung-der-erneuerbaren-energien-in-deutschland.html).
19. König, A., Nicoletti, L., Schröder, D., Wolff, S., Waclaw, A. & Lienkamp, M. An overview of parameter and cost for battery electric vehicles. *World Electr. Veh. J.* **12**, 1–29 (2021).
20. Kwade, A., Haselrieder, W., Leithoff, R., Modlinger, A., Dietrich, F. & Droeder, K. Current status and challenges for automotive battery production technologies. *Nat. Energy* **3**, 290–300 (2018).
21. Gallagher, K. G. & Nelson, P. a. Manufacturing Costs of Batteries for Electric Vehicles. in *Lithium-Ion Batteries* 97–126 (2014).
22. Zhang, N., Zaker, N., Li, H., Liu, A., Inglis, J., Jing, L., Li, J., Li, Y., Botton, G. a. & Dahn, J. R. Cobalt-Free Nickel-Rich Positive Electrode Materials with a Core-Shell Structure. *Chem. Mater.* **31**, 10150–10160 (2019).
23. Sun, Y. K., Lee, D. J., Lee, Y. J., Chen, Z. & Myung, S. T. Cobalt-free nickel rich layered oxide cathodes for lithium-ion batteries. *ACS Appl. Mater. Interfaces* **5**, 11434–11440 (2013).
24. SMM Information & Technology Co, Ltd., Nickel price, accessed 2/9/2021, <https://price.metal.com/Nickel>.
25. SMM Information & Technology Co, Ltd., Manganese price, accessed 2/9/2021, <https://price.metal.com/Manganese>.
26. Barsotti, A. F. Copper, Cobalt, Nickel and Manganese Availability from Land-based Endowments A Perspective. *Nat. Resour. Forum* **8**, 267–278 (1984).
27. Da Costa, P. & Attias, D. Towards a Sustainable Economy. Paradoxes and Trends in Energy and Transportation. *Springer Int. Publ.* (2018).
28. Becker, D., Börner, M., Friesen, A., Klein, S., Rodehorst, U., Diehl, M., Winter, M., Placke, T. & Schmuch, R. Towards High-Performance Li-rich NCM||Graphite Cells by Germanium-Polymer Coating of the Positive Electrode Material. *J. Electrochem. Soc.* **167**, 1–13 (2020).
29. Croy, J. R., Balasubramanian, M., Gallagher, K. G. & Burrell, A. K. Review of the U.S. Department of Energy’s “Deep Dive” Effort to Understand Voltage Fade in Li- and Mn-Rich Cathodes. *Acc. Chem. Res.* **48**, 2813–2821 (2015).

30. Blomgren, G. E. The Development and Future of Lithium Ion Batteries. *J. Electrochem. Soc.* **164**, A5019–A5025 (2017).
31. Jung, C. H., Shim, H., Eum, D. & Hong, S. H. Challenges and recent progress in  $\text{LiNi}_x\text{Co}_y\text{Mn}_{1-x-y}\text{O}_2$  (NCM) cathodes for lithium ion batteries. *J. Korean Ceram. Soc.* **58**, (2021).
32. Liu, C., Neale, Z. G. & Cao, G. Understanding electrochemical potentials of cathode materials in rechargeable batteries. *Mater. Today* **19**, 109–123 (2016).
33. Quarti, M. & Bessler, W. G. Model-Based Overpotential Deconvolution, Partial Impedance Spectroscopy, and Sensitivity Analysis of a Lithium-Ion Cell with Blend Cathode. *Energy Technol.* **9**, 1–16 (2021).
34. Mizushima, K., Jones, P. C., Wiseman, P. J. & Goodenough, J. B.  $\text{Li}_x\text{CoO}_2$  ( $0 < x < 1$ ): A new cathode material for batteries of high energy density. *Mater. Res. Bull.* **15**, 783–789 (1980).
35. Li, H. Practical Evaluation of Li-Ion Batteries. *Joule* **3**, 911–914 (2019).
36. Julien, C., Mauger, A., Zaghbi, K. & Groult, H. Comparative Issues of Cathode Materials for Li-Ion Batteries. *Inorganics* **2**, 132–154 (2014).
37. Liu, Q., Su, X., Lei, D., Qin, Y., Wen, J., Guo, F., Wu, Y. a., Rong, Y., Kou, R., Xiao, X., Aguesse, F., Bareño, J., Ren, Y., Lu, W. & Li, Y. Approaching the capacity limit of lithium cobalt oxide in lithium ion batteries via lanthanum and aluminium doping. *Nat. Energy* **3**, 936–943 (2018).
38. Trading Economics, accessed 1/4/2022, <https://tradingeconomics.com/commodity>.
39. Sovacool, B. K. When subterranean slavery supports sustainability transitions? power, patriarchy, and child labor in artisanal Congolese cobalt mining. *Extr. Ind. Soc.* **8**, 271–293 (2021).
40. Liu, Z., Yu, A. & Lee, J. Y. Synthesis and characterization of  $\text{LiNi}_{1-x-y}\text{Co}_x\text{Mn}_y\text{O}_2$  as the cathode materials of secondary lithium batteries. *J. Power Sources* **81–82**, 416–419 (1999).
41. Jang, Y.-I., Huang, B., Wang, H., Maskaly, G. R., Ceder, G., Sadoway, D. R., Chiang, Y.-M., Liu, H. & Tamura, H. Synthesis and characterization of  $\text{LiAl}_y\text{Co}_{1-y}\text{O}_2$  and  $\text{LiAl}_y\text{Ni}_{1-y}\text{O}_2$ . *J. Power Sources* **81–82**, 589–593 (1999).
42. Agus Purwanto, Cornelius Satria Yudha, U Ubaidillah, Hendri Widiyandari, T. O. and H. H. NCA cathode material- synthesis metho.pdf. *Mater. Res. Express* **5**, 1–65 (2018).
43. Ryu, H. H., Sun, H. H., Myung, S. T., Yoon, C. S. & Sun, Y. K. Reducing cobalt from lithium-ion batteries for the electric vehicle era. *Energy Environ. Sci.* **14**, 844–852 (2021).
44. Li, H., Cormier, M., Zhang, N., Inglis, J., Li, J. & Dahn, J. R. Is Cobalt Needed in Ni-Rich Positive Electrode Materials for Lithium Ion Batteries? *J. Electrochem. Soc.* **166**, A429–A439 (2019).
45. Manthiram, A. A reflection on lithium-ion battery cathode chemistry. *Nat. Commun.* **11**, 1550 (2020).

46. Armand, M., Axmann, P., Bresser, D., Copley, M., Edström, K., Ekberg, C., Guyomard, D., Lestriez, B., Novák, P., Petranikova, M., Porcher, W., Trabesinger, S., Wohlfahrt-Mehrens, M. & Zhang, H. Lithium-ion batteries – Current state of the art and anticipated developments. *J. Power Sources* **479**, (2020).
47. Ding, Y., Cano, Z. P., Yu, A., Lu, J. & Chen, Z. Automotive Li-Ion Batteries: Current Status and Future Perspectives. *Electrochem. Energy Rev.* **2**, 1–28 (2019).
48. Wu, F., Maier, J. & Yu, Y. Guidelines and trends for next-generation rechargeable lithium and lithium-ion batteries. *Chem. Soc. Rev.* **49**, 1569–1614 (2020).
49. Nitta, N., Wu, F., Lee, J. T. & Yushin, G. Li-ion battery materials: present and future. *Mater. Today* **18**, 252–264 (2015).
50. Lee, W., Muhammad, S., Sergey, C., Lee, H., Yoon, J., Kang, Y. M. & Yoon, W. S. Advances in the Cathode Materials for Lithium Rechargeable Batteries. *Angew. Chemie - Int. Ed.* **59**, 2578–2605 (2020).
51. Rozier, P. & Tarascon, J. M. Review—Li-Rich Layered Oxide Cathodes for Next-Generation Li-Ion Batteries: Chances and Challenges. *J. Electrochem. Soc.* **162**, A2490–A2499 (2015).
52. Rana, J., Papp, J. K., Lebens-Higgins, Z., Zuba, M., Kaufman, L. A., Goel, A., Schmuck, R., Winter, M., Whittingham, M. S., Yang, W., McCloskey, B. D. & Piper, L. F. J. Quantifying the Capacity Contributions during Activation of  $\text{Li}_2\text{MnO}_3$ . *ACS Energy Lett.* **5**, 634–641 (2020).
53. Yu, D. Y. W., Yanagida, K., Kato, Y. & Nakamura, H. Electrochemical Activities in  $\text{Li}[\text{sub } 2]\text{MnO}[\text{sub } 3]$ . *J. Electrochem. Soc.* **156**, A417 (2009).
54. Robertson, A. D. & Bruce, P. G. Mechanism of Electrochemical Activity in  $\text{Li}_2\text{MnO}_3$ . *Chem. Mater.* **15**, 1984–1992 (2003).
55. Thackeray, M. M., Kang, S.-H., Johnson, C. S., Vaughey, J. T., Benedek, R. & Hackney, S. a.  $\text{Li}_2\text{MnO}_3$ -stabilized  $\text{LiMO}_2$  (M = Mn, Ni, Co) electrodes for lithium-ion batteries. *J. Mater. Chem.* **17**, (2007).
56. Lee, G., Wu, J., Kim, D., Cho, K., Cho, M., Yang, W. & Kang, Y. Reversible Anionic Redox Activities in Conventional  $\text{LiNi}_{1/3}\text{Co}_{1/3}\text{Mn}_{1/3}\text{O}_2$  Cathodes. *Angew. Chemie* **132**, 8759–8766 (2020).
57. Zhao, S., Yan, K., Zhang, J., Sun, B. & Wang, G. Reaction Mechanisms of Layered Lithium-Rich Cathode Materials for High-Energy Lithium-Ion Batteries. *Angew. Chemie - Int. Ed.* **60**, 2208–2220 (2021).
58. Assat, G. & Tarascon, J.-M. Fundamental understanding and practical challenges of anionic redox activity in Li-ion batteries. *Nat. Energy* **3**, 373–386 (2018).
59. Kraft, L., Zünd, T., Schreiner, D., Wilhelm, R., Günter, F. J., Reinhart, G., Gasteiger, H. A. & Jossen, A. Comparative Evaluation of LMR-NCM and NCA Cathode Active Materials in Multilayer Lithium-Ion Pouch Cells: Part II. Rate Capability, Long-Term Stability, and Thermal Behavior. *J. Electrochem. Soc.* **168**, (2021).
60. Pan, H., Zhang, S., Chen, J., Gao, M., Liu, Y., Zhu, T. & Jiang, Y. Li- and Mn-rich layered oxide cathode materials for lithium-ion batteries: a review from fundamentals to research progress and applications. *Mol. Syst. Des. Eng.* **3**, 748–803 (2018).

61. Zheng, J., Myeong, S., Cho, W., Yan, P., Xiao, J., Wang, C., Cho, J. & Zhang, J. Li- and Mn-Rich Cathode Materials: Challenges to Commercialization. *Adv. Energy Mater.* **7**, (2017).
62. Hu, S., Pillai, A. S., Liang, G., Pang, W. K., Wang, H., Li, Q. & Guo, Z. Li-Rich Layered Oxides and Their Practical Challenges: Recent Progress and Perspectives. *Electrochem. Energy Rev.* **2**, 277–311 (2019).
63. Schreiner, D., Zünd, T., Günter, F. J., Kraft, L., Stumper, B., Linsenmann, F., Schüßler, M., Wilhelm, R., Jossen, A., Reinhart, G. & Gasteiger, H. A. Comparative Evaluation of LMR-NCM and NCA Cathode Active Materials in Multilayer Lithium-Ion Pouch Cells: Part I. Production, Electrode Characterization, and Formation. *J. Electrochem. Soc.* **168**, (2021).
64. Liu, H., Chen, Y., Hy, S., An, K., Venkatachalam, S., Qian, D., Zhang, M. & Meng, Y. S. Operando Lithium Dynamics in the Li-Rich Layered Oxide Cathode Material via Neutron Diffraction. *Adv. Energy Mater.* **6**, (2016).
65. Strehle, B., Zünd, T., Sicolo, S., Kiessling, A., Baran, V. & Gasteiger, H. a. Correlating the Voltage Hysteresis in Li- and Mn-Rich Layered Oxides to Reversible Structural Changes by Using X-ray and Neutron Powder Diffraction. *J. Electrochem. Soc.* **169**, (2022).
66. Assat, G. & Tarascon, J. M. Fundamental understanding and practical challenges of anionic redox activity in Li-ion batteries. *Nat. Energy* **3**, 373–386 (2018).
67. Hong, J., Seo, D.-H., Kim, S.-W., Gwon, H., Oh, S.-T. & Kang, K. Structural evolution of layered  $\text{Li}_{1.2}\text{Ni}_{0.2}\text{Mn}_{0.6}\text{O}_2$  upon electrochemical cycling in a Li rechargeable battery. *J. Mater. Chem.* **20**, (2010).
68. Gu, M., Belharouak, I., Zheng, J., Wu, H., Xiao, J., Genc, A., Amine, K., Thevuthasan, S., Baer, D. R., Zhang, J.-G., Browning, N. D., Liu, J. & Wang, C. Formation of the Spinel Phase in the Layered Composite Cathode Used in Li-Ion Batteries. *ACS Nano* **7**, 760–767 (2013).
69. Mohanty, D., Li, J., Abraham, D. P., Huq, A., Payzant, E. A., Wood, D. L. & Daniel, C. Unraveling the Voltage-Fade Mechanism in High-Energy-Density Lithium-Ion Batteries: Origin of the Tetrahedral Cations for Spinel Conversion. *Chem. Mater.* **26**, 6272–6280 (2014).
70. Croy, J. R., Balasubramanian, M., Gallagher, K. G. & Burrell, A. K. Review of the U.S. Department of Energy's 'deep Dive' Effort to Understand Voltage Fade in Li- and Mn-Rich Cathodes. *Acc. Chem. Res.* **48**, 2813–2821 (2015).
71. Kraft, L., Hoefling, A., Zünd, T., Kunz, A., Steinhardt, M., Tübke, J. & Jossen, A. Implications of the Heat Generation of LMR-NCM on the Thermal Behavior of Large-Format Lithium-Ion Batteries. *J. Electrochem. Soc.* **168**, (2021).
72. Gallagher, K. G., Croy, J. R., Balasubramanian, M., Bettge, M., Abraham, D. P., Burrell, A. K. & Thackeray, M. M. Correlating hysteresis and voltage fade in lithium- and manganese-rich layered transition-metal oxide electrodes. *Electrochem. commun.* **33**, 96–98 (2013).
73. Metzger, M., Strehle, B., Solchenbach, S. & Gasteiger, H. A. Origin of  $\text{H}_2$  Evolution in LIBs:  $\text{H}_2\text{O}$  Reduction vs. Electrolyte Oxidation. *J. Electrochem. Soc.* **163**, A798–A809 (2016).

74. Freiberg, A. T. S., Sicklinger, J., Solchenbach, S. & Gasteiger, H. A. Li<sub>2</sub>CO<sub>3</sub> decomposition in Li-ion batteries induced by the electrochemical oxidation of the electrolyte and of electrolyte impurities. *Electrochim. Acta* **346**, (2020).
75. Kim, K., Park, I., Ha, S. Y., Kim, Y., Woo, M. H., Jeong, M. H., Shin, W. C., Ue, M., Hong, S. Y. & Choi, N. S. Understanding the thermal instability of fluoroethylene carbonate in LiPF<sub>6</sub>-based electrolytes for lithium ion batteries. *Electrochim. Acta* **225**, 358–368 (2017).
76. Pritzl, D., Solchenbach, S., Wetjen, M. & Gasteiger, H. A. Analysis of Vinylene Carbonate (VC) as Additive in Graphite/LiNi<sub>0.5</sub>Mn<sub>1.5</sub>O<sub>4</sub> Cells. *J. Electrochem. Soc.* **164**, A2625–A2635 (2017).
77. Freiberg, A. T. S., Roos, M. K., Wandt, J., Vivie-riedle, R. De & Gasteiger, H. A. Singlet Oxygen Reactivity with Carbonate Solvents Used for Li-Ion Battery Electrolytes. *The Journal of Physical Chemistry A* **45**, 8828–8839 (2018).
78. Solchenbach, S., Hong, G., Freiberg, A. T. S., Jung, R. & Gasteiger, H. a. Electrolyte and SEI Decomposition Reactions of Transition Metal Ions Investigated by On-Line Electrochemical Mass Spectrometry. *J. Electrochem. Soc.* **165**, A3304–A3312 (2018).
79. Liu, Q., Du, C., Shen, B., Zuo, P., Cheng, X., Ma, Y., Yin, G. & Gao, Y. Understanding undesirable anode lithium plating issues in lithium-ion batteries. *RSC Adv.* **6**, 88683–88700 (2016).
80. Eshetu, G. G., Zhang, H., Judez, X., Adenusi, H., Armand, M., Passerini, S. & Figgemeier, E. Production of high-energy Li-ion batteries comprising silicon-containing anodes and insertion-type cathodes. *Nat. Commun.* **12**, 1–14 (2021).
81. Obrovac, M. N. & Chevrier, V. L. Alloy Negative Electrodes for Li-Ion Batteries. *Chem. Rev.* **114**, 11444–11502 (2014).
82. Wetjen, M., Pritzl, D., Jung, R., Solchenbach, S., Ghadimi, R. & Gasteiger, H. A. Differentiating the Degradation Phenomena in Silicon-Graphite Electrodes for Lithium-Ion Batteries. *J. Electrochem. Soc.* **164**, A2840–A2852 (2017).
83. Luo, F., Liu, B., Zheng, J., Chu, G., Zhong, K., Li, H., Huang, X. & Chen, L. Review—Nano-Silicon/Carbon Composite Anode Materials Towards Practical Application for Next Generation Li-Ion Batteries. *J. Electrochem. Soc.* **162**, A2509–A2528 (2015).
84. Li, H., Li, H., Yang, Z., Yang, L., Gong, J., Liu, Y., Wang, G., Zheng, Z., Zhong, B., Song, Y., Zhong, Y., Wu, Z. & Guo, X. SiO<sub>x</sub> Anode: From Fundamental Mechanism toward Industrial Application. *Small* **17**, 1–21 (2021).
85. Graf, M., Berg, C., Bernhard, R., Haufe, S., Pfeiffer, J. & Gasteiger, H. a. Effect and Progress of the Amorphization Process for Microscale Silicon Particles under Partial Lithiation as Active Material in Lithium-Ion Batteries. *J. Electrochem. Soc.* **169**, 020536 (2022).
86. Holtstiege, F., Bärman, P., Nölle, R., Winter, M. & Placke, T. Pre-lithiation strategies for rechargeable energy storage technologies: Concepts, promises and challenges. *Batteries* **4**, 1–39 (2018).
87. Xu, K. Electrolytes and Interphases in Li-Ion Batteries and Beyond. *Chem. Rev.* **114**, 11503–11618 (2014).

88. Song, W., Harlow, J., Logan, E., Hebecker, H., Coon, M., Molino, L., Johnson, M., Dahn, J. & Metzger, M. A Systematic Study of Electrolyte Additives in Single Crystal and Bimodal  $\text{LiNi}_{0.8}\text{Mn}_{0.1}\text{Co}_{0.1}\text{O}_2$  /Graphite Pouch Cells . *J. Electrochem. Soc.* **168**, (2021).
89. Zhang, S. S. A review on electrolyte additives for lithium-ion batteries. *J. Power Sources* **162**, 1379–1394 (2006).
90. Janek, J. & Zeier, W. G. A solid future for battery development. *Nat. Energy* **1**, (2016).
91. Famprikis, T., Canepa, P., Dawson, J. A., Islam, M. S. & Masquelier, C. Fundamentals of inorganic solid-state electrolytes for batteries. *Nat. Mater.* **18**, 1278–1291 (2019).
92. Orendorff, C. J. The role of separators in lithium-ion cell safety. *Electrochem. Soc. Interface* **21**, 61–65 (2012).
93. Landesfeind, J., Hattendorff, J., Ehrl, A., Wall, W. A. & Gasteiger, H. A. Tortuosity Determination of Battery Electrodes and Separators by Impedance Spectroscopy. *J. Electrochem. Soc.* **163**, A1373–A1387 (2016).
94. L bberding, H., Wessel, S., Offermanns, C., Kehrer, M., Rother, J., Heimes, H. & Kampker, A. From cell to battery system in BEVs: Analysis of system packing efficiency and cell types. *World Electr. Veh. J.* **11**, 1–15 (2020).
95. Bilgin, B., Magne, P., Malysz, P., Yang, Y., Pantelic, V., Preindl, M., Korobkine, A., Jiang, W., Lawford, M. & Emadi, A. Making the Case for Electrified Transportation. *IEEE Trans. Transp. Electrif.* **1**, 4–17 (2015).
96. Batterieforum, ExZellTUM II, accessed 7/9/2022, <https://db.batterieforum-deutschland.de/projekte/exzelltum-ii-einzelprojekt/>.
97. Oswald, S., Riewald, F. & Gasteiger, H. A. Novel Method for Monitoring the Electrochemical Capacitance by In Situ Impedance Spectroscopy as Indicator for Particle Cracking of Nickel-Rich NCMs: Part III. Development of a Simplified Measurement Setup. *J. Electrochem. Soc.* **169**, (2022).
98. Yu, C., Wang, H., Guan, X., Zheng, J. & Li, L. Conductivity and electrochemical performance of cathode  $x\text{Li}_2\text{MnO}_3 \cdot (1-x)\text{LiMn}_{1/3}\text{Ni}_{1/3}\text{Co}_{1/3}\text{O}_2$  ( $x = 0.1, 0.2, 0.3, 0.4$ ) at different temperatures. *J. Alloys Compd.* **546**, 239–245 (2013).
99. Matthias Lex. *Optimization of Li-Rich Layered NMC Cathodes' Material Composition in regard to the Upscaling Process for Next- Generation Li-Ion Batteries*, Semester thesis, Chair of Technical Electrochemistry (TEC), Department of Chemistry, Technical University of Munich (2018).
100. Rebecca Wilhelm. *Improving the electrical conductivity of HE-NCM in Li-Ion Batteries by optimizing calendaring and conductive carbon composition*, Bachelor thesis, Chair of Technical Electrochemistry (TEC), Department of Chemistry, Technical University of Munich (2018).
101. Teufl, T., Strehle, B., M ller, P., Gasteiger, H. a. & Mendez, M. a. Oxygen Release and Surface Degradation of Li- and Mn-Rich Layered Oxides in Variation of the  $\text{Li}_2\text{MnO}_3$  Content . *J. Electrochem. Soc.* **165**, A2718–A2731 (2018).

102. Erickson, E. M., Schipper, F., Tian, R., Shin, J.-Y., Erk, C., Chesneau, F. F., Lampert, J. K., Markovsky, B. & Aurbach, D. Enhanced capacity and lower mean charge voltage of Li-rich cathodes for lithium ion batteries resulting from low-temperature electrochemical activation. *RSC Adv.* **7**, 7116–7121 (2017).
103. Tsiouvaras, N., Meini, S., Buchberger, I. & Gasteiger, H. A. A Novel On-Line Mass Spectrometer Design for the Study of Multiple Charging Cycles of a Li-O<sub>2</sub> Battery. *J. Electrochem. Soc.* **160**, A471–A477 (2013).
104. Metzger, M., Marino, C., Sicklinger, J., Haering, D. & Gasteiger, H. A. Anodic Oxidation of Conductive Carbon and Ethylene Carbonate in High-Voltage Li-Ion Batteries Quantified by On-Line Electrochemical Mass Spectrometry. *J. Electrochem. Soc.* **162**, A1123–A1134 (2015).
105. Teufl, T., Pritzl, D. J., Hartmann, L., Solchenbach, S., Mendez, M. & Gasteiger, H. Implications of the Thermal Stability of FEC-Based Electrolytes for Li-Ion Batteries. *J. Electrochem. Soc.* **170**, (2023).
106. Teufl, T., Pritzl, D., Krieg, P., Strehle, B., Mendez, M. A. & Gasteiger, H. A. Operating EC-based Electrolytes with Li- and Mn-Rich NCMs: The Role of O<sub>2</sub> -Release on the Choice of the Cyclic Carbonate. *J. Electrochem. Soc.* **167**, 110505 (2020).
107. Solchenbach, S., Pritzl, D., Kong, E. J. Y., Landesfeind, J. & Gasteiger, H. a. A Gold Micro-Reference Electrode for Impedance and Potential Measurements in Lithium Ion Batteries. *J. Electrochem. Soc.* **163**, A2265–A2272 (2016).
108. Berkes, B. B., Schiele, A., Sommer, H., Brezesinski, T. & Janek, J. On the gassing behavior of lithium-ion batteries with NCM523 cathodes. *J. Solid State Electrochem.* **20**, 2961–2967 (2016).
109. Niamh Ryall and Nuria Garcia-Araez. Highly Sensitive Operando Pressure Measurements of Li-Ion Battery Materials with a Simply Modified Swagelok Cell. *J. Electrochem. Soc.* (2020).
110. Lepoivre, F., Grimaud, A., Larcher, D. & Tarascon, J.-M. Use of a Swagelok-Based Electrochemical Cell Enabling Long-Term and Reliable Investigation of Metal-Air Batteries through in-Operando Gas Monitoring. *ECS Meet. Abstr.* **MA2016-03**, 371–371 (2016).
111. Schipper, F., Erickson, E. M., Erk, C., Shin, J.-Y., Chesneau, F. F. & Aurbach, D. Review—Recent Advances and Remaining Challenges for Lithium Ion Battery Cathodes. *J. Electrochem. Soc.* **164**, A6220–A6228 (2017).
112. Andre, D., Kim, S.-J., Lamp, P., Lux, S. F., Maglia, F., Paschos, O. & Stiaszny, B. Future generations of cathode materials: an automotive industry perspective. *J. Mater. Chem. A* **3**, 6709–6732 (2015).
113. Kwade, A., Haselrieder, W., Leithoff, R., Modlinger, A., Dietrich, F. & Droeder, K. Current status and challenges for automotive battery production technologies. *Nat. Energy* **3**, 290–300 (2018).
114. Freiberg, A. T. S., Roos, M. K., Wandt, J., Vivie-riedle, R. De & Gasteiger, H. A. Singlet Oxygen Reactivity with Carbonate Solvents Used for Li-Ion Battery Electrolytes. *J. Phys. Chem. A* **122**, 8828–8839 (2018).

- 
115. Wandt, J., Freiberg, A. T. S., Ogrodnik, A. & Gasteiger, H. a. Singlet oxygen evolution from layered transition metal oxide cathode materials and its implications for lithium-ion batteries. *Mater. Today* **21**, 825–833 (2018).
  116. Croy, J. R., Gallagher, K. G., Balasubramanian, M., Chen, Z., Ren, Y., Kim, D., Kang, S.-H., Dees, D. W. & Thackeray, M. M. Examining Hysteresis in Composite  $x\text{Li}_2\text{MnO}_3 \cdot (1-x)\text{LiMO}_2$  Cathode Structures. *J. Phys. Chem. C* **117**, 6525–6536 (2013).
  117. Assat, G., Foix, D., Delacourt, C., Iadecola, A., Dedryvère, R. & Tarascon, J. M. Fundamental interplay between anionic/cationic redox governing the kinetics and thermodynamics of lithium-rich cathodes. *Nat. Commun.* **8**, (2017).
  118. Gent, W. E., Lim, K., Liang, Y., Li, Q., Barnes, T., Ahn, S.-J., Stone, K. H., McIntire, M., Hong, J., Song, J. H., *et al.* Coupling between oxygen redox and cation migration explains unusual electrochemistry in lithium-rich layered oxides. *Nat. Commun.* **8**, (2017).
  119. de Biasi, L., Schwarz, B., Brezesinski, T., Hartmann, P., Janek, J. & Ehrenberg, H. Chemical, Structural, and Electronic Aspects of Formation and Degradation Behavior on Different Length Scales of Ni-Rich NCM and Li-Rich HE-NCM Cathode Materials in Li-Ion Batteries. *Adv. Mater.* **31**, (2019).
  120. Kong, X., Zhang, Y., Peng, S., Zeng, J. & Zhao, J. Superiority of Single-Crystal to Polycrystalline  $\text{LiNi}_x\text{Co}_y\text{Mn}_{1-x-y}\text{O}_2$  Cathode Materials in Storage Behaviors for Lithium-Ion Batteries. *ACS Sustain. Chem. Eng.* **8**, 14938–14948 (2020).
  121. Langdon, J. & Manthiram, A. A perspective on single-crystal layered oxide cathodes for lithium-ion batteries. *Energy Storage Mater.* **37**, 143–160 (2021).



## 7 Acknowledgements

First of all, I would like to thank my PhD advisor **Hubert Gasteiger**. You have found a unique mix of leaving each student room for following their own way and ideas, yet at the same time, you improved each path with your astuteness and passion for the scientific truth. I learned a lot about electrochemistry from you but also, and not less importantly, about working in collaborations, choosing the right and not the simple way and to always question myself. Your maybe greatest achievement for me is the group and their attitude that you have generated at TEC. They offer and combine a scientifically challenging atmosphere with the security of mutual support from everyone and therefore we profited not only from you directly but also from the TEC collective knowledge that you maintain.

Many thanks go to **Veronika Pichler** who had the difficult duty to introduce me to German bureaucracy. Her patience was endless and to whatever problem, she found a solution, the money or just the right words.

I would also like to express my gratitude to **all current and former members** of the Chair of Technical Electrochemistry for the collegial working atmosphere. You all together were responsible for a group where one always found help and support, scientific challenges, an open ear at any time and of course company for a drink or two. Special thanks to my project collaborators **Benjamin Strehle** and **Franziska Friedrich**, working with you definitely improved my eye for details and I was happy to have you on my side during all the challenges we went through.

On that note, I also want to thank my former students **Rebecca Wilhelm, Aleksandr Kießling, Viola Knödler, Kaleigh Hunt, Matthias Lex, Alexander Salum and Artur Kupczak** for their scientific support. In particular, the ones who stayed in “Team Tanja” after their project and supported me with their enthusiasm, challenging questions, organization skills and great work on the mission “save the world with batteries”.

I acknowledge the financial support provided by the **German Federal Ministry of Education and Research (BMBF)** within the projects ExZellTUM II (grant number

03XP0081) and ExZellTUMIII (grant number 03XP0255). Furthermore, I greatly acknowledge our ExZellTUM team at TEC with the former and current members **Fabian Linsenmann, Robert Morasch** (even though he unsuccessfully tried to be not part of the team), **Johannes Landesfeind, Bharat Suthar and Philip Rapp**. I enjoyed our team spirit and the challenging but also supportive meetings on Wednesdays. Special thanks also go to Fabian and Robert, who gave me a very warm and funny welcome in Germany (and confirmed all my prejudices about Swabia).

I am very grateful for the ExZellTUM Collaboration with the **Institute for Electrical Energy Storage Technology (EES)**, especially to **Ludwig Kraft**, I still hope to reach one day even just partially your efficiency and I thank you for the great cooperation.

The place I would also call my second home at TUM, is the **Institute for Machine Tools and Industrial Management (iwb)**. Thanks to the support of **David Schreiner, Florian Günther, Benedikt Stumper, Nicolas Billot, Josef Keilhofer, Fabian Konwitschny and Jan Hagemeister**, we not only worked hard together, there were also many good memories of all the after-work meetings. Of course, the whole **iwb battery production team** made the ExZellTUM project into a real interdisciplinary project and therefore thanks to all of you.

The TEC mountaineering group with the founders **Stefan Oswald, Maximilian Graf, Christian Sedlmeier** and **Lennart Reuter** were reliable partners in the lab and on the mountain, thank you for all the unforgettable experiences.

Thanks to **Loredana Protesescu, Marc Walter, Laura Piveteau**, and **Maria Ibáñez** from the former Kovalenko group, you inspired and motivated me to follow a scientific path and have always been role models to me.

Finally, yet importantly, I would like to say thank you to **my Family (including Lea Pohlmeier)** who have been there for me unconditionally during all the ups and downs of my PhD time, the time before and after. Without your support and your continuous push, I would probably never have come to the point of finally writing this thesis.

Appendix: One additional loved person, **Markus Kammans**, joined me for my last writing steps and was immediately part of the pushing and supportive family, Thank you!

## 8 Scientific Contributions

### Articles created within the PhD time

1. F. Friedrich<sup>✉</sup>, **T. Zünd**<sup>✉</sup>, A. Hoefling, J. Tübke, H. A. Gasteiger, Classification of heat evolution terms regarding the OCV hysteresis in Li- and Mn-rich NCM in comparison to a regular NCA. *J. Electrochem. Soc.* **169**, 040547 (2022).
2. B. Strehle<sup>✉</sup>, **T. Zünd**<sup>✉</sup>, S. Siculo, A. Kießling, V. Baran, and H. A. Gasteiger, “Correlating the Voltage Hysteresis in Li- and Mn-Rich Layered Oxides to Reversible Structural Changes by Using X-Ray and Neutron Powder Diffraction. *J. Electrochem. Soc.* **169**, 020554 (2022).
3. L. Kraft, A. Hoefling, **T. Zünd**, A. Kunz, M. Steinhardt, J. Tübke, A. Jossen, Implications of the Heat Generation of LMR-NCM on the Thermal Behavior of Large-Format Lithium-Ion Batteries, *J. Electrochem. Soc.* **168**, 053505 (2021).
4. L. Kraft<sup>✉</sup>, **T. Zünd**<sup>✉</sup>, D. Schreiner, R. Wilhelm, F. Günter, H. Gasteiger, A. Jossen, Comparative Evaluation of LMR-NCM and NCA Cathode Materials in Multilayer Lithium-Ion Pouch Cells - Part II: Rate Capability, Long-Term Stability and Thermal Behavior, *J. Electrochem. Soc.* **168**, 020537(2021).
5. D. Schreiner<sup>✉</sup>, **T. Zünd**<sup>✉</sup>, F. Günter, L. Kraft, B. Stumper, F. Linsenmann, M. Schüßler, R. Wilhelm, A. Jossen, G. Reinhart, Hubert A. Gasteiger, Comparative Evaluation of LMR-NCM and NCA Cathode Materials in Multilayer Lithium-Ion Pouch Cells - Part I: Production, Electrode Characterization and Formation, *J. Electrochem. Soc.* **168**, 030507 (2021).

### Articles created outside the PhD time

6. A.N. Filippin, T.-Y. Lin, M. Rawlence, **T. Zünd**, K.V. Kravchyk, J. Sastre-Pellicer, S.G. Haass, A. Wäckerlin, M.V. Kovalenko, S. Buecheler, Ni–Al–Cr superalloy as high temperature cathode current collector for advanced thin film Li batteries, *RSC Adv.* **8**, 20304-20313 (2018).
7. K.V. Kravchyk, **T. Zünd**, M. Wörle, M.V. Kovalenko, M.I. Bodnarchuk, NaFeF<sub>3</sub> Nanoplates as Low-Cost Sodium and Lithium Cathode Materials for Stationary Energy Storage, *Chem. Mater.* **30**, 1825–1829 (2018).
8. A.N. Filippin, M. Rawlence, A. Wäckerlin, T. Feurer, **T. Zünd**, K.V. Kravchyk, M.V. Kovalenko, Y.E. Romanyuk, A.N. Tiwari, S. Buecheler, Chromium nitride as a stable cathode current collector for all-solid-state thin film Li-ion batteries, *RSC Adv.* **7**, 26960-26967 (2017).

9. C. Guntlin, **T. Zünd**, K.V. Kravchyk, M. Wörle, M.I. Bodnarchuk, M. Kovalenko, Nanocrystalline FeF<sub>3</sub> and MF<sub>2</sub> (M=Fe, Co, Mn) from Metal Tri-fluoroacetates and their Li (Na)-ion Storage Properties, *J. Mater. Chem. A* **5**, 7383–7393 (2017).
10. L. Protesescu, **T. Zünd**, M. Bodnarchuk, M. Kovalenko, Air-stable, near-to-mid-infrared emitting solids of PbTe/CdTe core-shell colloidal quantum dots, *ChemPhysChem* **17**, 670–674 (2016).
11. M. Walter, **T. Zünd**, M. Kovalenko, Pyrite (FeS<sub>2</sub>) Nanocrystals as Inexpensive High-Performance Lithium-Ion Cathode and Sodium-Ion Anode Materials, *Nanoscale* **7**, 9158 – 9163 (2015).

## Oral and Poster presentations

1. Correlating the Voltage Hysteresis in Li- and Mn-Rich Layered Oxides to Reversible Structural Changes using X-ray and Neutron Diffraction, Poster, GRC Batteries, Ventura 2020.
2. Impact of Calendering on Processability, Cell Performance and Material Structure of Electrodes in Multilayer Li-Ion Pouch Cells, Poster, Batterieforum, Berlin 2020.
3. Formation Strategies for Over-Lithiated NCMs – Cell Performance vs. Feasibility in Industrial Sized Cells, Oral presentation, 235th ECS Meeting, Dallas (USA), 2019.
4. Challenges of upscaling a laboratory coin cell to a semi-automatically processed 5 Ah pouch cell with a next-generation cathode material, Poster, Batterieforum, Berlin 2019.
5. ExZellTUM II – Cluster of Battery Research at the Technical University of Munich, Poster, Energy Colloquium (MSE), Munich, 2018.